# Alignment of the LHCb Tracking Stations and Selection of $X(3872)$ and $Z(4430)^{\pm}$ in $pp$ Collisions at 14 TeV

PAR

## Louis NICOLAS

*EPFL*

ÉCOLE POLYTECHNIQUE
FÉDÉRALE DE LAUSANNE

Suisse
2009

# Résumé

ℒ'EXPÉRIENCE LHCb est l'une des quatre expériences principales situées au Grand Collisionneur de Hadrons (LHC) au CERN, près de Genève en Suisse. Le détecteur LHCb est un spectromètre à un seul bras dédié à la mesure précise de la violation CP, et à l'étude de désintégrations rares des hadrons $b$. Autant l'énergie à laquelle les collisions proton–proton vont avoir lieu, que le nombre d'évènements qui seront sélectionnés sont sans précédent. Le détecteur LHCb va débuter ses mesures en novembre 2009 et être opérationnel durant plusieurs années.

Étant une expérience destinée à faire des mesures de précision, LHCb se fie à ses excellentes efficacités de reconstruction et de système de déclenchement, à ses exceptionnelles résolutions en temps propre et en masse, ainsi qu'à son système fiable d'identification des particules, autant pour la sélection d'évènements que pour l'étiquetage de la saveur des désintégrations de mésons $B$. Ces performances ne sont cependant pas possibles sans une construction et un alignement minutieux du détecteur. Une mesure précise de la position de tous les détecteurs a été opérée, spécialement pour le trajectographe interne (IT), un appareil de détection de traces qui utilise la technologie des pistes en silicium. Cependant, ces mesures ne sont précises qu'à l'ordre de la résolution spatiale du détecteur.

La première partie de cette thèse discute de l'alignement du détecteur. Une méthode informatique d'alignement a été mise au point afin d'améliorer la connaissance de la position des différentes parties du détecteur. La nouveauté de cette méthode réside dans le fait qu'elle utilise des traces venant de la procédure standard d'ajustement des traces, basée sur un filtre de Kalman, et non sur un modèle global. L'avantage de cette méthode est qu'elle permet de prendre correctement en compte la diffusion Coulombienne multiple due aux interactions dans la matière, le champ magnétique, ainsi que les corrections des pertes d'énergie. Elle permet aussi de prendre en compte les corrélations entre les points de mesures sur les traces. Ce document présente deux scénarios réalistes, utilisant des données simulées, dans lesquels l'alignement des trajectographes internes et externes (IT et OT) devra être effectué. Une stratégie générale est définie en alignant pas à pas le détecteur, en commençant par les plus gros éléments et en descendant dans la hiérarchie du détecteur en direction des plus petits objets. Une sélection de traces dédiée à l'alignement est aussi développée. En particulier, il est montré qu'une coupure évolutive sur le $\chi^2$ de l'ajustement des traces est nécessaire durant la procédure d'alignement.

En partant d'un détecteur désaligné, les deux scénarios utilisent des traces provenant soit de collisions entre les protons et le gaz résiduel à une énergie de $450\,\mathrm{GeV/c}$ sans champ magnétique, soit de collisions proton–proton générées avec une énergie dans le centre de masse de $\sqrt{s} = 14\,\mathrm{TeV}$ et lorsque le champ magnétique de l'expérience est enclenché. Il est montré que la méthode d'alignement est capable de corriger des désalignements de

l'ordre de 1–2 mm avec une précision meilleure que 20 % de la résolution propre pour l'IT et 5 % pour l'OT, dans les deux scénarios. La précision de l'alignement est ensuite validée en étudiant la distribution en masse de mésons $J/\psi$ et $K_S^0$ reconstruits et en montrant que la résolution en masse pour ces deux types de particules n'est pas dégradée de plus de 2 % entre le cas idéal et le cas après ré-alignement du détecteur.

Durant les étés de 2008 et 2009, des données ont été enregistrées par LHCb lors de tests de synchronisation du LHC. L'alignement de l'IT utilisant ces données à grande multiplicité de traces est présenté dans ce document. Une reconnaissance de structure et une sélection de traces dédiées sont utilisées afin d'obtenir un échantillon de traces de bonne qualité. L'IT est aligné jusqu'aux plus petites structures avec une précision de $20\,\mu$m. Cette précision est obtenue en étudiant la distribution des résidus non-biaisés par rapport aux traces reconstruites. Il est aussi montré que les résultats d'alignement ne dépendent pas de la position initiale du détecteur.

La deuxième partie de cette thèse traite des premières études à LHCb des particules $X(3872)$ et $Z(4430)^{\pm}$. Il y a six ans, la collaboration Belle a découvert une nouvelle particule appelée le $X(3872)$. Les théoriciens ont travaillé dur afin d'inclure cette particule, ainsi que les nombreuses autres découvertes faites depuis, dans leurs modèles. Les expérimentateurs de plusieurs collaborations, quant à eux, ont répété l'observation de cette particule dans différents modes de désintégration. Cependant, la nature et les nombres quantiques du $X(3872)$ restent incertains. Belle a aussi découvert un état chargé appelé le $Z(4430)^{\pm}$, mais cette découverte n'a pour l'instant pas pu être confirmée par quelqu'autre expérience que ce soit. Dans ces deux cas, LHCb devrait pouvoir jouer un rôle important. Des sélections des désintégration $X(3872) \rightarrow J/\psi\,\pi^+\pi^-$ dans le canal $B^{\pm} \rightarrow X(3872)K^{\pm}$ et de $B^0 \rightarrow Z(4430)^{\pm}K^{\mp}$ avec le $Z(4430)^{\pm}$ se désintégrant en $\psi(2S)\pi^{\pm}$ sont présentées dans ce document. Un nombre de 1'850 évènements de $B^{\pm} \rightarrow X(3872)K^{\pm}$ reconstruits et sélectionnées est obtenu par année nominale (correspondant à une luminosité intégrée de $2\,\text{fb}^{-1}$), pour un rapport bruit-sur-signal dans l'intervalle [0.3, 3.4] à 90 % CL. Avec une telle statistique, une demi-année nominale sera suffisante pour choisir entre les deux dernières possibilités pour le spin du $X(3872)$. Pour le $Z(4430)^{\pm}$, un nombre annuel de 6'200 évènements reconstruits et sélectionnés dans le canal $B^0 \rightarrow Z(4430)^{\pm}K^{\mp}$ est obtenu pour un rapport $B/S$ dans l'intervalle [2.7, 5.3]. Ainsi, la confirmation ou l'infirmation de la découverte de Belle sera possible, déjà durant la première phase de prise de données à LHCb, avec une énergie dans le centre de masse des collisions de $\sqrt{s} = 7 - 10\,\text{TeV}$.

**Mots clés :** CERN, LHC, LHCb, alignement, détecteur de traces au silicium, spectroscopie du charmonium, $X(3872)$, $Z(4430)^{\pm}$.

# Abstract

$\mathfrak{T}$HE LHCb experiment is one of the four large experiments located at the Large Hadron Collider (LHC) at CERN, close to Geneva, Switzerland. The LHCb detector is a single-arm forward spectrometer which is dedicated to precision measurements of CP violation, as well as to the study of rare $b$-hadron decays. Both the energy at which the proton–proton collisions will take place and the statistics of events that will be selected are unprecedented. The LHCb detector will start its measurements in November 2009 and operate for several years.

Being an experiment for precision measurements, LHCb relies on excellent reconstruction and trigger efficiencies, outstanding proper-time and momentum resolutions, as well as on a reliable particle identification, both for the event selection and the flavour tagging of $B$-meson decays. These performances are however not possible without a precise construction and alignment of the detector. An extensive survey of the detector geometry has been performed. However these measurements, for instance for the Inner Tracker, a silicon-strip tracking device, are only precise to the order of the detector resolution.

The first part of the thesis discusses the detector alignment. A software alignment method has been developed in order to improve the knowledge of the detector element position. The novelty of this method is that it uses the tracks from the standard track-fitting procedure, which is based on a Kalman filter, and not on a global track model. The advantage of this method is that it is possible to properly take the multiple Coulomb scattering, the magnetic field and the energy loss corrections into account. It also allows to correctly take into account the correlations between the hits on tracks. This document presents two realistic running scenarios, using simulated data, in which the alignment of the Inner and Outer Trackers (IT and OT) will need to be performed. A general strategy is defined for the alignment in a multi-step manner, starting from a coarse granularity and descending step-by-step to a finer detector granularity. A dedicated track selection is also developed. In particular, an evolving cut on the $\chi^2$ of the track fit is shown to be essential in the alignment procedure.

Starting from a misaligned detector, the two scenarios use tracks coming either from beam–gas collisions at an energy of $450\,\mathrm{GeV/c}$ without magnetic field, or from proton–proton collisions at a centre-of-mass energy of $\sqrt{s} = 14\,\mathrm{TeV}$ and when the magnetic field of the experiment is turned on. It is shown that the alignment software is able to recover from misalignments of the order of 1–2 mm with a precision better than $20\,\%$ of the single-hit resolution for the IT and $5\,\%$ for the OT, in both scenarios. The precision of this alignment is then validated by studying the mass distributions of reconstructed $J/\psi$ and $K_\mathrm{S}^0$ mesons and by showing that the mass resolution for these particles is not degraded by more than $2\,\%$ between the ideal case and the case after re-alignment of the detector.

In the Summer of 2008 and 2009, data were taken at LHCb during LHC synchronisation tests. The alignment of the IT using these high track-multiplicity data is presented in this document. A dedicated pattern recognition and track selection are used in order to obtain a sample of good-quality tracks. The IT is aligned down to the lowest granularity with a precision of $20\,\mu$m. This precision is obtained by studying the distributions of unbiased residuals with respect to the reconstructed tracks. It is also shown that the alignment results do not depend on the position of the detector before alignment.

The second part of this thesis discusses the first studies at LHCb of the $X(3872)$ and $Z(4430)^{\pm}$ particles. Six years ago, the Belle collaboration discovered a new state called the $X(3872)$. Several theoretical models have been developed in order to include this state, and the many others discovered since then. On the other hand, several collaborations have repeated the observation of this resonance in several decay modes. However, the nature and the quantum numbers of this state remain uncertain. Belle also discovered a charged state called the $Z(4430)^{\pm}$, but this discovery has not been confirmed by any other experiment yet. For both these states, LHCb is expected to play an important role. A Monte Carlo feasibility study of the selections of the $X(3872) \rightarrow J/\psi\,\pi^{+}\pi^{-}$ decay in the $B^{\pm} \rightarrow X(3872)K^{\pm}$ channel and of the $B^{0} \rightarrow Z(4430)^{\pm}K^{\mp}$ with $Z(4430)^{\pm}$ decaying to $\psi(2S)\pi^{\pm}$ are presented in this document. A yield of 1'850 reconstructed, selected and triggered $B^{\pm} \rightarrow X(3872)K^{\pm}$ events is obtained per nominal year (corresponding to an integrated luminosity of $2\,\text{fb}^{-1}$), for a background-to-signal ratio in the interval $[0.3,\,3.4]$ at 90 % CL. With such statistics, half a nominal year will be sufficient to disentangle between the two remaining spin hypotheses for the $X(3872)$ state. For the $Z(4430)^{\pm}$, an annual yield of 6'200 reconstructed, selected and triggered $B^{0} \rightarrow Z(4430)^{\pm}K^{\mp}$ events is obtained for a $B/S$ ratio within the interval $[2.7,\,5.3]$ at 90 % CL. Hence, the confirmation or ruling out of the Belle discovery will be possible, even in the early running phase of the LHC proton collider at $\sqrt{s} = 7 - 10\,\text{TeV}$.

**Keywords:** CERN, LHC, LHCb, Alignment, Silicon Tracker, Charmonium Spectroscopy, $X(3872)$, $Z(4430)^{\pm}$.

# Acknowledgements

# Contents

# Introduction

ℜEARLY fourteen billion years ago, a space-time singularity with an infinite density and temperature expanded quickly. This event is today known as the Big Bang. The rest of the expansion and development of the Universe is history. Really? It would be if the Earth, hosting Human Beings, did not exist. According to this cosmological model, the temperature of the very early Universe was so high that the particles of which it consisted were moving at relativistic speeds. Particle-anti-particle pairs were constantly created and annihilated. Suddenly, an unknown phenomenon broke this symmetry. Matter was slightly favoured over anti-matter. The so-called baryo-genesis consequently saw a small excess of quarks and leptons with respect to anti-quarks and anti-leptons, of the order of one in 30 millions. The Universe is then less than $10^{-6}$ seconds old.

In order for the baryo-genesis to happen, three conditions, known as the Sakharov Conditions, must be fulfilled. These conditions were proposed in 1967 by the physicist Andrei Sakharov. First, baryon number must be violated. This is not yet supported by an experimental observation. In the Standard Model, a static solution of the theory, called the sphaleron, can give this baryon number violation, but at a low rate. In other theories, such as lepto-genesis, the asymmetry between baryons and anti-baryons actually arise from an asymmetry between leptons and anti-leptons, which then leads to baryon number violation by sphaleron transitions. The proton decay would be an example of such process. This phenomenon is not observable under normal conditions, but would have been common at the higher temperatures of the early universe. The second of Sakharov conditions is that the CP symmetry (discussed in Section 1.2.4) must be violated. This has been experimentally discovered in 1964 in the neutral-kaon system. The third conditions is that the Universe must expand at a rate larger than the rate at which particle-anti-particle pairs are created. These pairs do not reach a thermal equilibrium and hence the pair-annihilation rate is decreased.

The second of the Sakharov conditions gained in interest when the first evidence for CP violation was seen [1]. The Standard Model of particle physics can naturally account for part of this effect (as discussed in Section 1.2). However, this doesn't hold at the level needed to explain the baryo-genesis. Phenomena due to New Physics beyond the Standard Model must occur. This fact, amongst others subject of particle physics, has driven scientists to develop machines, particle accelerators and colliders, reaching ever higher energies in order to study physical conditions closer and closer to what prevailed shortly after the Big Bang.

The LHCb experiment at CERN, Geneva, will study the products of proton–proton collisions from the Large Hadron Collider, at a total energy of 14 TeV, seven times higher than that of the currently most energetic hadron collider, the Tevatron at Fermilab, USA.

LHCb has been designed to do precision measurement of CP violation parameters in the $B$-meson system, as well as to study rare $B$-meson decays. These rare decays are sensitive to new particles that could arise in the loops of the suppressed Feynman diagrams.

The detector has been designed to provide an excellent vertex and momentum resolution in order to have a good proper-time resolution. This is necessary to study the fast $B_s^0 - \bar{B}_s^0$ oscillations. A good mass resolution, which follows from a good momentum resolution, is also needed to provide powerful constraints to reduce the combinatorial background in the selection of fully reconstructed decays of interest. Finally, the particle identification system needs to be efficient to clearly reconstruct exclusive decays such as $B_s^0 \to D_s^{\pm} K^{\mp}$ and $B^0 \to \pi^+ \pi^-$, which are essential to achieve LHCb's physics goals.

This outstanding performance relies on a good construction of the detector, as close to the ideal design as possible. Each part of the detector was carefully surveyed in order to give first corrections to the position of each element. A software method has been developed to improve the accuracy of the alignment of the detector elements from the survey precision (order of 1 mm for the large elements and $50 - 100\,\mu m$ for the fine granularity) to the micron level.

This thesis is organised as follows. First, the theory underlying the physics phenomena relevant to the LHCb experiment is discussed in Chapter 1. A few important measurements of the LHCb physics program are summarised.

Next, the experimental apparatus is presented in Chapter 2, together with the important sub-systems, such as the trigger and the standard software. This is followed, in Chapter 3, by the theory relevant to the alignment studies. The tracking methods as well as the alignment technique are described. The alignment of the detector is of utmost importance to reach the design performance of the experiment. A precise alignment of the VELO is crucial for primary vertex reconstruction and hence the precise measurement of decay length and proper time of $B$ mesons. Also, the alignment of the Tracking Stations (the Inner and Outer Trackers) plays the first role in the correct estimate of the track momentum at LHCb. This is important to have a good mass resolution.

The remaining three chapters present the work performed as part of the PhD studies, which led to the writing of this thesis. Studies of the alignment of the LHCb Tracking Stations are performed using the specific software method developed for this purpose. The technique in use includes some novel calculation compared to existing methods. In Chapter 4, studies are performed using Monte Carlo simulated data based on two different running scenarios. The first one, which will happen at the startup phase of the experiment, towards the end of 2009, uses collisions of protons with residual gas particles in the interaction region. The protons have an energy of $450\,\mathrm{GeV}$, which corresponds to the injection energy into the LHC. In this first scenario, the LHCb dipole magnet, which provides the magnetic field needed to bend the trajectory of charged particles in order to measure their momentum, is switched off. The second scenario uses Monte Carlo simulated data mimicking the nominal running conditions: proton–proton collisions at an energy of $14\,\mathrm{TeV}$, with the magnetic field turned on. A general strategy is defined for the alignment of the Inner and Outer Trackers. Crucial criteria for an efficient alignment procedure are presented, based on the studies performed. These include the momentum of the particles used to align the detector, the fraction of ghost tracks (tracks made of random combination of hits mimicking real tracks) and the constraints used on the detector elements. These alignment results are then validated by showing the value of the

$J/\psi$ mass resolution and bias before and after alignment.

Chapter 5 then presents the alignment studies of the Inner Tracker performed with the first data ever recorded by the LHCb detector: data taken with a cosmic trigger and data coming from the collisions of an injected beam with a beam stopper during LHC injection tests. The strategy developed with Monte Carlo simulation is applied to this first data. The results of the alignment are then validated by looking at distributions of track parameters before and after alignment.

Finally, Chapter 6 presents a first study at LHCb of the selection of new charmonium-like states that were discovered in the recent years at the $B$ factories by Belle and BaBar, and at the Tevatron collider by CDF and DØ. A selection is proposed for the $X(3872)$ found in decays of $B^{\pm}$ mesons. The emphasis is on a small background level in order to allow for a precise angular analysis to measure the $X(3872)$ quantum numbers and hence constrain further the models describing its nature. LHCb is expected to play a big role in this field. The work presented here is the first look at $X(3872)$ selection in $pp$ collisions at $\sqrt{s} = 14\,\text{TeV}$. Another selection is presented for the $Z(4430)^{\pm}$ found in $B^0$ decays. This state, the first ever charged state found in charmonium spectroscopy, has been observed only by one experiment and a confirmation of its existence is awaited. LHCb is again expected to play an important role in this field, with a large $b\bar{b}$ cross section and hence a large number of $Z(4430)^{\pm}$ decays produced. A first selection in $pp$ collisions at $\sqrt{s} = 14\,\text{TeV}$ is proposed in this thesis.

# Chapter 1

# LHCb Physics

CERN is introduced in this chapter, followed by a description of the physics program of one of its present experiment: LHCb. The Standard Model of particles is described along with other theory subjects covering various fields of interests at LHCb.

$\mathfrak{T}$HE European Organisation for Nuclear Research (CERN) is located across the French-Swiss border, close to Geneva. The first proposal for the creation of a European laboratory was put forward by French physicist Louis de Broglie. CERN officially came into being on September 29, 1954 after fourteen European states ratified the CERN Convention. CERN's mission is set in this Convention [2], which states that

> The Organization shall provide for collaboration among European States in nuclear research of a pure scientific and fundamental character (...). The Organization shall have no concern with work for military requirements and the results of its experimental and theoretical work shall be published or otherwise made generally available.

The Large Hadron Collider (LHC) is CERN's new accelerator, designed to provide proton–proton collisions at a centre-of-mass energy of $14\,\text{TeV}$. Its main goal is to test the Standard Model and search for New Physics. Figure 1.1 shows the four general purpose experiments situated in the LHC tunnel. ATLAS and CMS, the two largest experiments aim at finding the Higgs boson, whose existence is predicted by the Standard Model, but has yet never been observed. LHCb is designed to make precise measurements of CP-violation parameters in the $b$-physics sector. Finally, ALICE will study the behaviour of nuclear matter in extreme conditions by collecting data during heavy-ion runs at LHC (e.g. Pb–Pb, Ca–Ca). These four main experiments will benefit from the unprecedented conditions that the LHC will provide to search for physics phenomena beyond the Standard Model, such as supersymmetry [3] or Little Higgs [4].
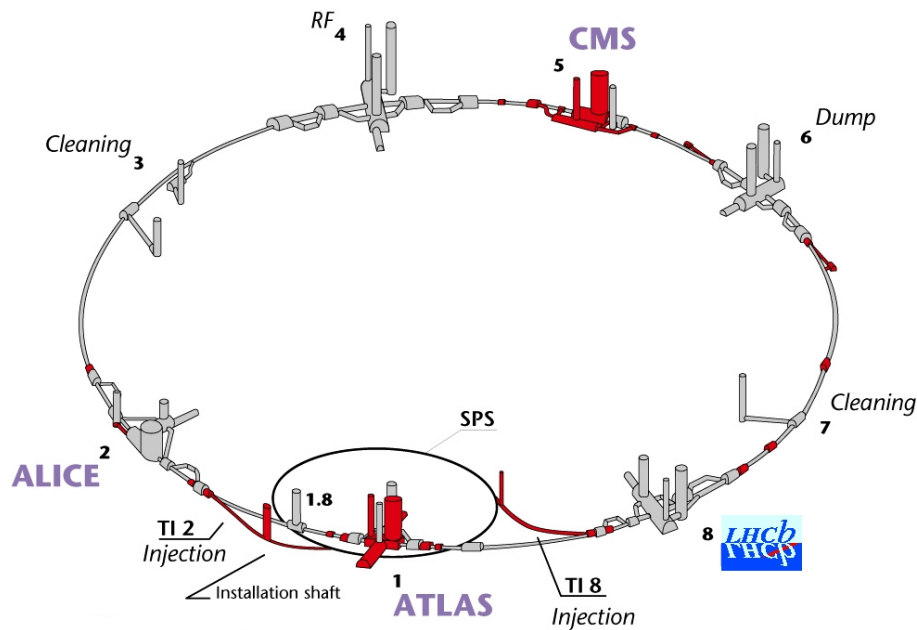
Figure 1.1: Layout of the LHC underground facilities showing the SPS (Super Proton Synchrotron used as injector into the LHC), the LHC ring and the four main experiments.

## 1.1    LHCb Physics Program

In 1964, observation of some rare neutral $K$-meson decays [1] demonstrated that matter and anti-matter, which were previously thought to be mirror images of each other, do not behave identically in space and time. This phenomenon is known as CP violation, C being the symmetry between a particle and its anti-particle and P representing an inversion of the spatial coordinates. This asymmetry is interesting as it may explain why the matter Universe exists, as we know it today. According to the theory of the Big Bang, equal amounts of matter and anti-matter were produced some 13.7 billion years ago. For some reasons, all the anti-matter vanished, leaving a sea of photons with a few particles combining into atoms, molecules and more complex systems. The Standard Model of particle physics can explain part of this effect, but not to an extent as large as what we observe today. The Large Hadron Collider beauty experiment (LHCb) has been designed to perform precise measurements of CP violation in the $b$-hadron sector.

Through these studies and the analysis of rare $b$-hadron decays, effects of physics phenomena beyond the Standard Model might be discovered, which could account for the matter–anti-matter discrepancy. Furthermore, measurement of rare decays open a field for searches of massive new particles, whose virtual effects could be seen as larger decay rates.

The LHCb collaboration is also investigating ways to discover the Higgs boson and measure its mass [5, 6, 7]. This boson, which has been predicted, but never observed, is thought to explain why the quarks, leptons and some bosons are massive, while other bosons are massless, e.g. the photon.

Another field of interest has arisen over the past few years when the Belle and BaBar

collaborations discovered new charmonium-like states (particles composed of a quark $c$ and an anti-quark $\bar{c}$): the $X(3872)$ in 2003 [8], the $Y(4260)$ in 2005 [9], the $Z(4430)^{\pm}$ in 2008 [10] and several other states. The interest grew even more when most of these states were shown not to fit in the charmonium-spectroscopy frame [11, 12, 13, 14, 15]. Since these states are produced in the decays of $B$ mesons, which will be produced in large number at the energy scale reached by the LHC, LHCb is expected to play a major role in the uncovering of the nature and properties (quantum numbers and masses) of these states.

All the physics measurements presented in this section rely on the outstanding performance of the LHCb detector. An excellent proper-time resolution as well as a precise mass resolution are needed to reconstruct the $B$-meson decays, to measure the time-dependent decay rates and to have a powerful handle on background rejection. A reliable particle identification is also needed, both for the event selection and for the flavour tagging, the determination of the initial flavour of $B$ mesons decaying inside the detector. All of these rely on a precise construction and commissioning of the detector. A rigorous alignment of the sub-detector parts is an important task of this early running phase of the experiment. The motivation for the alignment studies presented in Chapters 4 and 5 hence finds its roots directly in the physics program of LHCb.

This chapter presents some interesting items of the LHCb physics program. First, the Standard Model of particle physics is outlined. Then, some of the most promising analyses are presented. This chapter is however not supposed to be an exhaustive review.

## 1.2 The Standard Model of Particle Physics

The Standard Model (SM) of particle physics is a gauge theory of the elementary particles that describes the interactions of three of the four fundamental forces of nature: the electromagnetic and weak forces, which are unified as the electroweak interaction at high energy, and the strong interaction. However, it does not include the fourth fundamental force, gravity. Other features of the theory are unsatisfactory. For example, the coupling constants and particle masses are not explained and are thus arbitrary parameters of the model. The number of generations of particles is not predicted by the theory either. For these reasons, extensions of the SM, sometimes grouped under the name New Physics (NP), are emerging. Some of these new theories try to extend the SM into a theory of everything (TOE). This section gives an overview of the SM.

### 1.2.1 Standard Model Particles

The elementary particles of matter are spin-$\frac{1}{2}$ fermions of two kind: the leptons and the quarks. There are three generations of quarks, each made of an up-type quark (up, charm and top) and a down-type quark (down, strange and bottom). The leptons also come in three flavours with their corresponding neutrinos: the electron, the muon and the tau.

Table 1.1: Quark and lepton properties [16], where $Q$ is the electric charge, $M$ the mass and $B$ the baryon number of the particle.

| | $Q$ | | $M$ [MeV/$c^2$] | | | | | | $B$ |
|---|---|---|---|---|---|---|---|---|---|
| Quarks | 2/3 | $u$ | 1.5–3.3 | $c$ | $(1.27\,^{+0.07}_{-0.11}) \times 10^3$ | $t$ | $(171.2 \pm 2.1)\times 10^3$ | | 1/3 |
| | −1/3 | $d$ | 3.5–6.0 | $s$ | $104\,^{+26}_{-34}$ | $b$ | $(4.20\,^{+0.17}_{-0.07}) \times 10^3$ | | 1/3 |
| Leptons | 0 | $\nu_e$ | $< 2.2 \times 10^{-6}$ | $\nu_\mu$ | $< 0.170$ | $\nu_\tau$ | $< 15.5$ | | 0 |
| | −1 | $e$ | 0.511 | $\mu$ | 105.7 | $\tau$ | $1.78\times 10^3$ | | 0 |

These two families can be separated in three generations each as follows:

$$\text{quarks} = \begin{pmatrix} u \\ d \end{pmatrix}, \quad \begin{pmatrix} c \\ s \end{pmatrix}, \quad \begin{pmatrix} t \\ b \end{pmatrix} \text{ and} \tag{1.1}$$

$$\text{leptons} = \begin{pmatrix} \nu_e \\ e \end{pmatrix}, \quad \begin{pmatrix} \nu_\mu \\ \mu \end{pmatrix}, \quad \begin{pmatrix} \nu_\tau \\ \tau \end{pmatrix}, \tag{1.2}$$

where $\nu_{e,\mu,\tau}$ are the three neutrinos. Corresponding elements in different generations of the same family have an equal electric charge, but different masses. These properties are reported for the quarks and leptons in Table 1.1. Each of these twelve elementary particles is associated to a corresponding anti-particle of opposite electric charge. In the SM, the neutrinos are predicted to be massless. However, observations of neutrino flavour oscillations have demonstrated that neutrinos have small, but non-zero, mass differences. However, only upper limits on the absolute masses have been obtained (see Table 1.1). In any case, the SM needs an extension to explain non-zero masses.

The quarks also carry a colour charge, which can be one of red, green or blue. The anti-quarks carry an anti-colour charge. This property is related to the strong interaction which will be described in the next section. All particles that can be observed are colour-neutral, meaning that quarks are always observed in bound states, called hadrons. This property of quarks is the consequence of a principle called colour confinement, which is a feature of the strong interaction described in the next section.

**Mesons** are made of a quark and an anti-quark and are hence bosons. Any quark flavour can appear in a meson, except for the top quark, which is too heavy and decays before it can bind to another quark. All mesons have a corresponding anti-meson, where the quark is replaced by its anti-quark and vice versa. Examples of mesons are the bottom mesons $B^0$ formed of a $\bar{b}$ anti-quark and a $d$ quark and $B_s^0$ made of a $\bar{b}$ anti-quark and an $s$ quark, the charm meson $D^0$ composed of a $c$ quark and an $\bar{u}$ anti-quark, the pions and the kaons made of $u$, $d$ and $s$ quarks. $c\bar{c}$ bound states are called charmonium and $b\bar{b}$ states are called bottomonium.

**Baryons** are fermions composed of three quarks. All ordinary matter is composed of protons and neutrons in a nucleus surrounded by electrons. The nucleons are baryons made of $uud$ and $udd$ quarks for the protons and neutrons respectively. Any quark flavour, except for the top, can be bound to build a baryon. As for the mesons,

the baryons have a corresponding anti-baryon, where the quarks are replaced by anti-quarks.

Finally, hadrons are characterised by a property called the baryon number ($B$), which is conserved in any decay or interaction observed so far. Quarks are assigned a $+1/3$ baryon number, while anti-quarks have a baryon number of $-1/3$. This number being additive for composite particles, it can be derived that mesons have zero baryon number, while baryons have $B = +1$ and anti-baryons have $B = -1$.

## 1.2.2 Standard Model Interactions

The particles presented in Section 1.2.1 interact with each other through one of the three fundamental interactions described by the Standard Model. They do this by exchanging force-mediating bosons (spin 1).

The electromagnetic interaction couples electrically-charged particles. The mediator of this force is the massless neutral photon. The interaction has an infinite range. It is responsible for the cohesion of atoms with negatively-charged electrons surrounding the positive nucleus, the formation of molecular bonds, etc.

Electromagnetism is unified with the weak interaction under the electroweak interaction. The weak force is the only interaction described in the Standard Model which affects all quarks and leptons. It is mediated by three bosons: the neutral $Z^0$ and the charged $W^{\pm}$, which can couple amongst themselves and to the photon (for the $W^{\pm}$). Their large masses of respectively $91.2 \, \text{GeV}/c^2$ and $80.4 \, \text{GeV}/c^2$ lead to a short lifetime and a short spatial range, typically $3 \times 10^{-25} \, \text{s}$ and $10^{-18} \, \text{m}$ respectively. The weak interaction is responsible for the beta decays of nuclei. This natural radioactivity of some elements is an example of a unique feature of this interaction: flavour changing. Via this phenomenon, $u$, $c$ and $t$ quarks are coupled to $d$, $s$ and $b$ quarks through the so-called charged current, which involves a $W^{\pm}$ boson, according to the conservation of the electric charge. The same holds for the leptons and their corresponding neutrinos. The quark couplings will be described in a more formal way in Section 1.3.1.

The strong interaction is named after the fact that it couples particles with a strength $10^2$ times larger than the electromagnetic force and $10^{13}$ times larger than the weak interaction. It is also called the nuclear or colour force, and is responsible for the cohesion of quarks in the hadrons and of hadrons together, like the neutrons and the protons in an atomic nucleus. It is mediated between quarks by eight massless and electrically neutral gluons. Gluons carry colour charge, meaning they can interact among themselves. The eight linearly independent gluons which form the colour octet carry both a colour charge (like quarks) and an anti-colour charge (like anti-quarks). Hence, they have the property of being able to change the colour of the quarks.

## 1.2.3 Symmetries in the Standard Model

Three discrete symmetries, which play an important role in the Standard Model, are presented here. Parity P represents a space inversion, where the three spatial coordinates are reversed. Charge conjugation C interchanges a particle with its own anti-particle. The third discrete symmetry is the time-reversal transformation T.

Parity is known to be maximally violated by the weak interaction, which only couples left-handed components of particles and right-handed components of anti-particles. Parity violation has been discovered in 1956–57 by C.-S. Wu in the study of the $\beta$ decays of Cobalt-60 [17]. The weak interaction also maximally violates C, because a left-handed particle is transformed into a left-handed anti-particle, which doesn't interact with the weak interaction mediators.

The violation of the CP conjugated symmetry has been observed in the neutral kaon system $K_L \rightarrow \pi^+ \pi^-$ [1], mediated by the weak interaction, as well as in the $B_d$-meson system. Measurements have also been performed in the $B_s$-meson system, but no significant observation has been made yet. It is further discussed in Section 1.2.4.

There is however one symmetry which is conserved by all interactions. The CPT theorem states that any Lorentz invariant local quantum field theory with a Hermitian Hamiltonian must have CPT symmetry. CPT is the operation by which space and time are reversed at the same time as particles are changed into their anti-particles. This fundamental symmetry implies that the masses and lifetimes of a particle and the corresponding anti-particle are equal, and that their charge are of equal value with an opposite sign. A violation of CPT symmetry would mean that relativity doesn't hold. Finally, as a consequence of the CPT invariance and the violation of the CP symmetry by the weak interaction, the T symmetry is also expected to be violated. This symmetry violation has been measured in the Kaon system, for example by the CPLear collaboration [18].

### 1.2.4 CP Violation

The combination of C and P symmetries is not exact in the Standard Model and can naturally be violated by the weak interaction with three quark families. The general condition for CP violation in the $B$-meson sector is that the decay rate $\mathcal{R}_f$ of a $B_q$ meson (with quark content $\bar{b}q$, $q$ being either a $d$ or an $s$ quark) decaying to a final state $f$ is not equal to the rate $\bar{\mathcal{R}}_{\bar{f}}$ of a $\bar{B}_q$ anti-meson (with quark content $b\bar{q}$, $q$ being either a $d$ or an $s$ quark) decaying to a final state $\bar{f}$:

$$\mathcal{R}_f(t) \neq \bar{\mathcal{R}}_{\bar{f}}(t) \tag{1.3}$$

There are three different types of CP violation in $B$-meson decays. They are described hereafter.

CP violation in the decay amplitudes, also called direct CP violation, occurs both in charged and neutral decays. This type of CP violation occurs when the amplitude for a decay and its CP-conjugate process are different.

If CP is conserved, the two mass eigenstates in the $B_q$-meson system are CP eigenstates. CP violation in the mixing occurs when the two neutral mass eigenstates cannot be chosen to be CP eigenstates. The probabilities for an initially pure $B_q$ eigenstate to decay as $\bar{B}_q$ or an initially pure $\bar{B}_q$ eigenstate to decay as $B_q$ after a time t are then not the same. This kind of CP violation is small for the $B$ mesons, typically of the order of $10^{-2}$. Semi-leptonic decays and flavour-specific decays can be used to measure this amplitude of CP violation.

The third type of CP violation occurs in the interference between the decay amplitude and the mixing amplitude and is called mixing-induced CP violation. It can happen when

the final state $f$ of a particular decay is common to the $B_q$ and $\bar{B}_q$. The $B_q$ meson can hence either decay straight to the final state $f$, or oscillate into a $\bar{B}_q$, as discussed in Section 1.4.1, and then decay to $f$.

In order to study CP violation in neutral $B_q$-meson decays, a measurement of the time-dependent CP asymmetry $\mathcal{A}_{\mathrm{CP}}(t)$ is needed, where

$$\mathcal{A}_{\mathrm{CP}}(t) \equiv \frac{\mathcal{R}(\bar{B}_q(t) \to \bar{f}) - \mathcal{R}(B_q(t) \to f)}{\mathcal{R}(\bar{B}_q(t) \to \bar{f}) + \mathcal{R}(B_q(t) \to f)}. \tag{1.4}$$

In this definition, $\mathcal{R}(\overset{(-)}{B_q}(t) \to \overset{(-)}{f})$ is the time-dependent decay rate of the $\overset{(-)}{B_q}(t) \to \overset{(-)}{f}$ decay. The quality of the measurement of this asymmetry is degraded by the detector resolution and the $B$-meson tagging inefficiencies, which dilute the distribution of the fast $B$-meson oscillation, especially in the case of the $B_s^0$ meson.

## 1.3    Measurement of the CKM angle γ

The beauty sector is an exciting place to study CP violation and to look for traces of new physics beyond the Standard Model of particle physics. LHCb will benefit from the unprecedented statistics of $b$ hadrons produced to constrain further some of the SM parameters. This section presents three approaches to the measurement of a loosely constrained parameter: the CKM angle $\gamma$ of the Unitary Triangle. First, the CKM matrix and the Unitary Triangle are presented, followed by a discussion of three different methods to extract $\gamma$ [19].

### 1.3.1    Flavour Changing and the CKM Matrix

In the Standard Model, flavour-changing processes between quarks are due to charged currents from the weak interaction. The couplings between two different quarks are given by the elements of a $3 \times 3$ unitary matrix called the Cabibbo-Kobayashi-Maskawa (CKM) matrix [20, 21]. The eigenstates of the electroweak interaction are not the mass (or physical) eigenstates, but are called $(d', s', b')$. However, these two sets of eigenstates are connected by the CKM matrix:

$$\begin{pmatrix} d' \\ s' \\ b' \end{pmatrix} = \mathbf{V}_{\mathrm{CKM}} \begin{pmatrix} d \\ s \\ b \end{pmatrix} \quad ; \quad \mathbf{V}_{\mathrm{CKM}} = \begin{pmatrix} V_{ud} & V_{us} & V_{ub} \\ V_{cd} & V_{cs} & V_{cb} \\ V_{td} & V_{ts} & V_{tb} \end{pmatrix}. \tag{1.5}$$

There are several ways to parametrise the CKM matrix. It can be given in terms of three Euler angles ($\theta_{12}$, $\theta_{23}$ and $\theta_{13}$) and a complex phase $\delta_{13}$, which introduces CP violation in case it differs from zero. Denoting the sines and cosines of the Euler angle $\theta_{ij}$ as $s_{ij}$ and $c_{ij}$ respectively, the matrix becomes

$$\mathbf{V}_{\mathrm{CKM}} = \begin{pmatrix} c_{12}c_{13} & s_{12}c_{13} & s_{13}e^{-i\delta_{13}} \\ -s_{12}c_{23} - c_{12}s_{23}s_{13}e^{i\delta_{13}} & c_{12}c_{23} - s_{12}s_{23}s_{13}e^{i\delta_{13}} & s_{23}c_{13} \\ s_{12}s_{23} - c_{12}c_{23}s_{13}e^{i\delta_{13}} & -c_{12}s_{23} - s_{12}c_{23}s_{13}e^{i\delta_{13}} & c_{23}c_{13} \end{pmatrix}. \tag{1.6}$$

The angle $\theta_{12}$ is also called the Cabibbo angle, and was introduced in 1963 by Nicola Cabibbo [20] to preserve the universality of the weak interaction. It was introduced before the quarks were theorised [1] but can now be related to the probability that down and strange quarks decay into up quarks. The value of the Cabibbo angle is given as $s_{12} = 0.2257\,^{+0.0009}_{-0.0010}$.

Another convenient parametrisation for phenomenology, introduced by Lincoln Wolfenstein [24] in 1983, uses four real parameters $\lambda$, $\rho$, $\eta$ and A. The CKM matrix is expressed as a series expansion in powers of $\lambda \equiv s_{12}$. $\mathbf{V}_{\mathrm{CKM}}$ can then be written at the order $\mathcal{O}(\lambda^4)$,

$$\mathbf{V}_{\mathrm{CKM}} \approx \begin{pmatrix} 1 - \lambda^2/2 & \lambda & A\lambda^3(\rho - i\eta) \\ -\lambda & 1 - \lambda^2/2 & A\lambda^2 \\ A\lambda^3(1 - \rho - i\eta) & -A\lambda^2 & 1 \end{pmatrix} + \delta\mathbf{V}_{\mathrm{CKM}}, \qquad (1.7)$$

where

$$\delta\mathbf{V}_{\mathrm{CKM}} = \begin{pmatrix} -\frac{1}{8}\lambda^4 + \mathcal{O}(\lambda^6) & \mathcal{O}(\lambda^7) & 0 \\ \frac{1}{2}A^2\lambda^5\left[1 - 2(\rho + i\eta)\right] + \mathcal{O}(\lambda^7) & -\frac{1}{8}\lambda^4(1 + 4A^2) + \mathcal{O}(\lambda^6) & \mathcal{O}(\lambda^8) \\ \frac{1}{2}A\lambda^5(\rho + i\eta) + \mathcal{O}(\lambda^7) & \frac{1}{2}A\lambda^4(1 - 2(\rho + i\eta)) + \mathcal{O}(\lambda^6) & -\frac{1}{2}A^2\lambda^4 + \mathcal{O}(\lambda^6) \end{pmatrix}.$$
$$(1.8)$$

CP violation occurs when the CKM matrix is complex, i.e. when $\eta \neq 0$, as already discussed above with the phase $\delta_{13}$.

The flavour-changing processes described above in the frame of the CKM matrix can be represented graphically by the Feynman diagrams. These diagrams were developed by R. P. Feynman in the second half of the 1960s and can be interpreted as the physics mechanism for the interaction of real particles by the mean of the exchange of virtual unobservable force-mediating bosons and other quark loops. There are two main types of Feynman diagrams: the tree diagrams and the loop or penguin diagrams. Figure 1.2 (a) represents a typical tree diagram for a transition of a quark $b$ to a top-type quark. A transition from a quark $b$ to a down-type quark is depicted in Fig. 1.2 (b) in the case of QCD penguin diagram (strong interaction) and in Fig. 1.3 in the case of the electroweak penguin diagram. Reference [25] gives an overview of how to build Feynman diagrams and what to calculate with them.

### 1.3.2 The Unitary Triangles

Since the CKM matrix is unitary, which is expressed mathematically as $V_{\mathrm{CKM}}^{\dagger}V_{\mathrm{CKM}} = V_{\mathrm{CKM}}V_{\mathrm{CKM}}^{\dagger} = \mathbb{1}$, nine orthonormality conditions can be set on its elements. The constraints on the diagonal terms are

$$\sum_{k} |V_{ik}|^2 = 1 \qquad (1.9)$$

---

[1] The quark model was independently proposed by physicists Murray Gell-Mann and George Zweig in 1964 [22, 23].
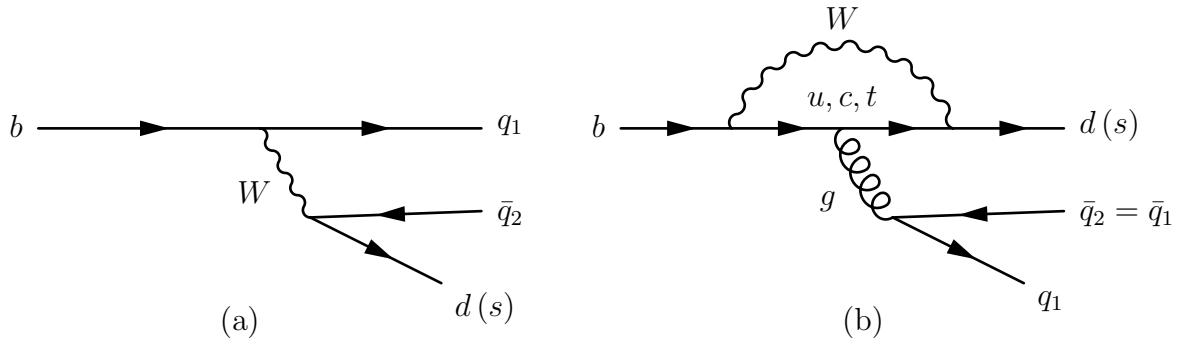
Figure 1.2: Two Feynman diagrams: (a) tree diagram ($q_1, q_2 \in \{u, c\}$) and (b) QCD penguin diagram ($q_1 = q_2 \in \{u, d, c, s\}$).
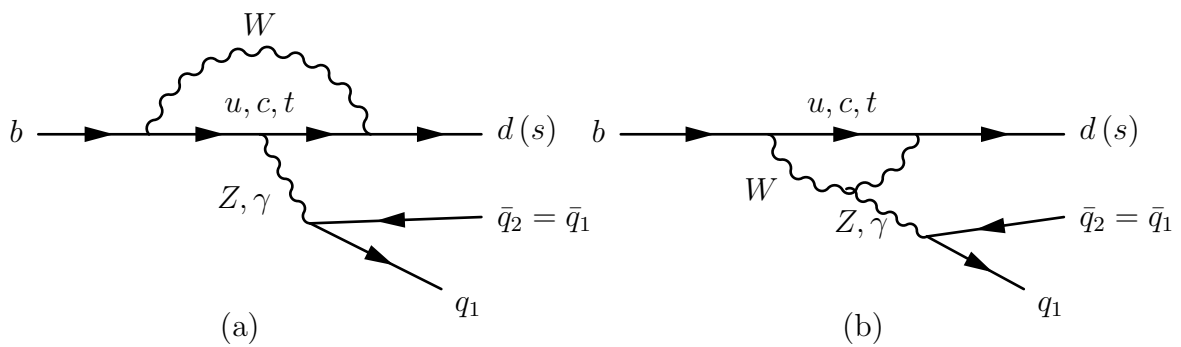


Figure 1.3: Electroweak penguin diagrams ($q_1 = q_2 \in \{u, d, c, s\}$).

(a) *db* triangle

(b) *sb* triangle
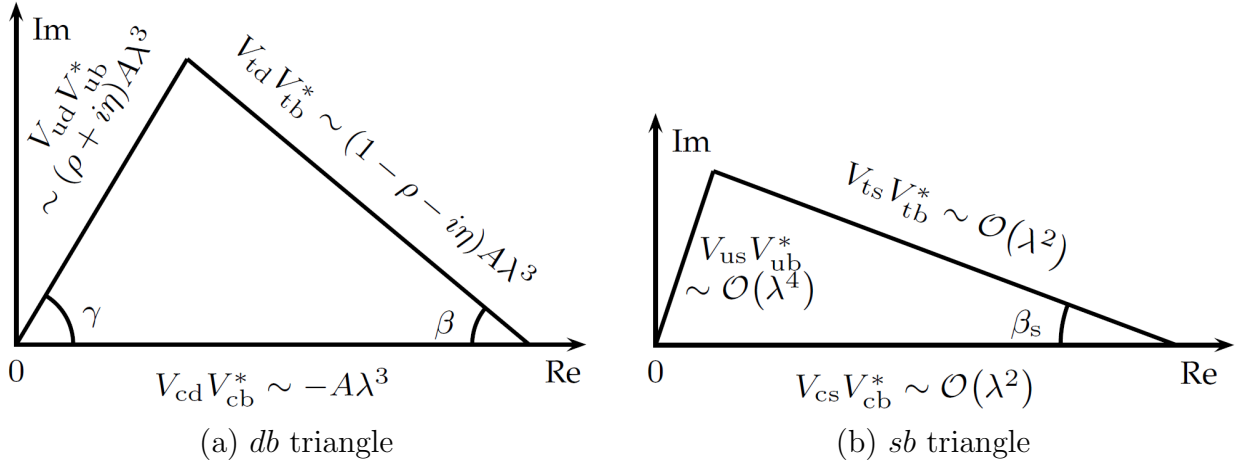
Figure 1.4: Two unitarity relations (Equations 1.11 and 1.12) drawn in the complex plane.

for the three generations. This implies the so-called weak universality, which states that the sum of all couplings of any of the up-type quarks to all the down-type quarks is the same.

The six other constraints, which express the orthogonality of the rows and columns of the CKM matrix, are given by

$$\underbrace{V_{ud}V_{us}^*}_{\mathcal{O}(\lambda)} + \underbrace{V_{cd}V_{cs}^*}_{\mathcal{O}(\lambda)} + \underbrace{V_{td}V_{ts}^*}_{\mathcal{O}(\lambda^5)} = 0 \quad (ds \text{ triangle}), \quad (1.10)$$

$$\underbrace{V_{ud}V_{ub}^*}_{(\rho+i\eta)A\lambda^3} + \underbrace{V_{cd}V_{cb}^*}_{-A\lambda^3} + \underbrace{V_{td}V_{tb}^*}_{(1-\rho-i\eta)A\lambda^3} = 0 \quad (db \text{ triangle}), \quad (1.11)$$

$$\underbrace{V_{us}V_{ub}^*}_{\mathcal{O}(\lambda^4)} + \underbrace{V_{cs}V_{cb}^*}_{\mathcal{O}(\lambda^2)} + \underbrace{V_{ts}V_{tb}^*}_{\mathcal{O}(\lambda^2)} = 0 \quad (sb \text{ triangle}), \quad (1.12)$$

$$\underbrace{V_{ud}^*V_{cd}}_{\mathcal{O}(\lambda)} + \underbrace{V_{us}^*V_{cs}}_{\mathcal{O}(\lambda)} + \underbrace{V_{ub}^*V_{cb}}_{\mathcal{O}(\lambda^5)} = 0 \quad (cu \text{ triangle}), \quad (1.13)$$

$$\underbrace{V_{cd}^*V_{td}}_{\mathcal{O}(\lambda^4)} + \underbrace{V_{cs}^*V_{ts}}_{\mathcal{O}(\lambda^2)} + \underbrace{V_{cb}^*V_{tb}}_{\mathcal{O}(\lambda^2)} = 0 \quad (tc \text{ triangle}), \quad (1.14)$$

$$\underbrace{V_{ud}^*V_{td}}_{(1-\rho-i\eta)A\lambda^3} + \underbrace{V_{us}^*V_{ts}}_{-A\lambda^3} + \underbrace{V_{ub}^*V_{tb}}_{(\rho+i\eta)A\lambda^3} = 0 \quad (tu \text{ triangle}). \quad (1.15)$$

These relations can be represented as triangles in the complex plane. The angles of these triangles, which correspond to the weak phases, along with the sides need to be measured in order to test the CKM picture. As given in Equations 1.10 to 1.15, only two of these six triangles have their three sides of comparable size ($\mathcal{O}(\lambda^3)$): the *db* triangle, shown in Fig. 1.4, and the *tu* triangle. These two triangles are actually identical up to $\lambda^3$ order. The *db* unitary triangle is determined from the $B_d^0$-meson system. Amongst the other triangles, one is related to the physics of the $B_s^0$-meson system and is hence interesting at LHCb, the *sb* triangle. This triangle is also represented in Fig. 1.4.

Another way to parametrise the CKM matrix is given in terms of the angles appearing

in the unitary triangles. It involves four independent phases:

$$\beta_{(d)} \equiv \phi_1 \equiv \arg\left(-\frac{V_{cd} V_{cb}^*}{V_{td} V_{tb}^*}\right) = (21.07\,^{+0.90}_{-0.88})^\circ, \tag{1.16}$$

$$\gamma \equiv \phi_3 \equiv \arg\left(-\frac{V_{ud} V_{ub}^*}{V_{cd} V_{cb}^*}\right) = (70\,^{+27}_{-30})^\circ, \tag{1.17}$$

$$\beta_s \equiv \chi \equiv \arg\left(-\frac{V_{cb} V_{cs}^*}{V_{tb} V_{ts}^*}\right) = (0.01807\,^{+0.00086}_{-0.00081})\,\text{rad}, \tag{1.18}$$

$$\beta_K \equiv \chi' \equiv \arg\left(-\frac{V_{us} V_{ud}^*}{V_{cs} V_{cd}^*}\right), \tag{1.19}$$

where the numerical values are taken from Ref. [26]. In the $db$ triangle, the angle $\alpha$ can be defined from the constraint that $\alpha + \beta + \gamma = \pi$:

$$\alpha \equiv \phi_2 \equiv \arg\left(-\frac{V_{td} V_{tb}^*}{V_{ud} V_{ub}^*}\right) = (89.0\,^{+4.4}_{-4.2})^\circ. \tag{1.20}$$

The $\beta_s$ phase, which describes the $B_s$ system, can further be related to the Wolfenstein parameters, especially to the CP-violating parameter $\eta$:

$$\beta_s = \arg\left[1 - \lambda^2\left(\frac{1}{2} - \rho - i\eta\right) + \mathcal{O}(\lambda^4)\right] \approx \lambda^2 \eta, \tag{1.21}$$

and finally $\beta \approx -\arg(V_{td})$, $\gamma \approx -\arg(V_{ub})$ and $\beta_s \approx \arg(V_{ts}) - \pi = \arg(-V_{ts})$.

The angle $\gamma$ is the the least constrained angle in this model. LHCb is expected to contribute to this measurement and three different approaches to extract this parameter are summarised in Section 1.3.3. The measurement of a non-zero value of $\gamma$ is a direct measurement of CP violation [2]. Indeed, if $\gamma \neq 0$, then $\eta \neq 0$, as seen in Fig. 1.4 (a), which means that the CKM matrix is complex and hence that CP violation occurs.

### 1.3.3 Three Approaches to the Measurement of $\gamma$

A first way to measure the angle $\gamma$ is to study the interference between the amplitudes of the $b \to c$ and $b \to u$ quark transitions to a common $D^0$ and $\bar{D}^0$ final state in the tree decays $B^- \to D^0 K^-$ and $B^- \to \bar{D}^0 K^-$ [19]. These two amplitudes depend on the $V_{cb}$ and $V_{ub}$ CKM-matrix elements respectively. The weak phase difference between these two elements is $-\gamma$. Therefore, when the $D^0$ and $\bar{D}^0$ decay to the same final state, interference between the two amplitudes gives sensitivity to $\gamma$. The neutral decays $\bar{B}^0 \to D^0 K^*$ and $\bar{B}^0 \to \bar{D}^0 \bar{K}^*$ can also be used. The branching ratio is smaller than in the charged $B$-meson case, but the interference between the two amplitudes is larger. Depending on the nature of the common final state of the $D$ meson, several analysis strategies have been developed. These analyses depend on the values of strong phases and on the background assumption. The combined statistical precision on $\gamma$ for these analyses is around $5\,^\circ$ with $2\,\text{fb}^{-1}$ of data.

A second method to extract $\gamma$ from data is to study decays that are preferably described by tree diagrams (as depicted in Fig. 1.2), such as $B_s^0 \to D_s^\pm K^\mp$ [19]. The $B_s^0$

---

[2] This is also true for the measurement of other angles, but only the example of $\gamma$ is treated here.

meson can either decay to the final state via a $b \to c$ quark transition, or oscillate into a $\bar{B}_s^0$ anti-meson and then decay to the final state through a $b \to u$ transition. These two amplitudes interfere and give rise to a phase difference, which is equal to $\gamma + \phi_s$, the first term describing the interference between the two quark transitions and the second term accounting for the mixing effect (as discussed in Section 1.4.1). The angle $\gamma$ is then extracted by constraining the value of $\phi_s$, e.g. from $B_s^0 \to J/\psi \, \phi$ decays. With this method, the value of $\gamma$ is determined with an eightfold discrete ambiguity. This problem can be addressed by invoking the U-spin flavour symmetry of strong interactions, which relates strange and down quarks the same way as isospin relates up and down quarks. Another way is to perform measurements from related channels with differing strong phases, such as $B^0 \to D^{*\pm}\pi^{\mp}$. With this approach, a statistical precision of $\sim 10\,^{\circ}$ on $\gamma$ is expected with $2\,\mathrm{fb}^{-1}$ of data.

Unlike the two first methods, which exclusively study tree amplitudes, the third way of measuring $\gamma$ includes the study of penguin diagrams [27], as depicted in Fig. 1.3. In the decay $B_{s,d}^0 \to hh$, where $h$ is either a charged pion or a charged kaon, the amplitude of the $b \to u$ tree transition interferes with the $b \to d/s$ penguin transition. The $B_d^0 \to \pi^+\pi^-$ and $B_s^0 \to K^+K^-$ are symmetric under the U-spin flavour symmetry: they are related through an interchange of all down and strange quarks. The U-spin symmetry allows to derive relations between the parameters of the two decays, such that the CKM angle $\gamma$ can be extracted from the data. The statistical precision on the measurement of $\gamma$ with $2\,\mathrm{fb}^{-1}$ of data is around $10\,^{\circ}$ with this method. The value measured with this method might differ from the measurements performed with other $B$ decays, because the penguin decays are potentially sensitive to new physics particles appearing in loops.

## 1.4 Measurement of the $B_s^0$ Mixing Phase $\phi_s$

The Standard Model describes a possible violation of the CP symmetry in the $B$-meson sector. In particular, it predicts an asymmetry due to CP violation in the time dependent decay rates of a $B_s^0$ meson and the corresponding anti-meson $\bar{B}_s^0$ to a common CP eigenstate. This asymmetry originates from the interference between the decay and the $B_s^0 - \bar{B}_s^0$ mixing amplitudes, and is described with an observable weak phase $\phi_s$ resulting from the phase mismatch between the two amplitudes.

The value of the $B_s^0$ mixing phase has been measured, for example the combined CDF and DØ result gives $\beta_s = -\frac{1}{2}\phi_s \in [0.10, 1.42]\,\mathrm{rad}$ at $95\,\%$ CL [28]. Improving the precision of this measurement is one of the key point of the LHCb physics program. In this section, first the phenomenon of $B$-meson mixing is reviewed. Next, the measurement of the $B_s^0$ mixing phase at LHCb is explained [29].

### 1.4.1 $B$-Meson Mixing

The weak interaction is responsible for flavour-changing interactions. Without this phenomenon, the neutral $b$ mesons have well defined flavours, and the eigenstates of the strong and electromagnetic interactions can be denoted $B_q$ and $\bar{B}_q$, where $q \in \{d, s\}$ for the $B_d$ and $B_s$ systems respectively. Their quark content is well defined:
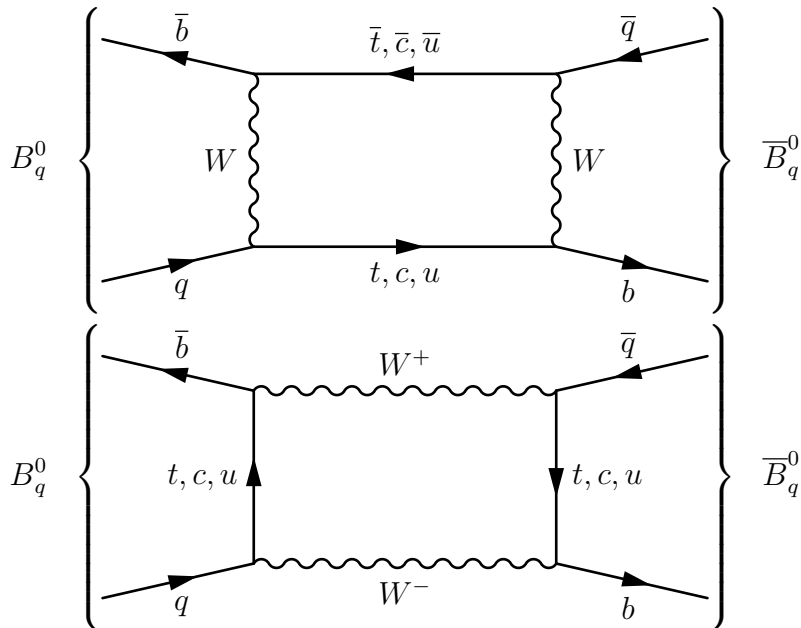
Figure 1.5: Box diagrams of the $B_q - \bar{B}_q$ oscillation, where $q \in \{d, s\}$.

$$B_d = \bar{b}d, \qquad \bar{B}_d = b\bar{d},$$
$$B_s = \bar{b}s, \qquad \bar{B}_s = b\bar{s}.$$

The mass of the $B_q$ and $\bar{B}_q$ mesons must be identical, following the CPT invariance of the strong and electromagnetic interactions, and can be denoted as $M_q$.

Once the effect of the weak interaction is added, the $B$-meson states start to mix and decay. The flavour states $B_q$ and $\bar{B}_q$ can either remain unchanged or oscillate into each other. This is called particle–anti-particle mixing. The oscillation frequency depends on the mass difference between the two mass eigenstates of the $B_q$ system, $\Delta M_q$. The oscillation is relatively slow in the $B_d$ system, where the mass difference $\Delta M_d = (0.507 \pm 0.005\,\mathrm{ps}^{-1}$ [16] is small. On the other hand, the oscillation is fast in the $B_s$ system, due to a larger mass difference of $\Delta M_s = (17.77 \pm 0.10(\mathrm{stat.}) \pm 0.07(\mathrm{sys.}))\,\mathrm{ps}^{-1}$, as measured by CDF [30]. In the Standard Model, the transitions corresponding to this oscillation at the quark level are shown in the box diagrams of Fig. 1.5 and are dominated by internal top-quark exchange. The phase of the mixing is $\phi_q = 2\arg[V_{tq}^* V_{tb}]$. Comparing this expression to the results of Section 1.3.2, the two phases corresponding to the $B_d$ and $B_s$ systems can be linked to the angles of the unitary triangles:

$$\phi_d \equiv 2\arg[V_{td}^* V_{tb}] \approx 2\beta_d \qquad (1.22)$$
$$\phi_s \equiv 2\arg[V_{ts}^* V_{tb}] \approx -2\beta_s. \qquad (1.23)$$

The SM predicts a small value for $\phi_s = (-0.0368 \pm 0.0017)\,\mathrm{rad}$ [16].

## 1.4.2    Measurement of $\phi_s$

Due to the precisely determined theoretical value of $\phi_s$ in the SM, any deviation from that expectation will be a clear sign of new physics. The study of $B_s^0$ decays to CP

eigenstates via the $\bar{b} \rightarrow \bar{c}c\bar{s}$ quark transitions allows the determination of the $B_s^0 - \bar{B}_s^0$ mixing phase. There is no CP violation in the decay amplitudes, because the decays are dominated by tree amplitudes with a negligible contribution from penguin amplitude and CP violation in the mixing can be neglected. Hence, the time-dependent mixing-induced CP asymmetry can be measured in the phase mismatch between the decay and mixing weak phases. Two different sets of signal events can be studied for this measurement [31].

The first type of data contains pure CP-even eigenstates, such as $B_s^0 \rightarrow \eta_c\phi$, $B_s^0 \rightarrow J/\psi\,\eta$, $B_s^0 \rightarrow J/\psi\,\eta'$ or $B_d^0 \rightarrow D_s^+D_s^-$. The fact that the final states are CP eigenstates means that no angular analysis is needed. However, the expected annual yields for these channels are low (2–8'000 events per channel in $2\,\text{fb}^{-1}$). An expected statistical precision of $0.046\,\text{rad}$ can be reached on $\phi_s$ with these channels [31].

The second set of data is an admixture of CP eigenstates, the $B_s^0 \rightarrow J/\psi\,\phi$ decay. The $B_s^0$ meson decays to two vector particles, such that different polarisation need to be considered. An angular analysis is required in order to disentangle CP-even and CP-odd eigenstates. However, this golden channel has a large expected annual yield of 117'000 events and a clean signature. The loss of statistical precision from the angular analysis is compensated by the large event statistics. The resolution on $\phi_s$ from this analysis is expected to be $0.03\,\text{rad}$ [29].

# 1.5 Search for New Physics in the Study of Rare Decays

Based on the large number of $b$ hadrons produced each year, LHCb is an excellent place to study rare $B$-meson decays. These rare decays provide an excellent opportunity to look for New Physics (NP) effects in transitions such as $b \rightarrow s\ell^+\ell^-$ or $b \rightarrow s\gamma$. These transitions, which are described by flavour-changing neutral-current processes, are highly suppressed in the SM and only proceed via loop diagrams. NP particles could change the value of physics observables, such as branching ratios or asymmetries, by entering the loop diagrams. This section briefly describes two measurements that will be performed by LHCb in order to constrain NP in rare decays [32, 33].

## 1.5.1 Measurement of the $B_s^0 \rightarrow \mu^+\mu^-$ Branching Ratio

The $B_s^0 \rightarrow \mu^+\mu^-$ decay is described by a loop diagram involving both a $W^\pm$ and a $Z^0$ weak-mediating boson. The branching ratio of this decay is expected to be very small in the SM, with a theoretical prediction of $\mathcal{B}(B_s^0 \rightarrow \mu^+\mu^-) = (3.35 \pm 0.32) \times 10^{-9}$ [34]. The current combined upper limit given by the two Tevatron experiments is $3.6 \times 10^{-8}$ at $90\,\%$ CL [35, 36]. This means that if NP exists, new particles can still contribute an order of magnitude to the process. For example, in the minimal supersymmetric extensions of the SM (MSSM), this decay would receive additional contributions from loop diagrams involving SUSY particles. The branching ratio is then enhanced by a term proportional to the sixth power of the Higgs vacuum expectation ratio, $\tan\beta$.

The measurement to be performed at LHCb, described in Ref. [37], will take advantage of the excellent reconstruction, identification and trigger efficiencies for muons. Two selections have been developed, depending on how well the detector is understood in the

first phase of the experiment. The standard and robust selections differ only by the use of error estimates in the former. The measurement or upper limit on the branching ratio is then a function of the integrated luminosity. The sensitivity of the two selections is comparable and LHCb is likely to overtake the expected Tevatron-combined final sensitivity with about 0.2 fb$^{-1}$ of data collected at a centre-of-mass energy of $\sqrt{s} = 8$ TeV. If the branching fraction is equal to the SM prediction, LHCb will obtain a $3\,\sigma$ evidence of this decay with about 3 fb$^{-1}$ of data collected at a centre-of-mass energy of $\sqrt{s} = 14$ TeV. If NP effects enhance the branching fraction, then a signal will be observed sooner. For example, if the branching ratio is close to the current upper limit, as predicted by some models, then as little as 0.4 fb$^{-1}$ of integrated luminosity is needed for a $5\,\sigma$ discovery. In any case, even at the SM predicted value, 10 fb$^{-1}$ are sufficient for a $5\,\sigma$ discovery.

## 1.5.2 Measurement of the $B_d^0 \rightarrow K^*\mu^+\mu^-$ Forward-Backward Asymmetry

The branching ratio of the $B^0 \rightarrow K^*\mu^+\mu^-$ decay has been measured and is in agreement with the SM prediction of $\mathcal{B}(B^0 \rightarrow K^*\mu^+\mu^-) = (9.8 \pm 0.2) \times 10^{-7}$ [33]. New Physics could however still play a role in this decay by affecting the dynamics of the decay and in particular the muon forward-backward asymmetry in the di-muon rest frame as a function of the di-muon invariant mass squared, $A_{\mathrm{FB}}(s)$. This asymmetry is defined as

$$A_{\mathrm{FB}}(s) = \frac{N(\cos\theta > 0) - N(\cos\theta < 0)}{N(\cos\theta > 0) + N(\cos\theta < 0)}, \tag{1.24}$$

with $\theta$ defined as the angle between the flight directions of the $\mu^+$ and of the $B$ meson in the di-muon rest frame. The shape of $A_{\mathrm{FB}}(s)$ is known in the SM and for some NP models. A very interesting observable will be the zero-crossing point ($s_0$, such that $A_{\mathrm{FB}}(s_0) = 0$). This point is predicted to be $s_0 = (4.39 \, ^{+0.38}_{-0.35}) \, \mathrm{GeV}^2/c^4$ in the SM and differs for various extension models. The asymmetry has already been measured at BaBar, Belle and CDF [38, 39, 40], but the statistics are too low to prove or disprove any deviation from the SM prediction. The annual yield (in 2 fb$^{-1}$) at LHCb is expected to be around 7'000 events, with a background-to-signal ratio around 0.2. For comparison, the largest statistics collected by another experiment amount to 230 events by Belle [39]. Therefore, LHCb is expected to compete with the current measurement with only a few hundreds of pb$^{-1}$. With 2 fb$^{-1}$ of integrated luminosity, the expected statistical precision on $s_0$ is expected to be $0.46 \, \mathrm{GeV}^2/c^4$. The theoretical precision should be overtaken with 10 fb$^{-1}$ of data with which a statistical precision of $0.27 \, \mathrm{GeV}^2/c^4$ should be reached. This precision should allow to discriminate between supersymmetric models.

# 1.6 Charmonium Spectroscopy and the New $X$, $Y$ and $Z$ States

The recent resurgence of interest in charmonium spectroscopy has triggered interest at LHCb. Since 2008, studies have started at LHCb on the newly-discovered $X$, $Y$ and $Z$ states at the $B$ factories and at the Tevatron. An overview of this arising subject is given here, and some specific aspects of it are studied in more detail in Chapter 6.

In the early 1970s, Sheldon Glashow, John Iliopoulos and Luciano Maiani explained the observed suppression of flavour-changing decays of a strange quark into a down quark by the introduction of a fourth quark: the charm quark $c$. This so-called GIM mechanism [41] eliminates flavour-changing tree-decays by coupling the $c$ quark to the strange quark $s$. In Summer 1974, theoretical predictions of what a $c\bar{c}$ meson would be like were ignored. A few months later, two teams based at the Stanford Linear Accelerator Center and at the Brookhaven National Laboratory accidentally discovered a new narrow resonance [42, 43]. This new state was called $J$ by one team and $\psi$ by the other. The discovery of the $J/\psi$ meson, which was later referred to as the November Revolution, led to the wide acceptance of the idea that particles are not elementary particles but are made of smaller entities called quarks.

In the years following the November Revolution, nine other charmonium states were observed and named $\eta_c(1S)$, $\chi_{c0}(1P)$, $\chi_{c1}(1P)$, $\chi_{c2}(1P)$, $\psi(2S)$ [3], $\psi(3770)$ [4], $\psi(4040)$, $\psi(4160)$ and $\psi(4415)$. These states are shown in the charmonium spectrum of Fig. 1.6. The spectrum of observed states is analogous to atomic spectroscopy. The states are either described using the $J^{PC}$ notation, where $J$ is the total angular momentum, $P$ is the intrinsic parity and $C$ is the charge conjugation quantum number. Another notation is the spectroscopic notation $n^{2S+1}L_J$, where $n$ is the radial quantum number, $S$ the spin, $L$ is the orbital angular momentum, which can be given as a numerical value, $L = 0, 1, 2, 3, 4, 5$ or a corresponding letter S, P, D, F, G, H, etc. The expected states can be modelled using a combination of linear and coulombic potential:

$$V_{\mathrm{conf}} = -\frac{4\alpha_s}{3r} + br\,, \tag{1.25}$$

where $a = 0.5462$ and $b = 0.1425\,\mathrm{GeV}^2$ can be extracted from a fit of the charmonium spectrum [44].

The width of the states depends whether they are produced above or below the open-charm threshold ($\approx 2 \times m_c = 3.73\,\mathrm{GeV}/c^2$). States above this threshold decay preferably to two $D$ mesons and are broad resonances. Below this threshold, narrow resonances are observed because any hadronic mode is strongly suppressed, following the OZI rule. This rule, independently proposed by Okubo, Zweig and Iizuka in the 1960s [23, 46, 47], explains why certain decays appear less frequently than expected. It states that strong interaction processes where the final states can only be reached through quark anti-quark annihilation are suppressed. This means for example that the decay $\phi \to \pi^+\pi^-\pi^0$ is suppressed relative to $\phi \to K^+K^-$ (shown respectively in Fig. 1.7 (a) and (b)).

No other charmonium state was observed in the following twenty years. However, charmonium spectroscopy was not abandoned and the already discovered states were studied in detail, with their properties being specified precisely. Their mass, width, quantum numbers and decay modes were described and theoretically modelled with good precision.

## 1.6.1   Discovery of the $X$, $Y$ and $Z$ States

In 2003, the Belle collaboration, working at the KEKB $e^+$–$e^-$ collider in Japan, reported the observation of a narrow charmonium-like state in the exclusive decay $B^\pm \to$

---

[3] This state is reported as $\psi'$ in Fig. 1.6.
[4] This state is reported as $\psi''$ in Fig. 1.6.
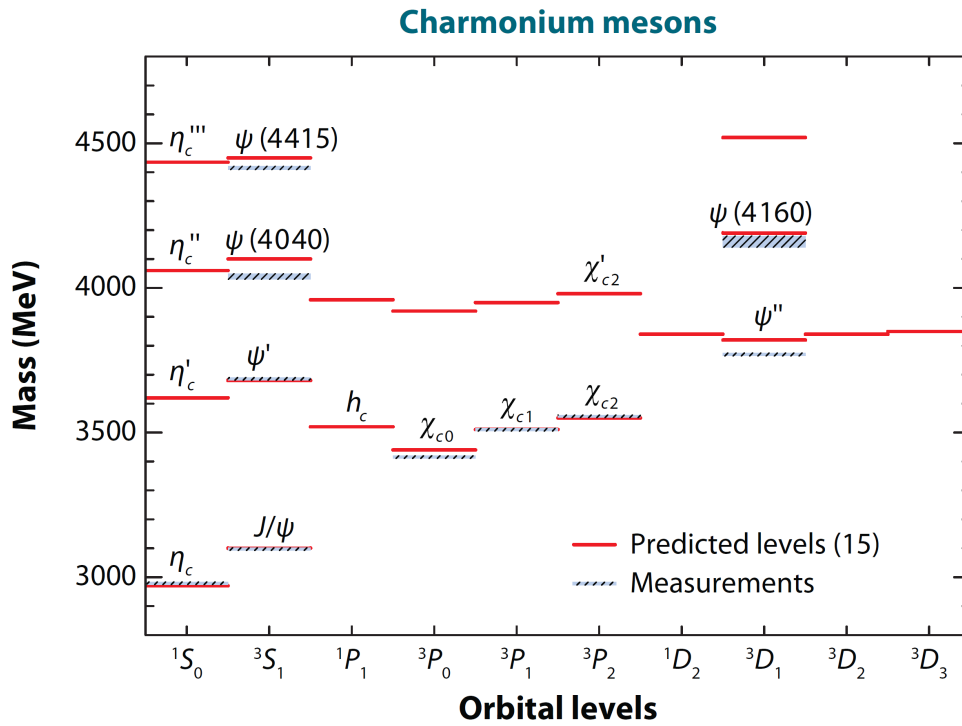
Figure 1.6: Status of the charmonium spectroscopy. Solid red lines are predicted states, whereas dashed light-blue lines are experimental states. Figure taken from [45].
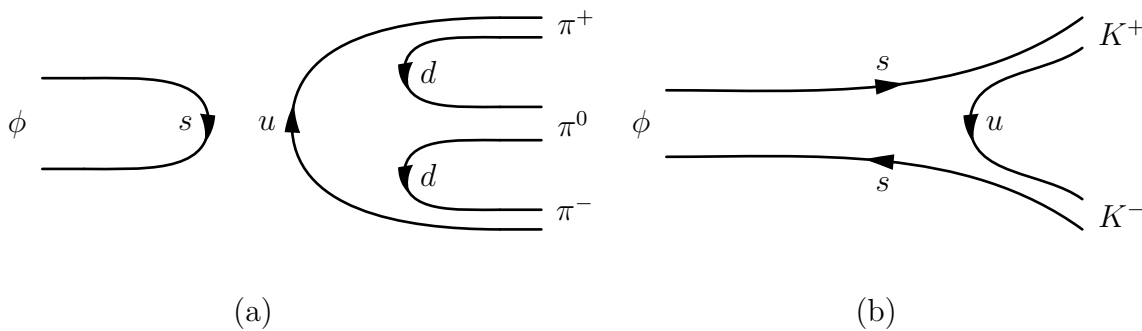


Figure 1.7: Two Feynman diagrams showing (a) an OZI-suppressed decay $\phi \to \pi^+\pi^-\pi^0$ and (b) an OZI-allowed decay $\phi \to K^+K^-$.
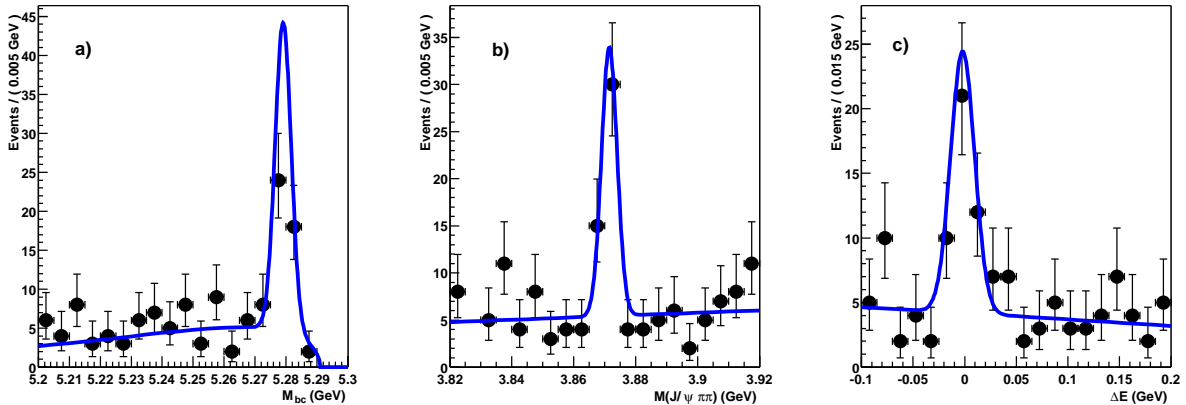
Figure 1.8: Discovery of $X(3872)$ in the $B \to J/\psi\,\pi^+\pi^- K$ channel by Belle [8]. (a) Beam-energy constrained mass $M_{\rm bc} = \sqrt{E_{\rm beam}^2 - \left(\sum_i \vec{P}_i\right)^2}$ for the $X(3872) \to J/\psi\,\pi^+\pi^-$ signal region. $M_{\rm bc}$ is expected to be close to the $B$ mass for signal events. (b) Invariant mass $M_{J/\psi\,\pi^+\pi^-}$ of the $J/\psi\,\pi^+\pi^-$ system. (c) Difference $\Delta E = \sum_i E_i - E_{\rm beam}$ between the measured centre-of-mass (CM) energy of the $B$ candidate and the CM beam energy. $\Delta E$ is expected to be close to zero for signal events. The curves are the results of unbinned fits.

$K^\pm\pi^+\pi^- J/\psi$ [8]. The $X(3872)$ state was reconstructed in the $J/\psi\,\pi^+\pi^-$ final state with a mass of

$$M(X(3872)) = 3872.0 \pm 0.6 \pm 0.5 \text{ MeV}/c^2 \tag{1.26}$$

and a width smaller than $2.3\,\text{MeV}/c^2$ at $90\,\%$ confidence level. The peak, shown in Fig. 1.8, has a statistical significance of $10.3\,\sigma$. The discovery was confirmed in 2004 both by the CDF [48] and the DØ [49] collaborations at the Tevatron through prompt production in $p\bar{p}$ collisions and in 2005 by the BaBar collaboration [50] at SLAC in the $B^\pm \to X(3872)K^\pm \to J/\psi\,\pi^+\pi^- K^\pm$ decay.

This discovery started a new era in charmonium spectroscopy, triggering the discovery of several other new states called $X$, $Y$ and $Z$ (see for example References [44, 51, 52] for detailed reports). Some of these newly discovered particles were identified as conventional charmonium states: $h_c(1P)$ [53], $\eta_c(2S)$ [54] and $Z(3930) \equiv \chi_{c2}(2P)$ [55]. However, the nature of others remains unclear. The next section gives an overview of various theoretical models developed to account for the properties of the new states. Then, the discovery and properties of two of these states are discussed: the $X(3872)$, and the $Z(4430)^\pm$, the only charged state in the $XYZ$ families.

## 1.6.2   Theoretical Models

The $X$, $Y$ and $Z$ states were first thought to be charmonium states (for example the $X(3872)$ in Ref. [56]). However, some of the new discoveries did not match any of the predicted states in the charmonium spectrum (see Fig. 1.6). Several models have been developed to explain the nature of the new states. Two possibilities are mesonic molecules

or tetraquark states. These models were already proposed thirty years ago to explain the properties of the light scalar mesons $f_0(980)$ and $a_0(980)$ [57].

### 1.6.2.a Mesonic Molecules

Shortly after the discovery of the $X(3872)$ state, Törnqvist suggested in Ref. [13] that it could be a mesonic molecule. The deuson is the equivalent of the deuteron (a proton and a neutron bound by pion exchange), with mesons replacing the baryons. A two-meson system bound by an attractive pion exchange could explain the properties of the $X(3872)$ state. $D^*D$ bound states with masses close to $3870\,\mathrm{MeV}/c^2$ were already predicted ten years prior to the discovery of the new charmonium-like states [58]. The motivation for such description comes from the fact that the measured $X(3872)$ mass is close to the $D^{*0}\bar{D}^0$ mass threshold. This deuson with $c\bar{u} - \bar{c}u$ quark content has quantum numbers equal to $J^{PC} = 1^{++}$.

Using an effective field theory approach, as for the description of the deuteron [59], this model predicts the ratio of branching fractions for neutral and charged $B$ mesons decaying to an $X(3872)K$ final state to be [44]

$$\frac{\mathcal{B}(B^0 \to XK_\mathrm{S}^0)}{\mathcal{B}(B^+ \to XK^+)} \approx 0.06 - 0.29\,. \tag{1.27}$$

Finally, the molecular model can be challenged by another measurement, the ratio of branching ratios of the $X(3872)$ state to two charmed mesons and to the $J/\psi$ charmonium state, predicted to be [44]

$$\frac{\mathcal{B}(X(3872) \to D^0\bar{D}^0\pi^0)}{\mathcal{B}(X(3872) \to J/\psi\,\pi^+\pi^-)} \approx 0.08\,. \tag{1.28}$$

A drawback of this model is the fact that a loosely bound molecular state is unlikely to be produced in a high energy $p\bar{p}$ collision, in contradiction with the CDF observation of sizable direct $X(3872)$ production.

### 1.6.2.b Tetraquark States

As an alternative to the colourless bound molecular states described above, Maiani *et al.* have constructed a model of the new $X$ states dominated by a diquark-diquark structure [14]. In this model, states with four valence quarks describe quarks grouping in colour-triplet scalar and vector clusters bound by a simple spin–spin interaction. Based on the measurement of the $X(3872)$ meson, a spectrum of new tetraquark states, shown in Fig. 1.9, is predicted. In this framework, the $X(3872)$ can be identified with the $J^{PC} = 1^{++}$ state of $[cq][\bar{c}\bar{q}]$, where $q \in \{d, u\}$. An important prediction from this model is that two neutral $X$ states, the $[cu][\bar{c}\bar{u}]$ and $[cd][\bar{c}\bar{d}]$, should mix and produce two mass states with a mass difference of

$$M(X_\mathrm{H}) - M(X_\mathrm{L}) \approx (8 \pm 3)\,\mathrm{MeV}/c^2\,. \tag{1.29}$$

In Ref. [15], the $X(3872)$ state decaying into $J/\psi\,\pi^+\pi^-$ is identified with the $[cd][\bar{c}\bar{d}]$ neutral state, while $[cu][\bar{c}\bar{u}]$ is identified with an other observed state close by, called
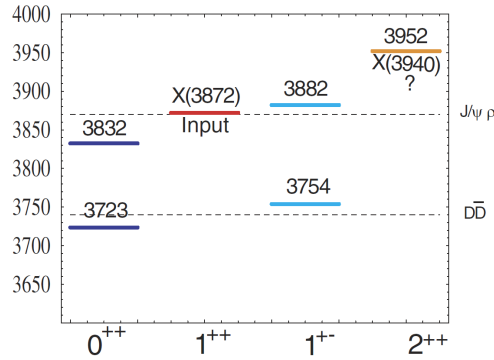
Figure 1.9: Full spectrum of the $X$ states in the tetraquark model. Figure taken from [14].

the $X(3876)$ decaying preferably to $D^0\bar{D}^0\pi^0$. Also, the former state will appear in $B^+$ decays, while the latter will populate $B^0$ decays. In addition, two charged partners should be observed, namely $X^+ = [cu][\bar{c}\bar{d}]$ and $X^- = [cd][\bar{c}\bar{u}]$.

This model also sets a prediction of unity for the ratio of branching fractions of neutral to charged $B$ meson decaying to $X(3872)$ (see Equation 1.27).

#### 1.6.2.c $c\bar{c}g$ Hybrid Mesons

This model tries to reconcile the charmonium-like nature of the $X(3872)$ and other new states with the observations by constructing an hybrid state comprised of a $c\bar{c}$ pair bound with a valence gluon [12]. However, the current models give expected masses for $c\bar{c}g$ hybrids in the range $4200 - 4400\,\mathrm{MeV}/c^2$, significantly higher than the observed $X(3872)$ state. This model predicts that the ratio of branching ratios given in Equation 1.27 should be unity.

#### 1.6.2.d Near-Threshold Enhancement

Due to the proximity of the $X(3872)$ mass to the $D^0\bar{D}^{*0}$ threshold, another possible scenario is that the $X(3872)$ is actually a cusp effect in the amplitude at the threshold [11, 60]. This effect would lead to a bump in the cross-section slightly above the threshold. Enhancements at thresholds due to cusps have width of the order $\mathcal{O}(\Lambda_{\mathrm{QCD}}) = 217\,^{+25}_{-23}\,\mathrm{MeV}$. The peak corresponding to this threshold opening should be visible in both decays $B^+ \to K^0 D^+\bar{D}^{*0}$ and $B^+ \to K^+ D^0\bar{D}^{*0}$ with similar amplitudes.

### 1.6.3 $X(3872)$

In the Summer 2008, Belle updated its mass measurement of the $X(3872)$ state [61]. The latest value is

$$M(X(3872)) = (3871.46 \pm 0.37 \pm 0.07)\,\mathrm{MeV}/c^2\,. \tag{1.30}$$

The current most precise measurement has been performed by CDF at the same time [62] and places the $X(3872)$ at a mass of

$$M(X(3872)) = (3871.61 \pm 0.16 \pm 0.19)\,\mathrm{MeV}/c^2\,. \tag{1.31}$$
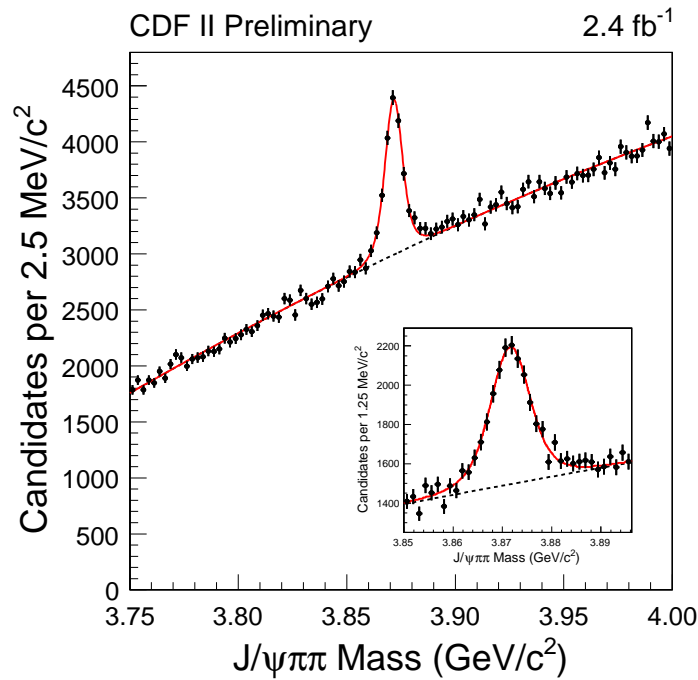
Figure 1.10: Latest CDF result (2008) for the measurement of the $X(3872)$ mass. The distribution of the $J/\psi\,\pi^+\pi^-$ mass is shown [62]. The points represent data, the full line the total fit and the dashed line the combinatorial background. The inset shows a zoom to the region of the $X(3872)$.

The current world average for the $X(3872)$ mass, taking into account the latest CDF results shown in Fig. 1.10, the DØ, BaBar and Belle measurements, places the $X(3872)$ mass at $(3871.46\pm0.19)\,\mathrm{MeV}/c^2$. This mass is close to the mass threshold of two $D$ mesons: $M_{D^0}+M_{D^{*0}}=(3871.81\pm0.36)\,\mathrm{MeV}/c^2$. An overview of the $X(3872)$ mass measurements is given in Fig. 1.11. The $D^*D$ production threshold is shown for comparison. The mass difference between the $X(3872)$ mass and the world average for the sum of the molecular components is slightly negative with a value of $(-0.3\pm0.4)\,\mathrm{MeV}/c^2$. However, due to the uncertainties, a simple S-wave bound state $D^{*0}\bar{D}^0$ is still possible.

The width has been determined to be below the detector resolution: $<2.3\,\mathrm{MeV}/c^2$ at 90 % confidence level in the $J/\psi\,\pi^+\pi^-$ channel. It is slightly larger in the $D^0D^{*0}$ decay with a value of $(3.0\,{}^{+1.9}_{-1.4}\pm0.9)\,\mathrm{MeV}/c^2$. The product of branching ratios were originally measured by Belle [63] and BaBar [64]:

$$\mathcal{B}(B^+\to X(3872)K^+)\times\mathcal{B}(X(3872)\to J/\psi\,\pi^+\pi^-) = (1.3\pm0.3)\cdot10^{-5} \text{ and} \quad (1.32)$$

$$\mathcal{B}(B^+\to X(3872)K^+)\times\mathcal{B}(X(3872)\to J/\psi\,\pi^+\pi^-) = (1.01\pm0.25\pm0.10)\times10^{-5} \quad (1.33)$$

The current world average [16] sets the combined branching ratio at $(1.14\pm0.2)\times10^{-5}$.

The $X(3872)$ state has also been observed decaying through other channels. Both Belle and BaBar have observed the decay $X(3872)\to J/\psi\,\gamma$ and $X(3872)\to\omega J/\psi$ [65, 66]. This combined observation fixes the charge conjugation quantum number to be $C_X=+1$.
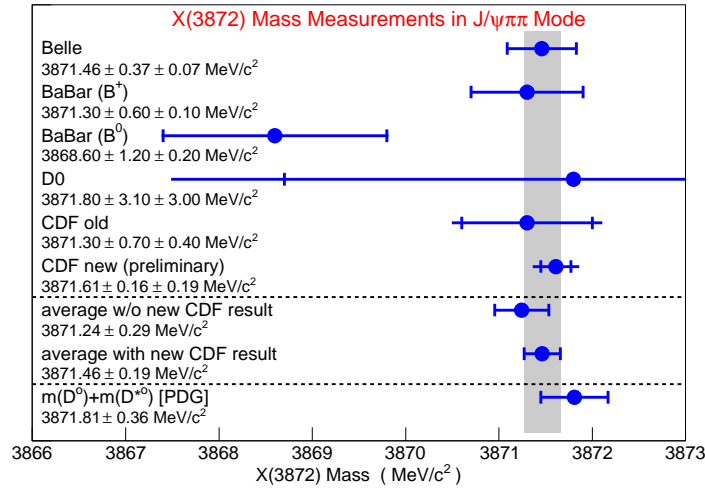
Figure 1.11: Overview of the $X(3872)$ mass measurements and average. Figure taken from [62].

Further analysis by CDF of the $\mu^+\mu^-\pi^+\pi^-$ final state for the $X(3872)$ decay has ruled out most of the $J^{PC}$ possibilities [67]. It has been demonstrated that only $J^{PC} = 1^{++}$ and $2^{-+}$ are still possible. A summary of all the observed $X(3872)$ decay channels is given in Table 1.2 with the statistical significance, along with the measured mass and width when available.

The charmonium model was first thought to describe the nature of the new state. However, neither the $\chi_{c1}(2P)$ (with $J^{PC} = 1^{++}$), nor the $\eta_{c2}$ ($J^{PC} = 2^{-+}$) states can account for the measured mass. Furthermore, analysis of the di-pion mass in the final state of the $X(3872) \rightarrow J/\psi\,\pi^+\pi^-$ decay indicates it preferably goes through an intermediate $\rho^0$. Figure 1.12 shows the di-pion mass spectrum obtained by the CDF collaboration. Events are clustered towards the upper bound of the spectrum, near the $\rho^0$ mass. This $J/\psi\,\rho^0$ final state violates isospin in case of a charmonium decay. It should be strongly suppressed, which is inconsistent with the Belle and CDF observations [8, 74]. The charmonium hypothesis is hence disfavoured.

Due to the close $D^0 - D^{*0}$ mass threshold, the $X(3872)$ has also been interpreted as an S-wave $D^0 D^{*0}$ molecular state [13]. In this model, the $X(3872)$ is a $J^{PC} = 1^{++}$ state which can decay to $\rho^0 J/\psi$, $\omega J/\psi$ and $\gamma J/\psi$. The $X(3872) \rightarrow D^{*0}\bar{D}^0$ decay has been observed by the BaBar collaboration in 2008, in a study based on a $347\,\mathrm{fb}^{-1}$ data sample. The statistical significance is of $4.9\,\sigma$. However, the observed mass is significantly larger than the world average and this state is sometimes called the $X(3875)$ with a mass of $M = (3875.1\,^{+0.7}_{-0.5} \pm 0.5)\,\mathrm{MeV}/c^2$. This mass was in agreement with a measurement of the Belle collaboration in the $D^0\bar{D}^0\pi^0$ invariant-mass spectrum of the $B \rightarrow D^0\bar{D}^0\pi^0 K$ channel. With a $414\,\mathrm{fb}^{-1}$ data sample, a mass of $M = (3875.18 \pm 0.68)\,\mathrm{MeV}/c^2$ was measured with a statistical significance of $6.4\,\sigma$. However, based on a more recent analysis of the $D^0\bar{D}^0\pi^0$ decay mode, assuming an intermediate $D^{*0}$ state decaying to $D^0\pi^0$ and $D^0\gamma$, Belle has updated this result and now finds a mass of $M(X \rightarrow D^0\bar{D}^0\pi^0) = (3872.6\,^{+0.5}_{-0.4} \pm 0.4)\,\mathrm{MeV}/c^2$, which is closer to the nominal $X(3872)$ mass [71].

Table 1.2: Observed $X(3872)$ decay channels, with corresponding mass and width if available.

| Channel | M [MeV/$c^2$] | $\Gamma$ [MeV/$c^2$] | Signif. | Seen by |
|---|---|---|---|---|
| $B \to J/\psi\,\pi\pi K$ | $3872.0 \pm 0.6 \pm 0.5$ | $< 2.3$ | $10\,\sigma$ | Belle [8] |
| $p\bar{p} \to J/\psi\,\pi\pi$ | $3871.3 \pm 0.7 \pm 0.4$ | $< 3.2$ | $11.6\,\sigma$ | CDF [48] |
| $p\bar{p} \to J/\psi\,\pi\pi$ | $3871.8 \pm 3.1 \pm 3.0$ | resolution | $5.2\,\sigma$ | DØ [49] |
| $B \to J/\psi\,\pi\pi K$ | $3873.4 \pm 1.4$ | – | $3.5\,\sigma$ | BaBar [50] |
| $B \to J/\psi\,\pi\pi K$ | $3871.5 \pm 0.4 \pm 0.1$ | – | $> 10\,\sigma$ | Belle [68] |
| $B \to J/\psi\,\pi\pi K$ | $3871.4 \pm 0.6 \pm 0.1$ | $< 3.3$ | $8.6\,\sigma$ | BaBar [69] |
| $B \to J/\psi\,\pi\pi K$ | $3871.46 \pm 0.37 \pm 0.07$ | – | – | Belle [61] |
| $p\bar{p} \to J/\psi\,\pi\pi$ | $3871.61 \pm 0.16 \pm 0.19$ | – | – | CDF [62] |
| $B \to D^0 \bar{D}^0 \pi^0 K$ | $3875.2 \pm 0.7 \pm 0.8$ | $5.7 \pm 1.3$ | $6.4\,\sigma$ | Belle [70] |
| $B \to D^0 \bar{D}^0 \pi^0 K$ | $3872.6\,^{+0.5}_{-0.4} \pm 0.4$ | – | $6.4\,\sigma$ | Belle [71] |
| $B \to D^{*0} \bar{D}^0 K$ | $3875.1\,^{+0.7}_{-0.5} \pm 0.5$ | $3.0\,^{+1.9}_{-1.4} \pm 0.9$ | $4.9\,\sigma$ | BaBar [72] |
| $B \to J/\psi\,\gamma K$ | – | – | $4.0\,\sigma$ | Belle [66] |
| $B \to J/\psi\,\gamma K$ | – | – | $3.6\,\sigma$ | BaBar [73] |
| $B \to \psi(2S)\gamma K$ | – | – | $3.5\,\sigma$ | BaBar [73] |
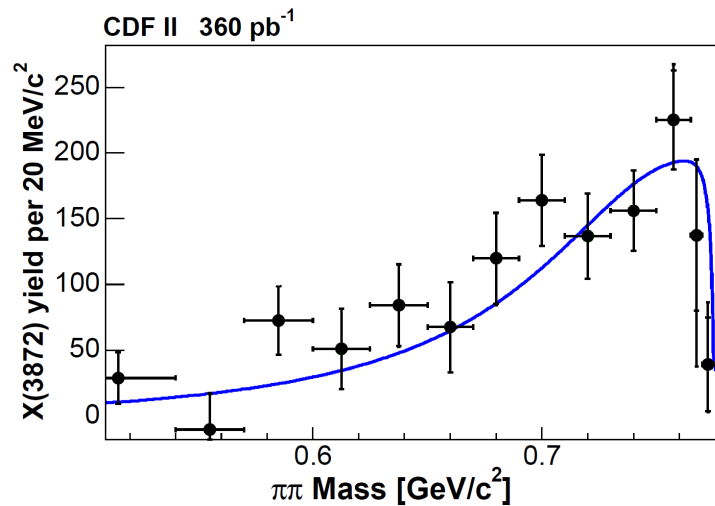


Figure 1.12: Invariant mass spectrum of the di-pion system in the $X(3872) \to J/\psi\,\pi^+\pi^-$ decay. Figure taken from [74].

According to the tetraquark model, two neutral $X$'s should be observed. Both BaBar and Belle collaborations have studied this possibility by measuring the $X(3872)$ mass in $B^+ \rightarrow X(3872)K^+$ and $B^0 \rightarrow X(3872)K^0_S$ decays, with $X(3872) \rightarrow J/\psi\,\pi^+\pi^-$ in both cases. The mass difference between the two $X(3872)$ states in charged and neutral $B$-meson decays is found to be

$$\Delta M \equiv M_{XK^+} - M_{XK^0_S} = \begin{cases} (2.7 \pm 1.6 \pm 0.4)\,\mathrm{MeV}/c^2 & \text{BaBar [69]}, \\ (0.18 \pm 0.89 \pm 0.26)\,\mathrm{MeV}/c^2 & \text{Belle [68]}, \end{cases} \quad (1.34)$$

consistent with zero and disagrees with the prediction of the tetraquark model given in Equation 1.29. This study has also been performed by the CDF collaboration [62]. The possibility to have two resonances merged in one peak was tested and it was found that the maximum mass splitting is $\Delta M < 3.2\,\mathrm{MeV}/c^2$ at $90\,\%$ CL. This measurement also disfavours the tetraquark model.

The ratio of branching fractions,

$$\frac{\mathcal{B}(B^0 \rightarrow XK^0_S)}{\mathcal{B}(B^+ \rightarrow XK^+)} = \begin{cases} 0.41 \pm 0.24 \pm 0.05 & \text{BaBar [69]}, \\ 0.82 \pm 0.22 \pm 0.05 & \text{Belle [68]}, \end{cases} \quad (1.35)$$

is consistent with unity and hence agrees with the tetraquark and hybrid models. However, due to the large experimental uncertainties in this measurement, it is not possible to rule out the molecular model whose prediction is given in Equation 1.27.

Another check of the tetraquark hypothesis has been performed by the BaBar collaboration by searching for the charged partner of the $X(3872)$ [75]. The obtained upper limits on the production of the charged partners of the $X(3872)$ in the $B^0 \rightarrow X(3872)^-K^+$ and $B^- \rightarrow X(3872)^-K^0_S$ decays with the $X(3872)^-$ decaying to $J/\psi\,\pi^-\pi^0$ have been set at $90\,\%$ CL to

$$\mathcal{B}(B^0 \rightarrow X(3872)^-K^+) \times \mathcal{B}(X(3872)^- \rightarrow J/\psi\,\pi^-\pi^0) < 5.4 \times 10^{-6}, \quad (1.36)$$
$$\mathcal{B}(B^- \rightarrow X(3872)^-K^0_S) \times \mathcal{B}(X(3872)^- \rightarrow J/\psi\,\pi^-\pi^0) < 22 \times 10^{-6}. \quad (1.37)$$

This measurement excludes the isovector hypothesis for the $X(3872)$.

Finally, the BaBar collaboration has released results inconsistent with a pure molecular hypothesis for the $X(3872)$ state. An evidence for $B \rightarrow X(3872)K$ radiative decays has been published with the $X(3872)$ decaying both to $J/\psi\,\gamma$ and $\psi(2S)\gamma$ with statistical significances of $3.6\,\sigma$ and $3.5\,\sigma$ respectively [73]. The latter has a branching ratio too high to be consistent with a purely $D^{*0}\bar{D}^0$ molecular interpretation. It is concluded that none of the proposed models fully explains the observed properties of the $X(3872)$. The best hypothesis currently is a mixed state with a molecular and a charmonium component.

## 1.6.4 $Z(4430)^{\pm}$

During the first 5 years of the new charmonium era, all the $XYZ$ states that were discovered were electrically neutral. Another revolution happened in 2008 when the Belle collaboration announced the discovery of a charmonium-like state with a non-zero charge [10]. Since it is electrically charged, it can neither be a conventional charmonium $c\bar{c}$ state, nor
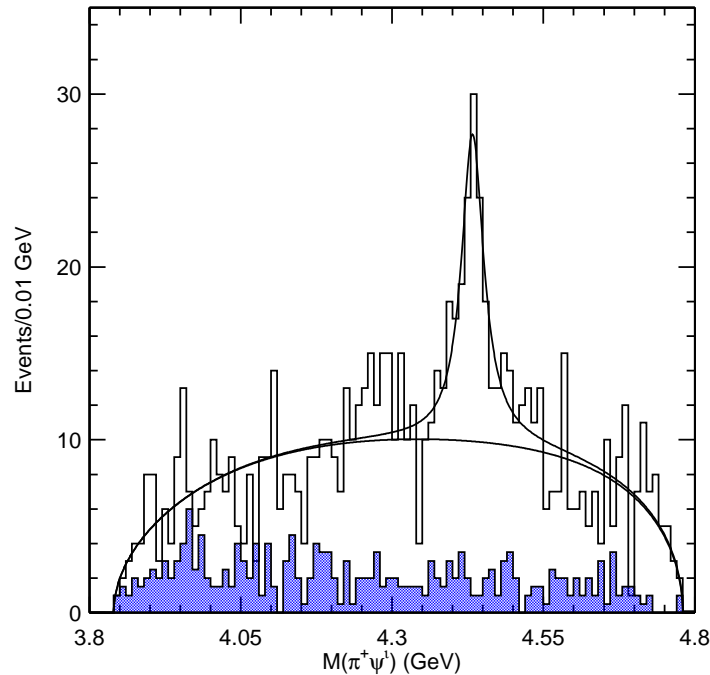
Figure 1.13: Discovery of $Z(4430)^+$ in the distribution of the $\pi^+\psi(2S)$ invariant mass $M(\pi^+\psi(2S))$ from $B \to \pi^+\psi(2S)K$ decays at Belle [10] (the $\psi(2S)$ is also called $\psi'$, as in the axis title). The curve is the sum of a relativistic Breit-Wigner function and a smooth phase-space-like function. The filled histogram shows scaled results from the $\Delta E$ sidebands.

a $c\bar{c}g$ hybrid state (see Section 1.6.2.c for details), which are neutral. This new state, called the $Z(4430)^\pm$, was found in the $\pi^\pm\psi(2S)$ invariant-mass distribution (shown in Fig. 1.13) in $B \to Z(4430)^\pm K \to \pi^\pm\psi(2S)K$ decays, with $K$ being either a $K^0_S$ or a $K^\mp$ and B either charged or neutral. The statistical significance of the signal is of $6.5\,\sigma$. The peak is a broad resonance centred at $M = (4433 \pm 4 \pm 2)\,\text{MeV}/c^2$ with a width of $\Gamma = (45\,^{+18}_{-13}(\text{stat.})\,^{+30}_{-13}(\text{syst.}))\,\text{MeV}/c^2$. The combined branching ratio was measured to be

$$\mathcal{B}(B \to KZ(4430)^\pm) \times \mathcal{B}(Z(4430)^\pm \to \pi^\pm\psi(2S)) = (4.1 \pm 1.0 \pm 1.4) \times 10^{-5}\,. \quad (1.38)$$

The BaBar collaboration has studied the $B \to K\pi^\pm J/\psi$ and $B \to K\pi^\pm\psi(2S)$ decays [76]. The $J/\psi$ sample showed no enhancement. For the $\psi(2S)$ sample, small signals were obtained with statistical significance smaller than $3\,\sigma$ leading BaBar to claim no evidence of the existence of the $Z(4430)^\pm$ state. Following this, the Belle collaboration reanalysed their data and confirmed the first observation of the $Z(4430)^\pm$ [77]. More statistics are needed in order to confirm or discard the Belle discovery.

The mass of the $Z(4430)^\pm$ state is close to the mass threshold of two $D$ mesons: $M_{D^*} + M_{D_1(2420)} = 4430\,\text{MeV}/c^2$. Therefore, it was interpreted as a loosely bound molecular state of $D^* - D_1$. Such a state can be reproduced using QCD sum rules [78, 79] with quantum numbers $J^P = 0^-$ [80]. As such, the $Z(4430)^\pm$ states could be understood as the first radial excitation of the hypothetical charged partners of the $X(3872)$ state [81].

### 1.6.5   Other $XYZ$ States

Several other states were found since the discovery of the $X(3872)$ by Belle in 2003. A review of these states can be found in References [44, 51, 52]. Two families are shortly presented here.

The $XYZ(3940)$ family is made of three charmonium-like states. These states have similar masses:

$$M_{X(3940)} = (3943 \pm 6 \pm 6)\,\mathrm{MeV}/c^2\,, \tag{1.39}$$

$$M_{Y(3940)} = (3943 \pm 17)\,\mathrm{MeV}/c^2\,, \tag{1.40}$$

$$M_{Z(3930)} = (3929 \pm 6)\,\mathrm{MeV}/c^2\,. \tag{1.41}$$

However, they have different widths:

$$\Gamma_{X(3940)} = (39 \pm 26)\,\mathrm{MeV}/c^2\,, \tag{1.42}$$

$$\Gamma_{Y(3940)} = (87 \pm 34)\,\mathrm{MeV}/c^2\,, \tag{1.43}$$

$$\Gamma_{Z(3930)} = (29 \pm 10)\,\mathrm{MeV}/c^2\,, \tag{1.44}$$

and are found in quite different processes. The $X(3940)$ was discovered by Belle [82] in $e^+e^- \to X(3940)J/\psi$ with $X(3940) \to D^*\bar{D}^0$, whereas the $Y(3940)$, also discovered by Belle [83], was found in $B \to Y(3940)K$ with $Y(3940) \to \omega J/\psi$ and confirmed by BaBar with a somewhat smaller mass of $(3914.6\,^{+3.8}_{-3.4} \pm 1.9)\,\mathrm{MeV}/c^2$. The $Z(3930)$ was discovered by Belle [55] in two-photon collisions $\gamma\gamma \to D\bar{D}$ and was interpreted as the $\chi_{c2}(2P)$ charmonium state.

Another family of unexpected charmonium-like states was found in initial-state-radiation events: $e^+e^- \to \pi^+\pi^- J/\psi\,\gamma_{\mathrm{ISR}}$ and $e^+e^- \to \pi^+\pi^-\psi(2S)\gamma_{\mathrm{ISR}}$ processes. These states have masses above the open-charm threshold, but yet do not preferably decay to two charm mesons. The $Y(4260)$ (discovered by BaBar [84] and confirmed by CLEO [85] and Belle [86]), $Y(4350)$ (discovered by BaBar [87] and confirmed by Belle [88]) and $Y(4660)$ (discovered by Belle [88]) have masses either above or below predicted $J^{PC} = 1^{--}$ charmonium levels (these quantum numbers are predicted for states produced with initial-state radiation).

The CDF collaboration has also recently reported the evidence for a narrow resonance in the $J/\psi\,\phi$ mass spectrum [89]. The $Y(4140)$ was found in the $B^+ \to J/\psi\,\phi K^+$ decay, with a statistical significance of $3.8\,\sigma$ in an analysis based on $2.7\,\mathrm{fb}^{-1}$ of integrated luminosity. The observed state has a mass and width of

$$M(Y(4140)) = (4143.0 \pm 2.9(\mathrm{stat.}) \pm 1.2(\mathrm{syst.}))\,\mathrm{MeV}/c^2\,, \tag{1.45}$$

$$\Gamma(Y(4140)) = (11.7\,^{+8.3}_{-5.0}(\mathrm{stat.}) \pm 3.7(\mathrm{syst.}))\,\mathrm{MeV}/c^2\,. \tag{1.46}$$

Finally, Belle also observed two other charged states $Z_1^+(4050)$ and $Z_2^+(4250)$ in $B^0 \to Z_{1,2}^+K^- \to \chi_{c1}\pi^+K^-$ decays [90]. The significance of these two signals exceeds $5\,\sigma$. However, neither of these has been confirmed by another collaboration.

Table 1.3 summarises the main properties of all the states discussed in this section, indicating the production and decay modes as well as the collaborations that observed the states.

Table 1.3: Overview of the properties of the charmonium-like $XYZ$ states.

| State | Production mode | Decay mode | $M$ ( MeV/$c^2$) | $\Gamma$ ( MeV/$c^2$) | Seen by |
|---|---|---|---|---|---|
| $X(3872)$ | $B \to X(3872)K$ | $J/\psi\,\pi^+\pi^-$ | $3871.5 \pm 0.4$ | $< 2.3$ | Belle [8], BaBar [50], CDF [48], DØ [49] |
| $X(3875)$ | $B \to X(3875)K$ | $D^0\bar{D}^0\pi^0, D\bar{D}^*$ | $3875.2 \pm 0.7$ | $3.0\,^{+2.1}_{-1.7}$ | Belle [70], BaBar [72] |
| $Z(3930)$ | $\gamma\gamma \to Z(3930)$ | $D\bar{D}$ | $3929 \pm 5$ | $29 \pm 10$ | Belle [55] |
| $X(3940)$ | $e^+e^- \to X(3940)J/\psi$ | $D\bar{D}^*$ | $3943 \pm 6$ | $39 \pm 26$ | Belle [82] |
| $Y(3940)$ | $B \to Y(3940)K$ | $J/\psi\,\omega$ | $3943 \pm 17$ | $87 \pm 34$ | Belle [83], BaBar [91] |
| $X(4160)$ | $e^+e^- \to X(4160)J/\psi$ | $D^*\bar{D}^*$ | $4156 \pm 29$ | $139\,^{+113}_{-65}$ | Belle [92] |
| $Y(4008)$ | $e^+e^-$(ISR) | $J/\psi\,\pi^+\pi^-$ | $4008\,^{+82}_{-49}$ | $226\,^{+97}_{-80}$ | Belle [86] |
| $Y(4140)$ | $B^+ \to Y(4140)K^+$ | $J/\psi\,\phi$ | $4143.0 \pm 2.3$ | $11.7\,^{+8.3}_{-5.0}$ | CDF [89] |
| $Y(4260)$ | $e^+e^-$(ISR) | $J/\psi\,\pi^+\pi^-$ | $4264 \pm 12$ | $83 \pm 22$ | BaBar [84], Belle [86], CLEO [85] |
| $Y(4350)$ | $e^+e^-$(ISR) | $\psi(2S)\pi^+\pi^-$ | $4361 \pm 13$ | $74 \pm 18$ | BaBar [87], Belle [88] |
| $Y(4660)$ | $e^+e^-$(ISR) | $\psi(2S)\pi^+\pi^-$ | $4664 \pm 12$ | $48 \pm 15$ | Belle [88] |
| $Z_1^+(4050)$ | $B^0 \to Z_1^+(4050)K^-$ | $\chi_{c1}\pi^+$ | $4051 \pm 14$ | $82\,^{+21}_{-17}$ | Belle [90] |
| $Z_2^+(4250)$ | $B^0 \to Z_2^+(4250)K^-$ | $\chi_{c1}\pi^+$ | $4248\,^{+44}_{-29}$ | $177\,^{+54}_{-39}$ | Belle [90] |
| $Z(4430)^\pm$ | $B \to Z(4430)^\pm K$ | $\psi(2S)\pi^\pm$ | $4433 \pm 5$ | $45\,^{+35}_{-18}$ | Belle [10] |

## 1.6.6　Measurement of the $X(3872)$ and $Z(4430)^\pm$ Properties

In Chapter 6, selections of the $X(3872)$ and $Z(4430)^\pm$ mesons in $B$ decays are discussed in the context of the LHCb experiment. With a good spatial resolution and a high luminosity, LHCb will reconstruct a large sample of $X(3872)$, giving the opportunity to set stronger constraints on its nature and measure its quantum numbers. LHCb will also play a major role in the confirmation of the $Z(4430)^\pm$ signal observed by Belle, but not by BaBar.

The study of the $XYZ$ spectroscopy at LHCb is promising. The already observed states at Belle, BaBar, CDF and other $B$-factories will be studied and other states might be discovered. Especially, the higher masses will be studied with a hope to find the $b$ counterparts of the $XYZ$ states made of $b$ quarks, the $Y_b$.

# Chapter 2

# The LHCb Experiment
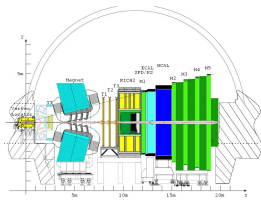


In this chapter a general description of the LHCb experiment is given. First the LHC accelerator is presented, then the LHCb detector and its sub-detectors and sub-systems are described.

## 2.1   The Large Hadron Collider

$\mathfrak{T}$HE Large Hadron Collider (LHC) is a 27 km proton collider situated 100 m underground in the old LEP tunnel at CERN, near Geneva, Switzerland. Proton–proton collisions will occur at a centre-of-mass energy of $\sqrt{s} = 14\,\text{TeV}$, more than seven times larger than that of the world's current largest accelerator, the Tevatron at Fermilab, USA.

Accelerating charged particles on a bent trajectory requires the use of dipole magnets. Although the curvature of the 27 km accelerator is not large, the tremendous design energy for the protons implies that a strong magnetic field is needed. This is done with the use of Nb-Ti superconducting magnets cooled to 1.9 K. A magnetic field of 8.34 T needs to be reached to maintain the high energy beams on track.

Two proton beams will circulate in opposite directions and in independent beam pipes. The two beam pipes merge at the four interaction points in order for the beams to cross and for proton–proton collisions to happen. An LHC beam will contain $N_{\text{bx}} = 2808$ proton bunches, each consisting of $\sim 10^{11}$ protons. These proton bunches are part of a complex structure of 3564 buckets shown in Fig. 2.1. This structure leaves empty spaces corresponding to SPS and LHC Injection Kicker rise times and to the LHC Dump Kicker rise time. The buckets will cross with a frequency of 40 MHz, i.e. two consecutive buckets will be separated by 25 ns. This frequency sets the requirement for the processing speed of the front-end electronics. The average crossing rate of two proton bunches $\nu_{\text{bx}}$ is of the order of $\sim 30\,\text{MHz}$ at the LHCb interaction point.

The number $N_{pp}$ of inelastic $pp$ collisions taking place at each interaction point depends on the number of protons circulating in the accelerator, the crossing frequency and the
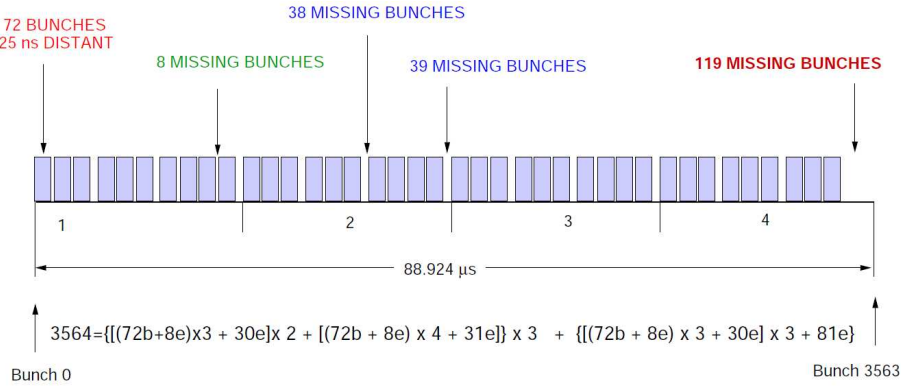
Figure 2.1: Structure of the proton bunch trains circulating in the LHC.

total proton–proton cross-section. $N_{pp}$ for a given time period can be calculated as

$$N_{pp} = \sigma_{pp}^{\text{inel}} \int \mathcal{L} \mathrm{d}t \,, \tag{2.1}$$

where $\sigma_{pp}^{\text{inel}} = 60 \, \text{mb}$ is the expected inelastic proton–proton cross-section at $\sqrt{s} = 14 \, \text{TeV}$ and $\mathcal{L}$ is the instantaneous luminosity. The latter gives the number of interactions at a crossing point. It depends on the beam characteristics, namely its transverse size at the interaction point (emittance), $N_{\text{bx}}$ and $\nu_{\text{bx}}$. The design luminosity of the LHC is $\mathcal{L} = 10^{34} \, \text{cm}^{-2}\text{s}^{-1}$, but this will not be reached in the first years.

The mean number of interactions per bunch crossing is

$$\langle n_{pp} \rangle = \frac{\sigma_{pp}^{\text{inel}} \mathcal{L}}{\nu_{\text{bx}}} \,. \tag{2.2}$$

At the LHC nominal luminosity, this means $\langle n_{pp} \rangle \sim 25$ interactions per bunch crossing. This is too large for LHCb's purposes, which require the correct matching of a reconstructed $b$ decay to the primary vertex in which it was created. Events with many interactions will lead to false matches which degrade the quality of the physics results. To solve this, the beam is slightly less focused prior to entering the LHCb interaction point compared to the other interaction points. In this way, the luminosity can be adjusted to a nominal value of $2 \times 10^{32} \, \text{cm}^{-2}\text{s}^{-1}$. Figure 2.2 shows the probability to get $n_{pp} = 0$, 1, 2, 3 or 4 interactions per bunch crossing as a function of the running luminosity. On average, there are 0.7 interactions per bunch crossing at LHCb nominal luminosity.

At a centre-of-mass energy of $14 \, \text{TeV}$ in $pp$ collisions, the LHCb tuning of the PYTHIA event generator (described in Section 2.2.5) gives the $b\bar{b}$-pair production cross-section to be $1040 \, \mu\text{b}$. Hence LHCb expects the production of $10^{12}$ $b\bar{b}$ pairs per nominal year [1]. These pairs will then hadronise into $b$ hadrons (namely $B^0$, $B^+$, $B_s^0$ mesons and $b$ baryons) according to the fractions $f_{\bar{b}}$ given in Table 2.1.

---

[1] A nominal year is defined as $10^7$ seconds of running time.
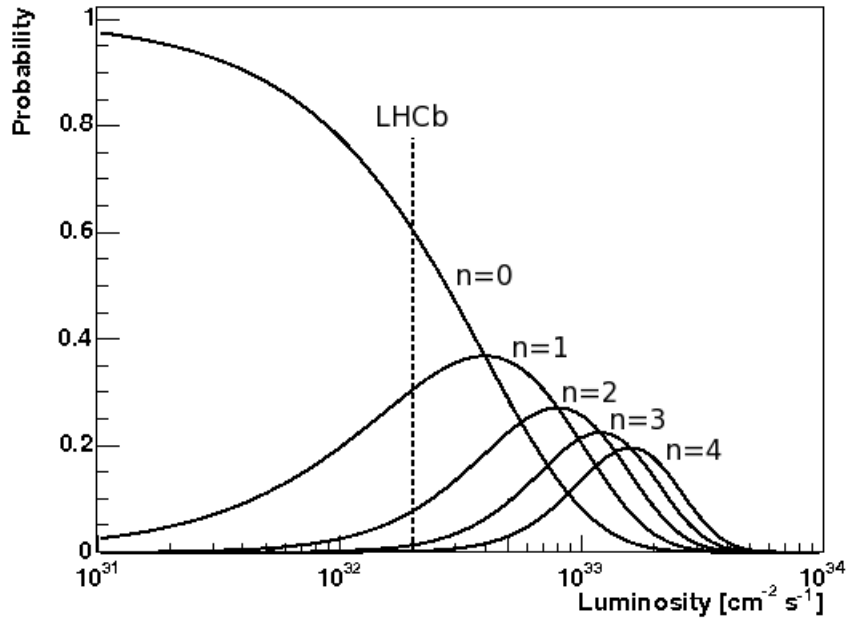
Figure 2.2: Probability of $n_{pp} = 0$, 1, 2, 3 or 4 proton–proton interactions in a bunch crossing as a function of the instantaneous luminosity. The design luminosity at LHCb is represented by the dashed line.

Table 2.1: $b$ hadron production fractions $f_{\bar{b}}$ [16].

| $b$ hadron | Production fraction [%] |
|---|---|
| $f_{\bar{b}}(B^+)$ | $39.9 \pm 1.1$ |
| $f_{\bar{b}}(B^0)$ | $39.9 \pm 1.1$ |
| $f_{\bar{b}}(B^0_s)$ | $11.0 \pm 1.2$ |
| $f_{\bar{b}}(b \text{ baryons})$ | $9.2 \pm 1.9$ |
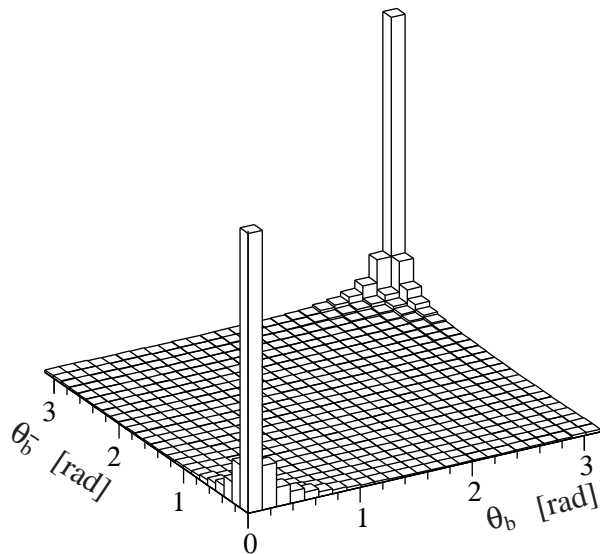
Figure 2.3: Polar angle of the $b$ and $\bar{b}$ hadrons calculated by the PYTHIA event generator.

## 2.2   The Detector

The fact that $b\bar{b}$-pair production is peaked in a narrow cone around the beam axis, as shown in Fig. 2.3, has driven the design of the detector, shown in Fig. 2.4. Due to the limited space in the existing cavern (which was dug for the DELPHI experiment at LEP) and to budget constraints, only the forward direction is instrumented. The chosen design leads to an excellent spatial and proper time resolution, a precise particle identification, giving a good hadron $\pi/K$ and lepton $e/\mu$ separation, and an efficient trigger covering the selection of a wide range of rare decays.

The experimental setup has dimensions of about 6 m in the horizontal transverse direction (the $x$ coordinate), 5 m in the vertical direction (the $y$ coordinate) and 20 m in the horizontal longitudinal direction (the $z$ coordinate). The coordinate system is centred on the nominal interaction point. The $y$ axis points upwards and the $z$ axis towards the Muon Stations. The direction of the $x$ axis follows the definition of a right-handed coordinate system. The angular acceptance covers an approximate range of $10-300$ mrad in the horizontal plane (bending plane) and $10-250$ mrad in the vertical plane (non-bending plane). It is limited by the beam pipe at small angles and the magnet at large angles.

The detector consists of the following parts (represented in Fig. 2.4):

- the beam pipe;

- the **VE**rtex **LO**cator (VELO);

- the first **R**ing and **I**maging **CH**erenkov counter (RICH1);

- the **T**racker **T**uricensis (TT);

- the dipole magnet;
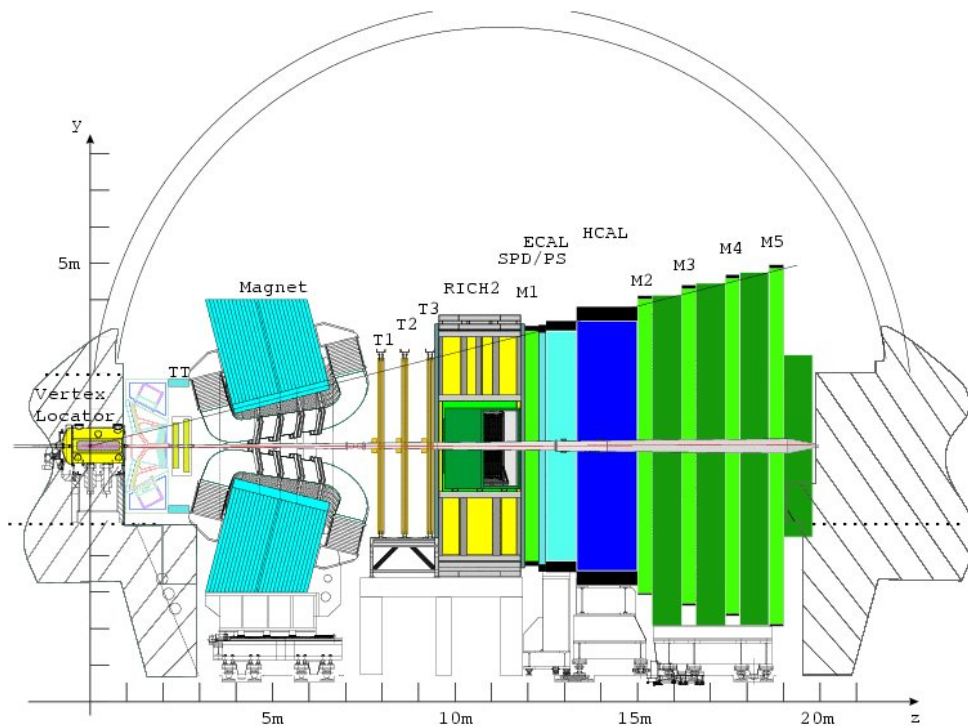
Figure 2.4: Side-view of the LHCb spectrometer. The LHCb reference coordinate system is shown.

- the three **T**racking Stations (T1, T2 and T3). Each of these stations is made of a central **I**nner **T**racker (IT) station surrounded by an **O**uter **T**racker (OT) station;

- the second **R**ing and **I**maging **CH**erenkov counter (RICH2);

- the first **M**uon Station (M1);

- the **S**cintillating **P**ad **D**etector and the **P**re-**S**hower detector (SPD/PS);

- the **E**lectromagnetic **CAL**orimeter (ECAL);

- the **H**adronic **CAL**orimeter (HCAL);

- the four other **M**uon Stations (M2, M3, M4 and M5).

## 2.2.1   The Beam Pipe

The beam pipe [93] traverses the whole detector, apart from the VELO, which is enclosed in a vacuum vessel connected to the beam pipe at its two ends. The first 12 m section is made of 1 mm thick Beryllium with Aluminium flanges and bellows. Beryllium is chosen as it has a relatively long radiation length of 35.28 cm, reducing the amount of secondary interactions, which would increase the occupancy in the detector. It is also resistant enough to hold the vacuum in the region of the LHCb detector. The last seven metres of the beam pipe, located downstream of the tracker, are made of stainless steel, which
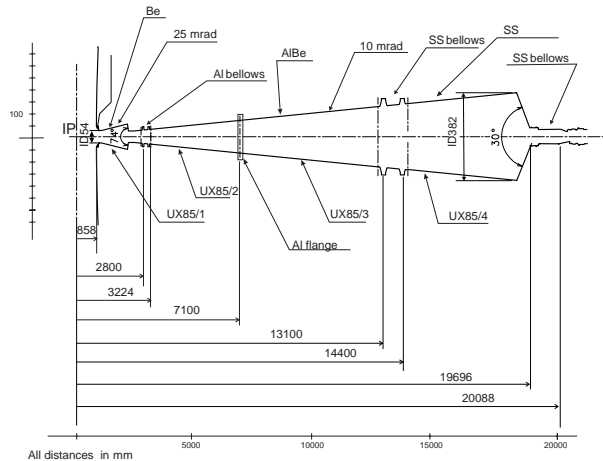
Figure 2.5: Layout of the beam pipe through the LHCb experimental setup.

is mechanically less fragile and less expensive. Figure 2.5 shows a schematic view of the beam pipe, with its two conical sections. The first one is 1840 mm long with an aperture of 25 mrad, while the second has an aperture of 10 mrad over the remaining length of the detector.

## 2.2.2   The Tracking System

The tracking system (see Fig. 2.4) consists of the VELO, a large area silicon detector (TT) located upstream of the dipole magnet of the experiment, and three Tracking Stations (the T Stations) located downstream of the magnet. The latter are divided into the Inner and Outer Tracker (IT and OT).

   The tracking system reconstructs the trajectories of charged particles that fly through the detector. The ratio of the electric charge and the momentum of these particles $(q/p)$ can be computed from the curvature of the tracks induced by the magnetic field. The most important tracks for physics studies are the so-called 'long tracks' (defined in Section 3.1.1) that traverse the spectrometer at least down to the Tracking Stations [94]. An event-weighted tracking efficiency [2] of 91.4 % is expected for a ghost rate of 14.6 % [3]. Above 10 GeV/$c$, the efficiency reaches a plateau at $\sim$ 97 %. For these tracks a momentum resolution of $\delta p/p \approx 4$ ‰ is achieved with simulated data.

### 2.2.2.a   The Vertex Locator

The $b$ hadrons produced in the detector have a long enough lifetime to give secondary vertices displaced by $\sim 1$ cm with respect to the primary vertices. A precise measurement of these displaced vertices is important for some of LHCb key measurements, e.g. time-dependent analysis of $B_s^0 - \bar{B}_s^0$ oscillations. It is also used in the trigger to select particles

---

   [2] The event-weighted efficiency is calculated as the mean of the distribution of the per-event efficiencies. It is different to the track-weighted efficiency, which is calculated as the efficiency over all events, ignoring the event structure.
   [3] Ghost tracks are reconstructed with hits from more than one particle [95].
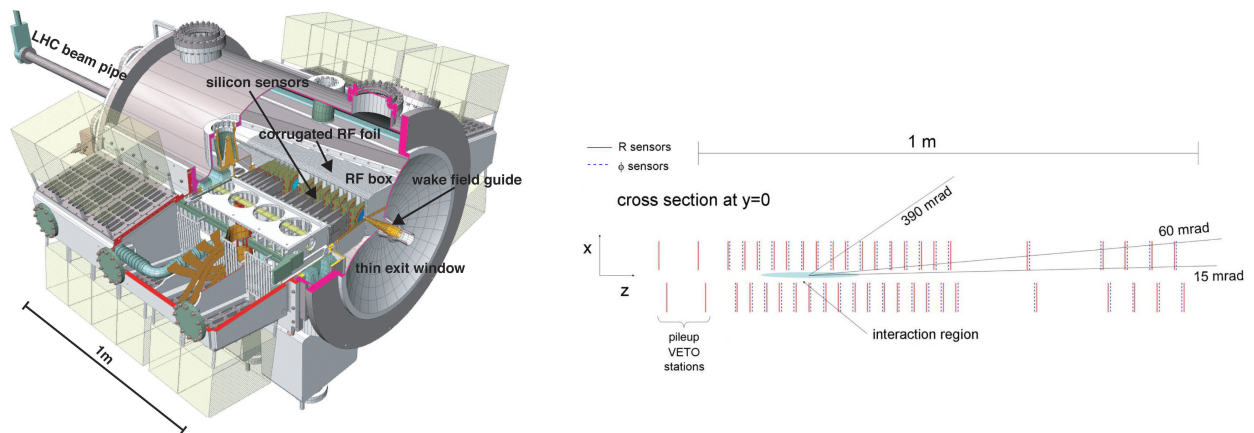
Figure 2.6: Layout of the VELO vacuum vessel (left) showing the LHC beam pipe and the silicon sensors. The layout of the 21 sensors inside the vessel is shown on the right. The two stations of the pile-up detector are also shown.

with large impact parameter significances (IPS) with respect to the primary vertex [4]. These are the main roles of the Vertex Locator.

The VELO [93], pictured in Fig. 2.6, is made of 21 stations spread along the beam line, with a minimal distance of 8 mm to the beam. Eight of these are used for backward-tracking purposes, the rest for forward tracking. Two additional upstream stations form the Pile-Up Detector, used in the L0 Trigger (Section 2.2.4.a) to veto events with multiple interactions. During the filling and ramping of the LHC, the beams do not collide and a bigger aperture is needed in the beam pipe. The VELO is hence designed as two halves which can be moved away from the beam by 3 cm. This system is contained inside a vacuum vessel sealed at both ends to the beam pipe.

A station consists of two pairs of half-discs mounted back to back, one pair on each side of the beam. Each pair consists of an $r$- and a $\phi$-measuring sensor (Fig. 2.7). These sensors are built with $300\,\mu$m thick $n$-on-$n$ single-sided silicon-strip modules, which are able to cope with the high radiation flux around the interaction region. For $10^7$ s of operation at nominal luminosity, this is estimated to be a 1 MeV equivalent neutrons flux of $1.3 \times 10^{14}\,n_{\mathrm{eq}}/\mathrm{cm}^2$ for the inner region and $5 \times 10^{12}\,n_{\mathrm{eq}}/\mathrm{cm}^2$ for the outer region. The $r$ sensors have $4 \times 512$ circular strips centred on the beam axis to measure the distance $r$ of the track to the centre, while the $\phi$ sensors have 683 (inner region) + 1365 (outer region) radial strips to measure the azimuthal angle $\phi$. The two half-stations are separated in $z$ by a 1.5 cm gap which allows for an overlap between sensors on the left and on the right of the beam. This is particularly valuable for alignment as it gives a powerful means to constrain the two halves with respect to each other (see Section 3.3.1).

With these parameters, the VELO achieves a hit resolution between 5 and $25\,\mu$m depending on the track angle and on the strip pitch, which varies between $\sim 40\,\mu$m and $\sim 100\,\mu$m from the inner part of the sensors outwards. The vertex reconstruction resolution is expected to be $40\,\mu$m in the offline reconstruction and twice larger for the on-line reconstruction.

---

[4] The IPS is defined as the impact parameter divided by its error, where the impact parameter is the distance of closest approach between the trajectory of the particle and the vertex of interest.

R-measuring sensor

101.6µm outer pitch

40µm
inner pitch

512
strips

512
strips

512
strips

512
strips

Phi-measuring sensor

35.5µm
inner pitch

20⁰ stereo angle

683 inner strips

78.3µm pitch

-10⁰ stereo angle

39.3µm pitch

1365 outer strips

96.6µm pitch
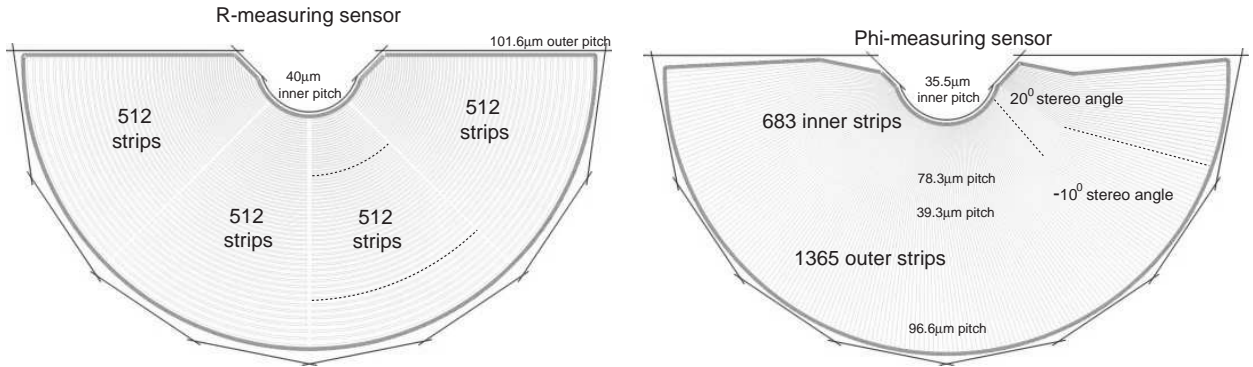
Figure 2.7: The VELO $r$ and $\phi$ sensors. The dotted lines illustrate the strips in both cases.

### 2.2.2.b The Tracker Turicensis

The Tracker Turicensis (TT) [5] was originally foreseen to provide momentum information as part of a Level-1 Trigger [96]. This level of trigger has now been abandoned, but the TT still plays an important role in LHCb [93]. It is located between the RICH1 and the magnet, $\sim 2.5\,\mathrm{m}$ away from the interaction region. Since it is in the fringe field of the magnet, it can be used to give a first estimate of the momentum of particles reconstructed in the VELO. It is also used to measure the momentum of slow particles which do not reach the Tracking Stations because of the magnet's bending power. Finally, it is used to reconstruct the decay product of long-lived particles, e.g. $K_\mathrm{S}^0$, which decay outside the VELO.

The TT is a large-area silicon-strip detector. It is made of four sensitive layers which cover an area of $\sim 130 \times 150\,\mathrm{cm}^2$ and add up to an active area of $8.4\,\mathrm{m}^2$. These four layers are arranged into two stations, TTa and TTb, separated in $z$ by $27\,\mathrm{cm}$. Each of these consists of an $X$ layer with vertical strips and a stereo layer with strips rotated by a stereo angle of $-5°$ in TTa (the U Layer) and $+5°$ in TTb (the V Layer). The layout of the TTbV and TTbX layers are shown in Fig. 2.8. Each layer consists of two seven-sensor ladders above and below the beam pipe, plus eight 14-sensor ladders (seven in TTa) on each side. This gives a total of 896 silicon-strip sensors (420 in TTa and 476 in TTb). The sensors are of the same type as those used in the CMS outer barrel. They are $500\,\mu\mathrm{m}$ thick, $9.64\,\mathrm{cm}$ wide and $9.44\,\mathrm{cm}$ long. Each has 512 readout strips with a strip pitch of $183\,\mu\mathrm{m}$.

The strip occupancy reaches a maximum of $3.5\,\%$ for the one-sensor sectors located around the beam pipe [97]. This drops to $2.2\,\%$ for the three-sensor sectors closest to the beam pipe. In all the other sectors, it is below $2\,\%$. For high momentum particles, a $10 - 40\,\%$ accuracy on $p_\mathrm{T}$ is expected for tracks reconstructed with the VELO and TT alone. The spatial resolution is $\sim 50\,\mu\mathrm{m}$.

---

[5] Until November 2007, this sub-detector was named the Trigger Tracker. The name was changed because of the decreasing use of the TT in the trigger.
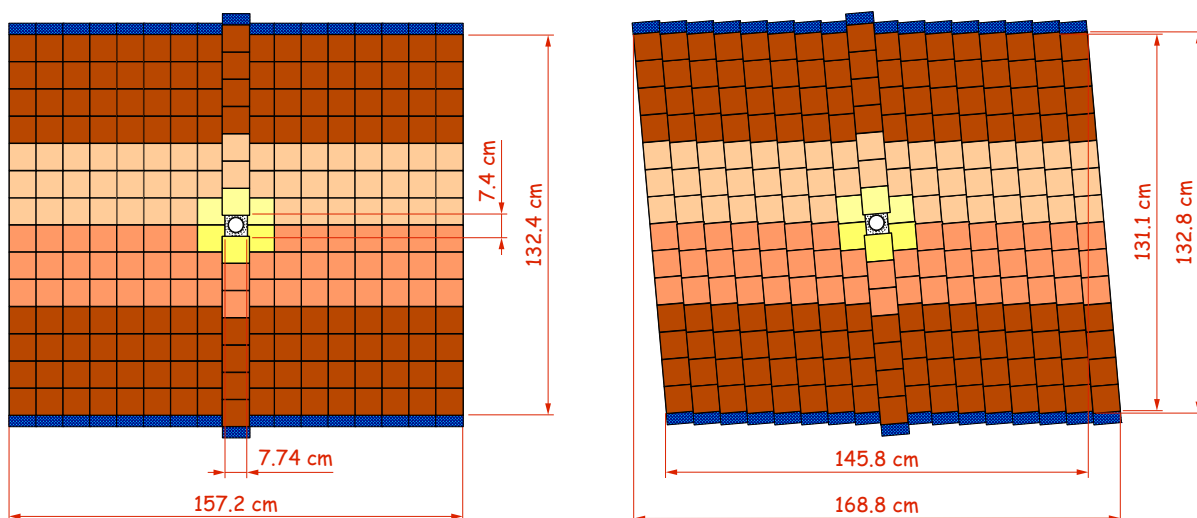
Figure 2.8: Layout of the two silicon-sensor layers of the TTb Station: the vertical $X$ layer on the left and the $+5°$-tilted stereo layer on the right. Different colours indicate different readout sectors.

### 2.2.2.c   The Dipole Magnet

LHCb uses a dipole magnet [93] to deflect the charged particles and hence determine their momentum from the curvature. The magnet, pictured in Fig. 2.9 surrounded by its iron yoke, is located close to the interaction point in order to maximise the geometrical acceptance with a limited size. The main component of the field is along the vertical ($y$) axis and the total integrated field is $\int B dl \sim 4\,\text{Tm}$. This enables precise measurement of the momentum, with a resolution of $\delta p/p \approx 4\,\text{‰}$ for $40\,\text{GeV}/c$ tracks that traverse the detector at least down to the T Stations.

A warm magnet was preferred over a superconducting one. This choice allows LHCb to regularly flip the field polarity in order to reduce systematics arising from left-right detector asymmetries. The spectrometer magnet provides also a short ramping time of the field and a good spatial uniformity.

### 2.2.2.d   The Inner Tracker

The boundary between the Inner and Outer Tracker is motivated by the detector occupancy. This is largest close to the beam pipe and in the horizontal (bending) plane and leads to a cross-shaped layout.

The Inner Tracker [93] consists of three stations. Station 1 is located at an average distance of 7.75 m from the nominal interaction point, Station 2 at $z = 8.44\,\text{m}$ and Station 3 at $z = 9.13\,\text{m}$. A station consists of four boxes (called Top, Bottom, A-side and C-side) placed around the beam pipe, as shown in Fig. 2.10. Each of the boxes contains four layers of seven silicon-strip modules called the IT ladders. Two $x$ layers ($X1$ and $X2$, with vertical strips) are placed on the outer part of the boxes while two stereo layers ($U$ and $V$, with strips tilted by $\pm 5°$ to allow for a measurement in the vertical direction) are
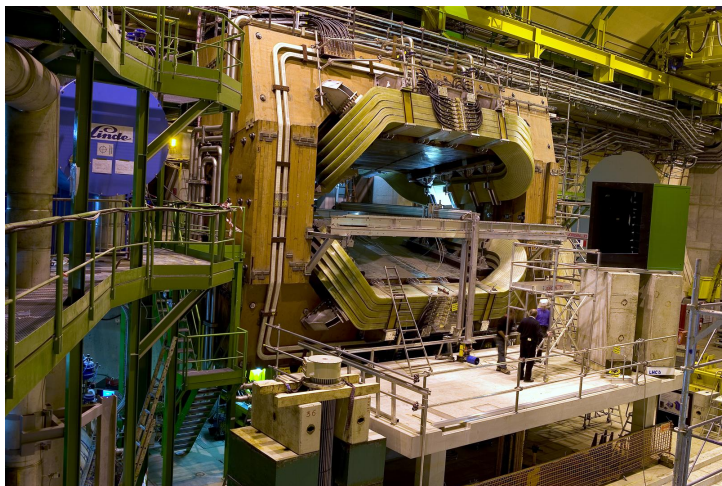
Figure 2.9: LHCb's dipole magnet with its two 27-ton coils surrounded by the 1500-ton iron yoke.

situated in the central part.

For the side boxes of Station 1, the maximum strip occupancy is 3.3 % for an average occupancy of 1.4 % [97]. In the Top and Bottom Boxes, occupancies are around 0.6 %. They are lower for the two other stations, with an average occupancy in the side boxes of 1.1 % and 0.9 % respectively. This is due to their increasing distance from the beam pipe supports which are a source of many secondary particles. These occupancies correspond to charged-particle densities between $1.5 \times 10^{-2}\,\mathrm{cm}^{-2}$ close to the LHC beam pipe and $2 \times 10^{-3}\,\mathrm{cm}^{-2}$ further away.

The choice of silicon-strip technology follows from the requirements of a detector able to cope with high particle fluxes and to provide excellent momentum resolution. The sensors used are 11 cm long and 7.6 cm wide. The thickness has been chosen to ensure a high signal-to-noise ratio whilst minimising the amount of material in the detector. A- and C-side modules (Fig. 2.10 (b)) are each made of two $410\,\mu$m sensors while Top and Bottom modules each consist of a single $320\,\mu$m silicon sensor. They are one-sided $p^+$-on-$n$ wafers carrying 384 silicon strips each with a strip pitch of $198\,\mu$m.

The Inner Tracker has a spatial single hit resolution of $\sim 57\,\mu$m. With this spatial resolution, the momentum resolution is dominated by multiple scattering up to $\sim 80\,\mathrm{GeV}$ and ranges from 0.35 % to 0.5 % (see Section 3.1.4).

### 2.2.2.e   The Outer Tracker

The Outer Tracker [93] covers the rest of the Tracking Stations, with a small overlap with the Inner Tracker acceptance. The total area of the OT adds up to $5971 \times 4850\,\mathrm{mm}^2$ per station, including the cross-shaped hole in the centre, which is filled by the beam pipe and the Inner Tracker. The inner boundary has been defined such that the maximum occupancy is 10 %. The layout, shown schematically in Fig. 2.11, is similar to that of the IT. The OT also consists of three stations, each having four layers. As in the IT, the layers are arranged as $X1$-$U$-$V$-$X2$.

(a)

(b)
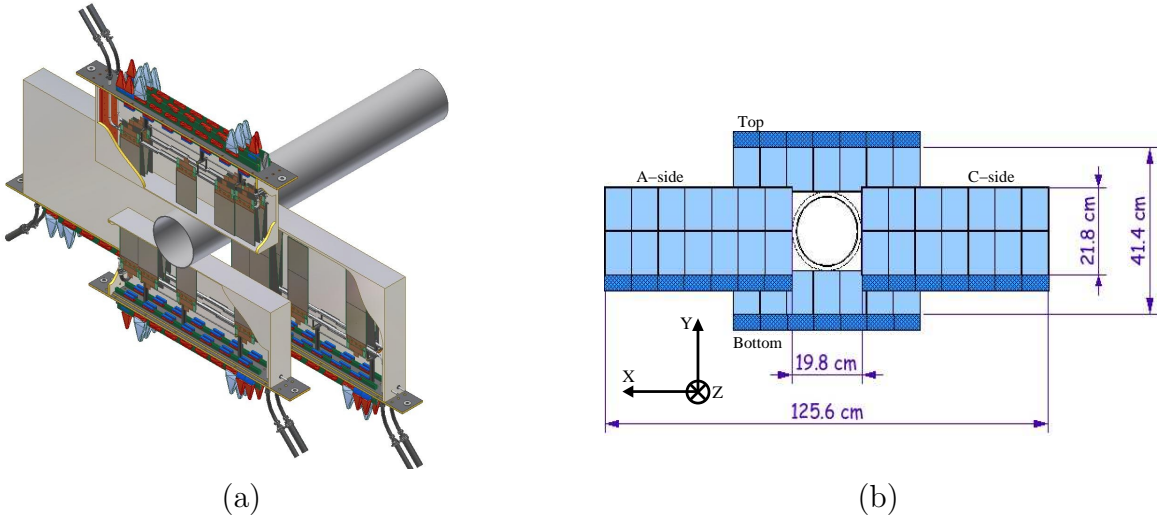
Figure 2.10: (a) 3D-view of the four boxes in one Inner Tracker station arranged around the beam pipe. (b) Layout of an $x$ layer in Station 2 of the Inner Tracker. Each light-blue cell represents one silicon-strip sensor.
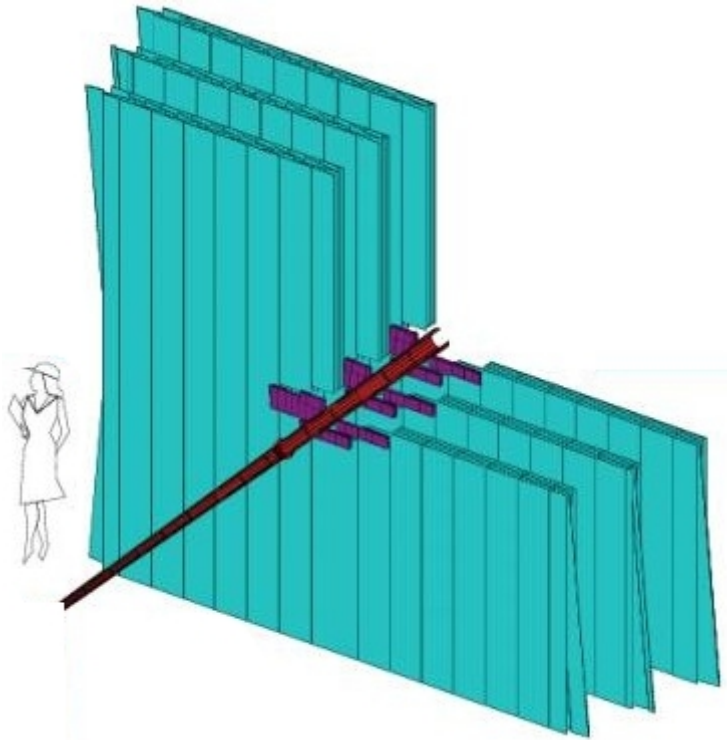


Figure 2.11: 3D view of the three Tracking Stations. The blue area is the Outer Tracker, around the purple Inner Tracker area. The beam pipe is also shown.

Because of the small particle fluxes compared to those in the Inner Tracker, the choice of technology for the OT is driven by low cost, the large area and the need for a good spatial resolution. Straw tubes filled with 70 % Ar and 30 % $CO_2$ were chosen in order to give a fast drift time (less than 50 ns) and a spatial resolution of $\sim 200\,\mu$m. Each layer is built from two halves of seven long and four short modules each. Long modules, with an active length of 4850 mm, contain 256 straw tubes each. The short modules, located above and below the IT, are about half the length of the long modules and contain 128 drift tubes each. In total, the OT consists of 168 long and 96 short modules, giving a total of 55'000 readout channels.

### 2.2.3 Particle Identification Systems

The LHCb requirements for particle identification (PID) are stringent. Good $K$-$\pi$ separation is of utmost importance for the reconstruction of selected $b$-hadron decays. Similarly, the identification of muons plays an important role both in the trigger and in the reconstruction of important CP-sensitive $B$-meson decays. A reliable particle identification is also crucial for the flavour tagging [98]. As discussed in Section 1.4.1, the neutral $B$ mesons oscillate between particle and anti-particle. The identification of the initial flavour of the reconstructed $B$ meson is necessary for the CP-asymmetry measurement. Flavour tagging is based on the reliable identification of muons, kaons and pions. These requirements have driven the design of the three sub-detectors described in the following sections.

#### 2.2.3.a The RICH Counters

Two Ring-Imaging Cherenkov (RICH) detectors [93] provide hadron identification in LHCb. They give information that permits discrimination between various particle hypotheses, e.g. $K$ vs $\pi$. This information is needed for the reconstruction of many $b$ decays of interest, such as $B_s^0 \rightarrow D_s h$ where $h$ is either a pion or a kaon [99].

Due to the wide momentum range of the particles traversing the detector, two Cherenkov detectors are used, covering two different ranges. RICH1 is located between the VELO and the TT and covers the low-momentum range, from $\sim 1$ to $60\,$GeV$/c$, using silica aerogel and $C_4F_{10}$ radiators. It has a geometrical acceptance similar to that of LHCb, from $\pm 25\,$mrad to $\pm 300\,$mrad (bending plane) and $\pm 250\,$mrad (non-bending plane). RICH2, situated between the T Stations and the first Muon Station, covers a smaller area, between $\pm 15\,$mrad to $\pm 120\,$mrad (bending plane) and $\pm 100\,$mrad (non-bending plane) and uses a $CF_4$ radiator. This is sufficient to identify high-momentum particles, from $\sim 15\,$GeV$/c$ up to $100\,$GeV$/c$.

Both detectors make use of the Cherenkov effect. When a particle traverses a medium with a speed $\beta$c greater than the speed of light $c/n$ in the medium, $n$ being the refractive index of the medium, it emits photons. These Cherenkov photons are emitted with an angle $\theta_C$ with respect to the particle path. The Cherenkov angle satisfies the relation:

$$\cos\theta_C = \frac{1}{\beta n}\,,\tag{2.3}$$

which implies that the condition $n\beta \geq 1$ must be satisfied in order to be able to detect
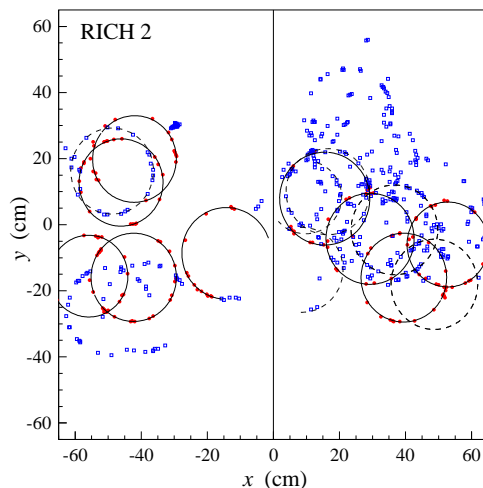
Figure 2.12: An example of Cherenkov photoelectrons detected by RICH2. The reconstructed rings are superimposed. The picture is taken from Ref. [96].

the Cherenkov light. This relation also drives the choice of radiators, depending on the momentum range to cover. In RICH1, the silica aerogel has a refractive index of $n = 1.03$ and the $C_4F_{10}$ has $n = 1.0014$. In RICH2, the tetrafluorocarbon $CF_4$ has a refractive index of $n = 1.0005$.

The light cones emitted by the moving charged particles are projected as rings by mirrors onto a plane of photodetectors, the HPDs (Hybrid Photon Detectors). A typical example of an event in RICH2 is shown in Fig. 2.12. The radius of the ring gives a measure of the opening angle of the corresponding light cone, which in turn gives a value of the particle velocity. Combining this information with the measurement of the particle momentum (obtained from the track curvature in the Tracking Stations) allows an estimate of the particle mass.

### 2.2.3.b The Calorimeters

The calorimeter system [93] is situated between the first and the second Muon Stations, M1 and M2. This system is composed of the Scintillating Pad Detector (SPD), the Pre-Shower (PS), the Electromagnetic and the Hadronic Calorimeters (ECAL and HCAL). The transverse energy ($E_T$) information it provides is used in the decision of the Level-0 Trigger (described in Section 2.2.4.a). The calorimeters also identify electrons and reconstruct neutral particles such as photons and neutral pions. All particles except for the muons, which interact less and are detected by the Muon Stations, and the neutrinos that escape the detector, are stopped in one of the calorimeter sub-systems.

**The Scintillating Pad Detector (SPD):** The SPD is used to separate photons and electrons. Charged particles going through the 15 mm thick scintillator pads release part of their energy through ionisation. This $e^{\mp}/\gamma$ separation is used in the early trigger stage to reject high-$E_T$ $\pi^0$ background. The scintillation light is transmitted to multi-anode photomultiplier tubes (PMT) by wavelength-shifting fibres (WLS).
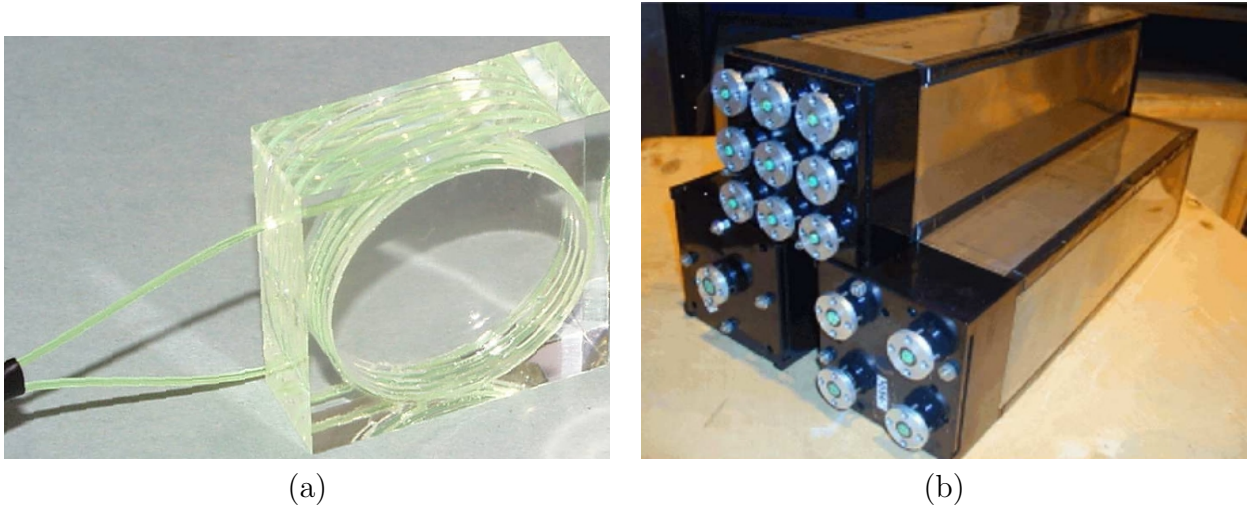
Figure 2.13: (a) An SPD/PS scintillator pad. (b) The three types of ECAL Shashlik modules. The inner ones have $3 \times 3$ readout cells, the middle ones have $2 \times 2$ while the outer modules have only one channel.

The probability of electrons being misidentified as photons by the SPD scintillator is $(0.8 \pm 0.3)\,\%$.

**The Pre-Shower (PS):** The SPD and the PS, which also uses the scintillating pad technology shown in Fig. 2.13 (a), are separated by a $12\,\mathrm{mm}$ thick lead wall. Incoming electrons are converted into an electromagnetic shower in this lead layer, which gives a distinction between electrons and charged pions, the latter leaving only little amounts of energy in the PS. The PS/SPD achieve pion rejection factors of $99.6\,\%$, $99.6\,\%$ and $99.7\,\%$ with electron retentions of $91\,\%$, $92\,\%$ and $97\,\%$ for 10, 20 and $50\,\mathrm{GeV}/c$ particle momentum, respectively.

**The Electromagnetic Calorimeter (ECAL):** The ECAL has been designed such as to contain the whole electromagnetic showers of incoming photons and electrons. This is achieved by the mean of 25 radiation-length Shashlik modules, which alternate $4\,\mathrm{mm}$ thick scintillating tiles with $2\,\mathrm{mm}$ thick lead absorber slices. Showers are initiated in the lead absorber and detected by individual PMTs connected to the scintillators by WLS fibre bunches. The large disparity of hit density depending on the distance to the beam pipe led to a layout with three different module types, pictured in Fig. 2.13. The difference between inner, middle and outer modules is the number of readout cells, $3 \times 3$, $2 \times 2$ and 1, respectively. The ECAL provides $e^{\mp}$ and $\gamma$ identification at the trigger level and measures their energy. The design energy resolution is given by

$$\sigma\left(E\right)/E = 10\,\%/\sqrt{E} \oplus 1\,\%, \tag{2.4}$$

with $E$ in GeV [93]. The first term describes the statistical fluctuation in the showers and the second term represents the systematic uncertainties coming from the inter-calibration of the cells.
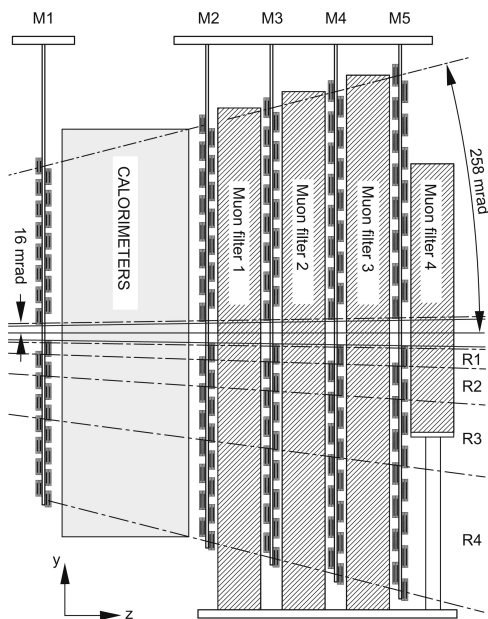
Figure 2.14: Side view of the muon system.

**The Hadronic Calorimeter (HCAL):** The HCAL is the last calorimeter sub-system and is located next to the Muon Station M2. Its purpose is to detect hadrons by the mean of their shower and to give an estimate of their energy. The trigger requirements in terms of resolution being less stringent for the HCAL than for the ECAL, the HCAL design has followed the space limitations rather than the need for full containment of the hadronic showers. Due to the wider lateral shower extension for hadrons than for electrons, the cell sizes are larger. It consists of 16 mm thick iron plates interspersed with 4 mm thick scintillating tiles. The total thickness corresponds to 5.6 interaction lengths. The design energy resolution of the HCAL is

$$\sigma\left(E\right)/E = 80\,\%/\sqrt{E} \oplus 10\,\%\,, \tag{2.5}$$

with $E$ in GeV.

### 2.2.3.c   The Muon System

The Muon System [93] is composed of five stations. Stations M2 to M5 are located after the calorimeters, which serve as muon filters. M1, on the other hand, is situated before the SPD. Except for the innermost part of M1, which uses gaseous triple GEM electron multiplier detectors, all stations are made of multi-wire proportional chambers. Each station is divided into four parts with different pad granularity, in order to ensure a constant relative $p_{\mathrm{T}}$ resolution over the whole detector surface. They are interleaved with 80 cm thick iron absorbers, as shown in Fig. 2.14. This amount of material, in addition to the calorimeter thickness, ensures that only penetrating muons with a momentum of at least 6 GeV/$c$ will cross all five stations.

Muon identification plays an important role in the trigger because muons are present in the final state of several $b$ decays of interest at LHCb. For this purpose, a standalone

muon reconstruction and $p_T$ measurement requiring hits in the five stations has been implemented in the Level-0 hardware-based Trigger (see Section 2.2.4.a). This leads to a fast track reconstruction with a 95 % track-finding efficiency and a 20 % momentum resolution, based on Stations M1 to M3 which have a high spatial resolution. M4 and M5 aim at identifying high-momentum particles.

In addition, muons from semi-leptonic $b$ decays are used in the tagging of neutral $B$ mesons via their charge. They will also play a major role in the search for New Physics through their appearance in rare $b$ decays. The importance of the muons imposes that the muon off-line tracking must be very efficient. The tracking software uses a track-segment in the T Stations as input and propagates it to the Muon System to confirm the muon hypothesis. This is achieved with a 99 % efficiency.

### 2.2.3.d   PID Likelihood

Using the information from the three previously described sub-detectors, a global PID information is derived for each charged particle as a log likelihood difference between a PID hypothesis and the pion hypothesis. This is expressed as

$$\Delta \ln \mathcal{L}_{a\pi} = \ln \mathcal{L}_a - \ln \mathcal{L}_\pi = \ln \left[ \frac{\mathcal{L}_a}{\mathcal{L}_\pi} \right] , \qquad (2.6)$$

where $\mathcal{L}_a$ combines the information of the Calorimeters, the RICH counters and the Muon Stations in a product of PID estimations. By definition, the delta log likelihood (DLL) for the pion hypothesis is equal to zero. Then, the DLL for two types of particles $a$ and $b$ can be obtained by subtracting the two corresponding DLL:

$$\Delta \ln \mathcal{L}_{ab} = \Delta \ln \mathcal{L}_{a\pi} - \Delta \ln \mathcal{L}_{b\pi} . \qquad (2.7)$$

## 2.2.4   The Trigger System

The luminosity at which LHCb will operate has been optimised such that events with a single interaction per bunch crossing dominate. This reduces the channel occupancy and leads to events which are easier to trigger and reconstruct. In addition, due to the LHC bunch structure described in Section 2.1 and the fact that the diffractive and elastic events do not leave tracks in the detector, the average visible interaction rate [6] is around 10 MHz, four times lower than the 40 MHz bunch crossing frequency. This is still much too large to be stored for offline analysis and contains many events which are not interesting for LHCb's physics goals. In fact, $b\bar{b}$ pairs are expected to be produced with a rate of around 100 kHz, with only 15 % of these including at least one $b$ hadron with all its decay products in the detector acceptance. To reduce the data rate from 10 MHz down to a value that can be stored for offline analysis, an efficient selection process had to be implemented. The trigger has to fulfil the requirements in terms of output rate, while selecting as many interesting $b$ decays as possible. To pursue these goals, two levels of trigger were developed at LHCb [93]. The overall layout of the trigger system is shown in Fig. 2.15. These two levels, called the Level-0 Trigger (L0) and the High-Level Trigger (HLT), are discussed in more details in the following sections.

---

[6] An interaction is defined as being visible if two tracks traversing the entire detector can be reconstructed.
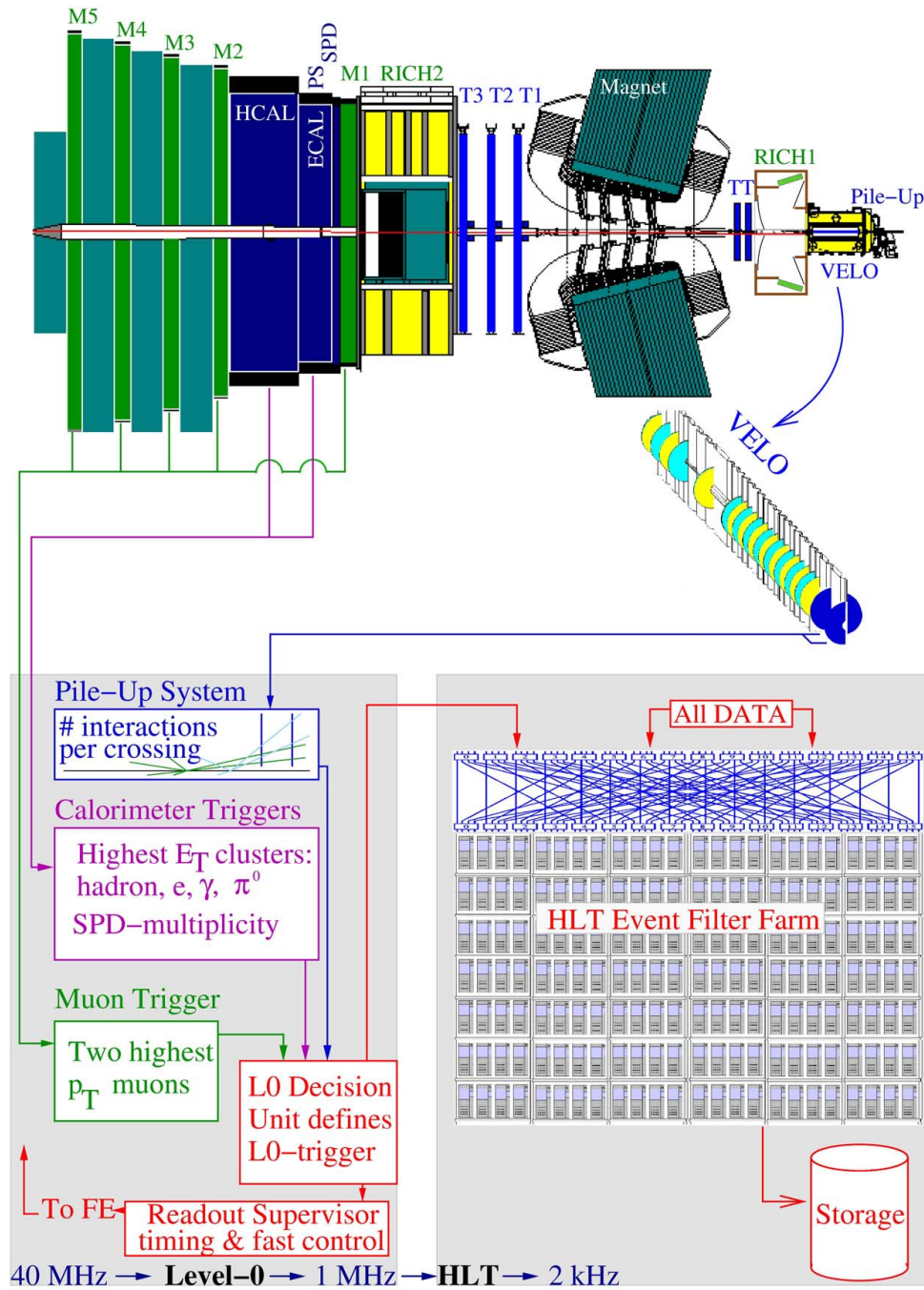
Figure 2.15: Overview of the trigger system showing both the Level-0 Trigger and the High-Level Trigger.

### 2.2.4.a  The Level-0 Trigger

The Level-0 Trigger has been designed to reduce the data rate from the LHC crossing rate of 40 MHz down to 1 MHz. It is a hardware-based trigger operating with a latency time of 4.2 $\mu$s and a clock rate of 40 MHz, synchronised with the LHC clock. A central decision unit (L0DU) combines the information from three sub-systems and yields a decision whether to keep the event or not. The three components are shown in Fig. 2.15.

The first component, the calorimeter trigger, uses the fact that the heavy $b$ hadrons decay to low-mass particles with large transverse momentum and energy. It attempts to reconstruct the hadron, electron and photon clusters with the largest $E_T$. It then sends a candidate to the decision unit if it reconstructs an electron, a photon or a $\pi^0$ with $E_T > 2.5$ GeV, or a hadron with $E_T > 3.5$ GeV. The decision taken by the L0DU is vetoed if the total energy in the calorimeters is below 5.0 GeV or if there are more than 280 clusters in the SPD.

The second component is the muon trigger. The transverse momentum resolution of the standalone muon reconstruction is around 20 %. The two muons with the largest $p_T$ are selected by the trigger. A candidate is sent to the L0DU if one of these muons has $p_T > 1.2$ GeV or if the sum of the $p_T$ of the two muons is above 1.5 GeV. In this case, any veto coming from another Level-0 sub-system is overruled and the event is accepted.

Finally, the pileup system, which uses four silicon planes identical to the VELO $r$ sensors, detects events with more than one interaction. Since the L0 Trigger is run online, tracks cannot be reconstructed at 40 MHz. However, by measuring the radial position of the hits in the silicon sensors, it gives an estimate of the $z$ position of the origin of these tracks. An event is vetoed if the pileup system detects more than 112 particles or if more than one peak is found in the histogram of the origin $z$ position.

### 2.2.4.b  The High-Level Trigger

The full detector is readout at a rate of 1 MHz. However, an additional trigger is needed to select 2 kHz of interesting events to write to physical storage for further analyses. At this stage, the trigger has access to the full detector data. The HLT is fully implemented in software, leading to high flexibility and the possibility to adapt when the first real data are collected. The HLT can also evolve with the physics priorities of the experiment. It is run on an Event Filter Farm consisting of 2000 CPUs. With such computing power, the HLT has an average total processing time available of 4 ms per event.

This High-Level Trigger is divided into two sub-levels: the HLT1 is an inclusive single track trigger, while the HLT2 runs more specific inclusive and exclusive selections. The HLT1 Trigger is used to refine the output of the Level-0 Trigger. Events are dispatched into independent alleys. The output rate of the HLT1 is about 30 kHz. This level of trigger uses each Level-0 Trigger types as input alleys. These Level-0 objects are then confirmed, in order to reduce the rate, by running a sequence of the following algorithms in each alley:

**L0→T:** T track-segments (called T seeds) are reconstructed in the T Stations using only hits in a window around the trajectory of the L0 object. The trajectory in the detector is assumed to originate from the interaction point. In the case of the calorimeter alley, two trajectories are assumed, corresponding to the two charge
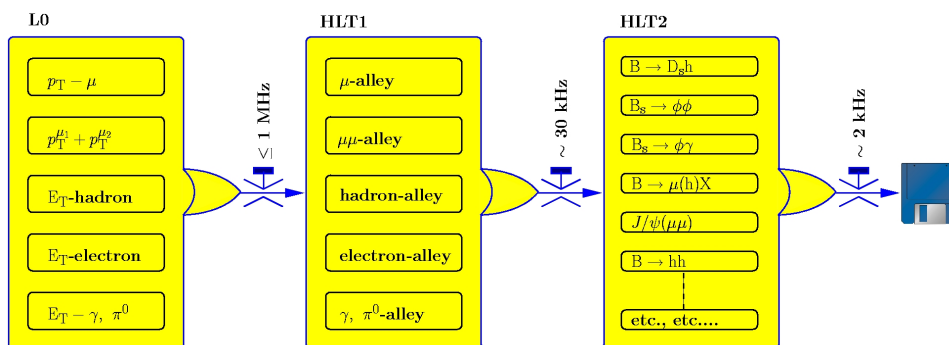
Figure 2.16: Schematic view of the LHCb trigger flow.

hypotheses. The Level-0 decision is confirmed if the seed matches the Level-0 object both in space and momentum.

**L0→VELO:** VELO track-segments (called VELO seeds, defined in Section 3.1.2) are reconstructed using the $r$ sensor information first. All 2D tracks are then used to reconstruct the primary vertices of the event. If this 2D track matches the L0 object with a sufficiently low $\chi^2$, the $\phi$ sensor information is added to reconstruct a VELO seed. This 3D seed is also required to match the Level-0 object with a small $\chi^2$.

**VELO→T:** A T seed (defined in Section 3.1.2) is reconstructed in the T Station around the trajectory defined by the VELO seed. This is done in a similar way than the L0→T algorithm described above, but starting from a VELO seed rather than an L0 object.

**T→VELO:** A VELO seed is found starting from a T seed rather than from an L0 object.

The HLT2 uses selection cuts looser than in the offline selection. The first reason for this is that the trigger does not have the final alignment and calibration constants. It also allows for further sensitivity studies to these cuts. First, a set of tracks are selected by their momentum and impact parameter to form intermediate composite-particles ($K^*$, $\phi$, $D^0$, $D_s$ and $J/\psi$), which will then be used in the inclusive/exclusive HLT2 Trigger decision. The inclusive trigger selects partially reconstructed $b$ decays to $\phi\,X$, $D^*\,X$, $\mu^\pm\,X$, $\mu^\pm\,h\,X$ and $\mu^+\mu^-\,X$. The exclusive selection produces a lower rate, due to the full event reconstruction which rejects part of the background. It can hence use less stringent cuts than the inclusive trigger. The output of these two sub-triggers are then passed to a logical OR to produce the final trigger decision. A schematic view of the different trigger sequences is shown in Fig. 2.16.

## 2.2.5 The LHCb Software

The LHCb software is based on the Object-Oriented GAUDI architecture [100, 101] written in C++. It provides a flexible framework shared by the main parts of the software chain, which can evolve during the development of the experiment. This software is separated in four applications, which correspond to the four steps of the physics studies performed

at LHCb, from the generation of the events to the physics analysis of simulated and real data. These steps are described below in terms of LHCb software.

**GAUSS:** The Monte Carlo generation step of the software chain can be separated in two different parts, both steered by the GAUSS package [102]. The *pp* collisions are generated with the PYTHIA program [103], which produces a set of particles with their corresponding momentum four-vectors. These particles are then decayed. The *b* hadrons are decayed by EVTGEN [104, 105], which was originally developed for the BaBar collaboration and has been adapted to the LHCb needs. The second step is the simulation of the detector response to the particles traversing its material. This task, which include the effect of the magnetic field on the path of charged particles, the energy loss through radiation, and the interactions with the detector material, is performed by GEANT4 [106].

**BOOLE:** The digitisation step of the simulation is done by the BOOLE package [107]. It applies the detector response to the hits deposited by the particles in the detector (from the GEANT4 step), taking into account the efficiency of the various sub-detectors, and simulates an electric signal corresponding to these hits. The L0-Trigger response is also simulated. Effects such as spill-over from the previous and next *pp* interactions are also added to the event. At this point, the events mimic the real data such that the rest of the software chain can be common for both types of data.

**BRUNEL:** The reconstruction phase is done by BRUNEL [108]. It associates hits to form tracks, does the track fitting described in Section 3.1.3, assigns a momentum value to this track based on the information from the tracking devices, defines the particle identity (PID) using the data from the RICH, calorimeters and Muon System, reconstructs the primary vertices, etc. The output of this phase is a DST ready for the physics analyses.

**DAVINCI:** Once the events have been reconstructed, the last phase is to select the events of interest by identifying specific decays. This is done within DAVINCI [109]. Particles are selected by their PID, their momentum, their impact parameter with respect to the primary-interaction vertex, etc. A vertex is fitted with tracks corresponding to groups of two or more particles and this leads to more selection criteria, e.g. the quality of the vertex fit (or fit $\chi^2$), the distance of flight of a particle defined as the distance between its production and its decay vertices, etc.

Other packages have been developed inside the GAUDI framework such as PANORAMIX [110] for the event visualisation, or ESCHER [111] for alignment purposes.

# Chapter 3

# Tracking and Alignment at LHCb
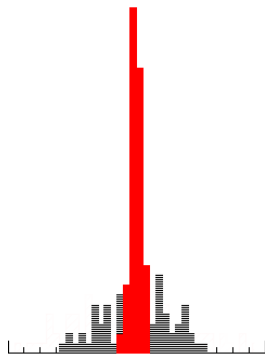
The LHCb tracking methods and alignment strategy are presented in this chapter. First, the track types going through the detector are described, followed by a discussion of the tracking methods used at LHCb. Next, the global alignment strategy is described, followed by each sub-detector internal alignment strategy. Finally, the LHCb alignment framework used in particular for the alignment of the Tracking Stations is detailed.

## 3.1   Track Reconstruction at LHCb

The proton–proton collisions that will occur in LHCb yield a high track density. The average track multiplicity in the VELO is around 100 in a typical $b\bar{b}$ event. In this environment, finding the trajectory of the particles through the various sub-detectors is a challenging task. Track reconstruction is divided into the pattern recognition (assignment of clusters to the tracks) and fitting (determining the optimal track parameters). The aim is not only to reconstruct the tracks from the decays of interest, but also all tracks coming from the primary vertex, in order to define it precisely. This is crucial for the determination of the $b$-hadron lifetime (or flight distance). A precise track reconstruction is also important for the flavour tagging of the decaying $B$ mesons, as described in Section 2.2.3.

### 3.1.1   Track Types

Depending on their origin vertex and their momentum, the charged tracks have different trajectories through the detector, leading to the following classification, pictured in Fig. 3.1:

**VELO tracks:** Tracks with large polar angles or which go backwards with respect to the
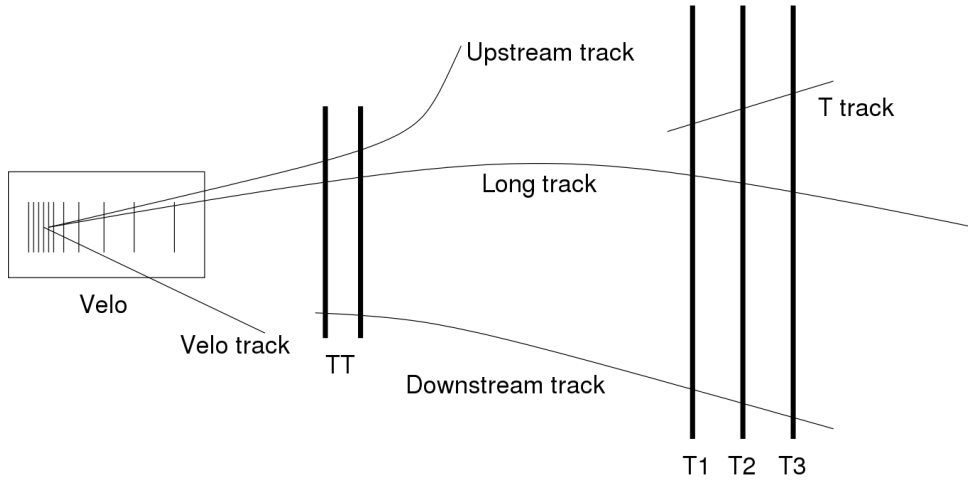
Figure 3.1: Schematic view of the different track types defined in LHCb. The view shows the $x$-$z$ (bending) plane. The dipole magnet is situated between the TT and the three T Stations, as visible in Fig. 2.4. The schema is not to scale.

detector. These tracks will only traverse the VELO and are useful for the precise fitting of the primary vertex.

**Upstream tracks:** Low momentum tracks bent out of the LHCb geometrical acceptance before they can reach the T Stations. These tracks only leave clusters in the VELO and TT and their momentum resolution is of the order 10–20 %. These tracks are used for the RICH pattern recognition and for the reconstruction of slow pions from $D^*$ mesons.

**Downstream tracks:** Tracks originating outside of the VELO and traversing the TT and T Stations. Such tracks can be decay products of long-lived particles ($K_S^0$, $\Lambda$). These tracks are important for the reconstruction of $b$-hadron decays, such as $B^0 \rightarrow J/\psi \, K_S^0$ and $B^0 \rightarrow \phi K_S^0$.

**T tracks:** Secondary interactions in the material of the upstream detectors lead to particles that only traverse the T Stations. They are mainly used for the RICH2 pattern recognition and for the T-Station internal alignment.

**Long tracks:** Tracks traversing the entire spectrometer. They are the most useful tracks for the physics studies, which benefit from the precise determination of the track parameters. The performances of the "long tracking" is discussed in Section 3.1.4.

## 3.1.2   Pattern Recognition

The track reconstruction starts with the pattern recognition, which consists of the building of track segments in the VELO and the T Stations and then matching these, or using seeds in one detector to extend tracks to another. Several algorithms are run in a sequence to find the various track types defined above.

**VELO seeds:** VELO clusters are collected along straight lines [112, 113]. This follows from the low magnetic field in this region, meaning that no momentum information can be assigned to the track segment at this stage. These VELO seeds are used as input to further tracking algorithms.

**T seeds:** Segments of tracks are reconstructed in the T Stations using both IT and OT clusters [114, 115, 116]. The algorithm starts by taking one $x$ hit in each of the three T Stations. A parabola is made out of them and other $x$ hits are collected in a window around it. Next, compatible stereo hits are added to the track candidate. Quality cuts are then used to clean the track sample.

**Forward tracking:** Starting from the parameters of a VELO seed and an individual hit in the T Stations, tracks are searched for by looking for hits in the other layers of the T Stations in a window around the predicted track [117]. If the track candidate passes some quality criteria, it becomes a long track. TT hits are then added to the track by collecting hits in windows around the predicted positions. About 90 % of the long tracks are reconstructed using this algorithm.

**Track matching:** This algorithm takes as input both VELO and T seeds and tries to match them by extrapolating both segments to the bending plane in the magnet and comparing their positions and slopes and the number of compatible TT hits [118, 119, 120]. Once a track is built from two seeds, TT hits are added if they are close enough to the track. This algorithm reconstructs an additional 5 % of long tracks. The missing 5 % of long tracks are not reconstructed due to inefficiencies of the tracking software.

**Up/Downstream tracking:** Tracks are made of VELO/T seeds respectively, if at least three TT hits can be matched to the seeds.

**VELO/T tracking:** Any VELO or T seed that has not been used in any of the previous algorithms is kept as a VELO or a T track respectively. The momentum resolution for these tracks is of $dp/p \sim 10 - 20 \%$.

**Clone killing:** Tracks may be reconstructed by more than one reconstruction algorithm. Clones are tracks that share a certain percentage of their hits. The tracks with the smaller number of hits are rejected by the clone-killing algorithm [121]. In case two or more tracks have the same number of hits, the highest quality one (based on its $\chi^2$) is retained.

### 3.1.3 Track Fitting

Once a track has been found by one of the tracking algorithms, it needs to be fitted in order to determine the most precise estimate of the track parameters. These parameters are then used to match the tracks with hits in the PID sub-systems, locate the origin and decay vertices and calculate invariant masses in physics analyses.

A track is described by a set of track states, which each consists of a track vector $\vec{x}$ and a $5 \times 5$ covariance matrix $C$. Given the geometry of the detector, the track states

are naturally parametrised as a function of $z$. The state vectors are calculated, at a given $z$-position, by the $x$ and $y$ positions, the track slopes and the particle momentum:

$$\vec{x} = \begin{pmatrix} x \\ y \\ t_x \\ t_y \\ q/p \end{pmatrix} , \tag{3.1}$$

where $t_x = \delta x/\delta z$, $t_y = \delta y/\delta z$, $q$ is the signed charge and $p$ is the momentum of the particle. This fifth parameter is obtained through the curvature of the track in the magnetic field.

For practical reasons, the track states are chosen in the track fit at the measurement planes. These can be used to obtain the optimal track coordinates at other measurement planes either by extrapolation or interpolation. In the case of extrapolation, the propagation relation is

$$\vec{x}_k^{k-1} = F_k \vec{x}_{k-1} + \vec{w}_k , \tag{3.2}$$

$F_k$ is called the transport matrix and $\vec{\omega}_k$ is the process noise describing for example the multiple scattering.

The quantities that are observed in the detector are the measurements. They are related by the projection equation to the track states:

$$m_k = h_k(\vec{x}_k) + \epsilon_k , \tag{3.3}$$

where $h_k$ is the projection function and $\epsilon_k$ the measurement noise. The projection function projects the track state vector into a one dimensional quantity.

### 3.1.3.a   The LHCb Kalman-Filter Track-Fit

The tracks are fitted using a Kalman filter, which is described in detail in Ref. [122]. The Kalman filter is a recursive least-squares method that gives optimal estimates of track parameters and allows multiple scattering and energy loss corrections to be properly taken into account. The principle of this technique is to add the measurements one after the other during the fitting procedure, updating the local track state at each step. This means that a state depends on all the previous states on the track. The method is based on a $\chi^2$ minimisation of the measurements on the tracks. This will be described in Section 3.1.3.b.

The Kalman filter proceeds in three steps:

**Prediction:** The track state $\vec{x}_{k-1}$ is used to predict the state $\vec{x}_k^{k-1}$ with the prediction equation (3.4).

**Filter:** The predicted track state is refined with the current measurement using the filter equation (3.9). The prediction and filter steps are repeated until each measurement have been added to the fit.

**Smoothing:** Once all the measurements have been added to the track, a smoothing procedure is run in the opposite direction in order to update all track states with the complete measurement information.

### Prediction

At the start of the fit, a first estimate of the track state $\vec{x}_0$ is needed. This is provided by a first fit in the track finding procedure. An initial estimate of the covariance matrix $C_0$ is also given with increased values for the errors on the diagonal, in order not to be biased by the estimate of $\vec{x}_0$. Starting from this, the prediction relation for the track state and the covariance matrix are

$$\vec{x}_k^{k-1} = F_k \vec{x}_{k-1} + \vec{w}_k \,, \tag{3.4}$$
$$C_k^{k-1} = F_k C_{k-1} F_k^T + Q_k \,. \tag{3.5}$$

The superscript indicates how many measurements have been incorporated in the determination of $\vec{x}_k$: $k-1$ means a predicted state, $k$ or no superscript means a filtered state and $n$ means a smoothed state. The matrix $Q_k$ in Equation 3.5 is the process-noise term coming from the multiple scattering, which has the effect of increasing the predicted error on the state vector $\vec{x}_k^{k-1}$.

From this predicted state, a prediction of the residual and its covariance can be made, by defining the residual as the distance between the measurement and the state vector projected in the measurement plane:

$$r_k^{k-1} = m_k - h_k(\vec{x}_k^{k-1}) \,, \tag{3.6}$$
$$R_k^{k-1} = V_k + H_k C_k^{k-1} H_k^T \,. \tag{3.7}$$

In Equation 3.7, $H_k$ is the measurement matrix and $V_k$ the measurement variance. The aim of the Kalman fit is to minimise the predicted contributions

$$(\chi_+^2)_k^{k-1} = r_k^{k-1}(R_k^{k-1})^{-1} r_k^{k-1} \tag{3.8}$$

of the current measurement to the total $\chi^2$ with respect to the track parameters. This minimisation is discussed in Section 3.1.3.b.

### Filter

The filter step adds the information of the current measurement $k$ to the predicted state based on the $k-1$ first measurements added to the track. The filtered state vector and its covariance matrix are obtained by the filter equation:

$$\vec{x}_k = \vec{x}_k^{k-1} + K_k r_k^{k-1} \,, \tag{3.9}$$
$$C_k = (\mathbb{1} - K_k H_k) C_k^{k-1} \,, \tag{3.10}$$

where $K_k$ is a $5 \times 1$ gain matrix given by

$$K_k = C_k^{k-1} H_k^T (V_k + H_k C_k^{k-1} H_k^T)^{-1} = C_k^{k-1} H_k^T (R_k^{k-1})^{-1} \,. \tag{3.11}$$

The complete derivation of this Kalman gain matrix is given in Ref. [122]. This also leads to the expression of the filtered residual and its covariance matrix:

$$r_k = m_k - h_k(\vec{x}_k) = (1 - H_k K_k) r_k^{k-1} \,, \tag{3.12}$$
$$R_k = (1 - H_k K_k) V_k = V_k - H_k C_k H_k^T \,. \tag{3.13}$$

The contribution of this measurement to the total $\chi^2$ becomes

$$(\chi^2_+)_k = r_k R_k^{-1} r_k \,. \tag{3.14}$$

**Smoothing**

After the best estimate of the state vector $\vec{x}_n$ is obtained at the last measurement by predicting and filtering each of the previous states, the procedure is reversed in order to propagate this full information back to all the previous states. The smoothed state vector and covariance matrix become

$$\vec{x}_k^n = \vec{x}_k + A_k(\vec{x}_{k+1}^n - \vec{x}_{k+1}^k)\,, \tag{3.15}$$
$$C_k^n = C_k + A_k(C_{k+1}^n - C_{k+1}^k)A_k^T\,, \tag{3.16}$$

where

$$A_k = C_k F_{k+1}^T (C_{k+1}^k)^{-1} \tag{3.17}$$

is the $5 \times 5$ smoother gain matrix. The smoothed residual and corresponding covariance matrix finally become

$$r_k^n = m_k - h_k(\vec{x}_k^n)\,, \tag{3.18}$$
$$R_k^n = V_k - H_k C_k^n H_k^T\,, \tag{3.19}$$

and the total $\chi^2$ to minimise in the fitting procedure is the sum of all the smoothed contributions:

$$(\chi^2_+)_k^n = r_k^n (R_k^n)^{-1} r_k^n\,. \tag{3.20}$$

### 3.1.3.b $\chi^2$ Minimisation

The fitting procedure consists of finding the best track parameters by minimising the sum of the $\chi^2_+$ given in Equation 3.20 and which add up to a total $\chi^2$ of the form

$$\chi^2 = r^T V^{-1} r\,. \tag{3.21}$$

The minimisation is expressed by

$$\frac{d\chi^2}{dx} \equiv 0\,. \tag{3.22}$$

Equation 3.22 can be rewritten by using an initial estimate $x_0$ of the track parameters and a linear expansion of the measurement model around it:

$$h(x) = h(x_0) + H(x - x_0)\,, \text{ where } H = \left.\frac{\partial h(x)}{\partial x}\right|_{x_0}$$

is the projection matrix. Equation 3.22 then becomes

$$
\begin{aligned}
0 \equiv \frac{d\chi^2}{dx}\bigg|_{x_0} \\
\sim & -\sum_{i=0}^{n}\sum_{j=0}^{n} \frac{dh(x)_i}{dx_k}\bigg|_{x_0} V_{ij}^{-1} r_j - \sum_{i=0}^{n}\sum_{j=0}^{n} r_i V_{ij}^{-1} \frac{dh(x)_j}{dx_k}\bigg|_{x_0} \\
\sim & -\sum_{i=0}^{n}\sum_{j=0}^{n} H_{ik} V_{ij}^{-1} r_j - \sum_{i=0}^{n}\sum_{j=0}^{n} r_i V_{ij}^{-1} H_{jk} \\
\sim & -\sum_{i=0}^{n}\sum_{j=0}^{n} H_{ki}^T V_{ij}^{-1} r_j - \sum_{i=0}^{n}\sum_{j=0}^{n} H_{kj}^T (V^{-1})_{ji}^T r_i \\
= & -2 H^T V^{-1} [m - h(x_0) - H(x - x_0)].
\end{aligned}
\tag{3.23}
$$

The solution of Equation 3.23 is

$$
x = x_0 - C H^T V [m - h(x_0)]
\tag{3.24}
$$

where the covariance matrix of the track parameters is given by

$$
C = 2 \left( \frac{d^2\chi^2}{dx^2}\bigg|_{x_0} \right)^{-1} = 2 \left( 2 H^T V^{-1} \frac{dh(x)}{dx}\bigg|_{x_0} \right)^{-1} = (H^T V^{-1} H)^{-1}.
\tag{3.25}
$$

If $H$ depends on $x$ (non-linearity), iterations are needed in order to reach some pre-defined convergence criterion. This criterion is usually a minimal change in the track $\chi^2$. This numerical method of successive approximations of real zeros of a real function is called the Newton-Raphson method. In this case, Result 3.24 becomes

$$
x = x_0 - \left( \frac{d^2\chi^2}{dx^2}\bigg|_{x_0} \right)^{-1} \frac{d\chi^2}{dx}\bigg|_{x_0}.
\tag{3.26}
$$

### 3.1.4 Long Tracking Performance

The performance of the track reconstruction at LHCb can be quantified by looking at

- the efficiency of the track finding procedure;

- the ghost rate;

- the resolution of the track parameters;

- the pull (quality of the error estimate) of the track parameters.

Performance studies are concentrated on the long tracks (defined in Section 3.1.1) [94]. Using the Monte Carlo truth, a track is defined as being reconstructible if

- the particle leaves at least 3 hits in the $r$ sensors and 3 hits in the $\phi$ sensors in the VELO (reconstructible as a VELO track);
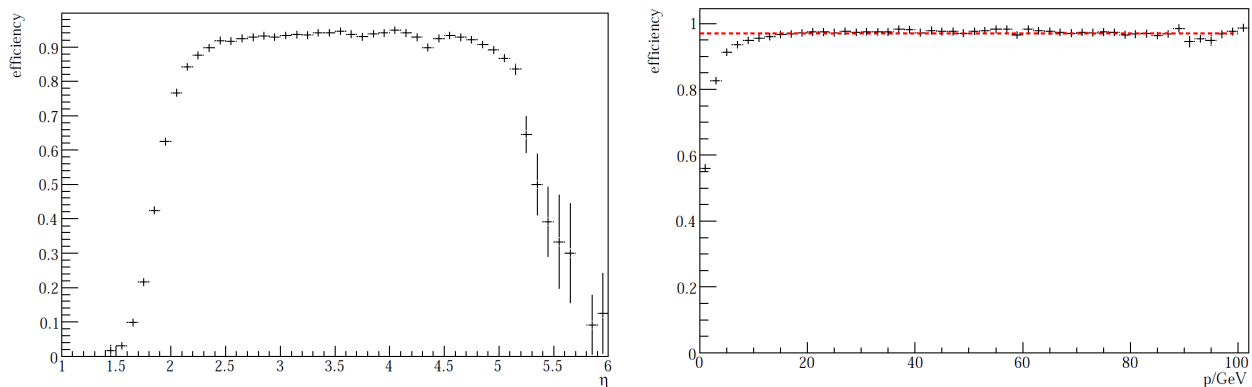
Figure 3.2: Efficiency of the long track finding procedure as a function of (a) the pseudo-rapidity and (b) the momentum. The dashed red line in plot (b) indicates 97 % efficiency. Both figures are taken from [94].

- the particle leaves at least 1 hit in the $x$ layers and 1 hit in the stereo layers of each of the T Stations (reconstructible as a T track).

A reconstructible long track is successfully reconstructed if both segments in the VELO and the T Stations are associated to the same MC particle with a hit purity (fraction of clusters that originate from this MC particle) of at least 70 % on average for the VELO and T segments. The track finding efficiency is then defined as the fraction of reconstructible tracks that are successfully reconstructed. The ghost rate is the fraction of reconstructed tracks which fail the above association criteria.

The track finding efficiency depends on the track parameters. It is shown in Fig. 3.2 as a function (a) of the pseudorapidity $\eta$, and (b) of the momentum $p$. The event-weighted efficiency (defined in Section 2.2.2) is 91.4 %, with a plateau at 97 % for tracks with a momentum above $10 \, \text{GeV}/c$. The dip below $10 \, \text{GeV}/c$ is due both to the effect of the multiple scattering and the bending of the trajectories in the magnetic field, which are larger for low-momentum tracks. The corresponding event-weighted ghost rate is 14.6 %.

The pulls of the track parameters are used to quantify the performance of the track fit to correctly determine the track parameters and their errors. The pull of a quantity corresponds to the difference between the reconstructed value and the value from the Monte Carlo truth, divided by the error estimate from the track fit. If the errors are correctly estimated, this distribution should be Gaussian, centred on zero and with a unit variance. The plots in Fig. 3.3 show no bias, but the variances are higher than one, in particular for the momentum. This indicates that the uncertainties on the track parameters are under-estimated. Several reasons account for this effect, including non-Gaussian tails in the resolution function of the silicon detectors, mis-resolved L/R signs in the OT [1] and differences in the multiple scattering and energy loss models between the reconstruction and the simulation software [123].

---

[1] The measurement of the distance of closest approach of the charged track with respect to the central wire in the OT straw tubes induce an ambiguity as whether the track passed left or right of the wire. The techniques used to solve this problem are not 100 % efficient, hence the mis-resolved left/right signs.
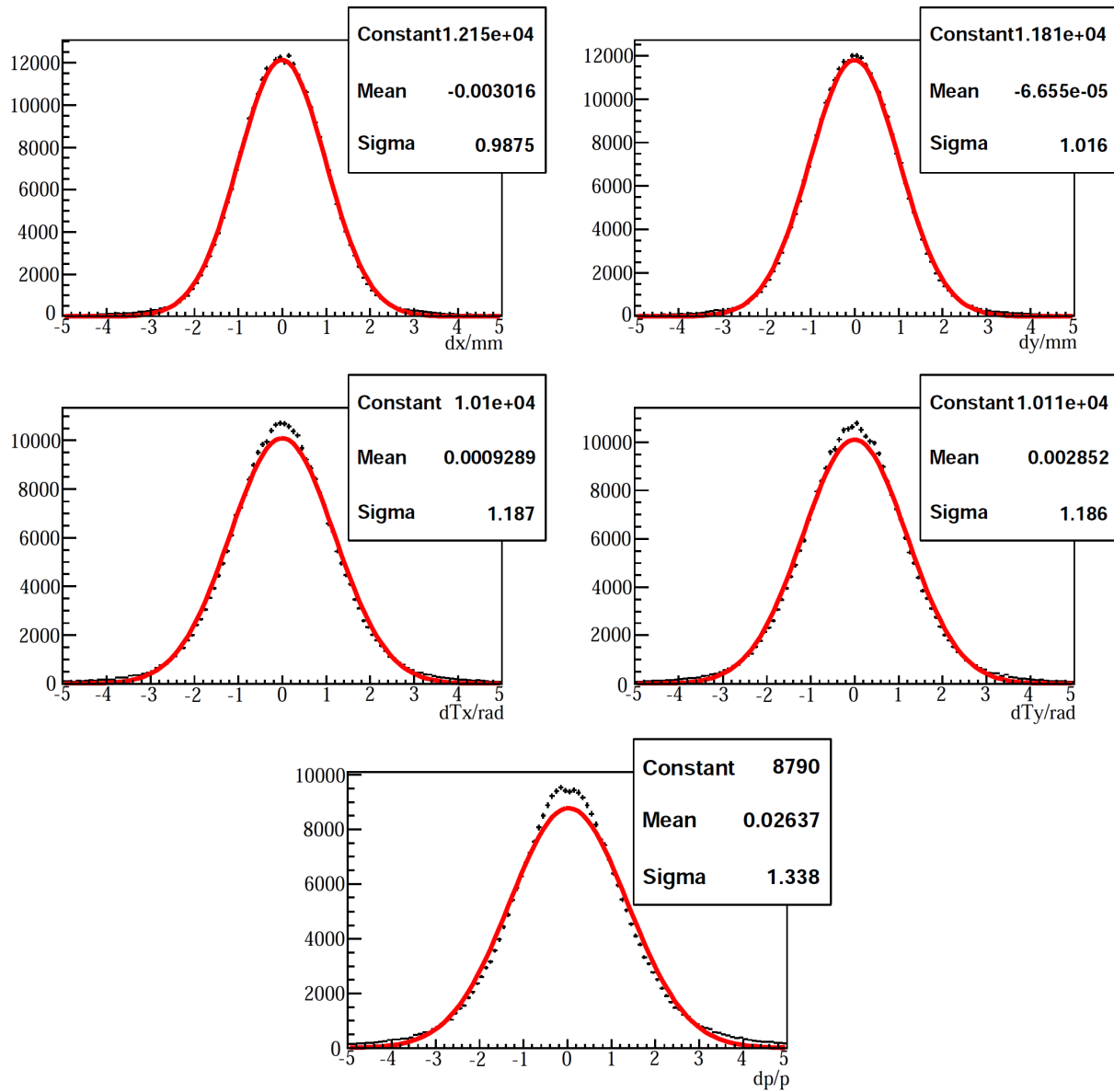
Figure 3.3: Pulls of the track parameters (positions $x$ and $y$, slopes $Tx$ and $Ty$ and curvature $q/$p) at the first measurement on long tracks.

### 3.1.5 Standard LHCb Particle Selection

Once the tracks are reconstructed using the information from the tracking system and assigned an energy, momentum and PID information from the dedicated sub-detectors, a first pre-selection is made in order to classify the tracks by type: muons, kaons, pions, electrons or protons. Three pre-selections are presented here, the so-called "standard loose" muon, kaon and pion selections.

**Standard Loose Muons**

The standard loose muons are selected amongst the long tracks, defined in Section 3.1.1. The selection is based on the number of hits on track that are found in the Muon Stations, depending on the momentum of the particle. Due to the amount of material in front of the Muon Stations M2 to M5, all tracks reaching the muon detector have a momentum above $3\,\text{GeV}/c$.

In the momentum range between 3 and $6\,\text{GeV}/c$, the tracks are required to have hits in Stations M2 and M3. For momenta between 6 and $10\,\text{GeV}/c$, the requirement is that tracks must have hits in Stations M2 and M3, and in M4 or M5. Tracks with a momentum above $10\,\text{GeV}/c$ must have hits in each of the Stations M2 to M5 to be classified as standard loose muons.

There are however no other PID requirement for these particles as the above requirements are already strong enough to ensure that the corresponding tracks are muons with a high enough confidence level.

**Standard Loose Kaons**

The standard loose kaons are selected amongst the long tracks, defined in Section 3.1.1. A requirement is set on the log likelihood difference (see Section 2.2.3.d) given by the RICH counters:

$$\Delta \ln \mathcal{L}_{K\pi}^{\text{RICH}} > -5 \,.$$

**Standard Loose Pions**

Any long track can be selected as a standard loose pion. There are no specific requirement for these particles.

## 3.2 Motivations for the Alignment Studies

The LHCb detector has been designed to achieve the physics goals discussed in Chapter 1. However, these measurements are only possible if the detector is built with a high precision, or if the actual position and performance of the detector can be known precisely. For example, if the VELO is not aligned correctly, the primary vertices are not reconstructed precisely and the time of flight of long-lived mesons cannot be measured correctly. The Tracking-Station alignment, which is described in Chapters 4 and 5 is also important. The T Stations provide a momentum estimate for the tracks that cross the detector. For low-multiplicity decays, this momentum estimate dominates the mass resolution. A
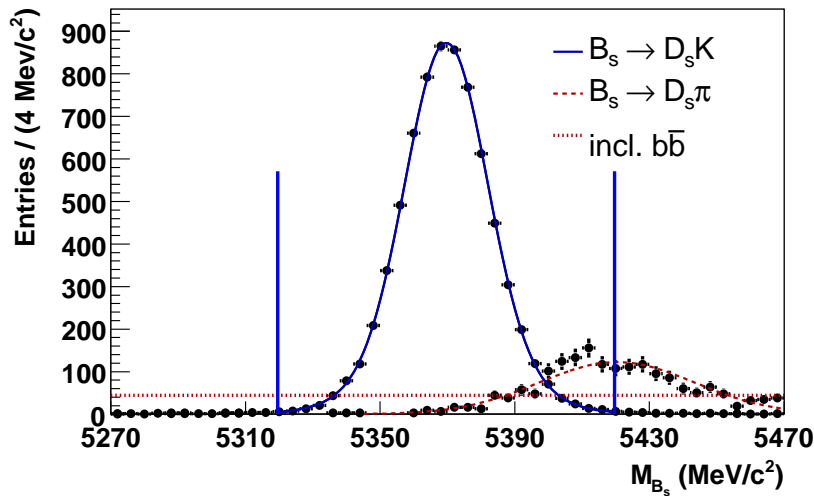
Figure 3.4: Reconstructed $B_s^0$ mass for the $B_s^0 \to D_s^{\mp} K^{\pm}$ decay, showing the reconstructed $B_s^0 \to D_s^- \pi^+$ background. Figure taken from Ref. [99].

good mass resolution is important in many cases. First, the mass is used in the proper time calculation. Next, a good mass resolution allows for the separation of various mass peaks that correspond to different decays. For example, the $B_s^0 \to D_s^- \pi^+$ background in the $B_s^0 \to D_s^{\mp} K^{\pm}$ selection produces a peak in the $D_s^{\mp} K^{\pm}$ invariant mass which is $50 \,\mathrm{MeV}/c^2$ above the signal peak to be compared with a mass resolution of $14 \,\mathrm{MeV}/c^2$ with a perfectly aligned detector [99]. Figure 3.4 shows the $B_s^0 \to D_s^{\mp} K^{\pm}$ mass peak with the $B_s^0 \to D_s^- \pi^+$ background peak. A precise mass measurement is also useful in the selection process of various decays. A better mass resolution allows to have smaller selection windows and hence have less background. A good Tracking-Station alignment also increases the tracking efficiency, which is crucial for the reconstruction of multi-body final states.

A specific example of the impact of misalignment on the detector performance is discussed in Ref. [124]. The authors have studied the effect of VELO and T-Station misalignments on the performance of the pattern recognition, and of the $B^0 \to \pi^+\pi^-$ reconstruction and event selection. The misalignments were applied to each VELO module and sensor, each IT box and OT layer following a Gaussian distribution with a sigma corresponding to one, three and five thirds of the detector single-hit resolution. The results are reported here only for the T Stations with the 5/3 misalignment scale. The pattern recognition efficiency is decreased by a relative loss of $0.6\,\%$ for the forward tracking, whereas the matching efficiency suffers from a $5\,\%$ relative loss. The number of selected events is reduced by $4.2\,\%$. The reduction is not large because none of the selection cuts used in the study are much affected by the T-Station misalignments. On the other hand, misalignments of the same scale applied to the VELO reduce the number of selected events by $73.9\,\%$. The effect on the primary and $B$ decay-vertex resolutions is small because these resolutions are dominated by VELO effects. On the other hand, the momentum resolution of the two pions is worsened by $17\,\%$ and the $B^0$ invariant-mass resolution is affected at the

level of 15 %. Finally, the proper-time resolution is not affected much as it is dominated by the decay length measurement done in the VELO.

The misalignments applied at the T-Station level in the studies discussed in Ref. [124] are small, with values of up to $75\,\mu$m at the IT box level. In the alignment studies with Monte-Carlo-simulated data, reported in Chapter 4, the misalignments applied at the IT box level, considered as realistic day-1 misalignments, are several times larger. These studies show the importance of having a powerful alignment software that can deal with large misalignments and correct for them with a precision of a fraction of the single-hit resolution. The LHCb alignment software is discussed in the next sections, whereas alignment studies with Monte-Carlo-simulated data are discussed in Chapter 4 and the alignment studies with the first real data recorded at LHCb are reported in Chapter 5.

## 3.3 Alignment Strategy

To fulfil LHCb's physics goals relies on the good space and momentum resolution and precise particle identification. These performances are influenced by the overall alignment of the LHCb detector. Poor spatial alignment will lead to a degradation of the mass measurement or to systematic biases, which would degrade sensitive asymmetry measurements. For this reason, each sub-detector must be aligned to a precision negligible with respect to its intrinsic resolution and their relative alignment must be precise enough in order to have no impact on physics parameters.

Since the VELO is the most precise device in the experiment, it will be used to define a global coordinate system for LHCb. However, the first VELO silicon-strip being so close to the $pp$ collisions ($\sim 8\,$mm), the two VELO halves will need to be retracted by $\sim 3\,$cm during the phase where LHC will establish stable beams, i.e. at the beginning of each fill. Since the Tracking Stations will be aligned with respect to the VELO, and the other sub-systems to the tracking system, the $10\,\mu$m precision of the motion controller is expected to be the largest uncertainty on the absolute position precision of the detector.

Misalignments can occur either due to wrong positioning of detector elements in the experimental area or due to inaccuracies during the construction phase. Although care was taken to mount each part precisely, shifts or rotations of up to a few millimetres or milliradians (for the larger elements) were observed with respect to the design position. A position survey was performed on each system to provide first corrections. However, the obtained precision is still outside the requirements coming from the physics measurements. For example, the Inner-Tracker position has been measured with a precision of $50\,\mu$m at the layer and ladder level, which is equivalent to the single-hit resolution of the detector. At the box level, this precision is $\sim 1\,$mm. Another method is needed in order to ensure a better internal alignment and to provide with alignment corrections to the relative position of different sub-detectors.

The fact that the polarity of the magnetic field will be inverted periodically during the running of the experiment will also influence the alignment of the spectrometer. Especially, the sub-systems close to the magnet may shift slightly when the magnetic field is turned on or the polarity of the magnets is swapped.

For these reasons, the following global LHCb alignment strategy has been defined [125]:

1. Internal VELO alignment.
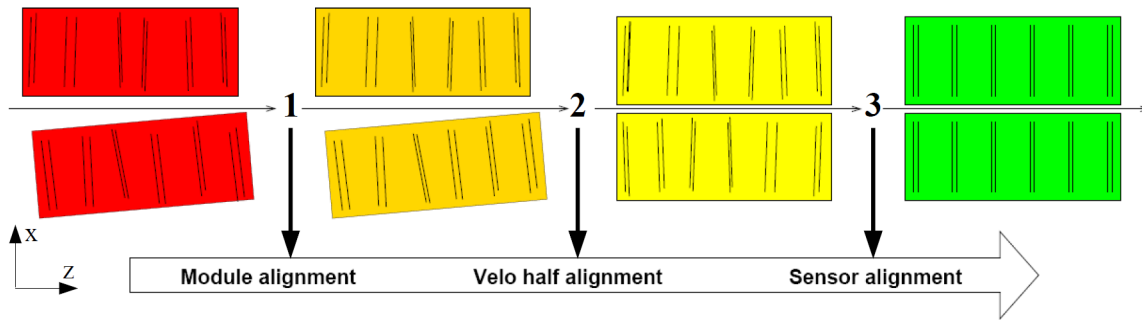
Figure 3.5: Schema of the VELO alignment strategy.

2. Standalone IT-OT alignment.

3. Relative alignment of the Tracking Stations to the VELO.

4. Alignment of the TT using VELO-to-T tracks.

5. Alignment of the RICH, calorimeters and muon system with respect to the Tracking Stations.

These steps are briefly described in the following sections.

### 3.3.1 VELO Alignment

As described in the introduction to this section, the alignment of the VELO is critical for LHCb as the global coordinate system relies on the precise knowledge of the position of the VELO. This alignment is divided into three main parts. First, the modules inside each of the VELO-halves are aligned in their own boxes [126]. Next, the two VELO halves are aligned to each other [127]. Finally, the sensors inside each module are aligned [128]. These three steps are schematised in Fig. 3.5.

The method used is a C++ implementation of the Millepede algorithm [129]. The trajectories of particles are expressed as a linear combination of the track and the alignment parameters. After a $\chi^2$ minimisation, which contains both the local (track) and global (alignment) parameters, a single matrix inversion leads to the alignment and track parameters. This matrix is usually very large, but can be reduced to a block diagonal form where one of the blocks has a dimension equal to the number of degrees of freedom that are taken into account in the alignment process. This number is 42 modules $\times$ 6 degrees of freedom = 252 for the alignment of all the modules inside the VELO halves.

Alignment of the modules inside the two VELO halves has been tested with Monte Carlo simulated data. A precision of $1.3\,\mu$m is obtained for the translations along the $x$ and $y$ axes. The accuracy on the rotation around the $z$ axis is $0.1\,$mrad [127].

The alignment of the two VELO halves with respect to one another is performed either by selecting tracks that go through the overlap region between the sensors on each side of the beam or by reconstructing the primary vertices. The former method requires some care as the overlap region suffers from the noise coming from the secondary interactions occurring in the larger amount of material at this position. A precision of $12\,\mu$m along

the two relevant translational degrees of freedom was obtained. The tilts around the $x$ and $y$ axes are known to $36\,\mu$rad, which is still within the system requirements [127].

The method using the primary vertices is less constraining than the overlap one. However, it is the only one usable when the VELO is open, which will happen at the beginning of each LHC fill. Precisions of $28\,\mu$m for the translations and $108\,\mu$rad for the rotations are obtained for the two VELO halves with respect to one another.

The alignment of the two boxes to fix a global LHCb coordinate system is performed by combining the two methods discussed above. Relative movements of the two VELO halves are allowed while constraining them to define the same primary vertex location. Accuracies of $18\,\mu$m for the $x$ and $y$ translations and $103\,\mu$rad for $x$ and $y$ tilts are found for the two VELO halves with respect to the beam.

Finally, the relative sensor alignment has been shown to be precise to $1.3\,\mu$m for translations along the $x$ and $y$ axes [128]. Combining these results with the precision of the module alignment, it follows that the absolute position of one sensor inside either VELO half will be determined to better than $2\,\mu$m.

Although the Millepede program has been used for the VELO alignment studies, another method has been developed which uses a local track model instead of the global track model used in Millepede. This new method is based on the tracks from the standard LHCb track-fitting procedure using a Kalman filter. It is described in Section 3.4 and gives similar results to the Millepede program [130].

### 3.3.2 Tracking-Station Alignment

The tracker consists of the Inner and Outer Trackers. Since the T Stations have a total of 12 active layers, a standalone alignment is possible. The IT and OT can be internally aligned separately using tracks going through either tracker only. Alternatively the two systems can be aligned together, using both tracks with larger angles with respect to the beam, and hence going through the two systems, and tracks going through the small overlap region between the silicon sensors and the straw tubes.

As for the VELO, several steps are needed to align the Tracking Stations. In order to recover from large residual misalignments, the alignment is performed at the IT box level and the OT C-frame or layer level. For a more precise alignment, a finer granularity is used, down to the IT-ladder and OT-module level. In addition, some elements are not sensitive to all the translation and rotation degrees of freedom. For example, the IT and OT $X$ layers, having vertical strips and straws, can be moved along the $y$ axis without changing the track parameters. For the same reason, they are not sensitive to rotations around the $x$ axis. However, an $X$ layer together with the corresponding stereo layer can recover part of these movements. Some strategies will be detailed in the result Sections 4.2 and 4.3.

Both the OT and the IT were surveyed during the construction of the detector. An extensive survey of the OT layers and modules was performed. Modules in the OT were adjusted in the cavern so as to be in the nominal position. An internal survey of the Inner Tracker was performed in the clean room and in the experiment cavern [131]. The position of the ladders and the overall position of the $X$ layers was determined with an accuracy of $50\,\mu$m. A survey of the stereo layers was not possible as they were visually obscured by the $X$ layers. Since each stereo layer is mounted on the same cooling rod as

an $X$ layer, it was assumed that the corrections for the position of the $X$ layers are valid for the corresponding stereo layer.

After installation of the detector in the experimental area, the position of the boxes was surveyed with a precision of $500\,\mu$m. This was carried out whilst the detector was in the open position and does not include possible systematic shifts during the closing. Taking these into account, an overall precision of $1-2\,$mm is quoted on the box positions [131].

In [132], a first alignment of the Inner Tracker boxes and layers in the most sensitive coordinate ($x$) is discussed. Using a technique based on histograms of residuals, these studies establish the validity of the survey and provide first alignment constants.

Chapter 4 discusses the alignment of the T Stations with a software method described in Section 3.4, using Monte Carlo simulated data. Then, the alignment of the Inner Tracker using the first data from the LHC recorded at LHCb during synchronisation tests is described in Chapter 5. T-Station alignment using Millepede is also under investigation, but will not be discussed here.

### 3.3.3 VELO to T-Stations Alignment

Once the T Stations are internally aligned, they will be aligned to the VELO, which is the reference for the global coordinate system. This will be done using the long tracks presented in Section 3.1. Results of this method are discussed in Section 4.3. Although this method is possible both with the magnetic field on and off, only the latter has been studied in this work.

The Tracker Turicensis consisting of only four active layers, a standalone alignment is not possible in this case. The long or downstream tracks will be used to align the TT with respect to both the VELO and the T Stations. For this detector, upstream tracks reconstructed in the VELO and the TT can also be used for alignment purposes.

### 3.3.4 RICH, Calorimeters and Muon System Alignment

The three systems that perform the particle identification in LHCb, namely the RICH counters, the calorimeters and the muon system, have less stringent alignment requirements (in terms of absolute precision) than the tracking system. However, misalignments are not harmless for these sub-detectors. For example, misalignments of mirror segments in one of the RICH counters will lead to inaccurate reconstruction of the Cherenkov angle of the photons emitted by the particles that traverse the detector. In the calorimeters, misalignments in the ECAL will degrade the mass resolution of the reconstructed $B$ decays involving prompt photons or $\pi^0$ by assigning an incorrect photon momentum. The measurement of the positions are also widely used in the process of electron identification. Finally the Muon Stations, although having a coarser granularity than the tracking system, is of such importance in the L0 Trigger (through muon identification and fast on-line $p_{\mathrm{T}}$ measurement), that misalignments must be taken into account.

These three sub-detectors will be aligned with respect to the fully aligned tracking system (after the steps described in the previous sections of this chapter). For the RICHes, several different components will need to be aligned using various methods. A standalone calibration system will be used for the HPDs. Then the mirrors will be aligned by comparing the reconstructed photon positions with the expectation coming from the charged

track parameters. The ECAL and the Muon System will be aligned using clean electron and muon samples to 0.5 and 1 mm respectively. For the latter, the method used is the same as for the Tracking Stations, using high momentum muon tracks going through the OT and the Muon Stations.

## 3.4 Alignment within the LHCb Alignment Framework

The LHCb alignment framework has been developed inside the LHCb GAUDI software framework. It provides a closed-form $\chi^2$ minimisation as in the well-known Millepede algorithm. In addition, it gives access to the detector elements and their conditions inside the LHCb framework and uses the same track model and track fit as in the standard reconstruction process. It also provides an easy-to-configure algorithm able to align for any combination of detector elements and for any degree of freedom (three translations and three rotations per element or group of elements). Since it uses the standard LHCb track model, it is able to properly take the multiple scattering, magnetic field and energy loss corrections into account. This is a gain with respect to the Millepede method, which uses a global track model. In addition, it will benefit from any improvement in the track model or track reconstruction software. Since it is able to access the detector elements inside the LHCb geometry databases, it can easily update the alignment constants, where these constants are consistent with the track model used in the reconstruction.

### 3.4.1 The Alignment Parameters

In Section 3.1.3.b, the $\chi^2$ minimisation in the track fitting procedure was discussed. However, this computation only took the track parameters into account. The measurement model needs to be extended to include the alignment parameters $\alpha$ of the detector:

$$h(x) \rightarrow h(x, \alpha) \,. \tag{3.27}$$

Contrary to the track parameters, the alignment parameters are common to all the tracks in the sample. They affect the detector elements themselves. Once the track parameters $x$ have been determined by fitting the tracks using a first estimate of the alignment parameters, these can be obtained by minimising the sum of the track $\chi^2$ with respect to $\alpha$, the dependence of $x$ on $\alpha$ being taken into account through the total derivative:

$$\frac{d}{d\alpha} = \frac{\partial}{\partial\alpha} + \frac{dx}{d\alpha}\frac{\partial}{\partial x} \,, \tag{3.28}$$

where

$$\frac{dx}{d\alpha} = -\frac{\partial^2\chi^2}{\partial\alpha\partial x}\left(\frac{\partial^2\chi^2}{\partial x^2}\right)^{-1} \tag{3.29}$$

which is a consequence of the minimisation of the $\chi^2$ with respect to the track parameters $x$:

$$\frac{d}{d\alpha}\frac{\partial\chi^2}{\partial x} = 0 \,. \tag{3.30}$$

The $\chi^2$ minimisation equation 3.22 hence becomes

$$\frac{d\chi^2}{d\alpha} \equiv 0\,. \tag{3.31}$$

This system of $M$ coupled non-linear equations, where $M$ is the number of alignment parameters, is solved using the Newton-Raphson method discussed in Section 3.1.3.b. As in the case of the track fitting, the solution is obtained by using a linear expansion around an initial estimate $\alpha_0$ of the alignment parameters. The system of $M$ linear equations to solve becomes

$$\left.\frac{d^2\chi^2}{d\alpha^2}\right|_{\alpha_0}\Delta\alpha = -\left.\frac{d\chi^2}{d\alpha}\right|_{\alpha_0}\,, \tag{3.32}$$

where $\Delta\alpha$ is the parameter to find.

Using a first order linearisation of the residual $r = m - h(x, \alpha)$ around the expansion point $(x(\alpha_0), \alpha_0)$ and rewriting its derivative with respect to $\alpha$ as

$$A_{ij} \equiv \frac{\partial r_i}{\partial \alpha_j}\,, \tag{3.33}$$

the derivative of the track parameters with respect to $\alpha$ given in Equation 3.29 becomes

$$
\begin{aligned}
\frac{dx}{d\alpha} &= -\frac{\partial^2\chi^2}{\partial\alpha\partial x}\left(\frac{\partial^2\chi^2}{\partial x^2}\right)^{-1} \\
&\sim -\left(\frac{\partial^2}{\partial\alpha_k\partial x_l}\sum_{i=0}^{n}\sum_{j=0}^{n}r_iV_{ij}^{-1}r_j\right)\left(\frac{\partial^2}{\partial x_m\partial x_n}\sum_{i=0}^{n}\sum_{j=0}^{n}r_iV_{ij}^{-1}r_j\right)^{-1} \\
&\sim -\left(-\sum_{i=0}^{n}\sum_{j=0}^{n}H_{il}V_{ij}^{-1}\frac{\partial r_j}{\partial\alpha_k} - \sum_{i=0}^{n}\sum_{j=0}^{n}\frac{\partial r_i}{\partial\alpha_k}V_{ij}^{-1}H_{jl}\right)\times \\
&\qquad\left(\sum_{i=0}^{n}\sum_{j=0}^{n}H_{in}V_{ij}^{-1}H_{jm} + \sum_{i=0}^{n}\sum_{j=0}^{n}H_{im}V_{ij}^{-1}H_{jn}\right)^{-1} \\
&\sim -\left(-\sum_{i=0}^{n}\sum_{j=0}^{n}H_{il}V_{ij}^{-1}A_{jk} - \sum_{i=0}^{n}\sum_{j=0}^{n}A_{ik}V_{ij}^{-1}H_{jl}\right)\times \\
&\qquad\left(\sum_{i=0}^{n}\sum_{j=0}^{n}H_{in}V_{ij}^{-1}H_{jm} + \sum_{i=0}^{n}\sum_{j=0}^{n}H_{im}V_{ij}^{-1}H_{jn}\right)^{-1} \\
&\sim -\left(-\sum_{i=0}^{n}\sum_{j=0}^{n}A_{kj}^{T}(V^{-1})_{ji}^{T}H_{il} - \sum_{i=0}^{n}\sum_{j=0}^{n}A_{ki}^{T}V_{ij}^{-1}H_{jl}\right)\times \\
&\qquad\left(\sum_{i=0}^{n}\sum_{j=0}^{n}H_{ni}^{T}V_{ij}^{-1}H_{jm} + \sum_{i=0}^{n}\sum_{j=0}^{n}H_{mi}^{T}V_{ij}^{-1}H_{jn}\right)^{-1} \\
&= -(-2A^{T}V^{-1}H)(2H^{T}V^{-1}H)^{-1} \\
&= A^{T}V^{-1}HC\,.
\end{aligned}
$$

Using this result, the total derivative given in Equation 3.28 can be written as

$$\frac{d}{d\alpha} = \frac{\partial}{\partial\alpha} + A^T V^{-1} HC \frac{\partial}{\partial x}.$$ (3.35)

The first and second order derivatives of the track $\chi^2$ used in Equation 3.32 become

$$\begin{aligned}
\frac{d\chi^2}{d\alpha} &= \frac{\partial\chi^2}{\partial\alpha} + A^T V^{-1} HC \frac{\partial\chi^2}{\partial x} \\
&= 2A^T V^{-1} r + A^T V^{-1} HC \left(-2H^T V^{-1} r\right) \\
&= 2A^T V^{-1} \left(r - HCH^T V^{-1} r\right) \\
&= 2A^T V^{-1} \left(V - HCH^T\right) V^{-1} r
\end{aligned}$$ (3.36)

and

$$\begin{aligned}
\frac{d^2\chi^2}{d\alpha^2} &= \frac{d}{d\alpha}\left(\frac{d\chi^2}{d\alpha}\right) \\
&= 2A^T V^{-1} \left(V - HCH^T\right) V^{-1} A.
\end{aligned}$$ (3.37)

The difference with respect to the equations derived for the track $\chi^2$ minimisation (Equations 3.23 and 3.25) is the addition of the term $HCH^T$, which is the covariance matrix of the track parameters in the measurement space. The residual covariance matrix $R = V - HCH^T$ is equivalent to that discussed for the Kalman filter in Section 3.1.3.a.

In the case where the track parameters are the best estimate for the given alignment parameters (i.e. $x$ satisfies Equation 3.23), Equation 3.36 simplifies to

$$\frac{d\chi^2}{d\alpha} = 2A^T V^{-1} r.$$ (3.38)

Hence, the equations to solve in order to extract the alignment parameters are Equations 3.37 and 3.38. In case of non-linearities of the residuals as a function of the track and alignment parameters, the procedure needs several iterations until the solution for $\Delta\alpha$ converges, i.e. reaches a plateau.

### 3.4.2 Global Track Covariance Matrix

The track covariance matrix is needed in order to solve the alignment problem given by Equations 3.37 and 3.38. However, the correlations between states are not computed in the Kalman filter. A method was hence proposed to determine the correlation matrix between states [133].

In the prediction step of the Kalman filter procedure, the prediction covariance matrix is given by Equation 3.5:

$$C_k^{k-1} = F_k C_{k-1} F_k^T + Q_k.$$

The process noise $Q_k$ has the effect of reducing the correlation between states. The full predicted covariance matrix for the pair of states $(x_{k-1}, x_k^{k-1})$ is then given by

$$\mathrm{Cov}(x_{k-1}, x_k^{k-1}) = \begin{pmatrix} C_{k-1} & C_{k-1} F_{k-1}^T \\ F_{k-1} C_{k-1} & C_{k-1} F_{k-1}^T + Q \end{pmatrix}.$$ (3.39)
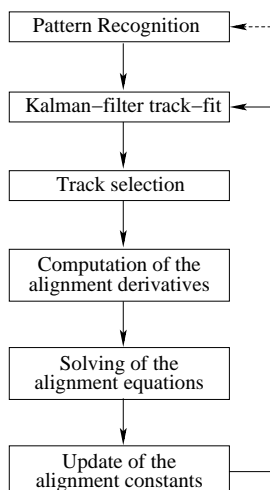
Figure 3.6: Flow diagram of the software procedure used for the Tracking-Station alignment. The pattern recognition can optionally be re-run at each iteration.

The information of the state $x_k$ is then added in the filter step and the information is propagated backwards in the smoothing step. The tracks used in the alignment are the output of the three steps procedure, including the smoothing. The covariance matrix needed is the correlation between the smoothed states. Using the definition of the smoother gain matrix from Equation 3.17, the correlation between the smoothed states is then given by

$$C_{k-1,k}^n = C_{k-1} F_{k-1}^T (C_k^{k-1})^{-1} C_k^n = A_{k-1} C_k^n \tag{3.40}$$

### 3.4.3  T-Station Alignment Procedure

The framework in which the alignment procedure is run is centred on a single C++ algorithm, which takes the tracks from the standard LHCb track fit as input. In parallel, it processes the detector elements specified by the user and assigns the hits on tracks to the corresponding elements. The correlations between the hits on tracks are computed and the global $\chi^2$ is minimised in order to provide the alignment constants to be written in the condition database.

The general software sequence is shown in Fig. 3.6. The alignment algorithm uses a set of dedicated tools. A first one gives access to the detector elements in order to get the initial geometry and update it when the alignment procedure is finished. The track reconstruction is also accessible. Both the pattern recognition and the track fit sequences can be easily adapted to each use-case. Once the tracks have been reconstructed, a second tool can be used to apply a track quality selection or select sub-samples of tracks based on their momentum (in case the magnetic field is turned on), the number of hits in each sub-detectors, the number of missed hits on the tracks, etc. The goal of this selection is to obtain a sample of clean tracks while rejecting most of the ghosts. Finally, the solver tools are used to find the solution of the system of $M$ linear equations

$$Ax = b \,, \tag{3.41}$$

where $A = \frac{\partial^2 \chi^2}{\partial \alpha^2}$, $x = \Delta \alpha$ and $b = \frac{\partial \chi^2}{\partial \alpha}$. $M$ is the number of alignment parameters.

The Inner Tracker is composed of 3 stations $\times$ 4 boxes $\times$ 4 layers $\times$ 7 = 336 silicon-strip IT ladders, each having six degrees of freedom (three translations and three rotations). This adds up to a total of 2016 degrees of freedom. On the other hand, the Outer Tracker is made of 3 stations $\times$ 4 layers $\times$ 22 modules = 264 straw-tube OT modules that need to be aligned, adding an extra 1584 degrees of freedom to the problem.

Throughout the next chapters of results, the following convention is used: the degrees of freedom are called $Tx$, $Ty$ and $Tz$ (translation of the detector elements along the horizontal measurement direction, the vertical direction and the beam axis respectively) and $Rx$, $Ry$ and $Rz$ (rotations about the three axes).

## 3.4.4   Weak Mode Suppression

The $\chi^2$ minimum reached by the alignment method may be invariant under linear combinations of alignment parameters, known as weak modes. These are global translations or rotations of the entire T Stations, or more complicated distortions. To avoid the influence of weak modes on the solution, constraints are applied. This can be done either using Lagrange multipliers or by performing a spectral analysis and removing the eigenvectors corresponding to the weak modes. The fit to the origin vertex of the tracks can also be included in the procedure [133], which helps constraining further the alignment parameters. However, since the origin vertex is located 7 m upstream in the VELO region, vertex fitting has little influence on the T-Station alignment.

Another way of constraining one sub-detector is to align for it with respect to another fixed sub-detector. For example, aligning for the T Stations using long tracks fixes both the Inner and Outer tracker to the nominal position of the VELO and Trigger Tracker. This corresponds to implementing simultaneously the T-Station internal alignment and the VELO–T Stations relative alignment. This method is used in Section 4.3.

Finally, the alignment of a sub-detector can also be constrained by fixing one or several of its components, i.e. not taking it into account in the alignment procedure. This is performed in Sections 4.2 and 5.1.

# Chapter 4

# Monte Carlo Alignment Studies
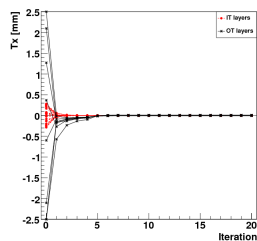


Results of the LHCb Tracking-Station alignment with Monte Carlo data are discussed in this chapter. Two scenarios are studied, with the LHCb magnetic field turned on and off, and with long or T tracks respectively. The alignment results are validated by comparing the $J/\psi$ mass resolution before and after alignment with the resolution of an ideal case.

This chapter presents the studies performed on the alignment of the Tracking Stations (the Inner and Outer Trackers) with Monte Carlo simulated data. First, general considerations on the event and track selection are presented in Section 4.1. Then, two scenarios, in which the alignment will be performed, are presented. The first, presented in Section 4.2, is a day-1 scenario which uses the conditions that are expected in the first days of LHC operation. In this first phase, protons will circulate in the LHC ring at the SPS injection energy of 450 GeV. No proton–proton collisions are expected at that stage and the only data recorded by the detectors will be collisions of the beam protons with residual gas nuclei in the beam pipe. At low energy, the LHCb detector will not be used to its full extent. Due to the risk of radiation damage because of poor collimation of the beam, the VELO will have to remain in open position. Also, the magnetic field will be off. With such conditions, the most useful tracks for the Tracking-Station alignment are T tracks or T–TT tracks, i.e. tracks reconstructed in the T Stations and in the TT only.

After this early first phase, collision data will be collected at $\sqrt{s} = 900$ GeV. Then, the beam energy will be ramped up until a centre-of-mass energy of $\sqrt{s} = 7$ TeV in a third phase and $\sqrt{s} = 10$ TeV later. At this point, the magnetic field will have been turned on and the VELO closed (at around $\sqrt{s} = 4$ TeV). Once the machine is repaired, the last phase will operate at the design luminosity and energy: $\mathcal{L} = 2 \times 10^{32}\,\mathrm{cm}^{-2}s^{-1}$ and $\sqrt{s} = 14$ TeV. The second scenario, presented in Section 4.3, uses data simulated in the nominal conditions. Since the VELO is closed, long tracks going through the whole detector can be reconstructed and used for the alignment process.

This chapter has been published as a public LHCb note [134].

## 4.1   Event and Track Selection

Since the alignment $\chi^2$, defined in Section 3.4.1, uses primarily track information, it is sensitive to the effect of ghost tracks (defined in Section 3.1.4) and particles with kinks in their trajectory due to interactions in the detector material. If such tracks are used in the procedure they can cause the algorithm to converge to a false minimum. Thus, it is important to obtain a sample of tracks with a minimum contamination from ghosts and other bad tracks. The following two sections present selection criteria that can be used to obtain a pure sample of T tracks for the first scenario and of long tracks for the second scenario.

### 4.1.1   Cuts on the Track Quality

One way of dealing with bad tracks is to cut on the track fit $\chi^2$. For long tracks it is also possible to cut on the $\chi^2$ of the matching of upstream and downstream track segments: $\chi^2_{\mathrm{m}}$. This is defined as

$$\chi^2_{\mathrm{m}} = \chi^2_{\mathrm{tot}} - \chi^2_{\mathrm{T}} - \chi^2_{\mathrm{VELO}}, \tag{4.1}$$

where $\chi^2_{\mathrm{T}}$ is the $\chi^2$ of the segment in the Tracking Stations and $\chi^2_{\mathrm{VELO}}$ is the $\chi^2$ of the segment in the VELO. This is valid in the present study because the TT hits are removed from the track during the fit. These variables need to be used with care since their quality is degraded in a misaligned detector. Therefore, an evolving strategy is developed. In the first iteration of the procedure a loose cut on the $\chi^2$ is made which is then tightened in subsequent iterations. To develop this strategy the distributions of good real tracks (called good tracks in the rest of the discussion), real tracks undergoing interactions (bad tracks) and ghosts are studied with the ideal geometry as well as with a misalignment scenario described in Section 4.3.1. Results with tracks going through both the Inner and the Outer Trackers are not satisfactory, as shown in Appendix A.1. However, since the IT has a better spatial resolution than the OT, it is also more sensitive to these bad tracks. With a proper selection, the purity of the track sample can be increased for tracks going through the IT only. This leads to a more precise alignment of this sub-detector, which can then be used as a constraint for the alignment of the OT. The plots and tables presented in this section report the results of studies performed on tracks going through the IT only (no OT hits on the tracks), whereas tracks going through any of the IT or OT are studied in Appendix A.1.

Figure 4.1 shows the distribution of the $\chi^2/\mathrm{dof}$ in the misaligned case. It can be seen that cutting on the track fit $\chi^2/\mathrm{dof}$ at 100 does not bias the sample of good tracks. Therefore, this is chosen as the starting value in the iterative procedure. Figure 4.2 shows the same distributions in the case of the ideal detector. From this plot it can be seen that a reasonable cut to apply at the end of the scheme is $\chi^2/\mathrm{dof} < 10$.

Figures 4.3 and 4.4 show the corresponding distribution of $\chi^2_{\mathrm{m}}$. In this case an initial cut value of 100 is reasonable. This is reduced to 30 during the iteration procedure.

Tables 4.1 and 4.2 summarise the performance of the cuts described above in removing ghosts for long tracks using the misaligned geometry (initial case) and the ideal geometry (final case) respectively. Tables 4.3 and 4.4 show the results in the case of T tracks. Table 4.5 presents the evolution chosen for the cuts on the track quality criteria: $\chi^2/\mathrm{dof}$ and $\chi^2_{\mathrm{m}}$. This strategy is used in Sections 4.2 and 4.3.

(a) good tracks

(b) bad tracks
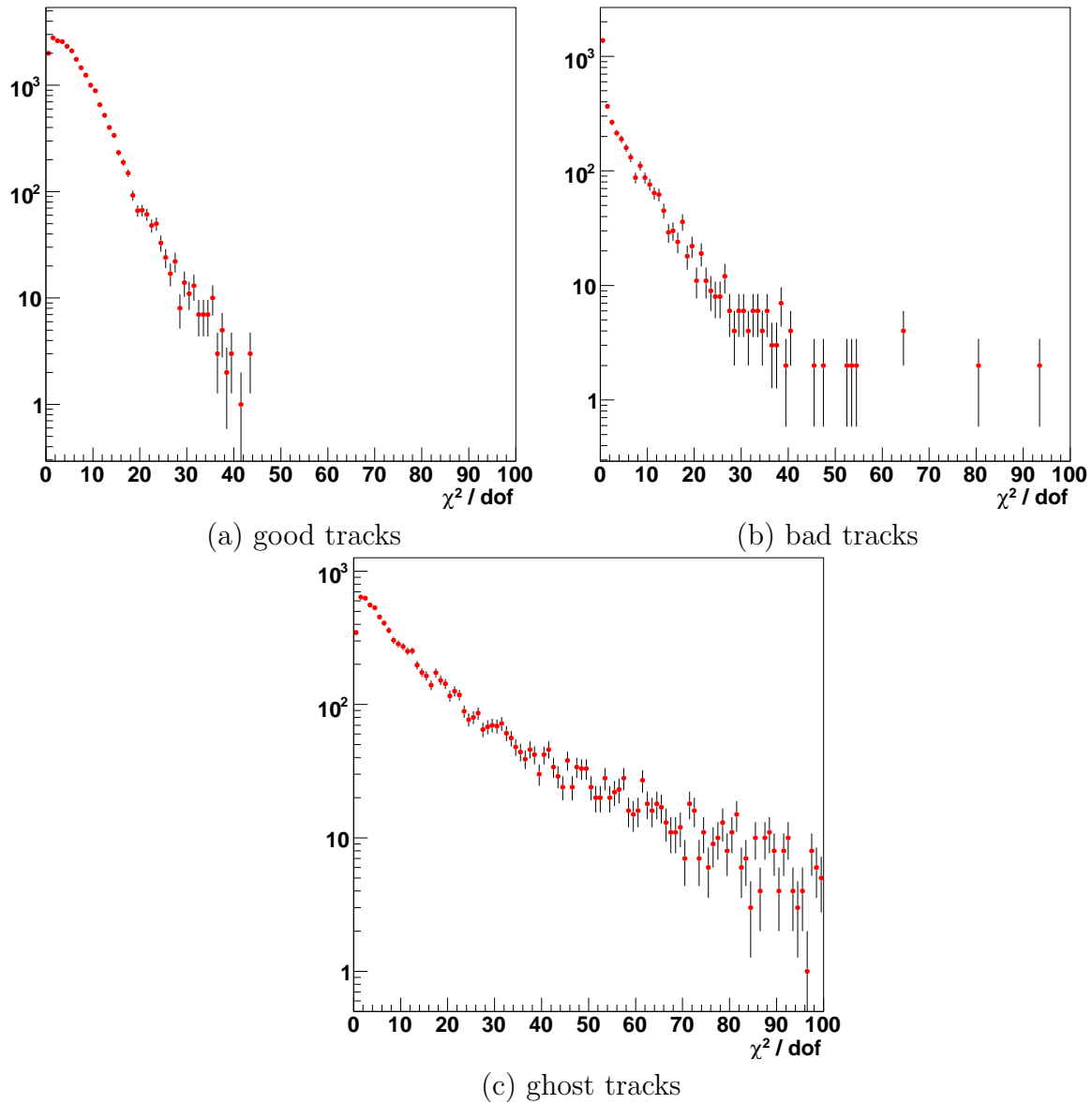
(c) ghost tracks

Figure 4.1: Distribution of track fit $\chi^2$/dof for (a) good, (b) bad and (c) ghost tracks going through IT only with the misalignment scenario presented in Section 4.3.1. The data used is a sample of minimum bias events.

(a) good tracks

(b) bad tracks

(c) ghost tracks

Figure 4.2: Distribution of track fit $\chi^2$/dof for (a) good, (b) bad and (c) ghost tracks going through IT only with the ideal geometry. The data used is a sample of minimum bias events.

(a) good tracks

(b) bad tracks

(c) ghost tracks

Figure 4.3: Distribution of track $\chi_m^2$ for (a) good, (b) bad and (c) ghost tracks going through IT only with the misalignment scenario presented in 4.3.1. The data used is a sample of minimum bias events.

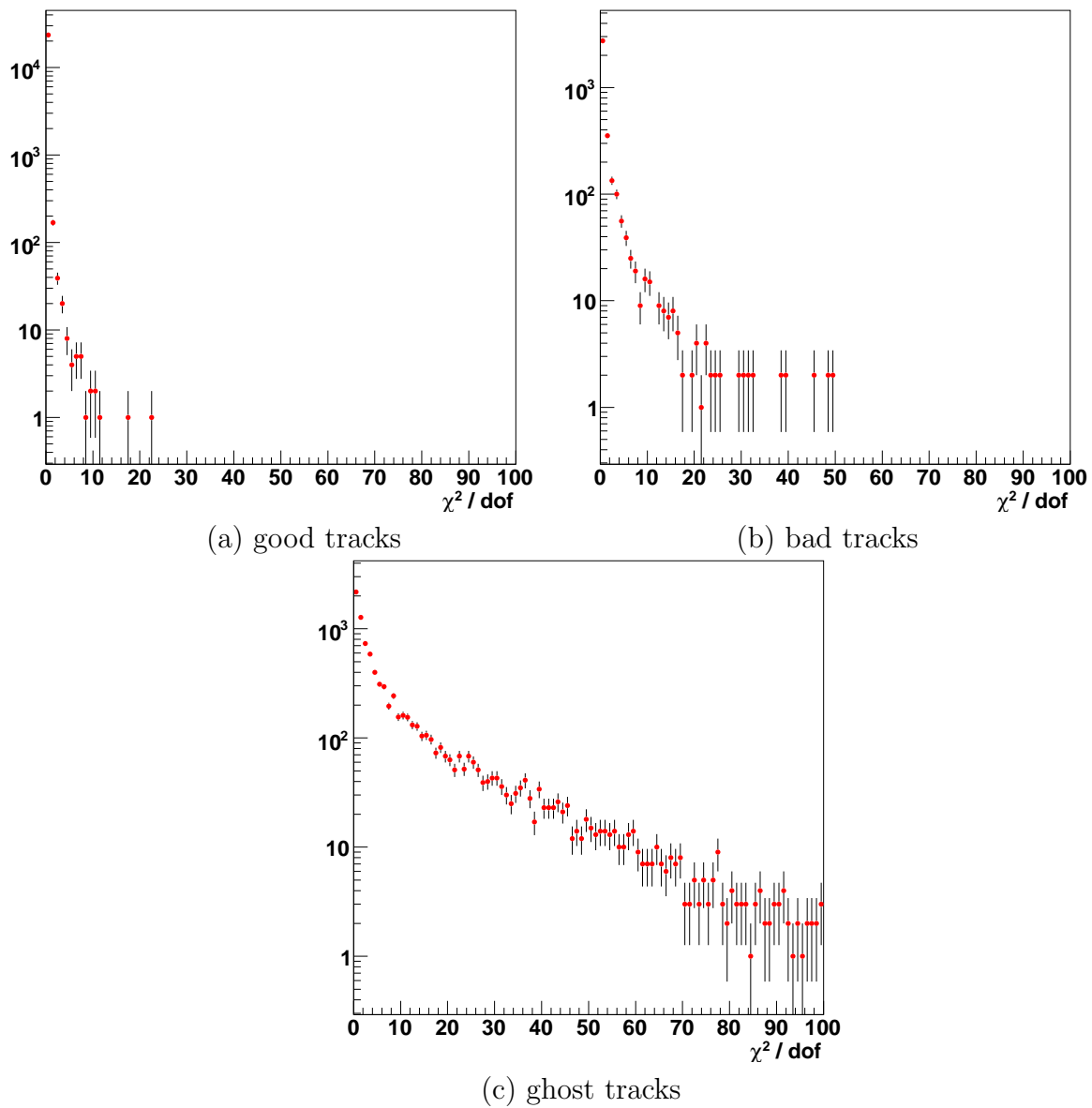(a) good tracks

(b) bad tracks

(c) ghost tracks

Figure 4.4: Distribution of track $\chi^2_{\mathrm{m}}$ for (a) good, (b) bad and (c) ghost tracks going through IT only with the ideal geometry. The data used is a sample of minimum bias events.
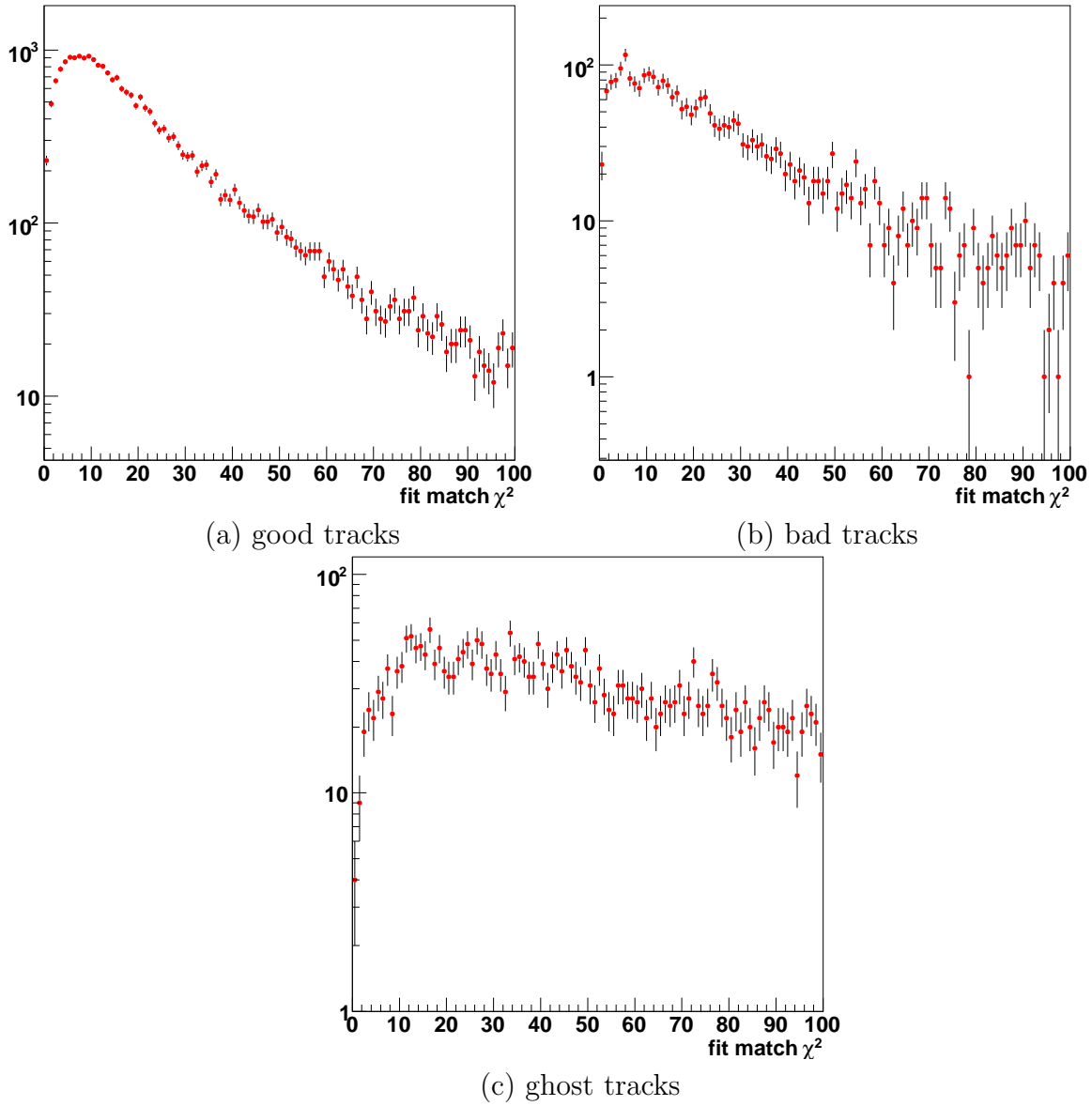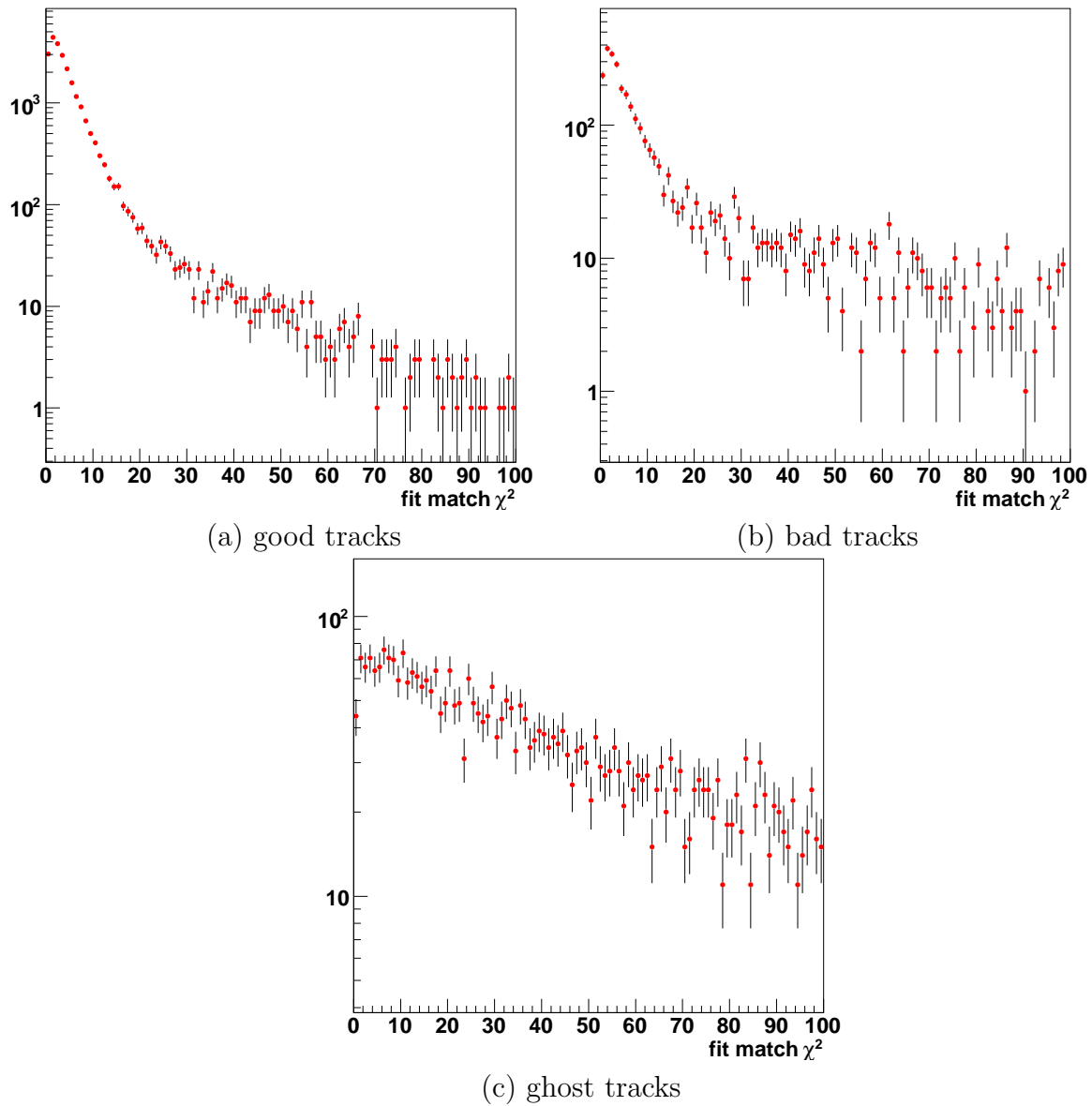
Table 4.1: Long-track selection efficiencies and ghost rate before and after track quality requirements on $\chi^2/\mathrm{dof}$ and $\chi^2_\mathrm{m}$ in the case of the misaligned geometry. The tracks are required to have no OT hit. The data used is a sample of simulated minimum-bias events.

| Cut | Efficiency | | Ghost rate |
|---|---|---|---|
| | Good tracks | Bad tracks | |
| No cut | 100 % | 100 % | 14.07 % |
| $\chi^2/\mathrm{dof} < 100$ | 100 % | 100 % | 14.01 % |
| $\chi^2_\mathrm{m} < 100$ | 95.28 % | 74.58 % | 6.54 % |

Table 4.2: Long-track selection efficiencies and ghost rate, before and after track quality requirements on $\chi^2/\mathrm{dof}$ and $\chi^2_\mathrm{m}$ in the case of the ideal geometry. The tracks are required to have no OT hit. The data used is a sample of simulated minimum-bias events.

| Cut | Efficiency | | Ghost rate |
|---|---|---|---|
| | Good tracks | Bad tracks | |
| No cut | 100 % | 100 % | 13.93 % |
| $\chi^2/\mathrm{dof} < 10$ | 99.99 % | 98.92 % | 12.34 % |
| $\chi^2_\mathrm{m} < 30$ | 96.67 % | 69.50 % | 4.47 % |

Table 4.3: T-track selection efficiencies and ghost rate before and after track quality requirements on $\chi^2/\mathrm{dof}$ in the misaligned case. The tracks are required to have no OT hit. The data used is a sample of simulated beam–gas events.

| Cut | Efficiency | | Ghost rate |
|---|---|---|---|
| | Good tracks | Bad tracks | |
| No cut | 100 % | 100 % | 6.89 % |
| $\chi^2/\mathrm{dof} < 100$ | 100 % | 99.98 % | 6.89 % |

Table 4.4: T-track selection efficiencies and ghost rate before and after track quality requirements on $\chi^2/\mathrm{dof}$ in the aligned case. The tracks are required to have no OT hits. The data used is a sample of simulated beam–gas events.

| Cut | Efficiency | | Ghost rate |
|---|---|---|---|
| | Good tracks | Bad tracks | |
| No cut | 100 % | 100 % | 6.71 % |
| $\chi^2/\mathrm{dof} < 10$ | 99.96 % | 99.11 % | 6.55 % |

Table 4.5: Strategy for the evolving cut on the track $\chi^2/\mathrm{dof}$ and on the track fit match $\chi^2_\mathrm{m}$.

|  | Iteration | | | |
|---|---|---|---|---|
| Selection criteria | 1 | 2 | 3 | > 4 |
| $\chi^2/\mathrm{dof}$ | 100 | 40 | 20 | 10 |
| $\chi^2_\mathrm{m}$ | 100 | 80 | 50 | 30 |

The cuts used in this study are loose and could be tightened when aligning the detector with real data. Especially, the cut on the $\chi^2/\mathrm{dof}$ for T tracks could be tightened. However, since the ghost rate is lower in this case, it is not as essential as in the case of long tracks. The values of the cuts need to be chosen with care in each case such that the sample of good tracks is not reduced while still removing a fraction of the ghost and bad tracks.

### 4.1.2 Other Cuts

Several other cuts are investigated to reduce the ghost rate further and give better convergence of the algorithm. The results shown below are obtained on a sample of 20'000 minimum-bias events reconstructed with the ideal geometry. The tracks are required to cross at least one of the elements to be aligned.

It has been shown for the long tracking that most ghosts originate in the matching between the VELO and T seeds [95]. These ghosts appear when there are many reconstructed segments in either of the sub-detectors. In order to reduce this source of ghosts, events with many VELO or Inner Tracker clusters are rejected. High Outer Tracker occupancy is not as big a problem as in the IT case because of the lower track density. The cuts are chosen to reduce the ghost rate to an acceptable level. For the studies presented here, less than 400 IT clusters and less than 900 VELO clusters are required. These cuts are summarised in Table 4.6.

Poorly reconstructed tracks also have a negative impact on the alignment results, as discussed above. For example, tracks with large multiple scattering in the detector tend to have a bad fit quality. As this process most strongly affects low-momentum particles, it can be reduced by cutting on the track momentum at $10\,\mathrm{GeV}/c$, when this information is available (see Table 4.6). Finally, the ghost rate can also be reduced by cutting on the track pseudo-rapidity. The LHCb acceptance in this variable is between 1.9 and 4.9. Ghosts tend to have a large pseudo-rapidity in the VELO [94]. A reasonable cut is at $\eta < 5.2$. Combining these four cuts leads to an overall selection efficiency for good tracks of 11.6 % with a ghost rate of 7.8 %.

## 4.2 Alignment with Beam–Gas Interactions

During the machine startup only one beam will circulate in the beam pipe. In this period LHCb will acquire events from beam–gas interactions, giving the opportunity to calibrate, commission and align the detector. In the following sections, the alignment scenario under study is reported along with the achieved results.

Table 4.6: Summary of the cuts applied to reduce the ghost rate for long tracks with ideal geometry.

| Cut | Efficiency | Ghost rate |
|---|---|---|
| No cut | 100 % | 17.5 % |
| # IT Clusters < 400 | 56.0 % | 11.90 % |
| # VELO Clusters < 900 | 38.5 % | 10.6 % |
| $p > 10\,\mathrm{GeV}/c$ | 35.3 % | 15.2 % |
| $\eta < 5.2$ | 100 % | 16.7 % |
| All above cuts | 11.6 % | 7.75 % |

Table 4.7: Summary of the misalignments applied in the beam–gas scenario.

| Detector | dof | Gaussian width |
|---|---|---|
| IT layers | $Tx$ | 0.3 mm |
|  | $Rz$ | 2.5 mrad |
| OT layers | $Tx$ | 2.5 mm |
|  | $Rz$ | 1.0 mrad |

## 4.2.1   The Beam–Gas Scenario

The data used for this test is a Monte Carlo simulated sample of 50'000 beam–gas events with a beam energy of $450\,\mathrm{GeV}/c$. During the simulation and the reconstruction, the geometry is assumed to be the nominal geometry. However, the alignment procedure is performed using a misaligned geometry, meaning that the procedure assumes that the detector is misaligned and tries to move it back to its ideal position. This geometry is obtained by misaligning both the Inner Tracker and Outer Tracker layers with translations along the measurement axis and rotations around the beam axis. The amplitude of the misalignments for each of the detector elements to be aligned is chosen to follow Gaussian distributions with widths of $0.3\,\mathrm{mm}$ (IT $Tx$), $2.5\,\mathrm{mm}$ (OT $Tx$), $2.5\,\mathrm{mrad}$ (IT $Rz$) and $1\,\mathrm{mrad}$ (OT $Rz$). This misalignment scenario is summarised in Table 4.7.

No misalignment is added for the translations along the strips and beam axes nor for the rotations around the measurement direction and vertical axis, as these degrees of freedom are those to which the alignment procedure is the least sensitive. The amplitude chosen for the misalignments reflects a reasonable day-1 scenario.

To simulate the situation on day-1, standalone T-Station alignment is performed using T tracks only. The T Stations are aligned alone, without the constraint to the VELO that would be present if using long tracks. In addition, the magnet is assumed to be switched off, removing the knowledge of the momentum and hence the possibility to cut on this variable. This means that multiple scattering cannot be correctly accounted for, which means the covariance matrix is not properly estimated, resulting in a loss of statistical precision.
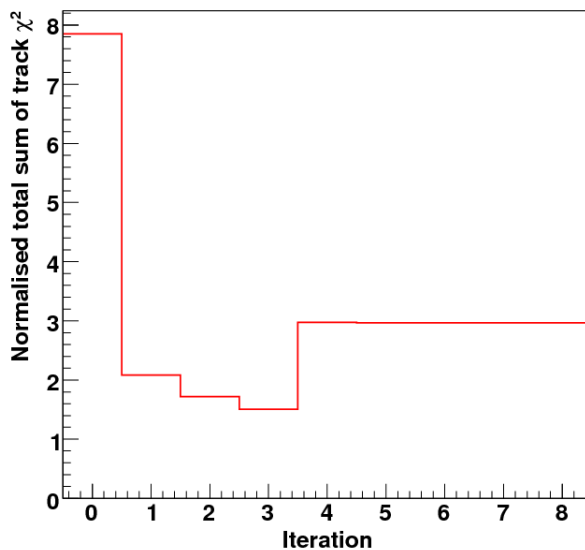
Figure 4.5: Convergence of the average track $\chi^2$/dof (beam–gas scenario).

Both the Inner and Outer Trackers are aligned at the layer level, for the two degrees of freedom that are misaligned [1]. In order to remove weakly constrained degrees of freedom, four IT layers in each stack of boxes and four OT layers are frozen to their ideal positions. These four layers are the first and last $X$ and stereo layers.

In order to gain in precision, the drift-time information should be used for the OT. Ignoring this, the resolution worsens from $200\,\mu\mathrm{m}$ to $2.5\,\mathrm{mm}/\sqrt{12} \sim 1\,\mathrm{mm}$. However, if the drift time is used, the left-right ambiguity of the measurement must be resolved. The convergence of the algorithm is less stable in this case. The strategy chosen to deal with this is to first get close to the minimum by running four iterations ignoring the drift times and to then use the power of drift-time information for the remaining iterations.

## 4.2.2    Beam–Gas Results

There are several possibilities to monitor the performance of the alignment. As described in Section 3.4.3, the procedure minimises the total track $\chi^2$ with respect to both the track and alignment parameters. The first way of looking at the results is to check that the track $\chi^2$/dof, averaged over the whole selected track sample, has indeed converged. Figure 4.5 shows the convergence of this parameter as a function of the iteration number.

Two different regions can be seen on this plot. The first one covers the first four iterations where a clear drop in the total $\chi^2$ is visible. The second, from iteration 4 to 8, shows a big jump and then a plateau. The plateau indicates that the procedure has converged. The jump is explained by the OT drift-time information used after four iterations. Turning on the drift times decreases the hit error and thus increases the $\chi^2$.

It is clear that the alignment algorithm has found a minimum of the total track $\chi^2$. However, it needs to be checked that a stable position of the detector elements is reached or if weak modes are active. This is done by looking at the evolution of the alignment

---

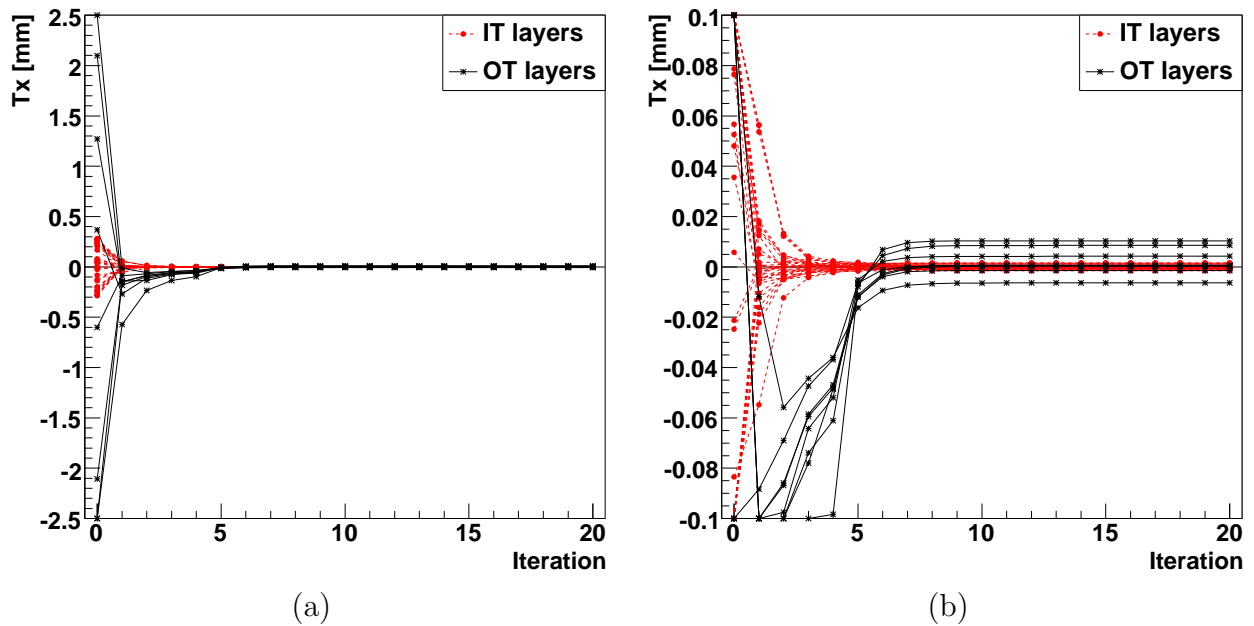[1] The four other degrees of freedom are frozen.

Figure 4.6: Convergence of the $Tx$ alignment parameter for each of the IT and OT layers (beam–gas scenario). (b) is a zoom of (a).

parameters as a function of the iteration. This study concentrates on the translation in the $x$ measurement-direction, which is the most sensitive alignment parameter. Figure 4.6 shows this evolution for all the IT and OT layers (each line representing one layer). The values of the first points correspond to the input misalignments set in the conditions. The goal of the alignment is to have all the curves converging to zero, the ideal position. The curves then show the value of the $Tx$ alignment parameter for each detector element, including the correction given by the current iteration. Figure 4.6 (b) is a zoom on Fig. 4.6 (a).

Figure 4.6 (a) shows that the OT layers, although initially misaligned by large values, converge well towards the ideal position in five to six iterations. All layers end up within $10\,\mu$m of the ideal geometry. The results will be discussed in detail in Section 4.2.3.

The IT layers converge in three to four iterations to within $2\,\mu$m of the ideal geometry. This corresponds to less than $5\,\%$ of the IT single hit resolution of $200/\sqrt{12} \sim 57.7\,\mu$m. Validation studies are shown in Section 4.2.4.

Another way of looking at the results is to calculate the residual misalignment after the alignment procedure has converged. This is done by subtracting the output misalignment (as given by the alignment algorithm) from the input misalignment set in the conditions. Figure 4.7 shows this value for all the IT and OT layers, i.e. the plot is a projection of the vertical coordinate of the last point of each graph in Fig. 4.6. The points with no error bars and no residual misalignment are the layers that are kept fixed during the alignment procedure as constraints.

The fact that the IT and OT layers are aligned simultaneously constrains the OT layers to the position of the IT layers through the overlap regions between the two sub-detectors. Since this is mainly driven by the intrinsic resolution, which is about four times
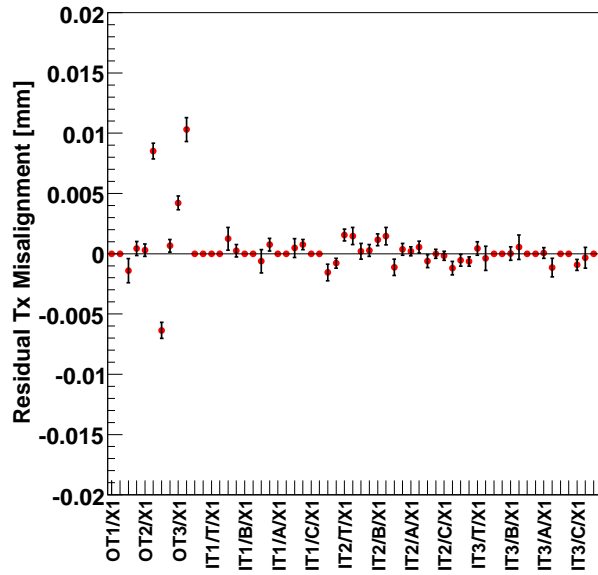
Figure 4.7: Residual $Tx$ misalignment for each of the IT and OT layers after alignment (beam–gas scenario).

better for IT than for OT, the OT alignment is improved by this constraint. The mean of the residual misalignment is 10 % smaller for the OT when aligning simultaneously with the IT compared to a standalone alignment. On the other hand, the spread of the final IT layer positions is 10 % larger when aligning with the OT compared to standalone. However, the residual misalignment being smaller for the IT than for the OT, the global effect of the constraint is beneficial for the overall detector.

### 4.2.3   Further Studies

Two issues need to be addressed at this point. The first is that the convergence for OT layers takes five iterations. With the method used, convergence is expected within one or two iterations. The second issue is the fact that some OT layers have a final position at about ten standard deviations from the true position (ideal geometry). That is to say, the error on the alignment parameters is under-estimated. Detailed studies of effects relevant to this are discussed in the following sub-sections.

#### 4.2.3.a   Effect of Drift-Time Information

The first effect that is studied is the influence of using the OT drift-time information on the alignment procedure. Using this gives a better resolution, but is expected to slow down the convergence of the algorithm, due to mis-resolved L/R signs. The results shown in Figs. 4.6 and 4.7 (with drift times) can be compared to those shown in Fig. 4.8 (no drift times). The convergence takes the same number of iterations. However, the second consequence of using the drift-time information can be seen. The precision on the final position after alignment for the OT layers is increased by a factor ten when using the drift-time information. This is a demonstration that this information is needed for the
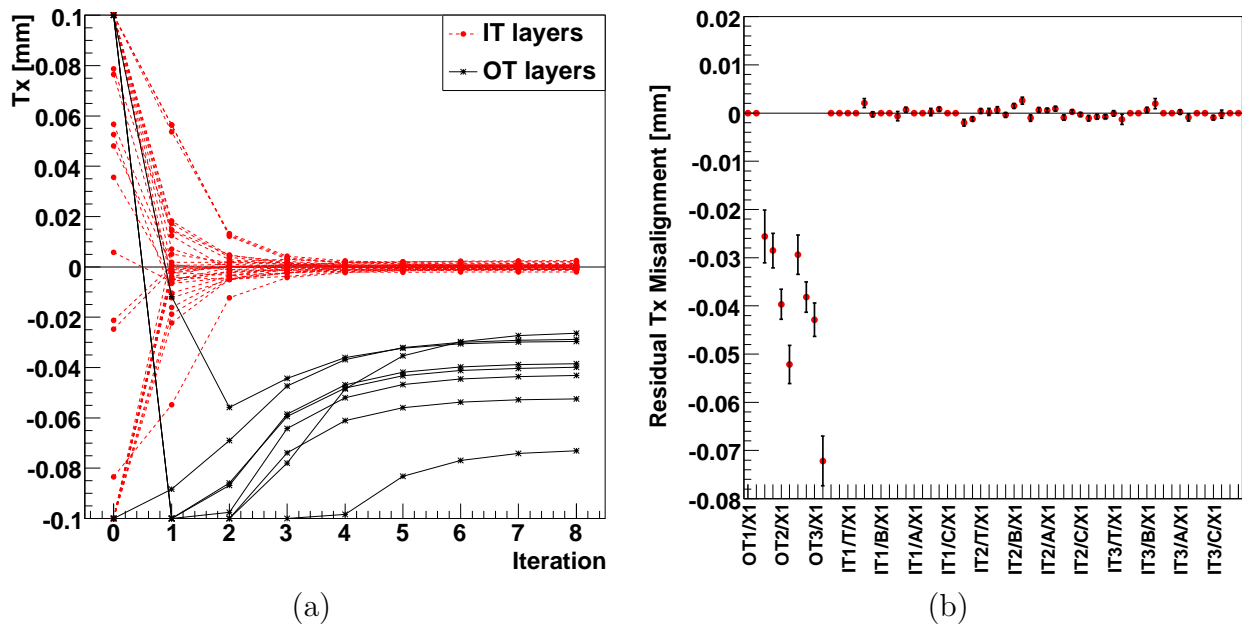
Figure 4.8: (a) $Tx$ alignment parameter evolution and (b) residual $Tx$ misalignment for each of the IT and OT layers after alignment (beam–gas scenario, no drift times).

alignment of the Outer Tracker.

### 4.2.3.b   Effect of the Cut on the Track Quality

The cut on the track quality is discussed in detail in Section 4.1.1. However, the effect of such a cut on the results of the alignment procedure is still not known. The same alignment scenario as shown in Section 4.2.2 is run without the evolving cut on the track $\chi^2/\mathrm{dof}$ (see Fig. 4.9) and with a fixed cut at $\chi^2/\mathrm{dof} < 10$ (shown in Fig. 4.10).

These two results show two very important things. First, the alignment procedure suffers from poor quality tracks, which are the consequence of a very misaligned detector. The procedure does not recover from the effect of these tracks. These plots also show that the IT suffers more from bad tracks. This is not surprising as the IT resolution is about four times better than the OT resolution.

The second thing that these studies show is that cutting too hard on the track quality in the first iteration worsens the results. This is due to the fact that with a very misaligned detector, cutting too hard on the track $\chi^2/\mathrm{dof}$ rejects a large number of tracks, which biases the track sample. The procedure is then not able to recover from this.

### 4.2.3.c   Effect of Low-Momentum Tracks

As explained in Section 4.2.1, aligning with beam–gas data with the magnet off prevents from using the momentum information. A momentum estimate (and error estimate) is not made during the track fit, and the multiple scattering is not taken into account. However the Monte Carlo truth information can be used to reject low-momentum tracks to understand the effect of these tracks in the simulation. Figure 4.11 shows the results of

Figure 4.9: (a) $Tx$ alignment parameter evolution and (b) residual $Tx$ misalignment for each of the IT and OT layers after alignment (beam–gas scenario, no cut on the track $\chi^2/\text{dof}$).



Figure 4.10: (a) $Tx$ alignment parameter evolution and (b) residual $Tx$ misalignment for each of the IT and OT layers after alignment (beam–gas scenario, fixed cut on the track $\chi^2/\text{dof} < 10$).
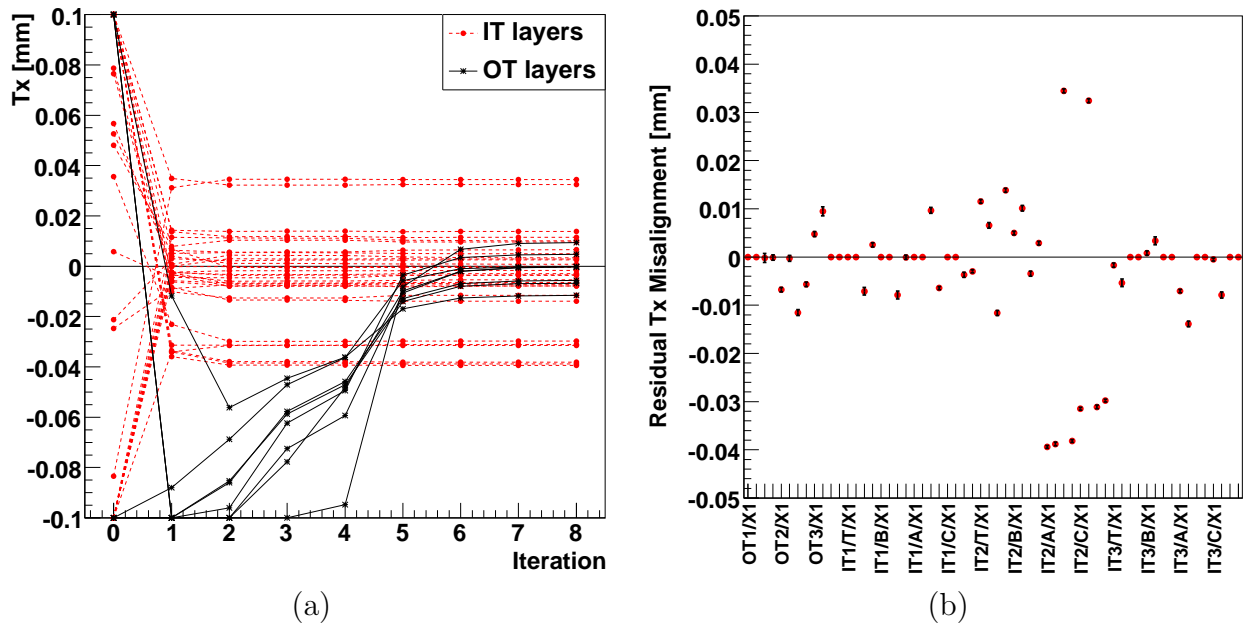
(a)

(b)

Figure 4.11: (a) $Tx$ alignment parameter evolution and (b) residual $Tx$ misalignment for each of the IT and OT layers after alignment (beam–gas scenario, cut on the momentum at $10\,\mathrm{GeV}/c$).

a run where tracks with $p < 10\,\mathrm{GeV}/c$ are removed by applying a cut on the Monte Carlo truth. The IT layers alignment parameters converge in one to two iterations as opposed to three to four without the momentum cut. However, as can be seen in the right-hand-side plot, the final position of the layers is slightly worsened with the cut applied.

Another effect visible here is related to the issue of the under-estimated errors. Compared to the other results shown in previous sub-sections, the errors here seem much better estimated with layers sitting only three to five standard deviations away from the true position. This is to be compared with the ten standard deviations seen before. Hence, the error estimate problem is related to the fact that, with no magnetic field, the track momentum is not estimated and the multiple scattering not properly taken into account.

In this study, the momentum cut is performed by using the Monte Carlo truth information. When running the algorithm on data, this is not possible. However, there are other possibilities, which need more study. For example, the tracks going through IT and OT can be extrapolated to either the calorimeters or to the muon system in order to provide a momentum estimate and hence remove the low-momentum tracks.

### 4.2.3.d  Reference Alignment Job (Ideal Geometry)

The goal of the alignment procedure is to move the detector to its real position. Alternatively, it can be understood as getting the same final position starting from a misaligned detector as starting with the ideal geometry. In Fig. 4.12, the results of the same scenario as above are shown, but starting from a null misalignment. These plots, and especially the plot on the right, could serve as a reference. The final results are the same as those shown in Figs. 4.6 and 4.7, to within $1\,\mu$m. This fact shows that the alignment algorithm
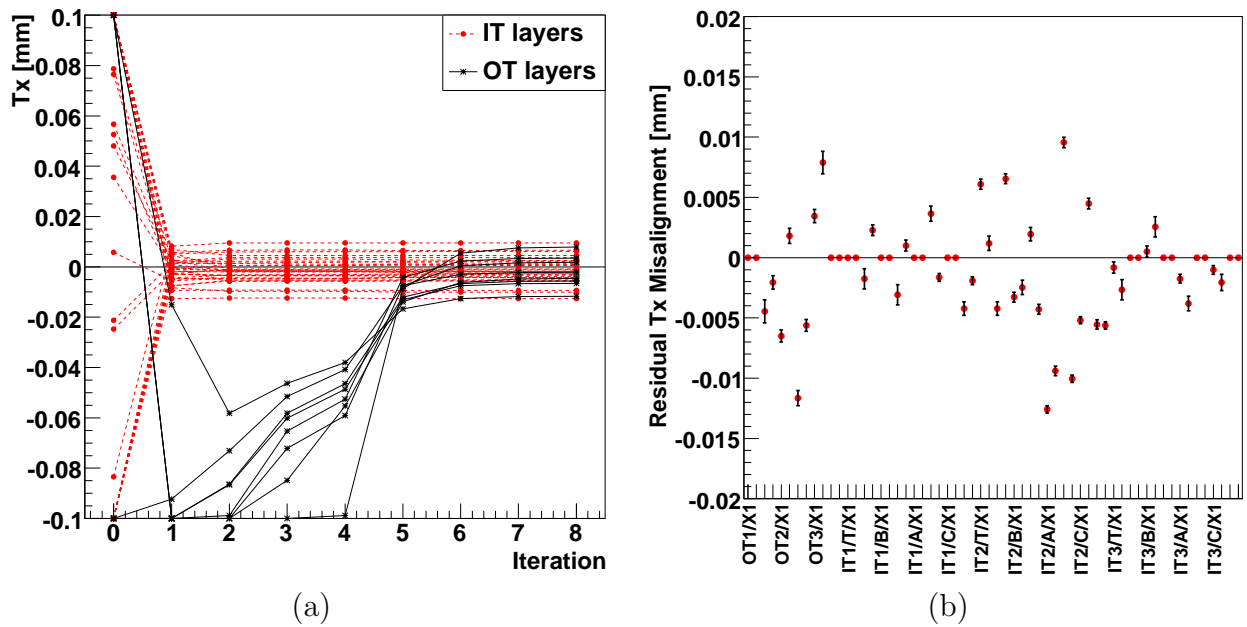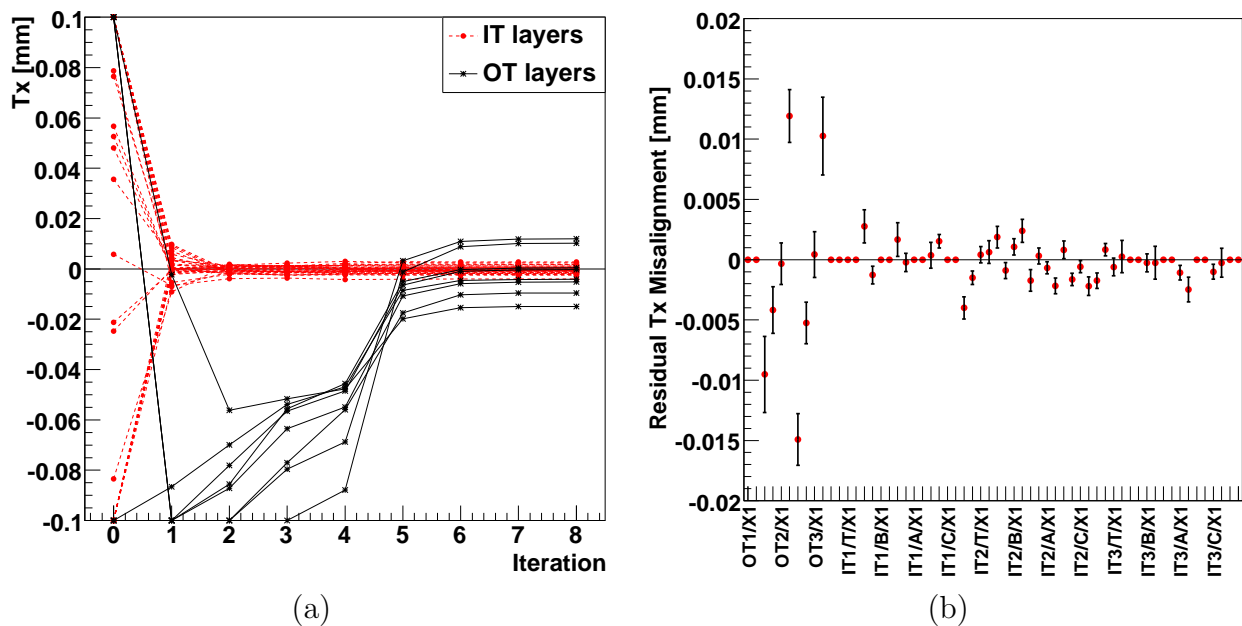
Figure 4.12: (a) $Tx$ alignment parameter evolution and (b) residual $Tx$ misalignment for each of the IT and OT layers after alignment (beam–gas scenario, ideal geometry).

is very robust against misalignments, that it does not depend on the initial misalignment of the detector. It means that the results depend only on the track selection, use of drift time and the other parameters presented above.

### 4.2.3.e  Adding More Degrees of Freedom

The previous sections showed the alignment of the IT and OT layers with four IT layers in each stack and four OT layers frozen to the ideal position. This large number of constraints doesn't allow to get the IT position with respect to the OT, for example. When the T Stations will be aligned with real data, this information will be needed. However, a larger number of degrees of freedom taken into account leads to more weak modes and to a worsened precision.

This is tested below. In the plots of Figs. 4.13 and 4.14, the results of the alignment procedure with no constraint on the IT layers are shown (all layers are free to move in the measurement direction and to rotate around the beam axis). In addition, the latter plot shows the effect of the cut on the momentum (taken from the Monte Carlo truth) at $10\,\text{GeV}/c$. The convergence for the IT layers requires an additional three iterations in these cases. Also, the final position is within $40\,\mu$m instead of $2\,\mu$m with the IT constraints. This is not surprising but is a good indication of what result can be expected when the detector is aligned with real data. Also, it can be seen that the layers closer to the Outer Tracker are less well aligned than the others. The OT layers are also less well aligned than in the original scenario, but to a smaller extent. This is a combined effect of the layers being pulled away from the true position by the IT layers, while still being constrained by the fixed layers.
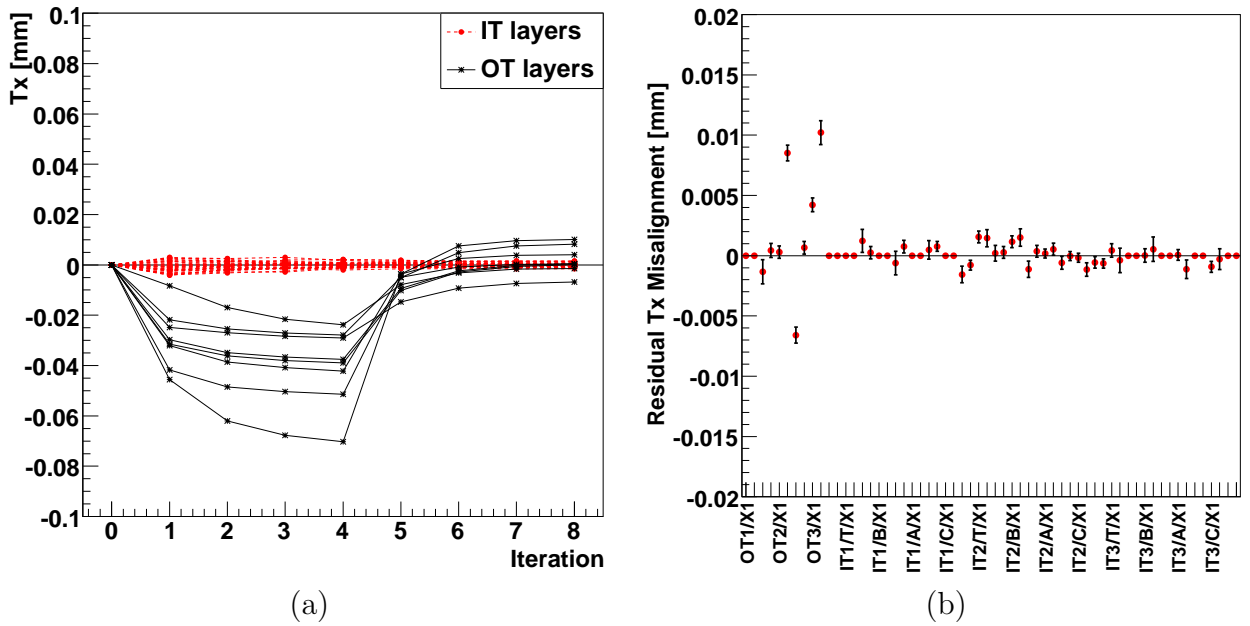
(a)

(b)

Figure 4.13: (a) $Tx$ alignment parameter evolution and (b) residual $Tx$ misalignment for each of the IT and OT layers after alignment (beam–gas scenario, no IT layers constrained).
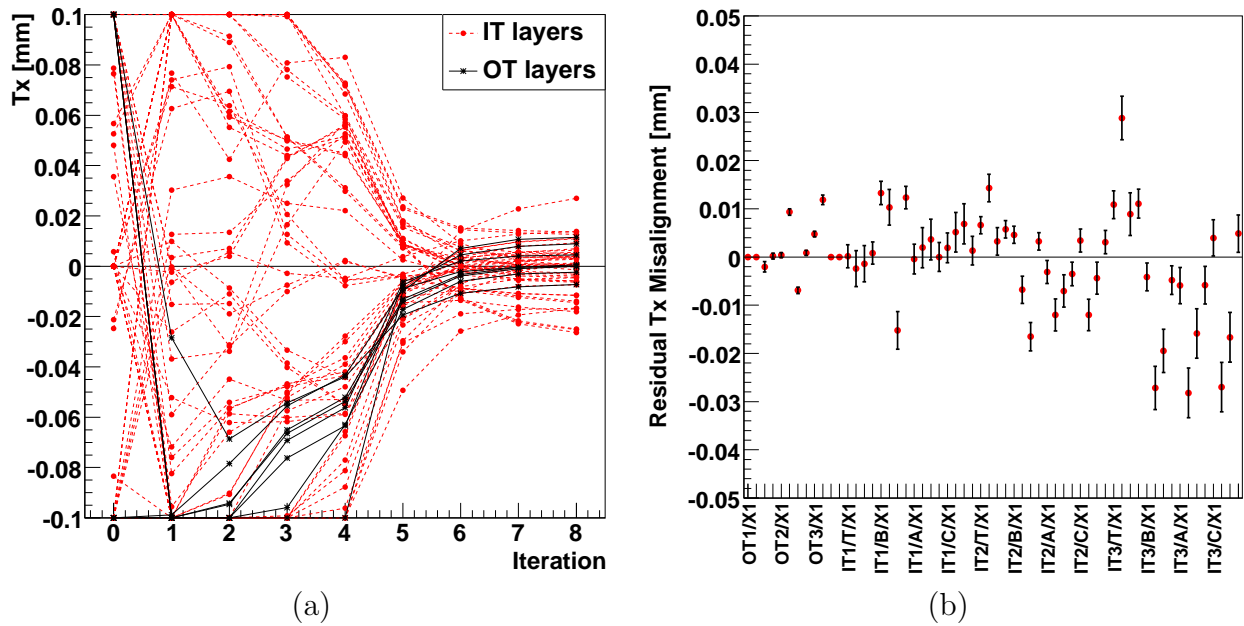


(a)

(b)

Figure 4.14: (a) $Tx$ alignment parameter evolution and (b) residual $Tx$ misalignment for each of the IT and OT layers after alignment (beam–gas scenario, no IT layers constrained, cut on the momentum at $10\,\mathrm{GeV}/c$).
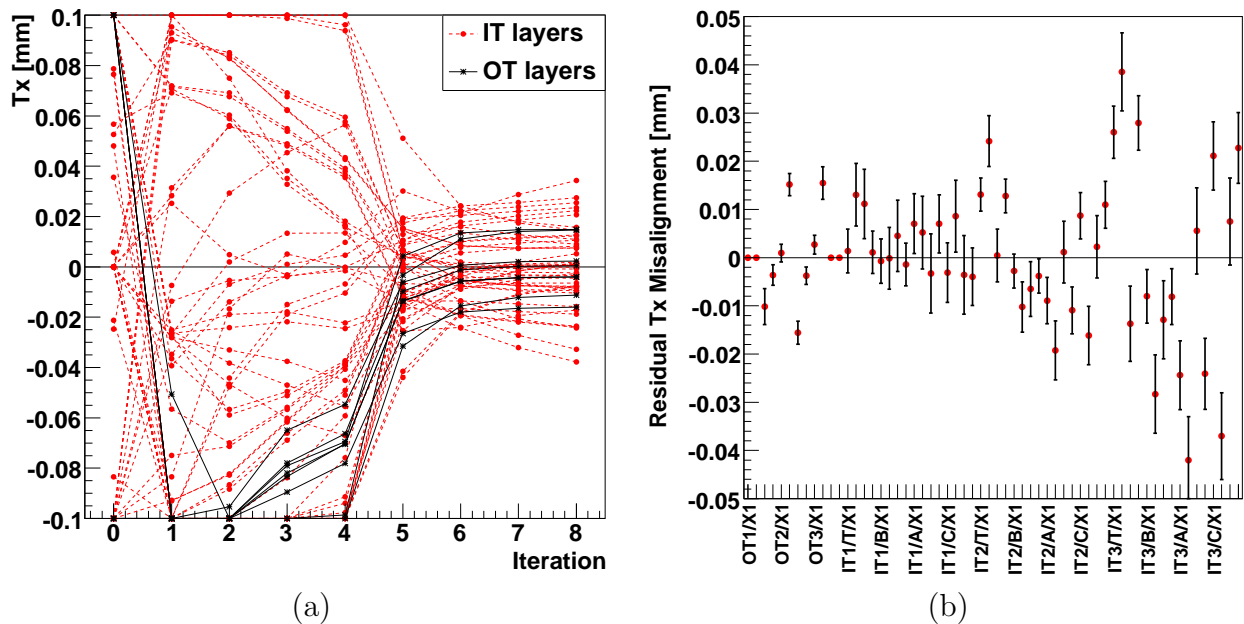
### 4.2.3.f   Summary of the Additional Studies

The following conclusions can be drawn from these studies. The first one is that, as expected, a factor four to five is gained in precision from using the drift-time information. However, care is needed to ensure that this gain is not lost due to poorly resolved L/R signs. It is found that running four iterations without the drift time information is enough to reach a point close enough to the minimum to be a good starting point for the use of the drift-time information.

The second conclusion is that the best way to reject poor-quality tracks is to use the evolving $\chi^2$ cut described before. Not cutting, or cutting at a fixed value gives worse results in terms of precision on the final position of the detector element.

It has also be shown that the lack of knowledge of the track momentum worsens the alignment precision. This can be seen in the bad estimation of the alignment parameters errors. Cutting on the true momentum (taken from the Monte Carlo truth) in order to reject low-momentum tracks reduces the problem. When running the alignment algorithm on magnet-off data, this momentum information can be provided by the calorimeters by linking the track to clusters in this sub-detector. The tracks can also be extrapolated to the muon system, which would allow for a selection of high momentum tracks (since only these reach the muon system). Multiple scattering, which leads to larger track parameter errors, is less of a problem once a momentum estimate can be made.

A demonstration is shown that the alignment procedure is robust against initial misalignment. Starting from a very misaligned detector (OT layers moved by up to $2.5 \, \mathrm{mm}$) or from the ideal geometry leads to the same final position.

Finally, the introduction of more degrees of freedom (releasing the constraints on the IT layers) leads to a slower convergence as well as to a worse alignment precision. Part of the loss in precision is due to correlated movements: this is also reflected in the larger estimated statistical errors.

## 4.2.4   Independent Validation of the Alignment Results

In Section 4.2.2 three methods of checking the alignment procedure convergence are discussed. However, this is not enough to ensure that the results of the alignment job are good enough for physics studies. Indeed, if the procedure converges but the detector elements still show some residual systematics, the physics performance of the detector will be degraded. Therefore, the quality of the alignment obtained is studied by reconstructing $J/\psi$ and $K_S^0$ decays. This method is used as part of this work to validate the alignment method used. Since the true position of the detector elements are not known with real data, this method can also be used in real running conditions to validate the results of the alignment. The results of these studies are described in the next two sections. The statistical uncertainties are small and do not significantly affect the results presented here.

### 4.2.4.a   $J/\psi \rightarrow \mu^+ \mu^-$ Studies

A sample of 65'500 inclusive $J/\psi \rightarrow \mu^+ \mu^-$ events from the 2006 Monte Carlo DST production is refitted using a standard loose $J/\psi$ selection. This selection uses standard loose muons (defined in Section 3.1.5). It requires the reconstructed $J/\psi$ mass to be
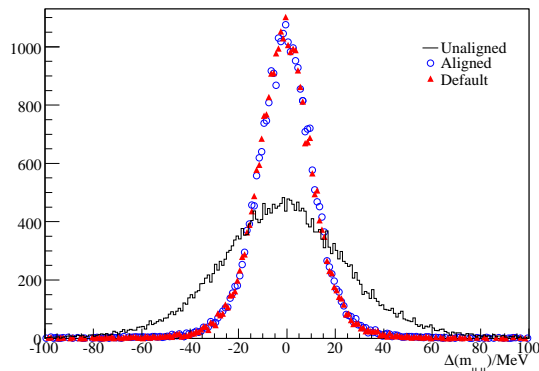
Figure 4.15: Di-muon mass resolution using the unaligned, aligned and ideal geometry (beam–gas scenario). The non-$J/\psi$ background level is insignificant.

within $100 \, \mathrm{MeV}/c^2$ of the true $J/\psi$ mass and cuts on the quality of the vertex fit at $\chi^2_{J/\psi \, \mathrm{vtx}}/\mathrm{dof} < 25$. This reconstruction is run with three different geometry databases:

1. Unaligned (before alignment job);

2. Aligned (after alignment job);

3. Ideal geometry.

To check the validity of the alignment results, the distribution of the di-muon mass resolution $M(\mu\mu)_{\mathrm{rec}} - M(\mu\mu)_{\mathrm{true}}$ (see Fig. 4.15) and of the track $\chi^2/\mathrm{dof}$ (Fig. 4.17) are then compared for the three different cases. The mass bias with respect to the true di-muon mass and the mass resolution are plotted as a function of the $J/\psi$ momentum (see Fig. 4.16). If the alignment is done correctly, then the results for the aligned and the ideal geometry databases should be very similar. Figure 4.15 shows that the shape of the distribution of the di-muon mass is fully recovered after alignment.

At both low and high momenta, the difference in the bias between aligned and ideal geometries (Fig. 4.16 (a)) increases by up to $0.5 \, \mathrm{MeV}/c^2$ [2]. However, the mean of the momentum distribution is at $60 \, \mathrm{GeV}/c$ where the bias is equal for the aligned and ideal geometries. The same plot also shows that most of the effect of the misalignment is removed after the alignment job, especially the rise at large momenta.

This recovery is even more obvious in the mass resolution. At low momentum (between 10 and $60 \, \mathrm{GeV}/c$), the difference between the aligned and ideal geometries is less than $1 \, \%$. This difference increases to $2 \, \%$ for a high $J/\psi$ momentum.

Finally, the distribution of the track $\chi^2/\mathrm{dof}$ also shows the same behaviour with the shape being recovered when aligning the T Stations (see Fig. 4.17).

---

[2] The bias with the ideal geometry is due to a non-optimal energy-loss correction in the track fit and a small bias in the minimisation procedure. Separating the bias due to alignment from other effects will be a challenge with the first data. A way of doing this is to study the profile of the bias as a function of many variables and to see how to disentangle the various effects.

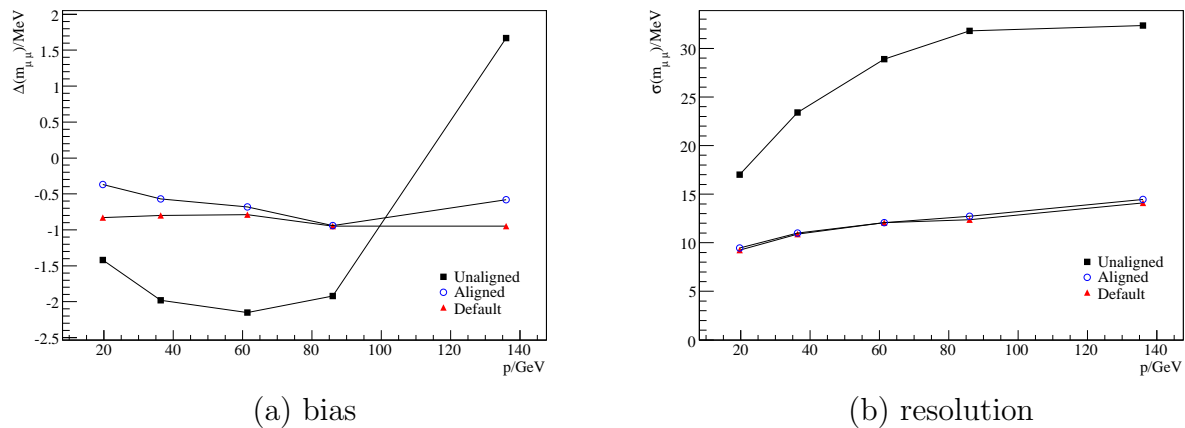(a) bias                                           (b) resolution

Figure 4.16: (a) Di-muon mass bias and (b) di-muon mass resolution as a function of the $J/\psi$ momentum (beam–gas scenario). Statistical error bars are not visible.
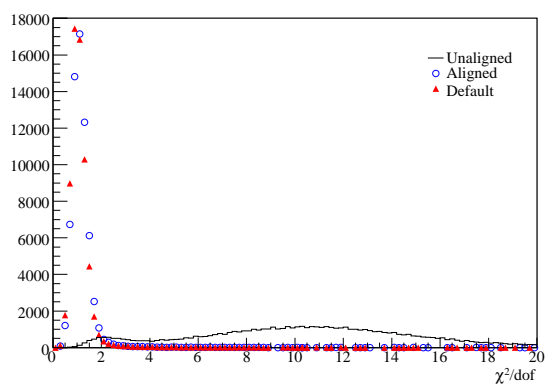


Figure 4.17: Track $\chi^2/\text{dof}$ for tracks in true $J/\psi$ candidates (beam–gas scenario).

Mean = 497.62 +/- 0.07
f = 0.286 +/- 0.006
sigma = 3.57 +/- 0.08

Mean = 497.66 +/- 0.05
f = 0.700 +/- 0.008
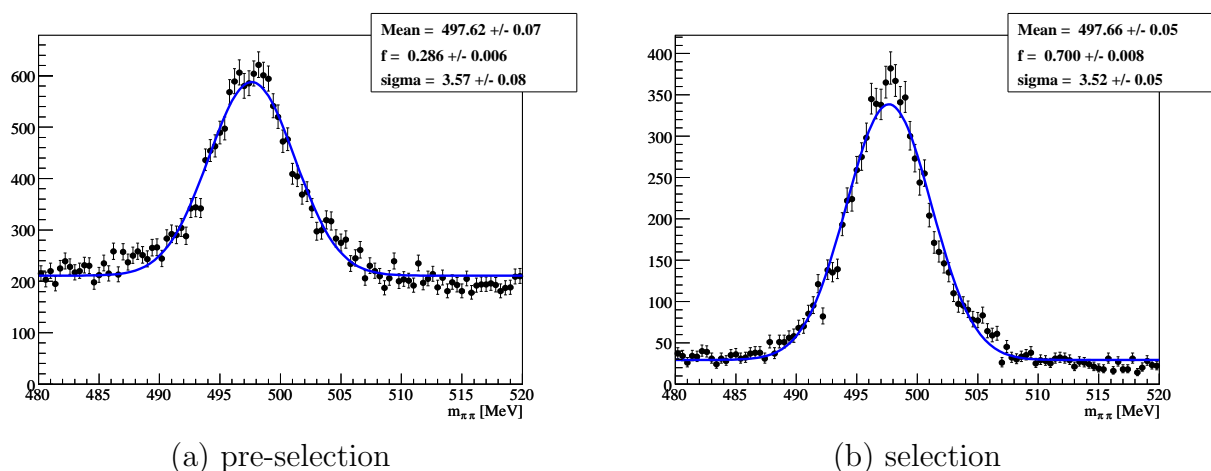sigma = 3.52 +/- 0.05

(a) pre-selection

(b) selection

Figure 4.18: Mass distribution for candidates selected by (a) the loose $K_S^0$ selection and (b) the $K_S^0$ selection described in the text. The result of a fit to a Gaussian plus a linear background component is superimposed.

### 4.2.4.b $K_S^0 \to \pi^+\pi^-$ Studies

The $K_S^0$ mass distribution is studied with a sample of $\sim 100'000$ L0-selected minimum-bias events from the 2006 Monte Carlo production [94]. Candidates are selected using the standard loose selection for $K_S^0$ decays that occur in the VELO. This selection uses the standard loose pions defined in Section 3.1.5. It requires the momentum of the pions to be higher than $2\,\mathrm{GeV}/c$. Furthermore, their impact parameter significance (IPS, as defined in Section 2.2.2.a) is required to be larger than 9 and a cut is set on the track quality at $\chi^2_{\pi\,\mathrm{tr}}/\mathrm{dof} < 20$. The mass of the di-pion is required to be within $50\,\mathrm{MeV}/c^2$ of the true $K_S^0$ mass and the reconstructed $K_S^0$ mass within $35\,\mathrm{MeV}/c^2$ of the true mass. Finally, a cut is set on the quality of the vertex fit at $\chi^2_{K_S^0\,\mathrm{vtx}}/\mathrm{dof} < 30$. To simplify the analysis, events with a single reconstructed primary vertex are considered. Figure 4.18 (a) shows the mass distribution obtained. The $S/B$ ratio is around 0.8. This is increased to 5.9 for a 17 % loss in efficiency by making the additional requirements that the $\chi^2$ of the vertex is less than 20 and that the flight distance between the primary and the $K_S^0$ decay vertex be greater than $5\,\mathrm{cm}$ (Fig. 4.18 (b)).

The shape of the distributions of the bias and resolution, shown in Fig. 4.19, is well recovered (with respect to the ideal geometry database) when aligning the T layers. However, the difference between the ideal geometry and the case before alignment is already very small. This is especially the case for the mass resolution at low momentum (10 % difference at the mean momentum – $\sim 17\,\mathrm{GeV}/c$ – and decreasing for lower momentum values). On the other hand, the distribution of the track $\chi^2/\mathrm{dof}$ (Fig. 4.20) shows a significant improvement after alignment. The overall comparison of these plots to the results shown in Section 4.2.4.a indicates that the validation process with $K_S^0$ is less powerful than the $J/\psi$ case. However, $K_S^0$ mesons are more abundant than $J/\psi$ and hence are more likely to give a day-1 check of the alignment.

(a) bias

(b) resolution

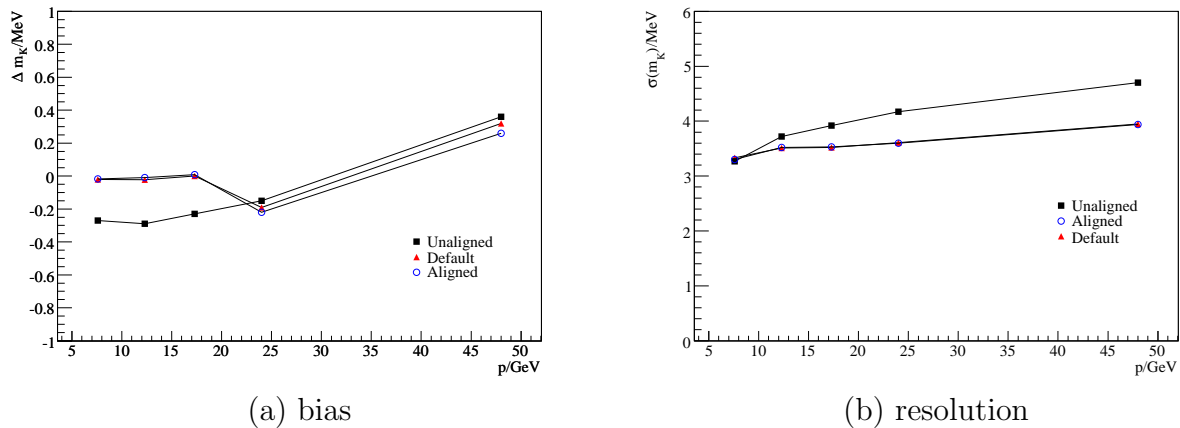Figure 4.19: (a) Bias on the $K_S^0$ mass and (b) $K_S^0$ mass resolution versus $p$ in GeV/$c$ (beam–gas scenario). Statistical error bars are not visible. The points are the results of a fit to the mass distribution shown in Fig. 4.18 (b), including a linear background component at a signal-to-background ratio of 5.9.
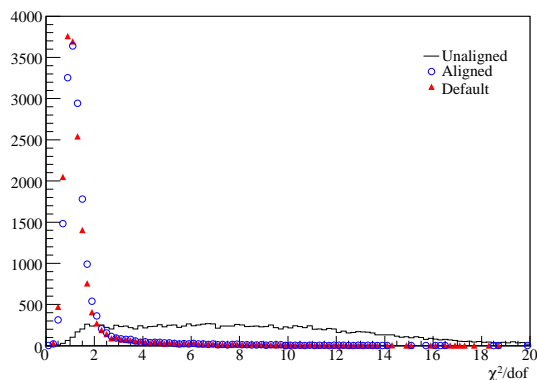


Figure 4.20: Track $\chi^2$/dof for tracks in true $K_S^0$ candidates (beam–gas scenario).

Table 4.8: Summary of the misalignments applied in the magnet-on scenario.

| Detector | | dof | Amplitude |
|---|---|---|---|
| IT | boxes | $Tx$ | 1.0 mm |
| | layers | $Tx$ | 0.1 mm |
| | innermost ladders | $Tx$ | 0.1 mm |
| | other ladders | $Tx$ | 0.05 mm |
| OT layers | | $Tx$ | 1.0 mm |
| | | $Rz$ | 0.15 mrad |

## 4.3  Studies with Magnet On

During the ramping up phase of the LHC beam energy, the VELO will be closed and the magnetic field switched on. Once the LHC startup phase is finished, proton–proton collisions at $\sqrt{s} = 14\,\text{TeV}$ will be the main focus in LHCb. These high-energy collisions will allow the detector to be used to its full extent. Long tracks (i.e. tracks going through the VELO, the Tracker Turicensis and the Tracking Stations) will be reconstructed and used for the alignment. As the VELO has a very precise standalone alignment (partly due to a high number of measurement planes), it can be used as a reference point for the alignment of the Inner and Outer Tracker. The sections below describe the scenario that is studied using long tracks from minimum-bias events produced and reconstructed with the magnet on. A sample of 20'000 minimum-bias events reconstructed with the ideal geometry is used for this analysis. The data is simulated with a centre-of-mass energy of 14 TeV, which is the design energy [3].

### 4.3.1  The Magnet-On Scenario

During the alignment procedure, the tracks are refitted using updated geometrical information from a misaligned database. In the scenario studied, only translations along the $x$ axis (measurement direction) are applied at the level of boxes, layers and ladders individually. The amplitude of these misalignments follows a flat distribution of 1 mm in width for the boxes, $100\,\mu\text{m}$ for the layers and $50\,\mu\text{m}$ for the ladders except for the innermost ones (closer to the beam pipe and hence the most illuminated during a run) which are misaligned with a value of up to $100\,\mu\text{m}$ (this is done to account for a structural effect, the cooling-rod bending, which will be discussed in Section 5.1.6.c). These values are summarised in Table 4.8.

To find an optimal set of alignment parameters, it is preferable to disentangle coherent movements at the IT box and layer level before determining the positions of the individual smallest units (ladders). Therefore, a multi-step approach is used for IT, aligning for detector elements deeper in the geometry tree at each step (see Fig. 4.21). The studies presented here only deal with the OT alignment at the layer level. At first, only the IT boxes are aligned, removing the constraint to the Outer Tracker by requiring tracks with

---

[3] In the early phase, the centre-of-mass energy will be limited to $\sqrt{s} \le 5\,\text{TeV}$.
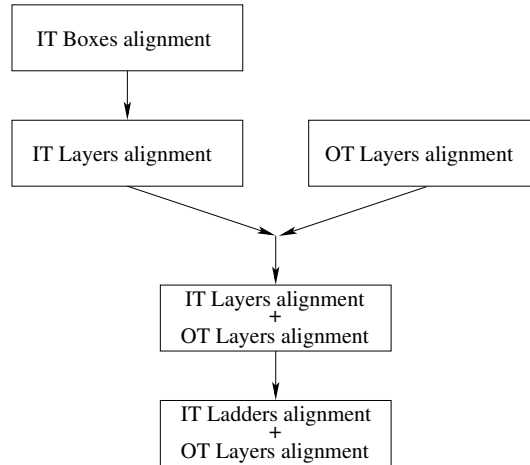
Figure 4.21: Diagram of the multi-step alignment procedure used in the magnet-on scenario.

no OT hits. At the end of this first job, the geometry conditions are written and used in the second job where the IT layers are aligned, requiring again no OT hits on the tracks. In parallel, the OT layers are also aligned, with no constraint to the IT (requiring no IT hits on the tracks). The OT drift-time information is not used in the fit. Once the IT and OT layers are aligned separately, they are again aligned together. This step is used to align the two detectors with respect to each other after their standalone internal alignment. Finally, the IT ladders and OT layers are again aligned together.

In the first step, the IT boxes are aligned for the translations in the plane perpendicular to the beam axis ($Tx$ and $Ty$) and the rotations around the $z$ axis ($Rz$). In the subsequent steps, only $Tx$ and $Rz$ are aligned for, while fixing $Ty$, $Tz$, $Rx$ and $Ry$ (the movements to which the track $\chi^2$ is the least sensible). The VELO is taken as a reference point during the whole procedure. This removes the need to use other external constraints such as those described in Section 3.4.4.

During this procedure, the track selection described in Section 4.1 is used. Especially, the evolving cut on the fit match $\chi^2$ is used.

## 4.3.2 Magnet-On Results

In this section, only the results of the last step of the whole alignment procedure are presented, namely the simultaneous alignment of the IT ladders and OT layers. As already explained in Section 4.2.2, there are several ways of looking at the results of the alignment job. The evolution of the 348 alignment parameters is not presented here because this plot would not be clear.

Figure 4.22 shows the convergence of the average track $\chi^2$/dof. During the iterative process, the number of tracks used for the alignment reduces, due to the cut on the track fit match $\chi^2_m$, from 293'000 down to 284'000 tracks. In this last step of the alignment procedure, three iterations are needed to converge. This is the same number as for the beam–gas studies discussed in Section 4.2.2.

Figures 4.23 (a) and (b) show the difference between the input (as set in the misaligned
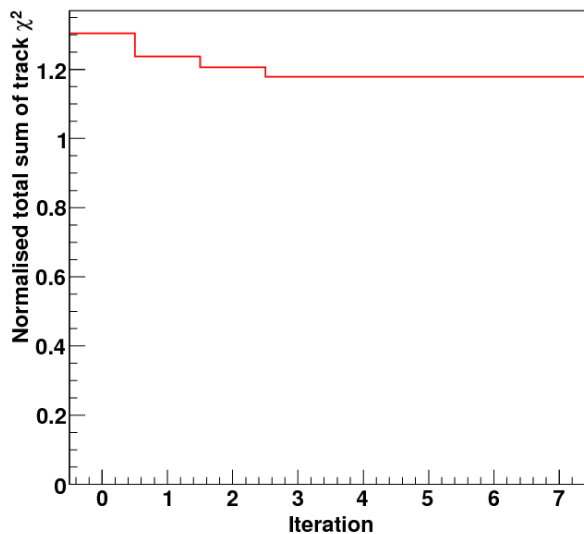
Figure 4.22: Convergence of the average track $\chi^2/\mathrm{dof}$ (magnet-on scenario). The number of tracks is reduced during the iterative process (due to the cut on the $\chi^2_\mathrm{m}$) from 293'000 to 284'000.

conditions) and the output (the result of the alignment job) misalignments for each of the OT layers and IT ladders respectively. Each point on these plots corresponds to one detector element, starting from the first OT layer (Station 1, Layer $X1$) until the last OT layer (Station 3, Layer $X2$), and from the first IT ladder (Station 1, Top Box, Layer $X1$, Ladder 1) until the last IT ladder (Station 3, C-side Box, Layer $X2$, Ladder 7). These plots show that all the detector elements have converged within $100\,\mu$m of the input misalignment, with only a few outliers found outside $\pm\,40\,\mu$m. The OT layers are even more precisely aligned with a residual misalignment within $10\,\mu$m.

It can also be seen in these plots that the alignment errors are correlated. Ladders with a larger displacement have larger errors, which indicates that there are some correlated movements to which the algorithm is not sensitive (for example the $x$ scale).

In order to have a better understanding of the alignment precision, these results can be projected on the vertical axis of Fig. 4.23 (b), leading to the distribution in Fig. 4.24. The RMS of the distribution is $24\,\mu$m, which corresponds to a Gaussian $\sigma$ of $13\,\mu$m, only $20\,\%$ of the IT resolution. The large number of tracks (about 290'000) used for this analysis and the fact that all parts of the detector receive a significant amount of hits means that the statistical error on the result is negligible. The mean of the distribution is shifted by about $10\,\mu$m. This shift is a weak mode related to the fact that no constraint is made on the magnet bending (which is related to the $q/p$ track parameter discussed in Section 3.1). The whole Tracking Stations (actually all sub-detectors situated after the magnet) can be moved sideways without the total sum of track $\chi^2$ being changed. This weak mode can be fixed by using a constraint on the reconstructed $J/\psi$ mass as a function of the di-muon momentum asymmetry $(p^{\mu^+} - p^{\mu^-})$ [135].

(a) OT layers
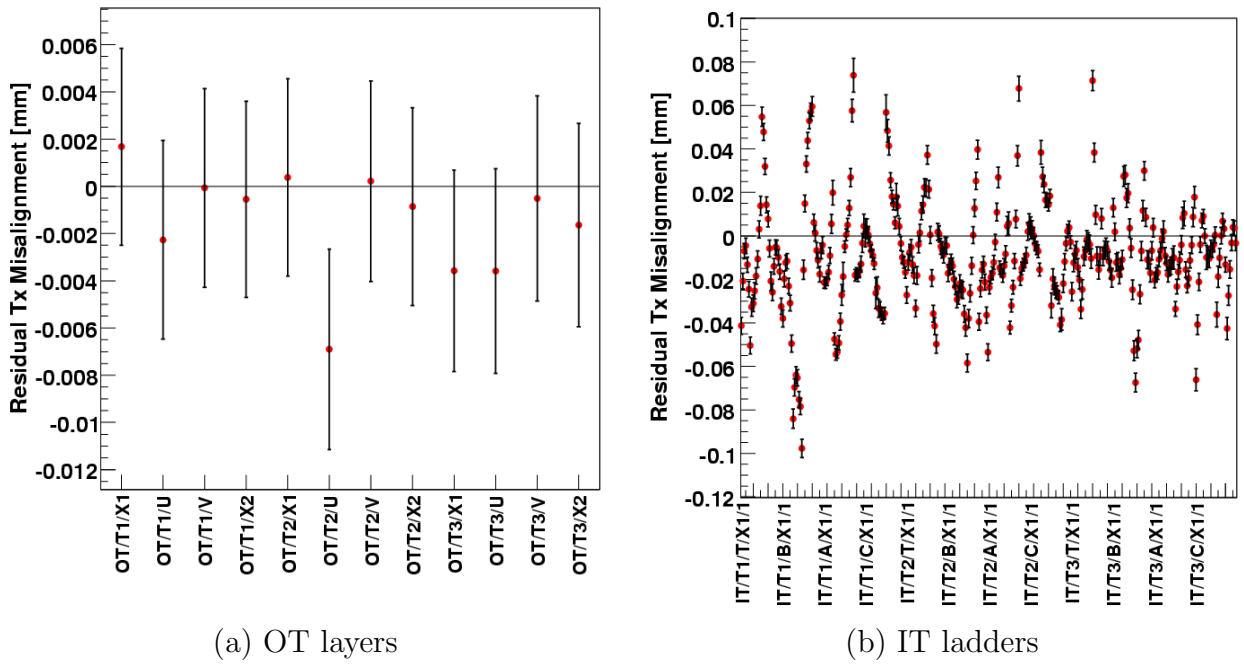


(b) IT ladders

Figure 4.23: Residual $Tx$ misalignment for each of (a) the OT layers and (b) the IT ladders after alignment (magnet-on scenario).
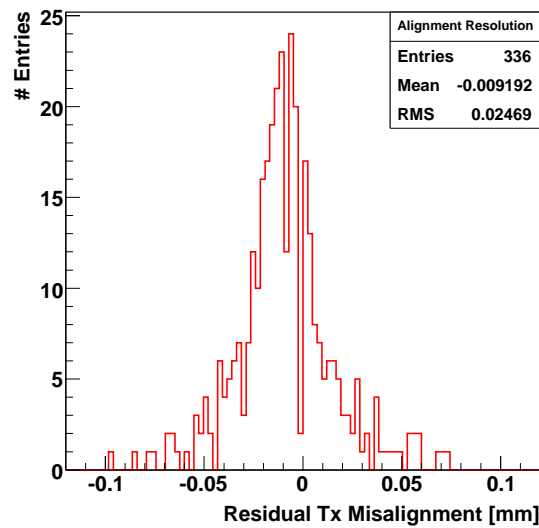


Figure 4.24: Alignment resolution in the $Tx$ direction for all the IT ladders (magnet-on scenario).
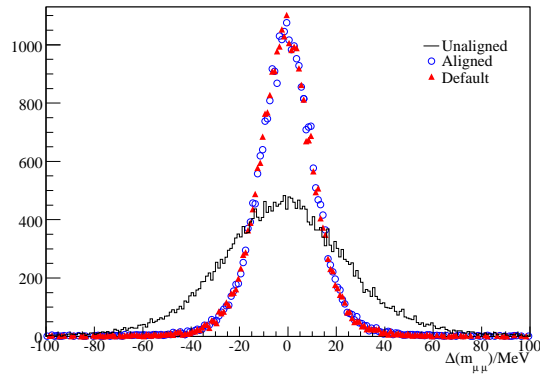
Figure 4.25: Di-muon mass resolution using the unaligned, aligned and ideal geometry (magnet-on scenario).
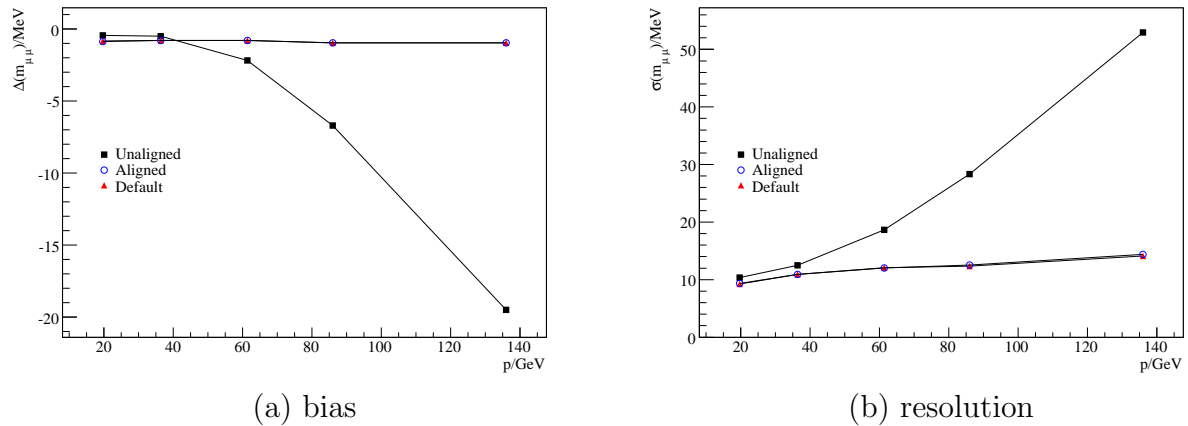


(a) bias

(b) resolution

Figure 4.26: (a) Bias on the $J/\psi$ mass and (b) $J/\psi$ mass resolution versus $p$ [GeV/$c$] (magnet-on scenario).

### 4.3.3   Independent Validation of the Alignment Results

The same method and same data samples described in Section 4.2.4 are used to validate the results of this magnet-on scenario.

#### 4.3.3.a   $J/\psi \rightarrow \mu^+\mu^-$ Studies

The shape of the distribution of the di-muon mass resolution is again well recovered after alignment (see Fig. 4.25). It can be seen that the mass resolution and bias as a function of the $J/\psi$ momentum (see Fig. 4.26) with the aligned database match well the results with the ideal geometry. The difference in resolution is less than 1%, even at high momentum, which is better than in the first scenario studied. On the other hand, the results with the misaligned database is very different, which shows that the alignment procedure is correctly doing its job.
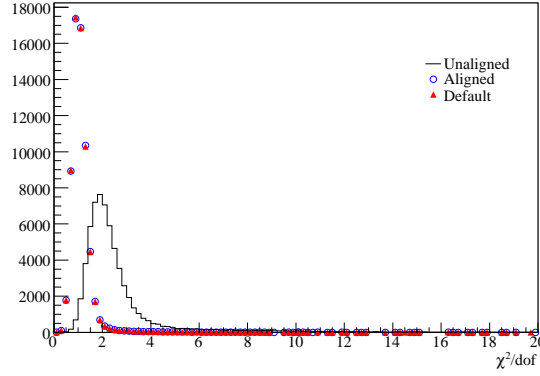
Figure 4.27: Track $\chi^2$/dof for tracks in true $J/\psi$ candidates (magnet-on scenario).
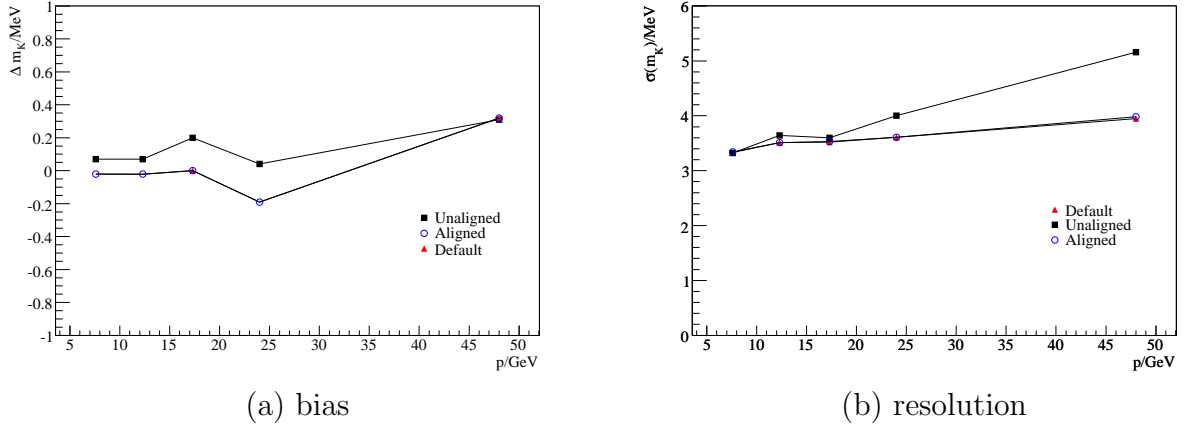


(a) bias                                        (b) resolution

Figure 4.28: (a) Bias on the $K_S^0$ mass and (b) $K_S^0$ mass resolution versus $p$ [GeV/$c$] (magnet-on scenario).

The same conclusion can be drawn for the distribution of the track $\chi^2$/dof (Fig. 4.27) which is fully recovered after the alignment, validating the procedure to a high confidence.

### 4.3.3.b   $K_S^0 \rightarrow \pi^+\pi^-$ Studies

As already seen in Section 4.2.4.b, the results of the validation using the $K_S^0$ sample are less convincing than those using a $J/\psi$ sample. The shape of the profiles and distributions seem to be recovered here as well. But as visible in Fig. 4.28, the difference between the misaligned and aligned geometries is very small (near the mean of the momentum spectrum, around $17\,\text{GeV}/c$, this difference is only $\sim 2\,\%$). Therefore the $K_S^0$ sample will not be as powerful as the $J/\psi$ for the validation of the alignment results. However, a $K_S^0$ peak will be obtained before a significant sample of $J/\psi$ is reconstructed.
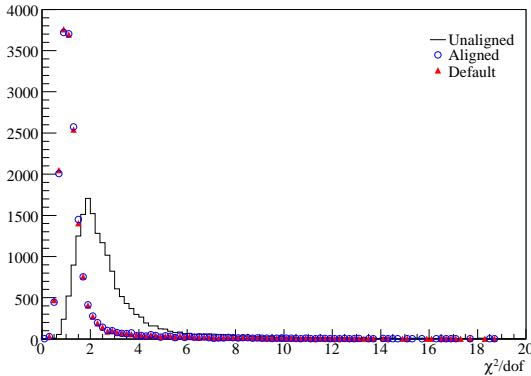
Figure 4.29: Track $\chi^2$/dof for tracks in true $K_S^0$ candidates (magnet-on scenario).

# Chapter 5

# Alignment Studies with Data
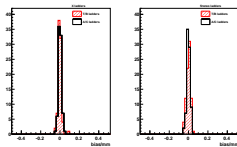
Results of the first Inner-Tracker alignment with real data are discussed in this chapter. The IT is aligned down to the ladder level using data collected during LHC synchronisation tests. The results of this alignment are validated by looking at the distribution of unbiased residual before and after alignment. A sample of data collected with a cosmic trigger is also studied.

$\mathfrak{I}$N the Summer of 2008, synchronisation tests were carried out by the LHC machine. During these tests, shots of $2-5\times10^9$ protons with an energy of $450\,\text{GeV}$ were extracted from the SPS and dumped onto a beam stopper, the 'TED', situated $350\,\text{m}$ downstream of LHCb (as shown in Fig. 5.1). This created a spray of particles which gave a clear signal in the detector. Though the track density is high – more than twenty times that expected in normal running, the tracks have a relatively high momentum and the magnetic field is off. This simplifies the pattern recognition and allows reliable track reconstruction to be performed.

A full Monte Carlo simulation of the TED data is under development. In this FLUKA-based simulation, $10^9$ protons were dumped onto the TED and the products transported through the various elements of the beam line to the entrance of the LHCb cavern. From
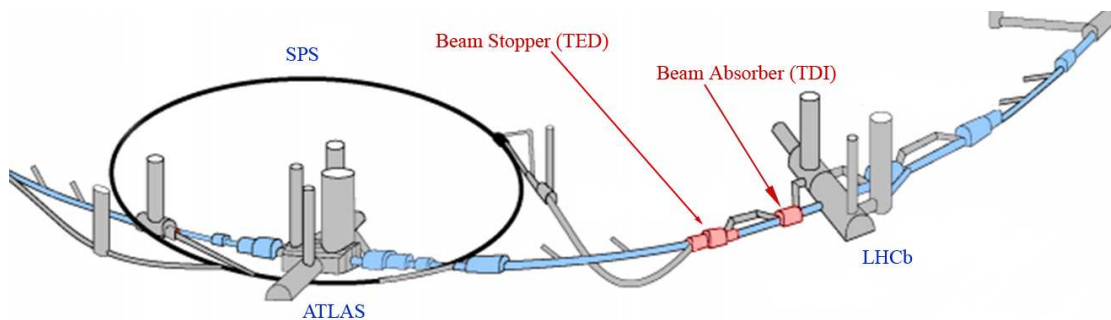


Figure 5.1: Layout of the LHC and SPS rings showing the LHCb experimental area and the TED beam stopper $350\,\text{m}$ downstream.
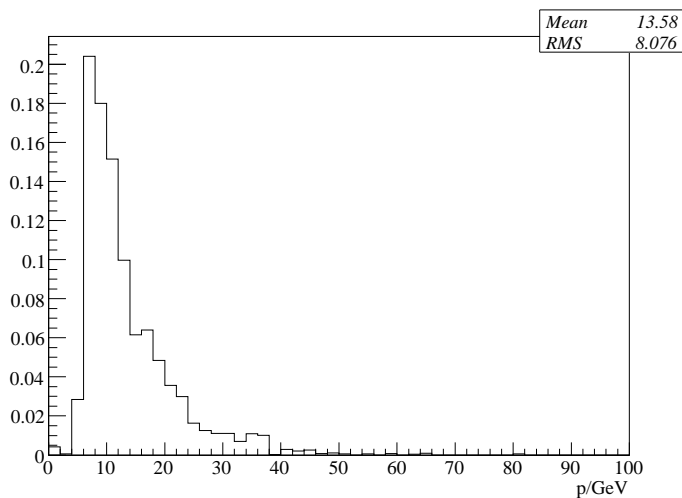
Figure 5.2: Momentum distribution of the muons produced in the TED. This plot shows the result of the full Monte Carlo simulation discussed in the text. The histogram is normalised such that the area is unity.

this point the standard LHCb simulation chain (Boole and Gauss) is used for processing. First results from this simulation indicate that the majority of particles that give hits in the IT are $10\,\text{GeV}$ muons (as shown in Fig. 5.2) decaying from pions produced in the TED.

Alignment with a data sample of events collected with a cosmic trigger is also studied. The low statistics in this case does not allow a precision alignment of the Inner Tracker, but demonstrates that the method can be used with this type of tracks.

This chapter has been published as a public LHCb note [136].

## 5.1   Alignment with TED Run Data

The following sections present studies of the Inner Tracker alignment performed with the TED data. First, the procedure is described. Next, some features of the TED data are discussed using Monte Carlo simulation, followed by a description on the track and event selection. Finally, the results of the alignment are discussed and validated by studying the evolution of the unbiased residuals [1] distributions during the alignment procedure.

### 5.1.1   Procedure

In these studies, each of the four stacks of detector boxes are individually aligned and no account is taken of the fact that $\sim 1\,\%$ of the tracks pass through the overlap region between the side and the Top/Bottom Boxes. This is because the high occupancy and misaligned detector make it difficult to find such tracks.

---

[1] Unbiased residuals are residuals, as discussed in Section 3.1.3.a, calculated by re-fitting the track without taking into account the information from the current hit.

The reconstruction software sequence is shown in Fig. 5.3. After collecting the IT clusters, the ITGenericTracking algorithm described in Ref. [137] is run. Then the tracks are fitted with the standard LHCb track-fitting code [138]. Obvious ghost tracks are removed by applying an evolving cut on the track $\chi^2$ (TrackContainerCleaner). Next, an algorithm that ranks the tracks according to their number of hits and $\chi^2$ is run to remove ghosts and clones and to select the optimal subset of tracks (TrackCompetition). After this sequence is run, the track quality and parameters can be monitored using the standard LHCb monitoring tools. In parallel, the alignment algorithm is run on the selected set of tracks. Finally, the algorithm produces a set of new alignment constants, which are used in the next iteration of the procedure.

As discussed in Chapter 4, a multi-step approach to the alignment is needed for two reasons. First, large overall misalignments in the measurement direction (more than $\sim 100 \, \mu\mathrm{m}$) cannot be recovered at the ladder level. The second reason is that layers and ladders cannot be aligned in the vertical ($y$) direction as they are only weakly sensitive to this parameter. Only global $y$ alignment at the box granularity can be obtained. Furthermore, the available statistics and the small angle of the tracks in the TED run mean that the data is not sensitive to other degrees of freedom, such as movements along the $z$ axis ($Tz$).

Therefore, the following approach is chosen:

1. Alignment of boxes in $Tx$, $Ty$ and $Rz$;

2. Alignment of layers in $Tx$ and $Rz$;

3. Alignment of ladders in $Tx$.

*A priori*, other choices are possible: for example, alignment at the box level, ignoring possible shifts in $y$ or alignment of ladders after boxes, without alignment of the layers. Studies of several of these possibilities were made and found to give identical results in terms of number of reconstructed tracks and unbiased residuals. This shows that the data does not allow to fully determine the best procedure. However, as discussed in Section 5.1.5, it is possible to justify the choice of $Rz$ as an alignment parameter. The above scenario is chosen because it deals with more degrees of freedom and hence seems more complete.

To constrain the global movements, the following objects are fixed during the procedure:

1. For the box alignment, all boxes in Stations 1 and 3 are fixed.

2. For the layer alignment, the two first layers in Station 1 ($X1$ and $U$) and the two last layers in Station 3 ($V$ and $X2$) are fixed.

3. For the ladder alignment, all the ladders from the two first layers in Station 1 ($X1$ and $U$) and from the two last layers in Station 3 ($V$ and $X2$) are fixed.

This leaves a total of three degrees of freedom ($Tx$, $Ty$ and $Rz$) per box type for the box alignment, 16 degrees of freedom ($Tx$ and $Rz$ for each of the eight free layers) per box type for the layer alignment and 56 degrees of freedom ($Tx$ for each of the eight layers $\times$ seven ladders) per box type for the ladder alignment.
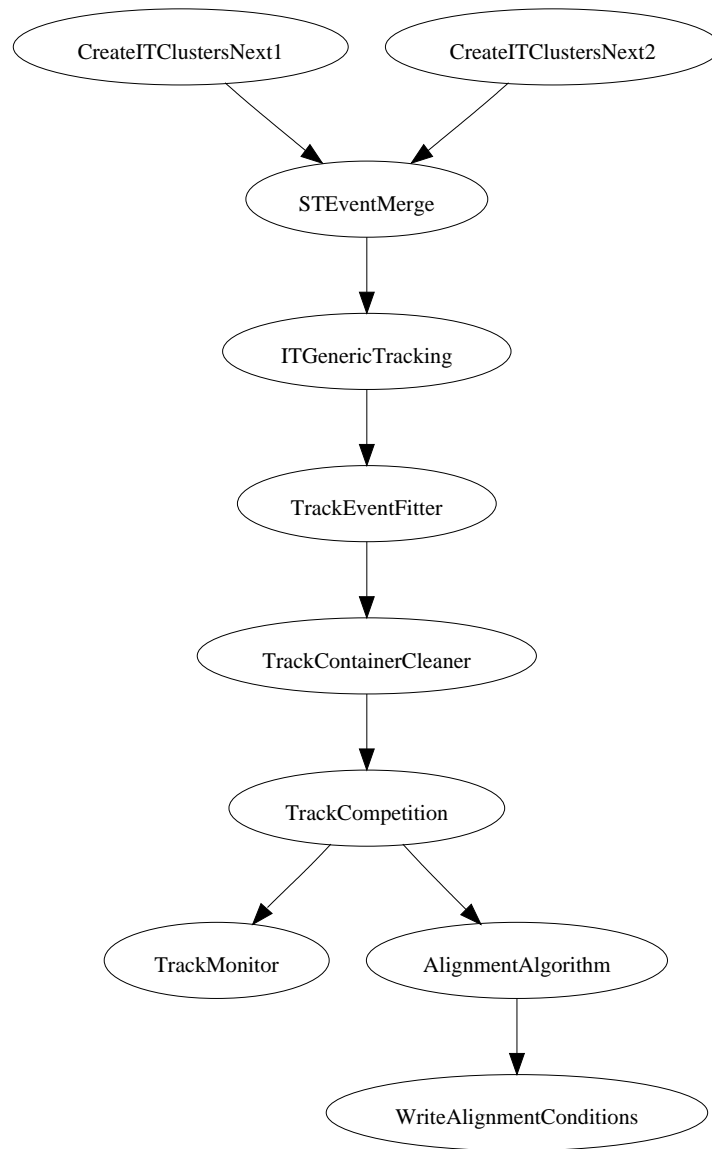
Figure 5.3: Flow diagram of the software procedure used for the tracking-station alignment with TED data.

Table 5.1: Summary of the misalignments applied in the realistic misalignment scenarios used with the Monte Carlo sample of TED-like simulated events. The amplitude is the width of the flat distribution used to generate the misalignments.

| Elements | DoF | Scenario 1 | Scenario 2 |
|---|---|---|---|
| $X$ layers | $Tx$ [mm] | 0.3 | 0.03 |
| Stereo layers | $Tx$ [mm] | 0.3 | 0.3 |
| All layers | $Rz$ [mrad] | 2.5 | 2.5 |
| Ladders | $Tx$ [mm] | 0.1 | 0.1 |

## 5.1.2 Results from Monte Carlo Events Simulating TED Data

This section presents the results obtained with a Monte Carlo simulation of TED-like events (not the complete FLUKA-based simulation). In these studies, a high multiplicity muon gun is used to mimic the TED environment. The track angles and origin are similar to those expected for particles produced in the TED. Particle energies of 5, 10, 20, 40 and 80 GeV are simulated in events with densities in the Inner Tracker between 0.01 and 0.08 particles per cm$^2$.

The performance of the pattern recognition is studied using these data with two misalignment scenarios, which are summarised in Table 5.1. Only the misalignment for the $x$ translation is different for the two scenarios. A flat distribution is used to generate random misalignment values. The amplitude of the $Tx$ distribution is of 300 $\mu$m for the $X$ layers in scenario 1 and for the stereo layers in both scenarios and 30 $\mu$m for the $X$ layers in scenario 2. The layers are also rotated about the $z$ axis by up to 2.5 mrad. Finally, all ladders are misaligned in $Tx$ with an amplitude of up to 100 $\mu$m. The second scenario considered has misalignment scales close to those thought to remain after the pre-alignment studies discussed in Ref. [132]. Figures 5.4 and 5.5 show the ghost rate and efficiency as a function of the detector occupancy. It can be seen that compared to the ideal detector, the ghost rate is significantly increased at high occupancies. However, the efficiency is reduced by only a few percent.

The ghost rate and track reconstruction efficiency in TED data can be extrapolated from the plots in Figs. 5.4 and 5.5, knowing that the detector occupancy is $\sim 4\%$ for the A-/C-side Boxes and $\sim 2\%$ for the Top and Bottom Boxes. The extrapolated numbers for the two misalignment scenarios are given in Table 5.2 for the A-side and the Top Boxes. The tight selection criteria presented in Section 5.1.3 (with a cut at $\chi^2/\text{dof} < 20$) reduce the ghost rate to 1.4 % for the A-side Box and a negligible value for the Top Box, where the occupancy is significantly lower. The reconstruction efficiencies are somewhat low, but the emphasis is on having a high purity track sample.

In Chapter 4, an evolving cut on the track $\chi^2$ is presented and shown to improve the results of the alignment. A similar strategy is used here. The plots in Figs. 5.6 (a) and (b) show the distribution of the track $\chi^2/\text{dof}$ after selection for tracks going through the Top Box running with the realistic misalignment scenario 2 given in Table 5.1 and the ideal geometry respectively. The cut in the first iteration is chosen to be loose: $\chi^2/\text{dof} < 250$ for the box alignment (first step in the procedure) and $\chi^2/\text{dof} < 100$ for the layer and
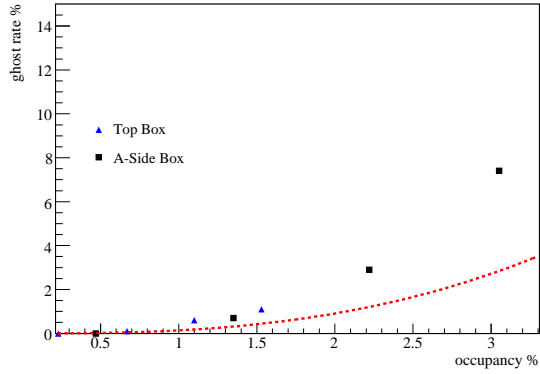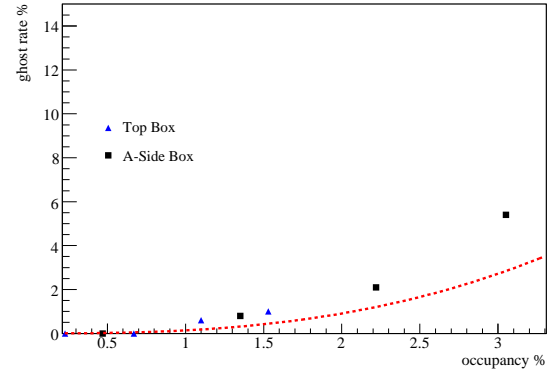
(a) misalignment scenario 1                    (b) misalignment scenario 2

Figure 5.4: Ghost rate in the Monte Carlo simulated TED-like data sample as a function of the IT occupancy for the two misalignment scenarios given in Table 5.1. The points show the ghost rate with a misaligned database, whereas the dotted curve is obtained with an ideal detector. Figures taken from Ref. [137].
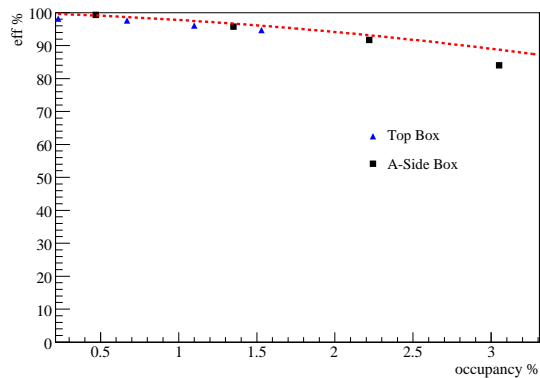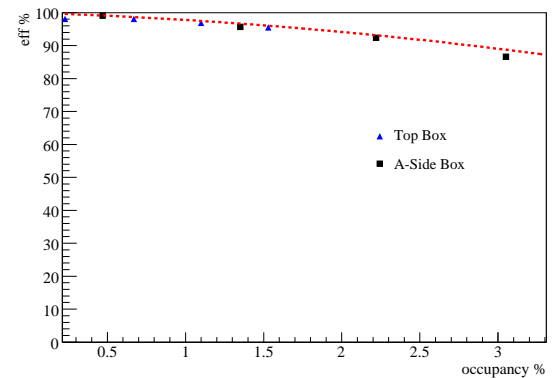


(a) misalignment scenario 1                    (b) misalignment scenario 2

Figure 5.5: Track-reconstruction efficiency in the Monte Carlo simulated TED-like data sample as a function of the IT occupancy for the two misalignment scenarios given in Table 5.1. The points show the efficiency with a misaligned database, whereas the dotted curve is obtained with an ideal detector. Figures taken from Ref. [137].

Table 5.2: Ghost rates and track-reconstruction efficiencies extrapolated from the Monte Carlo simulated TED-like data sample to the detector occupancies in the real TED data, as a function of the misalignment scenario.

| Misalignment scenario | Ghost rate | | Efficiency | |
|---|---|---|---|---|
| | A-side Box | Top Box | A-side Box | Top Box |
| None (ideal detector) | 6 % | 1 % | 82 % | 94 % |
| Scenario 1 | 18 % | 2 % | 73 % | 93 % |
| Scenario 2 ("realistic") | 12 % | 1 % | 78 % | 95 % |
| Tight cuts [137] | 1 % | 0 % | 68 % | 93 % |

Table 5.3: Strategy for the evolving cut on the track $\chi^2/$dof for each step of the alignment procedure.

| Alignment step | Iteration | | | |
|---|---|---|---|---|
| | 1 | 2 | 3 | > 4 |
| Box alignment | 250 | 100 | 50 | 30 |
| Layer alignment | 100 | 80 | 50 | 20 |
| Ladder alignment | 100 | 80 | 50 | 20 |

ladder alignment, when the large misalignments are already corrected for. A reasonable cut value in the last iteration is at $\chi^2/$dof $< 20$. This does not bias the track sample whilst rejecting most of the ghost tracks before the track competition algorithm [2]. The sequence for the cut on the track $\chi^2/$dof is given in Table 5.3.

Finally, the simulation can be used to estimate the width of the unbiased residuals distributions as a function of the track momentum. The results are shown in Fig. 5.7. The resolution is shown separately for $X$ and stereo layers. This is because all twelve layers per box type contribute to the measurement in the $x$ direction, while only the six stereo layers contribute to the measurement in the $y$ direction, leading to the residual being a factor of $\sqrt{2}$ worse. This plot can be used in two different ways. Knowing the momentum, the expected resolution of the unbiased residuals can be derived. Comparison of this number and the resolution obtained with data before alignment allows the residual misalignment to be estimated. On the other hand, if the residual misalignment can be correctly estimated from survey measurements or another method, the resolution found for the unbiased residuals gives an estimate of the average track momentum. Assuming a track momentum of $\sim 10\,\mathrm{GeV}/c$, as given by the first studies with the FLUKA-based simulation discussed in the introduction, a residual ladder misalignment of $\sim 85\,\mu$m is estimated.

---

[2] The cut is applied in the TrackContainerCleaner algorithm.

(a) scenario 2

(b) ideal geometry

Figure 5.6: Distribution of the track $\chi^2/\text{dof}$ after the track selection for tracks going through the Top Boxes. The plot in (a) shows the distribution with the misalignment scenario 2 and (b) with the ideal geometry. The data used is the Monte Carlo sample of TED-like simulated events.
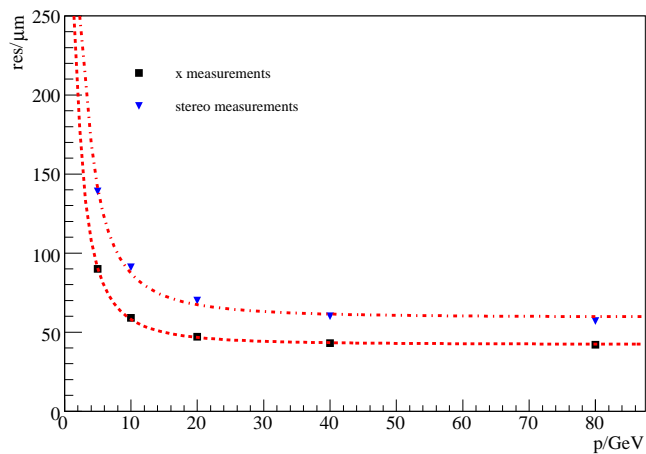


Figure 5.7: Resolution of the unbiased residuals as a function of the average track momentum for Monte Carlo simulated TED-like data. The results are shown for the $X$ and stereo layers separately. Figure taken from Ref. [137].
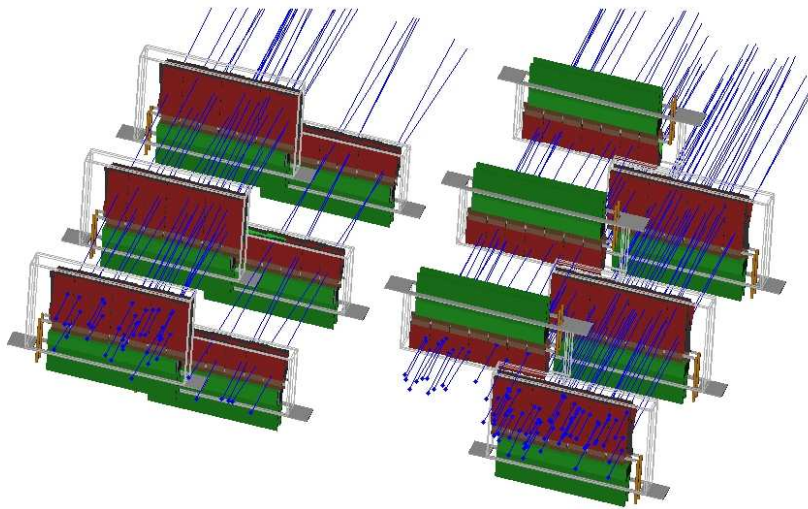
Figure 5.8: Panoramix event display of a typical event from the 2009 TED run where the IT is opened (see Section 5.2). The particles crossing the Inner Tracker are shown in blue. The red areas correspond to the IT active area. The larger boxes are the side boxes.

### 5.1.3 Track and Event Selection

The principal difficulty with the data collected during the synchronisation tests is the high occupancy [137]. Figure 5.8 shows a typical event from the 2009 TED run with the IT in its open position (see Section 5.2). The twelve IT boxes are shown with the active area in red and the particles crossing the detector in blue. The larger red areas correspond to the A- and C-side Boxes. There are twenty times more hits per event than expected in normal LHCb running conditions. For the side boxes where the strips are longest, the track multiplicity is larger than for the Top and Bottom Boxes. This leads to a sizable ghost rate, which degrades the quality of the alignment. To reduce the ghost rate, relatively low occupancy events are used. For the box and layer alignment, the statistics are high enough to align every element with at least 50 hits, even when rejecting the events where the occupancy is too high (more than 4500 clusters in the IT, corresponding to a 3.5 % occupancy). However, for the ladder alignment, where the number of hits per element is much smaller, this requirement is released to 5000 clusters per event in order to align every element with at least 25 hits [3]. With this requirement, the statistical precision is better than $\frac{57\,\mu\mathrm{m}}{\sqrt{25}} \approx 11.4\,\mu\mathrm{m}$ for the ladder alignment. However, releasing the requirement on the maximum number of clusters increases the ghost rate of about 0.4 %, which in turn adds a small systematic error on the resolution.

A second way to reduce the ghost rate is to use tight search windows in the pattern recognition. However, since the detector is misaligned, care is needed that search windows are not set too small. Based on the results presented in Refs. [132, 137], windows of 0.8 mm in the $x$ direction and 10 mm in the $y$ direction are chosen for the first step of the procedure described in Section 5.1.1. Assuming $100\,\mu\mathrm{m}$ misalignments remain for the $x$-measuring

---

[3] At this stage, smaller search windows are used, reducing the ghost rate and allowing the requirement on the maximum number of hits to be relaxed.
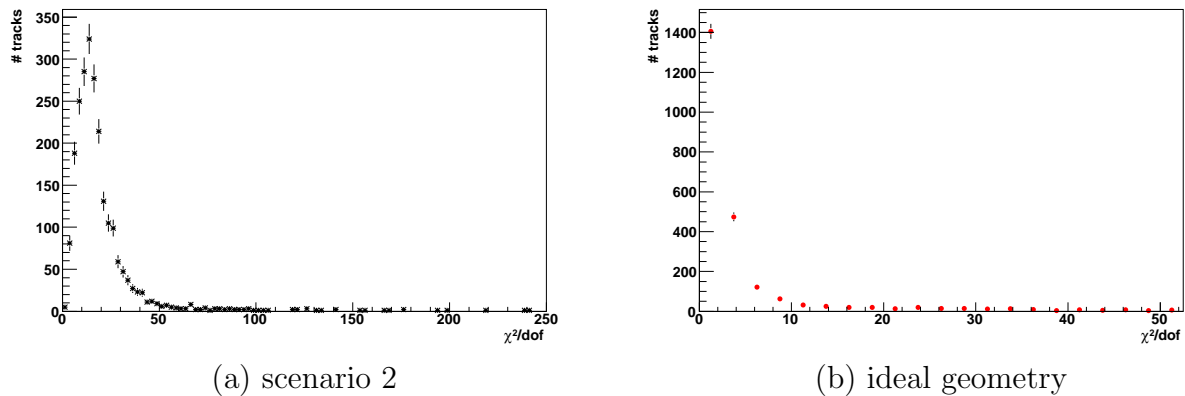
(a) before alignment
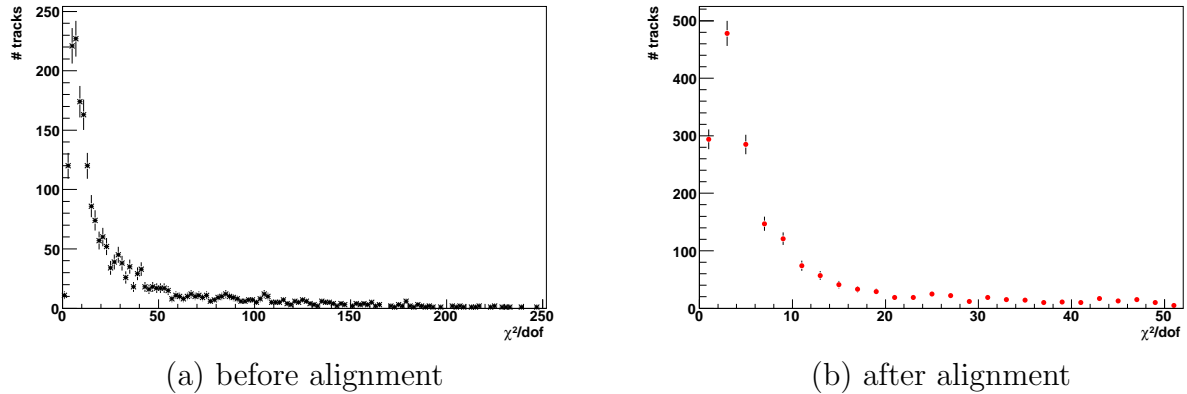


(b) after alignment

Figure 5.9: Distribution of track $\chi^2$/dof after the track selection for tracks going through the Top Box. The distributions are shown (a) before and (b) after the alignment procedure.

ladders and $200\,\mu$m for the stereo ladders, these cuts correspond to 4 or $5\,\sigma$ windows.

As discussed in Ref. [137], the pattern recognition performance can be improved once the detector is aligned by reducing the size of the search windows in the pattern recognition. After the box alignment in $y$, the $y$ search-window is tightened from $10\,$mm to $7\,$mm for the subsequent steps. Similarly, the window in $x$ is tightened from $0.8\,$mm to $0.5\,$mm after the box alignment.

Finally, the evolving cut on the track $\chi^2$/dof described in Section 5.1.2 is used. The value of the cut at each iteration is given in Table 5.3. Figure 5.9 shows the same distributions as in Fig. 5.6 with the real data. The plot on the left shows the distribution before alignment and on the right after the complete alignment procedure described in Section 5.1.1. The distribution obtained with the misalignment scenario 2 in Fig. 5.6 corresponds to the distribution before alignment in Fig. 5.9, whereas the distribution with the ideal geometry in Fig. 5.6 should match the distribution after alignment in Fig. 5.9 in case of a perfect alignment. As visible in the latter, the distribution is a broader than in the case of an ideal alignment. This effect can be related to the ghost tracks in the sample used.

## 5.1.4   First Alignment of the Inner Tracker in $x$

The following two sections present the results of a first alignment of the Inner Tracker boxes and layers for the most obvious degree of freedom, the translation along the horizontal $x$ axis.

### 5.1.4.a   Alignment of Boxes in $x$

The software alignment of the IT is performed for the boxes in Station 2 only in the measurement direction $(Tx)$. The geometry used as a starting point is the survey geometry described in Ref. [131]. The results of the alignment for the A- and C-side Boxes are reported in Fig. 5.10 (a), whereas the results of the Top/Bottom-Box alignment are

(a) survey geometry     (b) best pre-aligned geometry
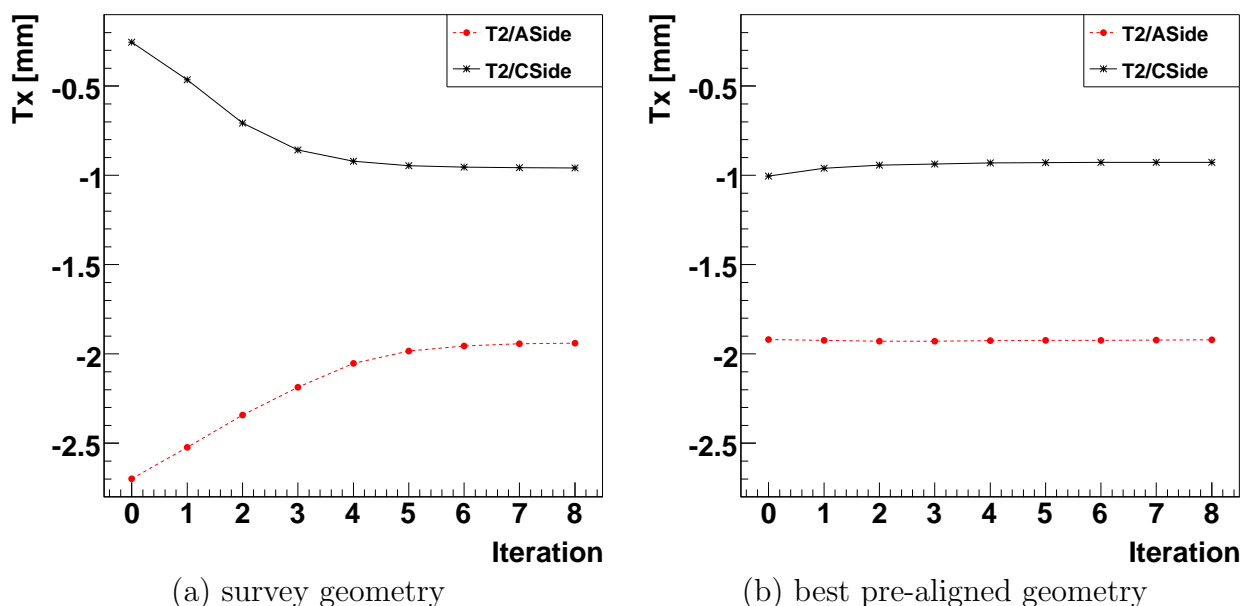
Figure 5.10: Evolution of the $Tx$ alignment constant during A- and C-side-Box alignment, (a) starting from the surveyed geometry and (b) starting from the geometry given by the method described in Ref. [132].

reported in Fig. 5.11 (a). The first observation is that the two alignment jobs converge, although it takes five iterations to the procedure to find the optimal position of the boxes. This relatively slow convergence is due to the large misalignments compared to the size of the search windows in the pattern recognition. Except for the Bottom Box, which moves by $100\,\mu$m, the three other boxes move by 7–800 $\mu$m.

In order to check the validity of these results, the alignment procedure is then run starting from another database, the output of the pre-alignment discussed in Ref. [132]. The results of the alignment of the A- and C-side Boxes can be seen in Fig. 5.10 (b), whereas the results of the Top/Bottom-Box alignment is reported in Fig. 5.11 (b).

From these two sets of plots, it can be seen that the alignment procedure converges within 60 $\mu$m to the same position. That is to say, whatever the assumed initial position of the detector, the alignment moves it to the same point (last points from plots (a) and (b) in Figs. 5.10 and 5.11). It can be seen that the alignment described in Ref. [132] is consistent within 100 $\mu$m with the alignment parameters determined with the software alignment, if a movement in $x$ only is assumed. However, this alignment scenario is simplistic and doesn't take other degrees of freedom into account. Section 5.1.5 discusses the alignment of the detector elements for the rotation around the $z$ axis and shows that it needs to be accounted for. Furthermore, the translation along the vertical axis is also important, as shown in Section 5.1.6.a. However, this first simple study shows that, although it is not necessary in the alignment procedure, the results from Ref. [132] are a better starting point than the survey measurements.

(a) survey geometry

(b) best pre-aligned geometry
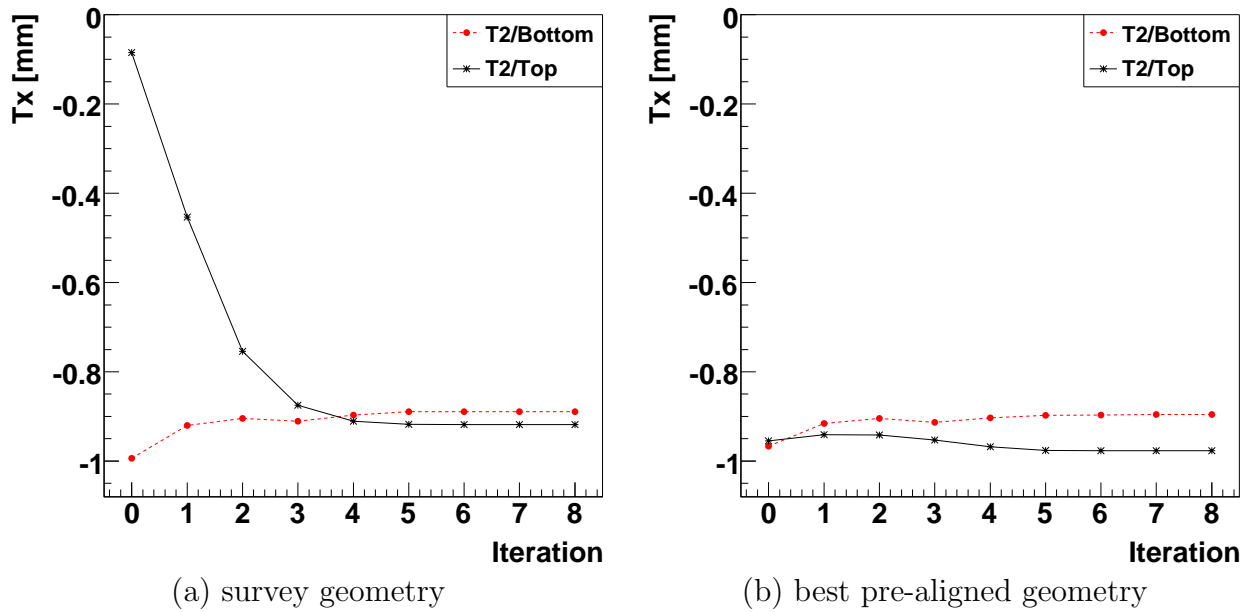
Figure 5.11: Evolution of the $Tx$ alignment constant during Top- and Bottom-Box alignment. (a) shows the alignment starting from the surveyed geometry and (b) starting from the geometry given by the method described in Ref. [132].

### 5.1.4.b   Alignment of Layers in $x$

Another consistency check is possible between these results and the geometry database based on the results given in Ref. [132]. In the first alignment studies performed using the software method (which are not reported in this document), movements of several hundreds of microns were seen for some stereo layers, but not for the corresponding $X$ layers. As those layers are mounted on the same cooling rod, they should move together. It was found that these apparent movements were due to wrong pre-alignment values for the pairs of $X$ and stereo layers. After correcting these mistakes, the expected correlation between the movements of the $X$ and stereo layers is seen. The precision of this assumption can be tested using the data itself. Figure 5.12 shows the correlation between the total corrections for the translation in $x$ applied to an $X$ layer and to its corresponding stereo layer [4]. The distribution of the difference between the two corresponding corrections has an RMS of $\sim 130 \, \mu$m. This should be compared to the mean and RMS of the layer survey corrections in $x$ of 400 and 285 $\mu$m respectively.

### 5.1.5   Justification of the Alignment in $Rz$

The alignment of the Inner Tracker detector elements for translations in the $x$ direction is natural since this is the most sensitive degree of freedom. Aligning the boxes for the translations in $y$ is also easy to justify through the combination of $X$ and stereo layers. Apart from these two degrees of freedom, the detector is also sensitive to the rotation $Rz$

---

[4] This information is available for both the $X$ and the stereo layers because 3D tracks are used to align the detector.
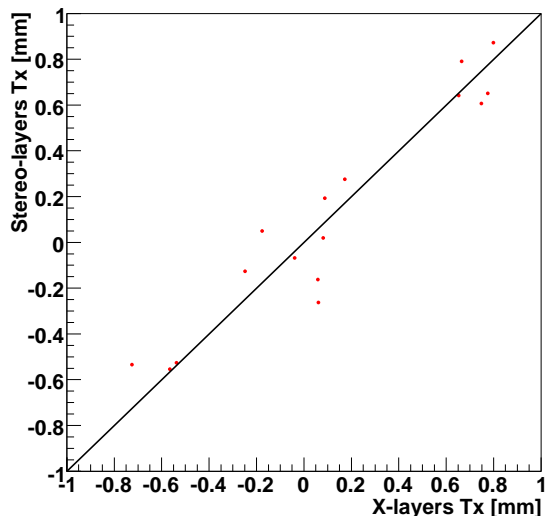
Figure 5.12: Correlation between the total $Tx$ corrections applied to the stereo layers and to their corresponding $X$ layers. The values plotted are after alignment of the layers in $Tx$. Only the layers being aligned are shown.

around the $z$ axis, which is coupled to the measurement in the $x$ and $y$ directions, since a rotation of a box around its $z$ axis can be transformed into a gradient in the $y$ direction of translations along the $x$ axis. That is to say that if the box is sliced along the $y$ axis and only the alignment in $Tx$ is considered, each slice should have different corrections.

In order to further justify the choice of the $Rz$ parameter in the alignment procedure, the following analysis is performed. Four $3\,\mathrm{cm}$ slices are defined in the Top and Bottom Boxes, with the centres along the $y$ axis being at $\pm10.5\,\mathrm{cm}$, $\pm13.5\,\mathrm{cm}$, $\pm16.5\,\mathrm{cm}$ and $\pm19.5\,\mathrm{cm}$ from the beam axis. As the illumination of the boxes is uniform, the same number of hits is seen in each slice, hence leading to the same statistical error. The alignment procedure is then run, aligning these slices for $Tx$ only. The two plots in Fig. 5.13 show that each slice needs a different correction, with a linear shape. This is expected in case the boxes are rotated around their $z$ axis. The same method is used on the A- and C-side Boxes and gives similar results. This justifies the alignment for $Rz$ as well as $Tx$ for the boxes and layers, as discussed in Sections 5.1.6.a and 5.1.6.b. The other degrees of freedom (translation along the beam axis and rotations around the $x$ and $y$ axes) are harder to align for because the Inner Tracker geometry implies a smaller sensitivity to these.

## 5.1.6 Alignment Results

### 5.1.6.a Box Alignment

The first step of the full alignment procedure is to align the boxes in Station 2, with the constraint that the boxes in Stations 1 and 3 are fixed. From Ref. [132], the box alignment in $x$ is known to be precise within $100\,\mu\mathrm{m}$. However, this doesn't take into
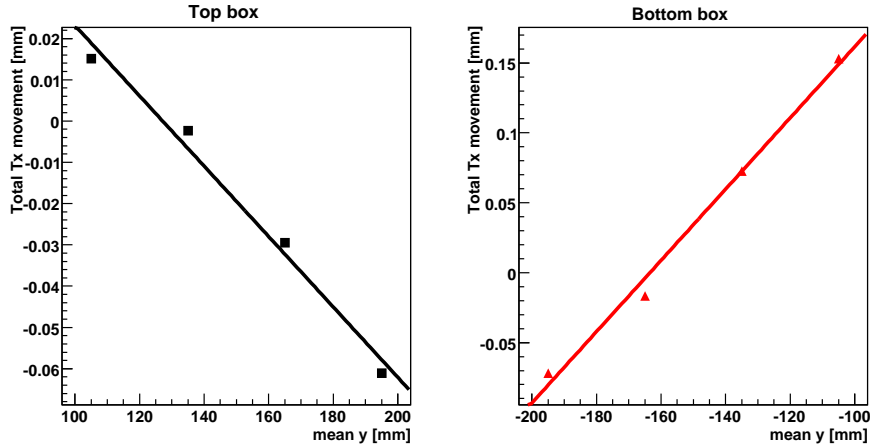
Figure 5.13: Corrections needed in the $x$ direction for slices in $y$ of the Top and Bottom Boxes in case only $Tx$ is aligned for in the procedure.

account rotations, especially around the beam axis, which are correlated to the movements in the $x$ measurement-direction, as discussed in the previous section. A proper software alignment of the Inner Tracker boxes is hence performed using the method discussed in Section 3.4, starting from the output of the alignment described in Ref. [132]. The procedure used is described in Section 5.1.1. Figures 5.14 (a) and (b) show the evolution of the alignment parameters of the A- and C-side Boxes, respectively the Top and Bottom Boxes.

The side boxes move in $x$ by 7 and $45\,\mu$m respectively, which is inside the precision of $100\,\mu$m quoted in Ref. [132]. On the other hand, the Top and Bottom Boxes move by 125 and $423\,\mu$m respectively. Both these movements are correlated to large rotations around the beam axis. These rotations could explain the discrepancy between the results quoted in Ref. [132] and the survey measurements given in Ref. [131].

The movement in the $y$ direction of the Top and Bottom Boxes is 2.1 and $3.0\,$mm respectively. The A- and C-side Boxes move by 1.6 and $0.5\,$mm. As discussed in Section 3.3.2 the survey was carried out with part of the detector in the open position. One explanation for these large movements is that the detector position changed during the closing of the other Inner Tracker and Outer Tracker half-stations.

The first method to check whether the alignment has converged properly is to look at the normalised total sum of track $\chi^2$/dof. Figures 5.15 (a) and (b) show that the alignment procedure has converged in four iterations both for the side boxes and for the Top and Bottom Boxes. The steps in these plots are due both to the convergence of the alignment procedure (which minimises the total sum of track $\chi^2$), and to the evolving cut on the track $\chi^2$/dof described in Section 5.1.3. The value of the track $\chi^2$/dof after alignment of 10 and 12 for the A-/C-side and Top/Bottom boxes respectively seems surprising at first. However, this large value can be explained. First, due to the large occupancy, two close-by clusters can be merged in one 3–4 strip cluster. This degrades the track $\chi^2$. Next, after these studies have been performed, it was realised that the track fit assumed the track had five degrees of freedom ($x$, $y$, $tx$, $ty$, $q/p$). Correcting this to four for the case of

(a) A- and C-side box alignment

(b) Top and Bottom box alignment

Figure 5.14: Evolution of the $Tx$, $Ty$ and $Rz$ alignment parameters during the box alignment for (a) A- and C-side Boxes and (b) Top and Bottom Boxes.

the magnet-off running improves the $\chi^2/\text{dof}$ distribution by $\sim 10\,\%$. Finally, the multiple scattering is not taken into account in the track fit, which adds a third effect.

### 5.1.6.b   Layer Alignment

The results of the alignment of the layers in the A- and C-side Boxes and in the Top and Bottom Boxes are shown in Figs. 5.16 (a) and (b) respectively. The studies described in Ref. [132] showed that the $X$ layers were aligned with a precision of $\sim 30\,\mu$m. The top two plots show that apart from two layers in the Top Boxes (Station 3 / Top Box / Layer $X1$ and Layer $U$) and two in the C-side Boxes (Station 1 / C-side Box / Layer $V$ and Station 3 / C-side Box / Layer $U$) that move by up to $190\,\mu$m, all the other layers move inside a $60\,\mu$m window around their initial position (corresponding to the result of the first alignment described in Ref. [132] plus the corrections to the boxes in Station 2 applied in the first step of the alignment procedure). The large movements of the four layers found above is justified by the fact that the constraints in the box alignment and in the layer alignment are not the same. In the first step, all layers in Stations 1 and 3 are fixed, while in the second step, the first two layers in Station 1 and the last two layers in Station 3 are fixed. This difference causes some global adjustments in the layer alignment step, to which the outer layers are more sensitive (especially since they were not aligned with their corresponding boxes in the first step). In addition, the stereo layers were not aligned in the procedure described in Ref. [132] and the $Rz$ rotation not taken into account. These effects explain the discrepancy between the average movements found with the two different methods discussed.

Figures 5.17 shows that the alignment has converged in four iterations. As for the boxes, this slow convergence is partly due to the evolving cut on the track $\chi^2$. Small

(a) A- and C-side box alignment
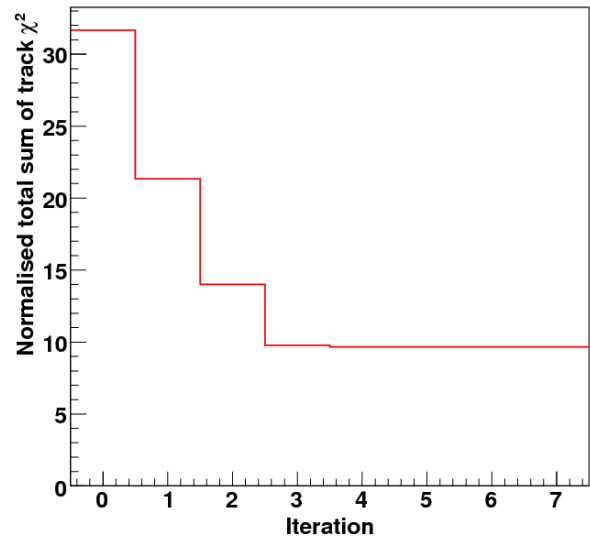
(b) Top and Bottom box alignment

Figure 5.15: Convergence of the normalised total sum of track $\chi^2$/dof during box alignment in $Tx$, $Ty$ and $Rz$ for (a) A- and C-side Boxes and (b) Top and Bottom Boxes.
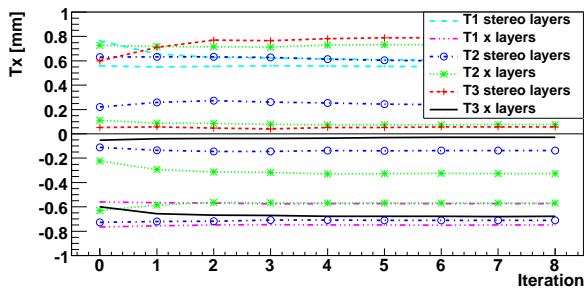


(a) A- and C-side layer alignment
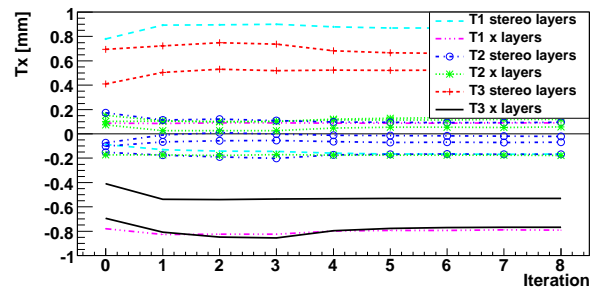
(b) Top and Bottom layer alignment
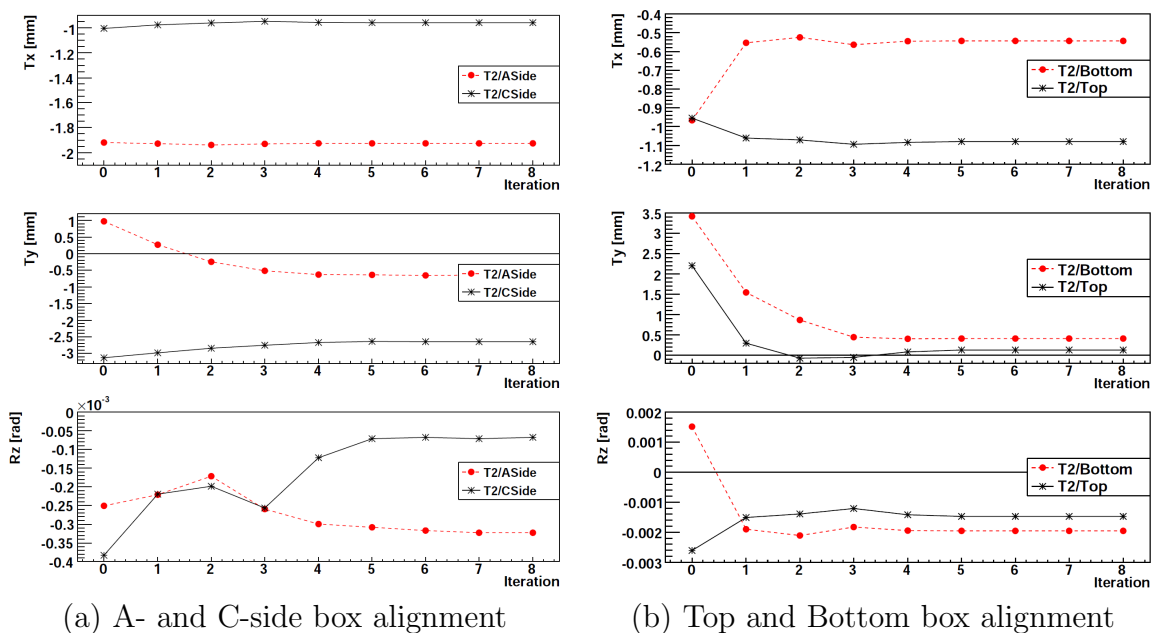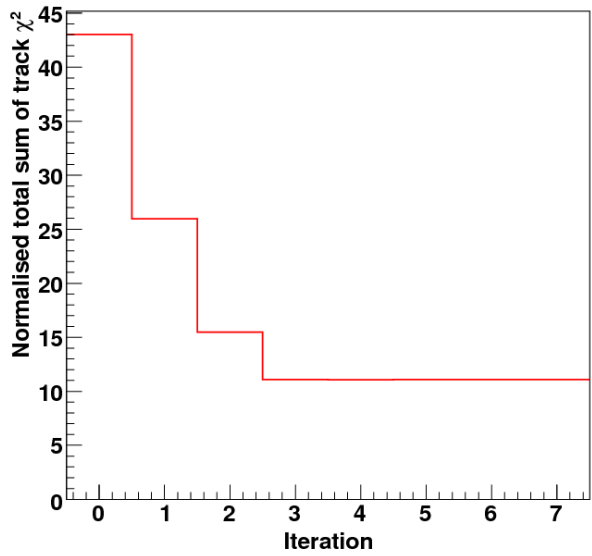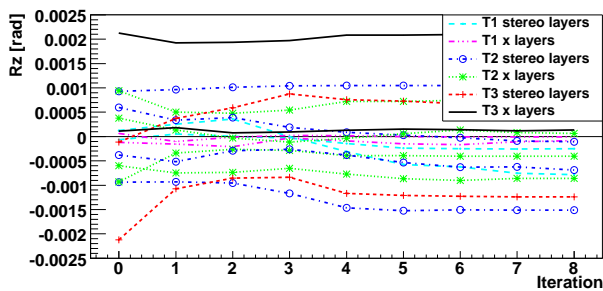
Figure 5.16: Evolution of the $Tx$ and $Rz$ alignment parameters during layer alignment for (a) A- and C-side layers and (b) Top and Bottom layers.

(a) A- and C-side layer alignment

(b) Top and Bottom layer alignment
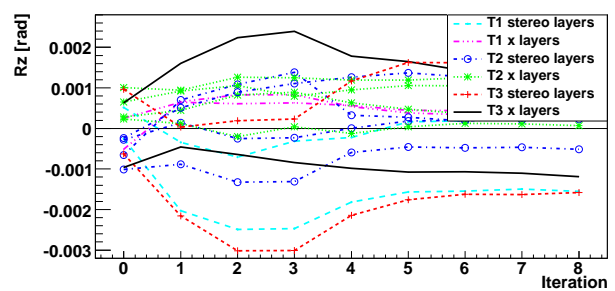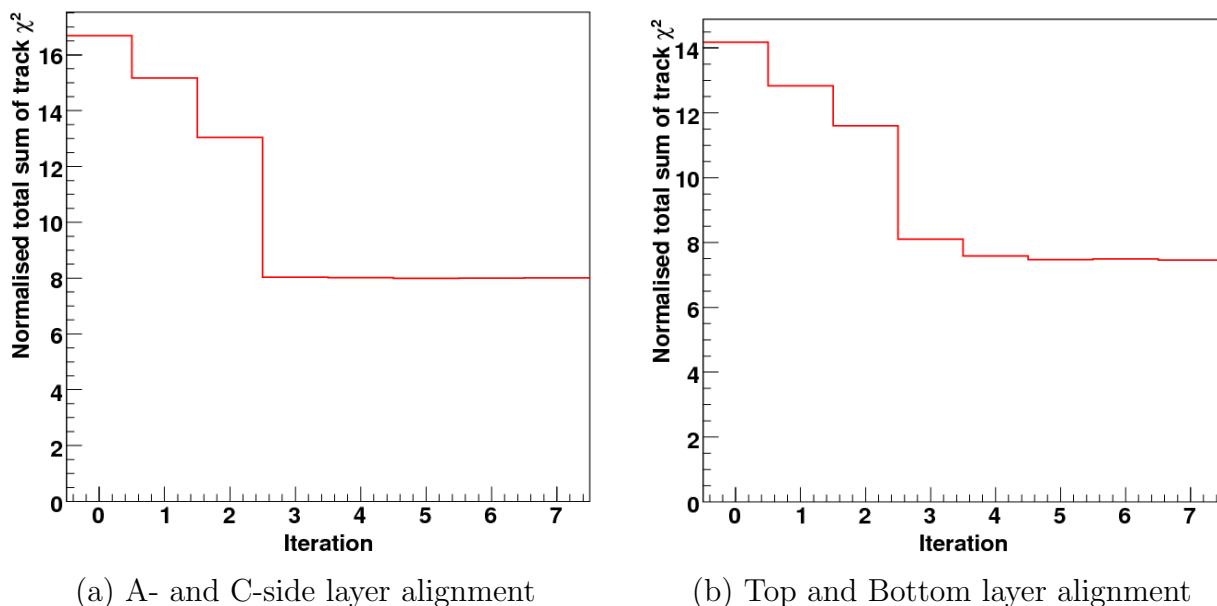
Figure 5.17: Convergence of the normalised total sum of track $\chi^2$/dof during layer alignment in $Tx$ and $Rz$ for (a) A- and C-side layers and (b) Top and Bottom layers.

oscillations in iterations five to seven are visible for the Top/Bottom Boxes. They are due to tracks being picked up and dropped between two subsequent iterations. A slight movement of the detector after one alignment iteration changes the output of the track finding. Since the track sample is different, the result of the alignment algorithm differs, moving again the detector.

### 5.1.6.c   Ladder Alignment

The next step is to align the ladders. Care needs to be taken to check that movements of all the elements are mechanically allowed. As discussed before, two layers of the Inner Tracker are mounted along an aluminium cooling rod. This pipe enters through a side wall of the box, crosses the box and is bent before the opposite wall such that it runs back across the box and exits it on the same side it entered [139]. A picture of this can be seen in Fig. 5.18. Care was taken to mount the ladders on a perfect plane along the rods. However, it was noticed during the survey that some ladders were misaligned due to the bending. Reference [131] quotes that the position of some ladders near the cooling-rod bending have been corrected by up to $300\,\mu$m. This is taken as an estimate of the maximum allowed movement for the ladders relative to the surveyed position.

Showing the evolution of the alignment parameters for all ladders is not meaningful because of the large number of elements. A better way to show the result is to histogram the total movement in the $Tx$ direction for all the ladders in the A-/C-side Boxes and in the Top/Bottom Boxes, as shown in Figs. 5.19 (a) and (b) respectively. Since fitting a Gaussian to these histograms is not satisfactory, the RMS of the distributions is quoted. For the A- and C-side Boxes, the RMS is $123\,\mu$m, whereas for the Top and Bottom Boxes, it is $202\,\mu$m. A single Gaussian fitted through the core of the distribution gives $\sigma = 98\,\mu$m

Figure 5.18: Photo of the IT layers fixed to the aluminium cooling rod. Both the $X$ and stereo layers are visible, as well as the cooling-rod bending on the right of the picture.

for the A- and C-side and $\sigma = 88\,\mu$m for the Top and Bottom ladders. Four ladder stacks, shown in Fig. 5.20, seem problematic: Ladder 1 in the A-side and Top Boxes and Ladder 7 in the C-side and Bottom Boxes. Some ladders have moved by up to $1\,$mm in the Top and Bottom stacks and up to $0.5\,$mm in the A- and C-side stacks. This is significantly larger than the largest deviation expected from the bending of the cooling rod. Part of this issue could be solved by aligning the ladders for the $Rz$ degree of freedom. This will need to be addressed in additional studies.

The problematic stack on the C-side is understood as one of the ladders and another nearby ladder are dead, as shown in Fig. 5.20, pulling the whole stack away. Dead ladders stay fixed during the alignment process. Possible corrections to a ladder in the same stack are hence biased by this artificial constraint. In addition, the problem of the cooling-rod bending can also explain the large $Tx$ corrections.

An explanation for the Bottom stack comes from the corrections applied after the survey. Ladder 7 in the Layer $X2$ in Station 3 is corrected by $550\,\mu$m. However, no correction is applied to the Ladder 7 in the Layer $V$, as these ladders were not surveyed. As these two ladders are fixed in the alignment procedure, if there really is a mismatch, the whole stack will be pulled away. A second explanation comes from an incident that occurred during the detector installation. The Bottom Box in Station 1 was damaged in an incident with another structural element. Although the box was shown to be fully operational and was re-surveyed after the incident, the layers and ladders were not re-surveyed. Unknown movements or rotations of some modules could account for the observed large movements in this box. These in turn induce large movements of the ladders in the Bottom Boxes of the two other stations, which are connected to the problematic box by the tracks crossing the three stations.

The ladders in the A-side stack that are moved a lot during the alignment are either stereo ladders not corrected during the survey, but adjacent to an $X$ ladder with large corrections, or $X$ ladders with large corrections that are moved back towards their nominal position. In addition, this stack is located close to the bend in the cooling rod.
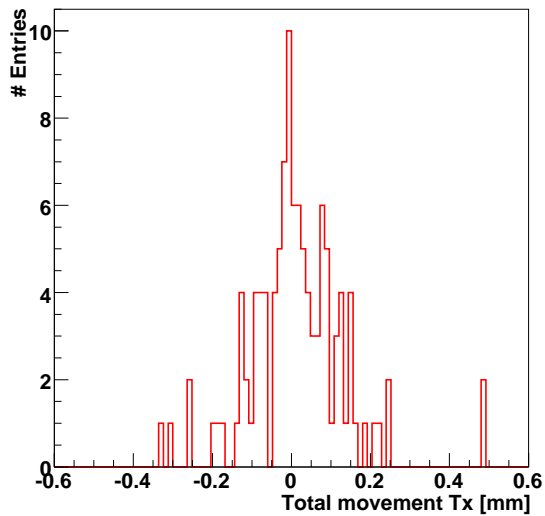
(a) A- and C-side ladder alignment
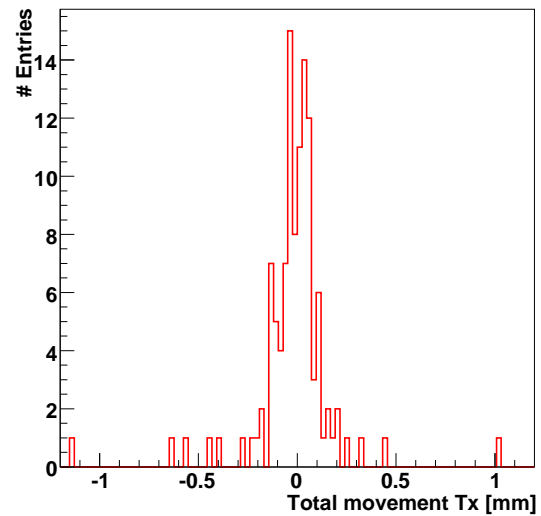


(b) Top and Bottom ladder alignment

Figure 5.19: Distribution of the total movement in the alignment parameter $Tx$ for all the ladders in the (a) A- and C-side Boxes and (b) Top and Bottom Boxes.
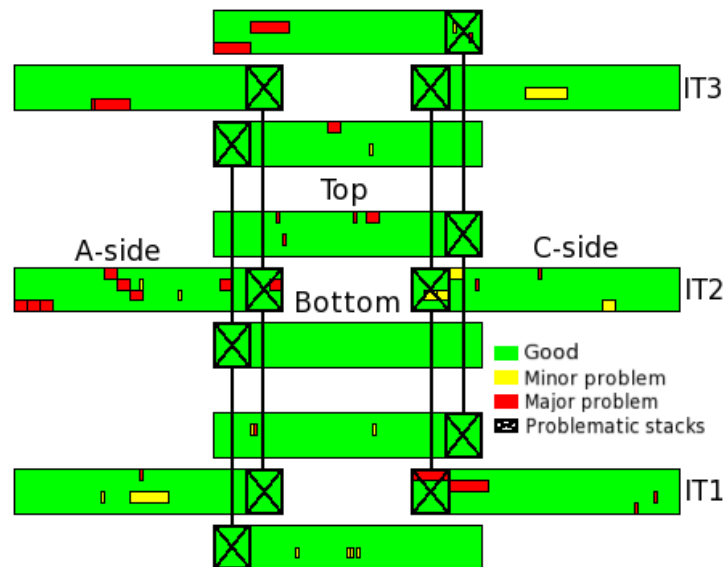


Figure 5.20: Schematic view of the three Inner Tracker stations showing the state of the detector at the time of the 2008 TED runs. Red zones indicate major problem, while yellow zones are minor problems. The crosses indicate the problematic ladder stacks.

Finally, the problem in the Top Box could come from large corrections in the survey, as in the case of the A-side Box. In addition, whilst the studies described here were being performed, a problem in the cabling of one of the modules in this stack was uncovered. Each module is read out by three front-end chips. In the case of this module, the cables

(a) A- and C-side ladder alignment      (b) Top and Bottom ladder alignment
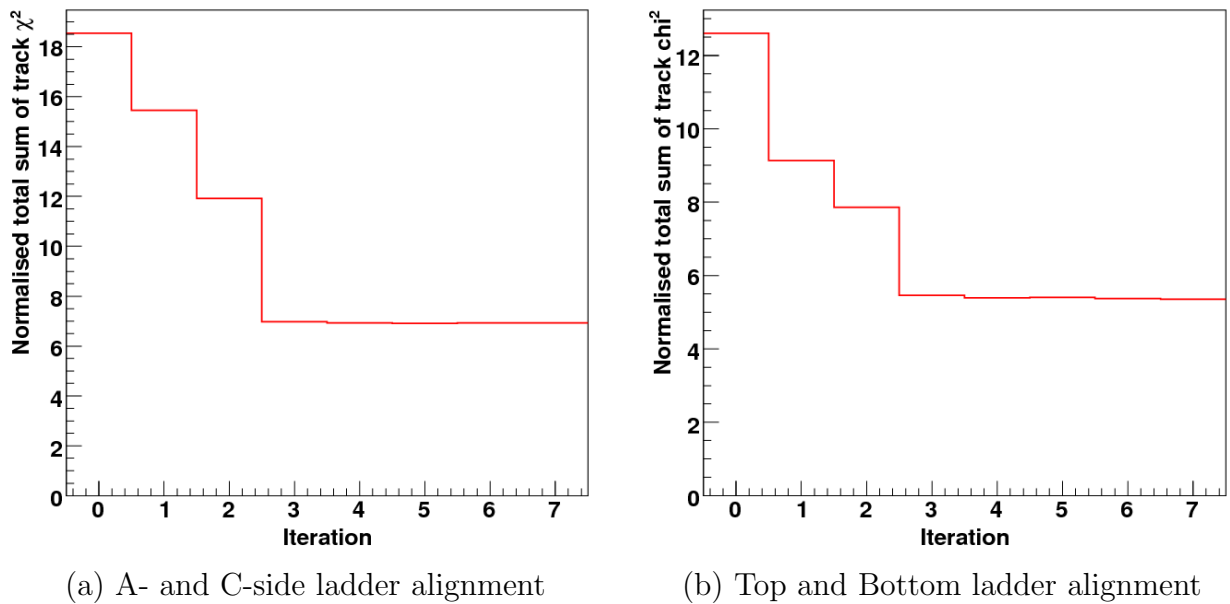
Figure 5.21: Convergence of the normalised total sum of track $\chi^2$/dof during ladder alignment in $Tx$ for (a) A- and C-side ladders and (b) Top and Bottom ladders.

related to two of these were swapped. Since two thirds of the hits in this module were incorrectly decoded, this module was inefficient. Taking this swap into account does not change significantly the alignment results. The largest movement in this stack is reduced from $550\,\mu$m to $490\,\mu$m (a difference of $60\,\mu$m), but the RMS of the distribution shown in Fig. 5.19 does not change significantly.

Removing outliers from the distributions shown in Fig. 5.19, the RMS drops down to $96\,\mu$m for the A- and C-side Boxes and $92\,\mu$m for the Top and Bottom Boxes. Despite the problematic ladders, the alignment for all ladders again converges in three iterations, as seen in Fig. 5.21.

In order to check whether uncertainties in the survey could cause large deviations, tests were performed where the survey corrections were subtracted from the problematic ladders. Running the procedure starting from this database, the problematic stacks moved back to the same point as above. This gives confidence that the survey measurements are not responsible for the large apparent movements, and confirms the robustness of the procedure.

### 5.1.7 Validation of the Results

Two different validation methods of the alignment results are presented in the following two sub-sections. They are based on the study of the unbiased residuals and on the number of reconstructed tracks. A third method based on the study of the residuals of hits in the Tracker Turicensis with respect to Inner Tracker tracks propagated back to the TT is tried but didn't give fully satisfactory results. This is mostly due to the constraint applied on some IT layers, which doesn't allow for a relative alignment of the IT with respect to the TT. This is discussed in Appendix B.2.

### 5.1.7.a   Unbiased Residuals

The first method used to validate the results of the alignment is to study the unbiased residuals (defined in Section 5.1) of the hits on the selected tracks before and after alignment. The alignment of the Inner Tracker detector elements has two effects. First, any bias on the mean of the distribution will be corrected for (alignment of global movements). Second, the resolution will improve (relative alignment of different detector elements). For these studies, an independent data sample to that used in the alignment procedure is used.

The residual distributions of the tracks selected for the alignment procedure are obtained by running a monitoring algorithm using the misaligned geometry (output of the procedure described in Ref. [132]) and the output geometry of the full alignment procedure. The distributions are separated ladder by ladder and fitted with a single Gaussian. The bias (mean) of the Gaussian fit is then used to draw the plots shown in Fig. 5.22. The ladders in stereo and $X$ layers are separated as it is expected that $X$ layers have a resolution 1.4 times better (as discussed in Section 5.1.2). The same distributions, but separated by layer can be found in Appendix B.1.

Comparing the distributions of the bias before and after alignment shows a clear improvement of the unbiased residuals for all ladders. The precision of the alignment is given by the RMS of the distributions shown in Fig. 5.22. This precision improves from 73 and 51 $\mu$m to 19 and 17 $\mu$m for the $X$ ladders in the Top/Bottom Boxes and A-/C-side Boxes respectively. For the stereo layers, the RMS improves from 185 and 102 $\mu$m to 22 and 18 $\mu$m for the Top/Bottom and A-/C-side Boxes respectively. The overall precision of the ladder alignment is hence on average 19 $\mu$m on $Tx$.

The same method as discussed above is repeated, with Gaussian distributions fitted to the distributions of unbiased residuals in each of the layers. Figure 5.23 shows the distribution of the width of these Gaussian fits [5]. The mean of this distribution is an indication of the spatial resolution of the detector. For the $X$ layers, the resolution improves from 105 and 106 $\mu$m before alignment to 87 and 95 $\mu$m after alignment for the Top/Bottom Boxes and the A-/C-side Boxes respectively. The evolution is from 169 and 180 $\mu$m before alignment to 126 and 148 $\mu$m for the stereo layers of the Top/Bottom and A-/C-side Boxes respectively.

The unbiased residuals therefore confirm that the alignment procedure is indeed doing the right job. The distribution of the bias of the unbiased residuals shows that the overall precision of the ladder alignment is on average 19 $\mu$m, whereas the distribution of the width of the unbiased residual distributions shows that the spatial resolution of the detector is improved by the alignment process down to $\sim 90$ $\mu$m for the Top and Bottom boxes.

### 5.1.7.b   Number of Tracks

The second check performed is to compare the number of reconstructed tracks before and after alignment. In order to give a fair comparison, tight selection cuts are applied to

---

[5] In order to have a reliable fit on the distributions, higher statistics are needed. Therefore, the distributions of unbiased residuals separated by layer are used. The distributions per ladder were used for the study of the bias because the mean of the distribution is less sensitive to low statistics than its width.

(a) $X$ ladders before alignment

(b) stereo ladders before alignment



(c) $X$ ladders after alignment

(d) stereo ladders after alignment
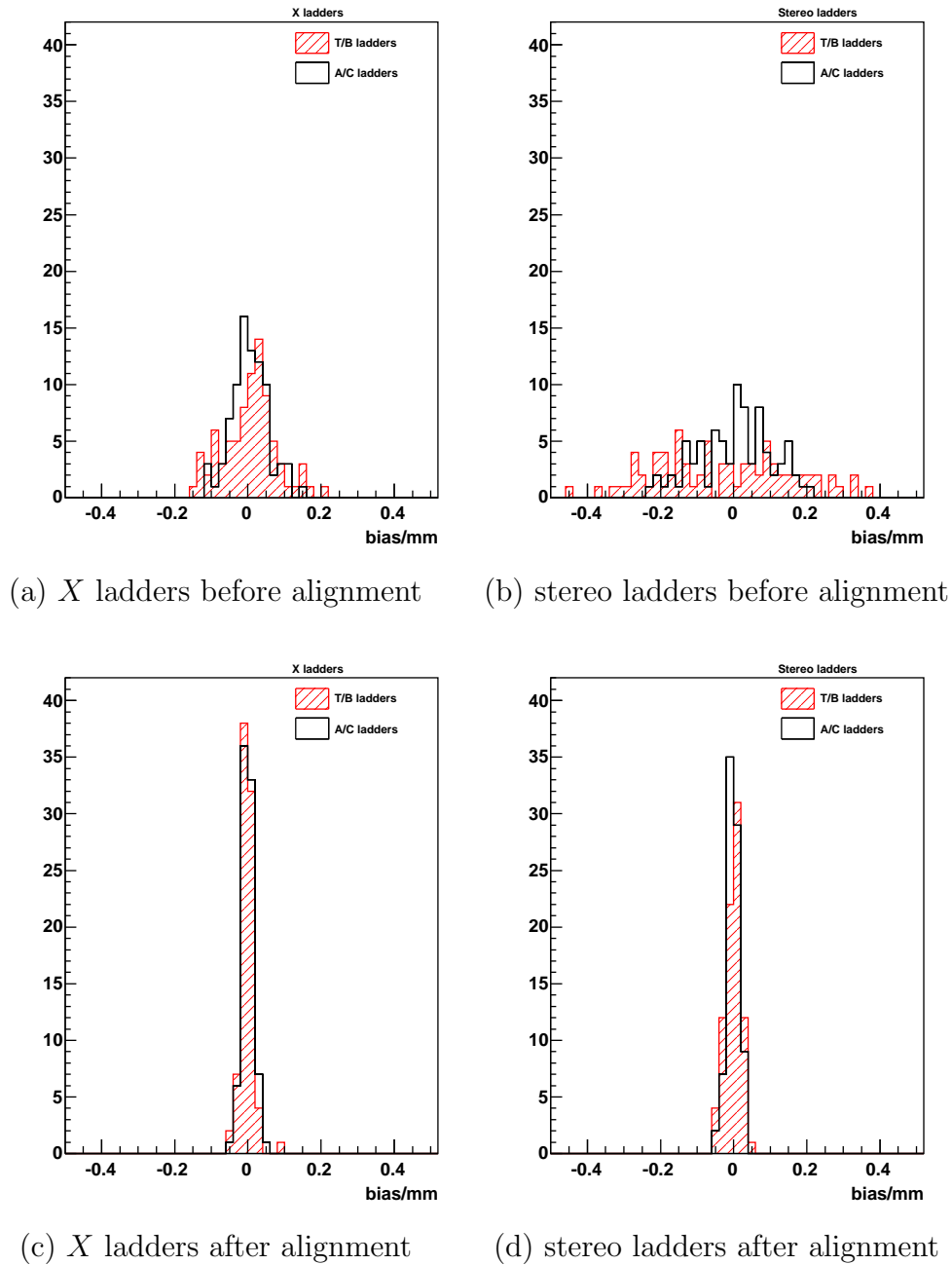
Figure 5.22: Bias of the distribution of unbiased residuals for individual ladders: (a) $X$ ladders before alignment, (b) stereo ladders before alignment, (c) $X$ ladders after alignment and (d) stereo ladders after alignment.
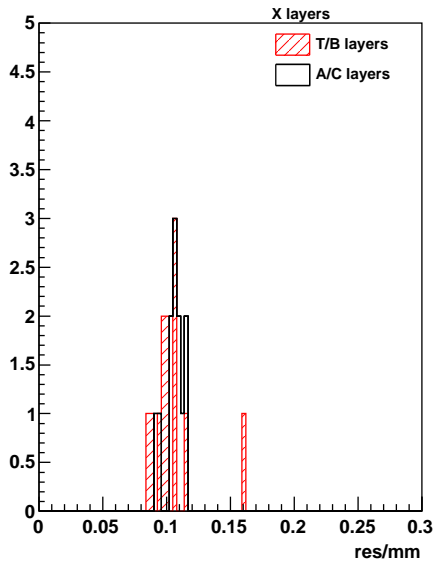
(a) *X* layers before alignment
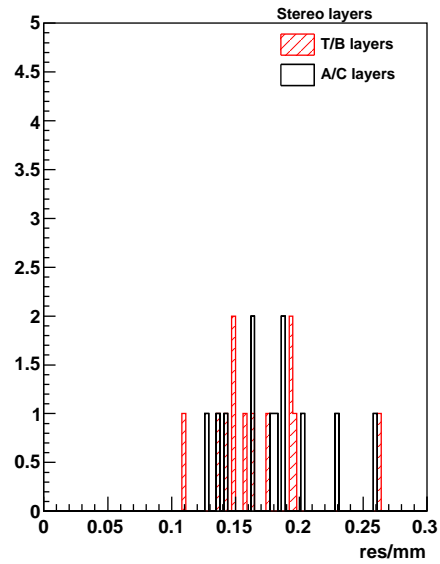
(b) stereo layers before alignment
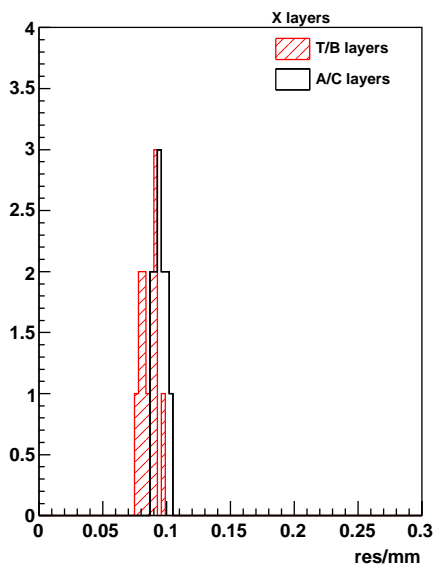


(c) *X* layers after alignment
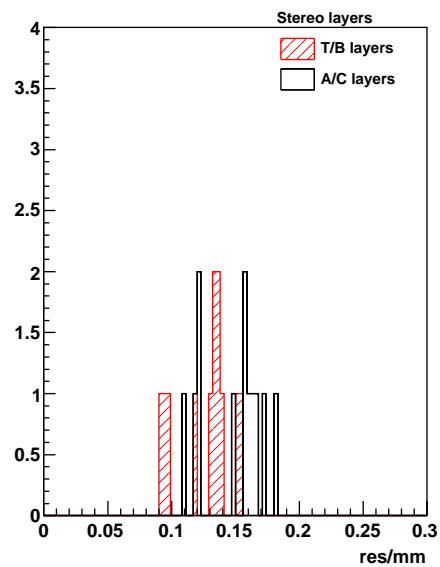
(d) stereo layers after alignment

Figure 5.23: Width of the distribution of unbiased residuals for individual layers: (a) *X* layers before alignment, (b) stereo layers before alignment, (c) *X* layers after alignment and (d) stereo layers after alignment.

Table 5.4: Number of tracks per box before and after the whole alignment procedure with TED data.

| Geometry | A-side Box | C-side Box | Top Box | Bottom Box |
|---|---|---|---|---|
| Before alignment | 2744 | 1339 | 697 | 559 |
| After alignment | 2927 | 1448 | 816 | 765 |
| Gain | 6.67 % | 8.14 % | 17.1 % | 36.9 % |

both geometries:

- $x$ search-window: 0.5 mm.

- $y$ search-window: 7.0 mm.

- Maximum number of clusters per event: 5000.

- Track quality: $\chi^2/\text{dof} < 20$.

The data set used is the same as during the alignment procedure. The number of tracks per box before and after the whole alignment procedure can be seen in Table 5.4. The gain is higher for the Top and Bottom Boxes, which indicates that the alignment of these boxes is more beneficial than for the side boxes. This can be related to the higher occupancy in the side boxes, as shown in Fig. 5.8, leading to a higher ghost rate and lower tracking efficiency. This, in turn, induces a worse alignment precision for the side boxes. Also, a higher occupancy means that the clone killing is more active in the side boxes than in the Top/Bottom boxes, reducing the gain due to the alignment. Finally, the larger increase for the Top/Bottom boxes is also due to the larger corrections determined for these boxes with respect to the A-/C-side boxes.

## 5.2 First Look at 2009 TED Data

New LHC synchronisation tests were performed in June 2009, giving the opportunity to validate the alignment parameters produced with the 2008 runs using an independent set of data. The main difference between the two runs is that the Inner Tracker is opened by $\sim 50$ cm in 2009 (see Fig. 5.24). In addition, most of the electronics-related faults shown in Fig. 5.20 were fixed (99 % channels are readout, compared to 97 % in 2008).

The first step is to add corrections to the 2008 aligned database in order to account for the shift of all the half-stations. To correct for any movements of the boxes during the opening or the maintenance of the detector, the boxes and layers were aligned using the histogram-based technique described in Ref. [132]. Corrections of $\sim 2$ mm for the boxes and 0.09 mm for the layers were needed (compared to the 0.16 mm for the layers discussed in Ref. [132] for the 2008 TED runs). After these the software procedure described in Section 5.1.1 is used.

The ladders are aligned using the software alignment process. The total movement after the eight iterations are shown in Fig. 5.25 for all ladders in (a) the A- and C-side
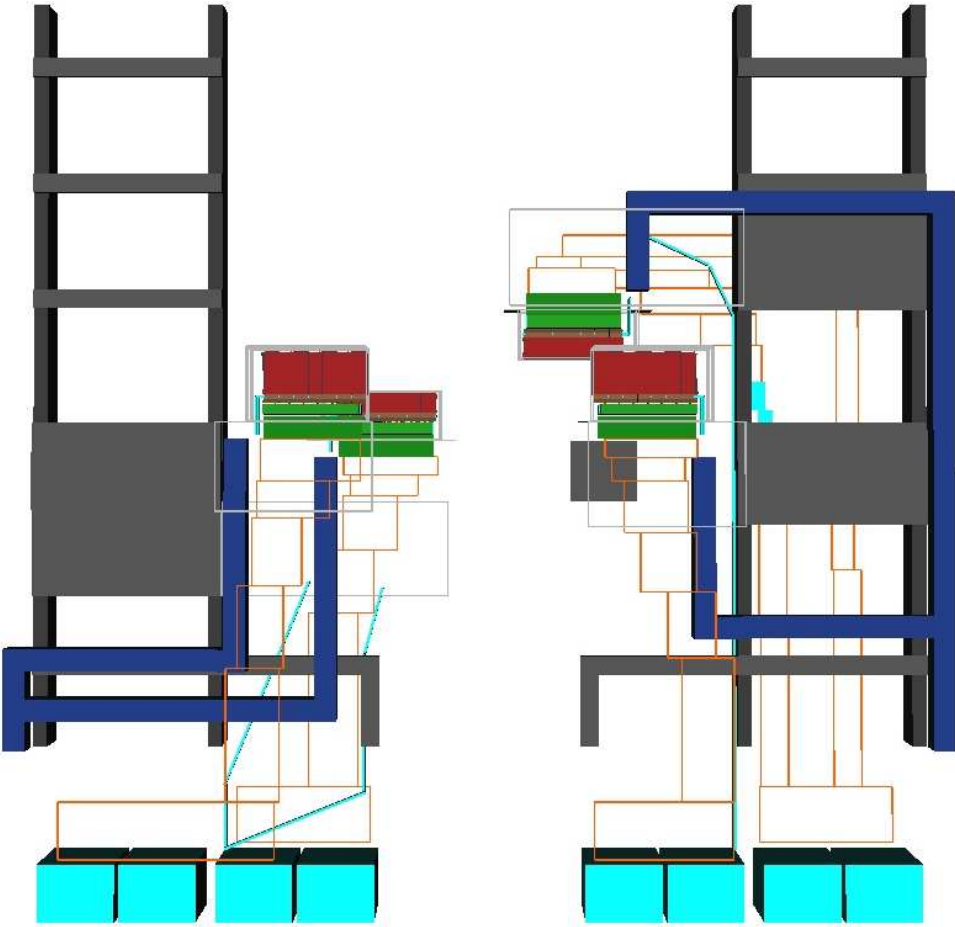
Figure 5.24: Layout of the Inner Tracker in the open position.

(a) A- and C-side ladder alignment

(b) Top and Bottom ladder alignment
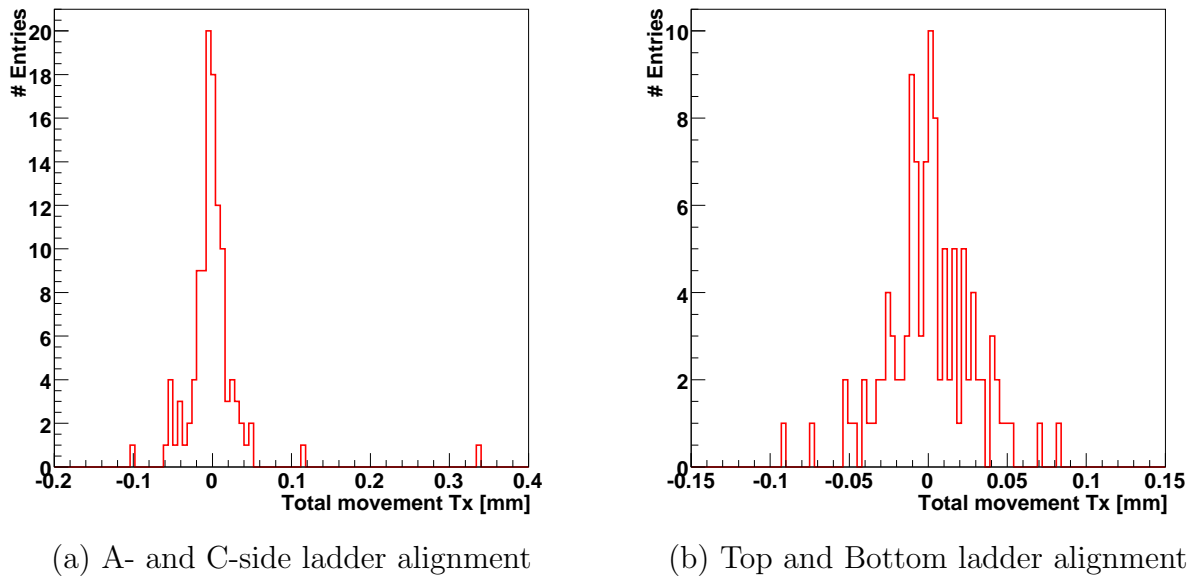
Figure 5.25: Distribution of the total change in the alignment parameter $Tx$ for all the ladders in the (a) A- and C-side Boxes and (b) Top and Bottom Boxes. Data from the 2009 TED runs are used.

Boxes and (b) the Top and Bottom Boxes. The RMS of these two distributions is 26 and $27\,\mu$m respectively [6]. This agrees with the precision of the ladder $Tx$ alignment of $19\,\mu$m quoted in Section 5.1.7.a.

## 5.3   Alignment with Cosmic Events

This section describes the studies performed on the alignment of the Inner Tracker using the cosmics data collected in August–September 2008.

### 5.3.1   Procedure

The alignment procedure with cosmics data, shown in Fig. 5.26, is similar to that for the TED data. The main difference is that the TrackCompetition algorithm after the track fit is not needed as the occupancy and hence ghost rate coming from wrong combinations is negligible. On the other hand, the tracking method creates clones that must be removed before the alignment algorithm is run. This clone killing is performed by the standard LHCb clone killing tool described in Ref. [121].

In this study, only the side boxes are aligned. No tracks are found in neither the Top nor the Bottom Boxes because of the shorter strips and the angle of the cosmic rays. In order to remove the global unconstrained modes, the first two layers in Station 1 ($X1$ and $U$) and the last two layers in Station 3 ($V$ and $X2$) are fixed to the value given by the

---

[6] The largest movement in plot (a), which corresponds to one of the two ladders that were repaired between the 2008 and the 2009 TED runs, is not taken into account.
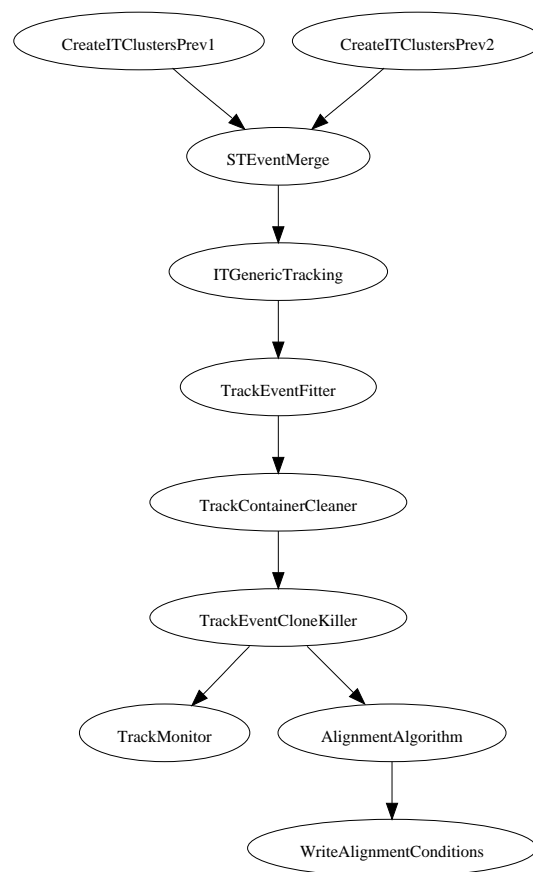
Figure 5.26: Flow diagram of the software procedure used for the tracking-station alignment with cosmics data.

(a)                                    (b)
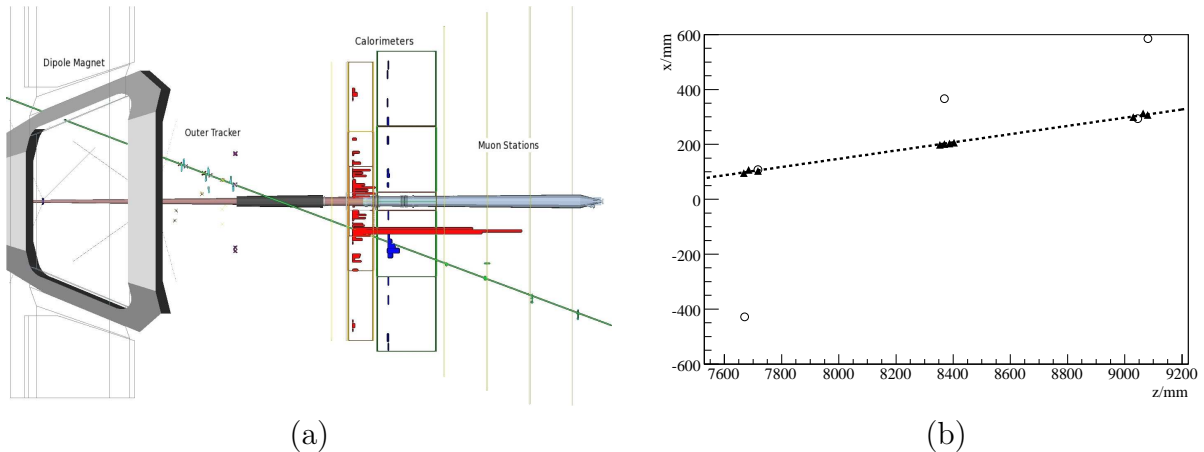
Figure 5.27: Typical cosmics event display: (a) a cosmic ray crossing the Outer tracker, the Calorimeters and the Muon Stations and (b) the "golden cosmic ray" in the $xz$ plane crossing the three IT stations.

first alignment given in Ref. [132]. However, the layers in Station 2 are also constrained by tracks going through Stations 1 and 2 on one hand and tracks going through Stations 2 and 3 on the other hand. The multi-step approach is not used here due to the lack of statistics.

## 5.3.2  Track and Event Selection

Due to the limited statistics of cosmic rays crossing at least two IT stations (and hence being reconstructible as tracks), the track selection cuts are kept loose (as described in Ref. [137]). A typical cosmic event is shown in Fig. 5.27. On the left-hand side, a cosmic ray crossing the Outer Tracker, the Calorimeters and the Muon stations is shown. On the right-hand side, the IT "golden track" crossing the three IT stations is represented in the $x - z$ plane.

In 2.6 millions events, only 82 tracks are found crossing at least two IT boxes in either the A- or the C-side sets of boxes. This is only $\sim 40$ tracks per stack, which gives a large statistical error and hence the results have a poor precision. In this sample, only two tracks cross the three Inner Tracker boxes.

In order to reject the bad candidates that arise during the reconstruction process, two criteria are used. A confirmation from the calorimeters is required. If the track deposits less than 300 MeV in the calorimeters, it is discarded. Also, a loose $\chi^2$ cut strategy is applied, starting from a cut at 250 and going down to 100. This way, bad tracks that pull some elements away are removed. Taking all these requirements into account, 64 tracks are used for the alignment of the two side boxes.

## 5.3.3  Alignment Results

Figure 5.28 shows the evolution of the alignment parameters for the translation in $x$ of the studied layers. Apart from two stereo layers in the C-side Box of Station 2, the values
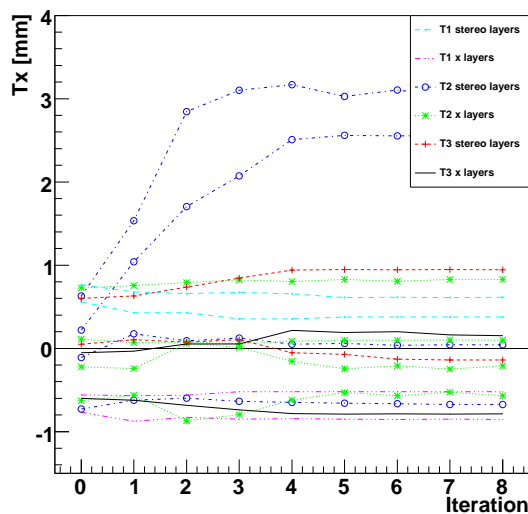
Figure 5.28: Evolution of the $Tx$ alignment constants for all layers in the A- and C-side stacks during layer alignment with cosmics data.

of the alignment parameters are on average consistent with the initial values from the survey. However, oscillations coming from the limited statistics can be seen. This is clearly not satisfactory and shows the limitations of aligning the Inner Tracker with the current cosmics sample. For a meaningful alignment to be performed, a sample ten times larger would be necessary.

Two reasons can account for the huge movement of the two stereo layers in the C-side Box. As explained in Section 5.3.1, the two first and two last layers are constrained. However, as described in Section 5.3.2, cosmics tracks only cross two boxes at a time. Due to the limited statistics, the constraint on the boxes in Station 2 from tracks crossing Stations 1 and 2 or Stations 2 and 3 is not sufficient to get rid of the weak mode. Tracks that interact in the detector material and have a kink in their trajectory could also explain such a behaviour. Cutting on the track fit quality will solve this problem. However, due to the low statistics, the cut had to be kept loose in order to keep enough tracks to align every layer with at least 10 hits.

This sample gives a proof of principle of the alignment method. Figures 5.29 (a) and (b) show respectively the distribution of unbiased residuals with respect to cosmic tracks before and after alignment. The number of selected tracks is lower with the aligned database than with the survey database. However, the unbiased residual distribution gets much narrower both for the A- and the C-Side Boxes. Fitting a Gaussian through the histograms shows that the width of the distribution of unbiased residuals in the two boxes is reduced from $350\,\mu$m to $245\,\mu$m for the A-side Box and from $230\,\mu$m to $185\,\mu$m for the C-side Box.
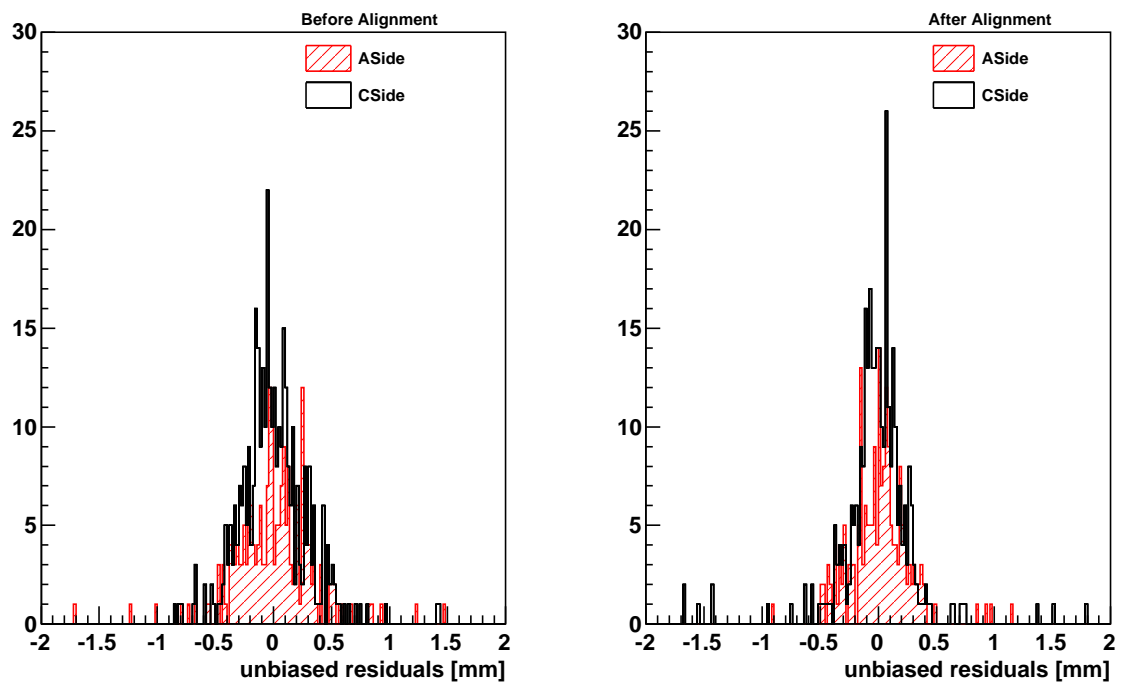
(a) before alignment                    (b) after alignment

Figure 5.29: Distribution of unbiased residuals for all hits on the cosmic tracks. (a) shows the distribution with the surveyed geometry and (b) with the geometry obtained after layer alignment in $Tx$.

# Chapter 6

# Selection of the $X(3872)$ and $Z(4430)^{\pm}$ Particles
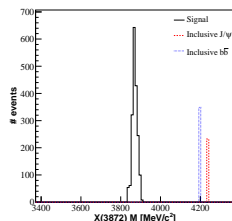


This chapter describes the selection of the $X(3872) \to J/\psi\,\pi^+\pi^-$ and $Z(4430)^{\pm} \to \psi(2S)\pi^{\pm}$ signals in $B$-meson decays at LHCb. These feasibility studies are performed on Monte Carlo simulated data. The total efficiency, annual yield and an estimate of the background-to-signal ratio are given for both studies.

$\mathfrak{T}$HE nature of the $X(3872)$ state (discussed in Section 1.6.3), discovered by Belle in 2003 and confirmed by BaBar, CDF and DØ, is still not known. Various studies and measurements have been performed on it in the past 6 years. However, the current observations do not allow to fully discriminate between the various theoretical models (presented in Section 1.6.2). In addition, no experiment has been able to fully disentangle between a $J^{PC} = 1^{++}$ and $2^{-+}$ state yet. Furthermore, it is not known so far whether there is one or two $X$ states around $3875\,\mathrm{MeV}/c^2$.

As for the $Z(4430)^{\pm}$ state, it was observed by Belle in 2008 but its existence couldn't be confirmed by BaBar. This state would be the first charged particle found in the exotic charmonium spectroscopy.

In this situation, LHCb will provide precise and valuable measurements in order to shed some light on the new charmonium spectroscopy. The following sections present the studies performed to provide a selection of the $X(3872) \to J/\psi\,\pi^+\pi^-$ and $Z(4430)^{\pm} \to \psi(2S)\pi^{\pm}$ signals in $B$ decays at LHCb. The $X(3872)$ and $Z(4430)^{\pm}$ states are studied for the first time in the LHCb collaboration. The work presented here is a first attempt to select the two decays and should be read as a feasibility study, more than a complete analysis of the decays.

The goal of the $X(3872)$ selection is to have a clean enough sample to allow for a precise angular-distribution measurement in order to determine the $X(3872)$ quantum numbers. In the case of a fully polarised $X(3872)$ state, the most powerful variable to discriminate between the two spin hypotheses is the $X(3872)$ decay angle, $\theta_X$, defined as the angle between the flight direction of the $J/\psi$ in the $X(3872)$ rest frame and of the $X(3872)$ in
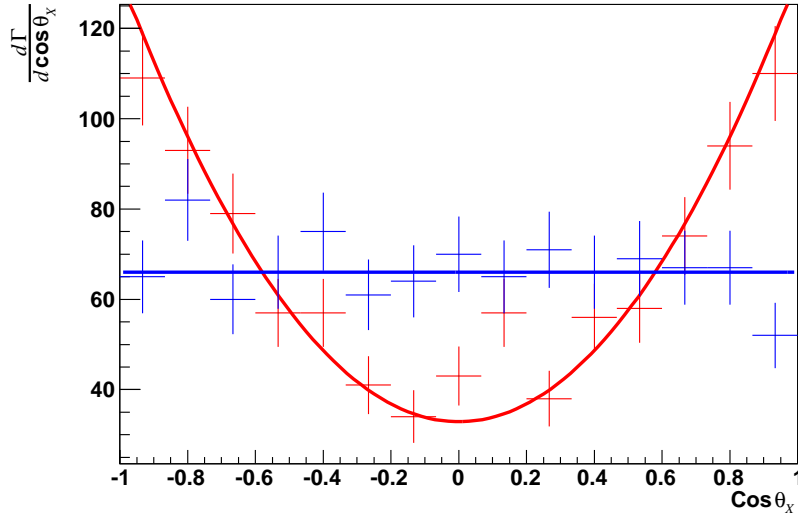
Figure 6.1: Expected $\cos\theta_X$ distribution of $X(3872)$ states produced in $B^{\pm} \to X(3872)K^{\pm}$ decays for the $1^{++}$ (blue) and $2^{-+}$ (red) spin hypotheses. Each histogram with error bars represents the distribution of 1'000 signal events at the Monte Carlo generator level. The curves represent the fits, using the distributions calculated in Ref. [140]. This figure is taken from the same reference.

the rest frame of the $B^{\pm}$. It has been shown in Ref. [140] that the distribution of $\cos\theta_X$ is sensitive to the spin of the $X(3872)$ state, as reported in Fig. 6.1. This distribution is based on the hypothesis that the helicity of the $X(3872)$ is equal to zero, which is the case for $X(3872)$ states from $B^{\pm} \to X(3872)K^{\pm}$ decays because of total angular momentum conservation. However, in the case of prompt $X(3872)$ production directly in $pp$ collisions, the helicity is not clearly defined and the $\cos\theta_X$ distributions for the two spin hypotheses depend on the $X(3872)$ polarisation. In the limit where the prompt $X(3872)$ is unpolarised, the $\cos\theta_X$ distribution is expected to carry negligible information on the $X(3872)$ spin. Hence, because $B$ decays are a guaranteed source of polarised $X(3872)$, the following studies present the selection of $B^{\pm} \to X(3872)K^{\pm}$ decays.

For the $Z(4430)^{\pm}$, the first goal at LHCb will be to confirm the Belle discovery from 2008. Since Belle discovered the $Z(4430)^{\pm}$ state in $B^0 \to Z(4430)^{\pm}K^{\mp}$ decays, a confirmation is needed in the same channel with a measurement of the branching fraction of the corresponding $B$ decay chain. Therefore the selection presented in this chapter is also performed on $B^0 \to Z(4430)^{\pm}K^{\mp}$ decays. However, this new state could also be searched in other processes, such as prompt production in the $pp$ collisions. Once the discovery is confirmed and the production rate is measured, more precise studies will be performed in order to determine the properties of the $Z(4430)^{\pm}$ state.

The two selections are presented in Sections 6.1 and 6.2, respectively, and discussed in Section 6.3.

# 6.1   $X(3872)$ Selection

The event selection is performed in three distinct steps. A first loose pre-selection is run in the LHCb software framework, with a selection code implemented in DaVinci v22r1. The properties of the retained candidates are saved in a ROOT nTuple. Then, after a first quantitative study of the event variables, a tighter pre-selection is implemented in ROOT (a data analysis toolkit [141]). The initial nTuples are stripped, saving the selected events and a subset of their properties in another nTuple. Finally, a set of selection cuts is defined by optimising the selection signal significance against a chosen background sample for a set of variables. In this feasibility study, which only concentrates on the selection of a signal (and not the full angular analysis), the choice was made to optimise the signal significance $\frac{S}{\sqrt{S+B}}$. For the final angular analysis, another optimisation might be needed which will also take into account the shape of the background distribution and potential systematics effects. These three selection steps are described in the following sections. The histograms presented in these sections show the $B^{\pm} \to X(3872)K^{\pm}$ signal in solid black line and the various types of backgrounds in dashed and dotted coloured lines. The normalisation of each histogram is chosen such that the integral over the histogram range is unity, unless specified otherwise.

## 6.1.1   Data Samples Used in the $X(3872)$ Study

The selection is run on two Monte Carlo data samples of $X(3872)$ signal events. Both samples were generated in the channel $B^{\pm} \to X(3872)K^{\pm}$ with $X(3872) \to J/\psi\, \pi^{+}\pi^{-}$ and $J/\psi \to \mu^{+}\mu^{-}$. A requirement is set at the generator level in order to ensure that the signal $B^{\pm}$ meson is found inside the detector geometrical acceptance. The efficiency of this generator-level cut, $\epsilon_{\theta}^{B^{\pm} \to X(3872)K^{\pm}} = (34.6 \pm 0.1)\,\%$, is taken into account in the calculation of the total selection efficiency, as discussed in Section 6.1.3. The first sample of 22'396 events was generated using GAUSS v35r1 and digitised with BOOLE v16r3. The events were then reconstructed using BRUNEL v33r3p1. The second sample of 28'338 events was generated using GAUSS v36r2, BOOLE v17r2 and BRUNEL v34r1p1. The observation made by CDF and Belle (discussed in Section 1.6.3) that the $X(3872)$ preferably decays via an intermediate $\rho^{0} \to \pi^{+}\pi^{-}$ meson was not taken into account in the generation, where a pure phase-space model was used for the $X(3872) \to J/\psi\, \pi^{+}\pi^{-}$ decay.

In order to study the background level and the type of problematic events that will need to be dealt with, the following additional samples are studied. The corresponding number of events and the efficiency of the generator level cuts are given in the third and fourth columns of Table 6.1 respectively.

**Inclusive $J/\psi$:** The requirements at the generator level are to have a $J/\psi$ meson in the event decaying to a $\mu^{+}\mu^{-}$ pair with each muon inside the geometrical acceptance. These generator-level requirements induce an efficiency $\epsilon_{\theta}^{\text{incl. } J/\psi} = (20.92 \pm 0.17)\,\%$ in the generation process that is taken into account in the calculation of the total efficiency. The expected total production cross-section in $4\,\pi$, given by the Pythia event generator, has a value of $\sigma_{\text{incl. } J/\psi} = (262 \pm 2)\,\mu\text{b}$.

In order to mimic the signal, two charged pions and a charged kaon must be combined with the charmonium particle. Although this is not likely, this background

is still dangerous in the selection process because of the large $J/\psi$ production rate. Three different samples from the 2008 configuration are combined in this study in order to increase the statistics. A first sample of 93'141 was generated with Gauss v35r1, Boole v16r3 and Brunel v33r3p1. The second sample of 95'603 events has been generated with Gauss v36r0, Boole v17r1 and Brunel v34r0. Finally, the third sample of 102'555 has been generated with Gauss v36r1, Boole v17r2 and Brunel v34r1p1.

**Inclusive $b\bar{b}$:** An important check to assess the background-rejection power of the selection is to run on a sample of inclusive $b\bar{b}$ events. The generator-level requirement here is that each event must contain a $b$ hadron inside the geometrical acceptance. This requirement has an efficiency of $\epsilon_\theta^{\text{incl. } b\bar{b}} = (43.21 \pm 0.29)\,\%$, which is taken into account in the calculation of the total efficiency. The production cross-section in $4\pi$ given by the event generator has a value of $\sigma_{\text{incl. } b\bar{b}} = (1040 \pm 10)\,\mu\text{b}$ [1]. A sample from the 2006 data challenge of 26.4 million events generated with Gauss v25r10, Boole v12r10 and Brunel v30r17 is used for this test. This sample was first stripped using the L0 Trigger requirements.

**Minimum bias:** Finally, one more check to perform is to run on a sample of minimum bias events, i.e. $pp$ collisions without generator-level requirements. A sample of 19.2 million minimum bias events from the 2006 data challenge (corresponding to less than a second of data taking at the nominal LHCb running conditions) was produced with Gauss v25r7, digitised with Boole v12r10 and reconstructed with Brunel v30r14. In order to reduce the duration of an analysis job, this sample was first passed through the L0 Trigger (described in Section 2.2.4.a). This step was performed with Brunel v31r10. Due to the small signal production cross-section, no minimum bias event should be selected in this study.

These various event types have not been generated with the same requirements. Furthermore, the different decay channels don't have the same branching ratio. A way to compare the statistics of the different samples is to calculate the corresponding integrated luminosity. This value is calculated as follows:

$$\mathcal{L}_{\text{int}}^{\text{sample}} = \frac{N_{\text{gen}}^{\text{sample}}}{\sigma_{\text{tot}}^{\text{sample}}} \tag{6.1}$$

where $N_{\text{gen}}^{\text{sample}}$ is the number of generated events that are analysed and $\sigma_{\text{tot}}^{\text{sample}}$ is the total cross section of the sample. For the four samples of interest described above, this total cross section is

$$\sigma_{\text{tot}}^{B^{\pm} \to X(3872)K^{\pm}} = \sigma_{b\bar{b}} \times 2 \times f_{B^{\pm}} \times \mathcal{B}_{\text{vis}}^{B^{\pm} \to X(3872)K^{\pm}} \times \epsilon_\theta^{B^{\pm} \to X(3872)K^{\pm}}, \tag{6.2}$$

$$\sigma_{\text{tot}}^{\text{incl. } J/\psi} = \sigma_{J/\psi} \times \mathcal{B}_{\text{vis}}^{\text{incl. } J/\psi} \times \epsilon_\theta^{\text{incl. } J/\psi}, \tag{6.3}$$

$$\sigma_{\text{tot}}^{\text{incl. } b\bar{b}} = \sigma_{b\bar{b}} \times \epsilon_\theta^{\text{incl. } b\bar{b}}, \tag{6.4}$$

$$\sigma_{\text{tot}}^{\text{min. bias}} = \sigma_{\text{min. bias}}. \tag{6.5}$$

---

[1] In order to give conservative results, a value of $\sigma_{b\bar{b}} = 500\,\mu b$ is often assumed at LHCb. However, to be consistent with the values of the $J/\psi$ and $\psi(2S)$ production cross-sections used in this chapter, which are taken from the event generator, the value of $1040\,\mu$b is used in this study.

Table 6.1: Summary of the Monte Carlo samples used to study the selection of the $B^\pm \rightarrow X(3872)K^\pm$ decay channel. The integrated luminosity $\mathcal{L}_{\text{int}}^{\text{sample}}$ corresponding to the sample and the efficiency $\epsilon_\theta$ of the acceptance cut at the generator level are reported.

| Data sample | $\mathcal{L}_{\text{int}}^{\text{sample}}$ | $\epsilon_\theta$ | # events |
|---|---|---|---|
| $B^\pm \rightarrow X(3872)K^\pm$ | $2.6 \times 10^5 \, \text{nb}^{-1}$ | $(34.6 \pm 0.1)\,\%$ | 50'734 |
| Inclusive $J/\psi$ | $90 \, \text{nb}^{-1}$ | $(20.92 \pm 0.17)\,\%$ | 291'299 |
| Inclusive $b\bar{b}$ | $60 \, \text{nb}^{-1}$ | $(43.21 \pm 0.29)\,\%$ | $\sim 26.4 \times 10^6$ |
| Minimum bias | $0.19 \, \text{nb}^{-1}$ | $1$ | $\sim 19.2 \times 10^6$ |

The generator-level efficiencies $\epsilon_\theta$ are reported in Table 6.1. $\sigma_{b\bar{b}}$ and $\sigma_{J/\psi}$ are the expected $b\bar{b}$ and $J/\psi$ production cross-sections discussed above. In Equation 6.2, the factor $f_{B^\pm}$ is the fraction of $b$ quarks that hadronise to a $B^\pm$ meson (taken from Table 2.1), the factor 2 accounts for the fact that two $b$ hadrons are produced in a $b\bar{b}$ event, and $\mathcal{B}_{\text{vis}}^{B^\pm X(3872)K^\pm}$ is the visible branching fraction of the signal decay. The visible branching ratio is the product of the known branching ratios involved in the decay chain:

$$
\begin{aligned}
\mathcal{B}_{\text{vis}}^{B^\pm \rightarrow X(3872)K^\pm} &= \mathcal{B}(B^\pm \rightarrow X(3872)K^\pm) \times \mathcal{B}(X(3872) \rightarrow J/\psi\,\pi^+\pi^-) \times \\
&\quad \mathcal{B}(J/\psi \rightarrow \mu^+\mu^-) \\
&= (1.14 \times 10^{-5}) \times (5.93\,\%) = 6.76 \times 10^{-7}\,,
\end{aligned} \tag{6.6}
$$

where the first term of this last expression is the combined branching ratio $\mathcal{B}(B^+ \rightarrow X(3872)K^+) \times \mathcal{B}(X(3872) \rightarrow J/\psi\,\pi^+\pi^-)$ given in Section 1.6.3 and the second term is the branching ratio of the $J/\psi$ decaying to two muons, taken from Ref. [16]. In Equation 6.3, the visible branching ratio $\mathcal{B}_{\text{vis}}^{\text{incl.}\,J/\psi}$ reduces to the branching ratio of the $J/\psi \rightarrow \mu^+\mu^-$ decay already quoted. Finally, in Equation 6.5, $\sigma_{\text{min. bias}} = 102.3\,\text{mb}$ is the estimated total $pp$ cross-section in $4\,\pi$ at $\sqrt{s} = 14\,\text{TeV}$.

The results of the calculations for the integrated luminosity corresponding to the data samples used in this study are reported in the second column of Table 6.1.

## 6.1.2   *X*(3872) Pre-Selection

The topology of the complete decay chain of interest $B^\pm \rightarrow X(3872)K^\pm$, $X(3872) \rightarrow J/\psi\pi^+\pi^-$, $J/\psi \rightarrow \mu^+\mu^-$ is shown in Fig. 6.2. The $B^\pm$ mesons have an average momentum of $p \approx 80\,\text{GeV}/c$ in the LHCb acceptance. Given their proper lifetime of $c\tau \approx 491.1\,\mu\text{m}$, $B^\pm$ mesons will fly on average $c\tau p/m \approx 7.4\,\text{mm}$ before decaying. On the other hand, the $X(3872)$ and $J/\psi$ are short-lived and decay before travelling any significant distances. The $J/\psi$ has a width of $\Gamma = (93.2 \pm 2.1)\,\text{keV}/c^2$, whereas the $X(3872)$ has a width of $\Gamma < 2.3\,\text{MeV}/c^2$ at $90\,\%$ CL, determined from the $J/\psi\,\pi^+\pi^-$ decay channel and $\Gamma = 3.0\,^{+1.9}_{-1.4} \pm 0.9\,\text{MeV}/c^2$ in the $\bar{D}^{*0}D^0$ decay.

Figure 6.2 shows that there are five charged tracks in the final state: a charged kaon (with the same charge as the $B$ meson in the initial state), two oppositely-charged pions and two oppositely-charged muons. Although in theory, there are three decay vertices,
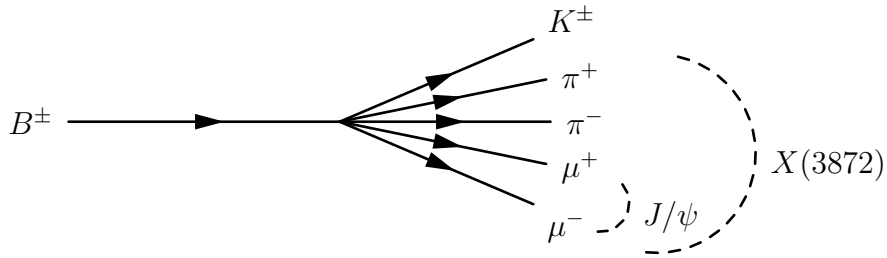
Figure 6.2: The topology of the $B^{\pm} \rightarrow X(3872)K^{\pm}$ decay, with $X(3872) \rightarrow J/\psi\,\pi^{+}\pi^{-}$ and $J/\psi \rightarrow \mu^{+}\mu^{-}$.

in practice, these vertices are located on the same point (the distance between the origin and decay vertex of a resonance is well below the detector spatial resolution).

In order to be as close as possible to the real conditions of data taking, the Level-0 and High-Level Triggers are applied prior to any other selection criteria.

The first step is the selection of $J/\psi$ candidates. Two oppositely-charged muons from the standard loose muon selection (see Section 3.1.5) are combined. The muon tracks are required to have each a track-fit quality of $\chi^2/\mathrm{dof} < 12$. Based on the distribution of Fig. 6.3 (a), this cut is subsequently tightened to $\chi^2/\mathrm{dof} < 2$. A cut on the $\chi^2/\mathrm{dof}$ of the $\mu\mu$-vertex fit at $\chi^2/\mathrm{dof} < 30$ is used to get rid of the worst di-muon combinations. A cut at $1\,\mathrm{GeV/c}$ is also applied on the transverse momentum of the muons to reject a large peak of background events (see Fig. 6.4). Finally, any candidate with a mass outside of a $\pm100\,\mathrm{MeV}/c^2$ window around the true $J/\psi$ mass of $M_{J/\psi} = 3096.916\,\mathrm{MeV}/c^2$ (as set in the Monte Carlo generation software, which corresponds to the current world average reported in Ref. [16]) is rejected.

Next, the $X(3872)$ candidates are formed by combining the reconstructed $J/\psi$ with two oppositely-charged pions from the standard loose pion selection (defined in Section 3.1.5). The same requirement as for the muons is set on the pion track fit quality ($\chi^2/\mathrm{dof} < 12$, subsequently tightened to $\chi^2/\mathrm{dof} < 2$, based on the distribution of Fig. 6.3 (b)). Also, the $\chi^2/\mathrm{dof}$ of the four-track vertex fit is required to be smaller than 25. Finally, the cut on the reconstructed $X(3872)$ mass is kept loose in order to allow for a study of the $X(3872)$ mass spectrum. All combinations within a $\pm500\,\mathrm{MeV}/c^2$ window around the Monte Carlo $X(3872)$ mass of $M_{X(3872)} = 3872.2\,\mathrm{MeV}/c^2$ (as reported in Ref. [16]) are retained.

Finally, a charged kaon from the standard loose kaon selection (defined in Section 3.1.5) is combined with the reconstructed $X(3872)$ to make a $B^{\pm}$ candidate. The requirement on the kaon track fit quality is the same as for the other four charged particles combined so far: $\chi^2/\mathrm{dof} < 12$, tightened to $\chi^2/\mathrm{dof} < 2$, based on the distribution of Fig. 6.3 (c). A cut on the five-track vertex quality is set at $\chi^2/\mathrm{dof} < 15$ and all combinations outside of a $\pm100\,\mathrm{MeV}/c^2$ window around the Monte Carlo true $B^{\pm}$ mass of $M_{B^{\pm}} = 5279.15\,\mathrm{MeV}/c^2$ [16] are rejected.

The requirements on the mass of the reconstructed $J/\psi$ and $B^{\pm}$ are then tightened to improve the selection. Figures 6.5 (a), (b) and (c) show the $J/\psi$, $X(3872)$ and $B^{\pm}$ mass
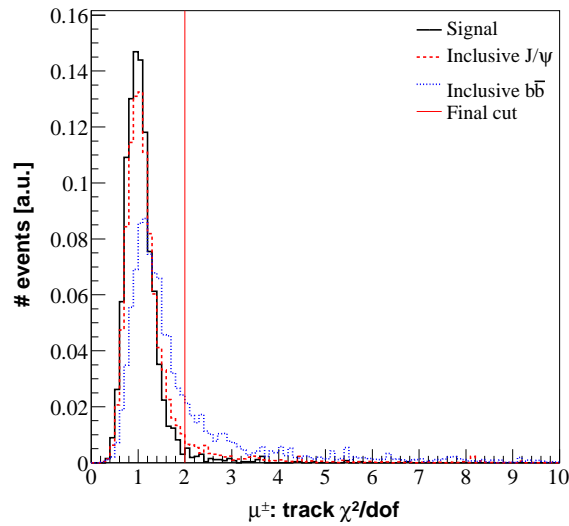
(a)
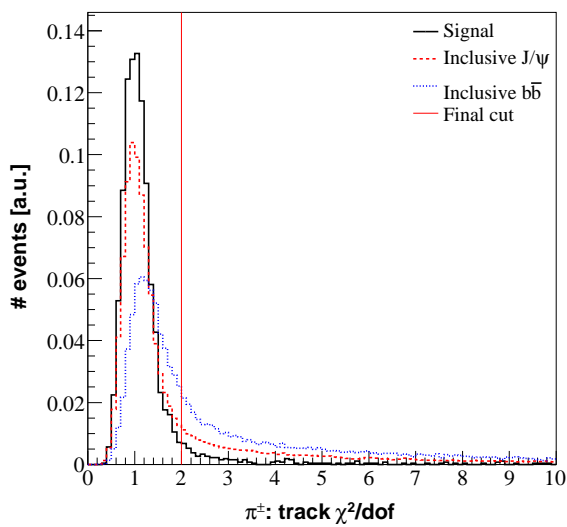
(b)
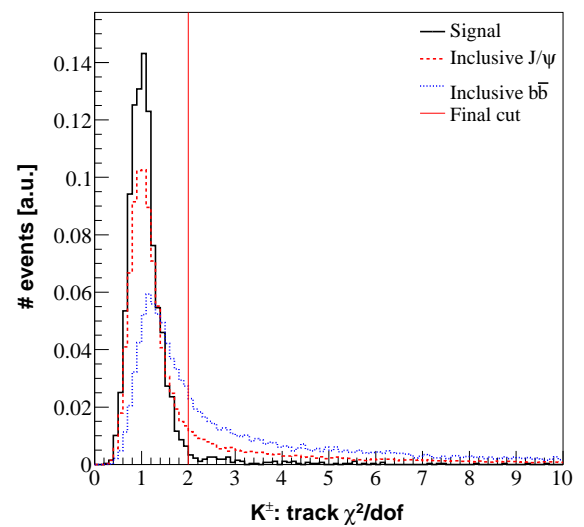
(c)

Figure 6.3: Distribution of the track fit $\chi^2$/dof for (a) the muons, (b) the pions and (c) the kaons in $B^\pm \rightarrow (X(3872) \rightarrow (J/\psi \rightarrow \mu^+\mu^-)\pi^+\pi^-)K^\pm$ decays. The red vertical lines indicate the value of the cut in the final selection.
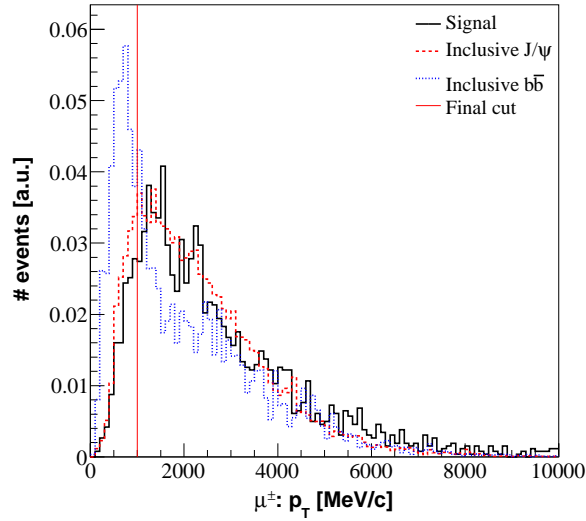
Figure 6.4: Transverse momentum distribution of the two charged muons in $B^{\pm} \rightarrow (X(3872) \rightarrow (J/\psi \rightarrow \mu^{+}\mu^{-})\pi^{+}\pi^{-})K^{\pm}$ events, after a loose pre-selection. The red vertical line indicates the value of the cut in the final selection.

distributions respectively. Only true signal events are shown, where the full reconstructed decay is matched to a decay in the Monte Carlo truth. Fitting the signal distributions with a single Gaussian yields the following mass resolutions:

$$\sigma_{M_{J/\psi}} = 12.2 \, \text{MeV}/c^2 \,, \qquad (6.7)$$

$$\sigma_{M_{X(3872)}} = 13.2 \, \text{MeV}/c^2 \,, \qquad (6.8)$$

$$\sigma_{M_{B^{\pm}}} = 14.8 \, \text{MeV}/c^2 \,. \qquad (6.9)$$

In order to reject a large fraction of the background while keeping the signal, a cut can be chosen as a $\pm 3\sigma$ window around the true Monte Carlo mass. Rounded values of $\pm 50 \, \text{MeV}/c^2$ and $\pm 35 \, \text{MeV}/c^2$ are chosen for the $B^{\pm}$ and the $J/\psi$ mass windows respectively. On the other hand, the cut on the $X(3872)$ mass is tightened to $\pm 40 \, \text{MeV}/c^2$. In a first step, this cut is only used for the signal sample. The requirement for the background samples is kept loose ($\pm 500 \, \text{MeV}/c^2$) in order to artificially increase the background statistics. In the calculation of the background level, a linear background distribution will be assumed and a factor of $\frac{40}{500}$ equal to the ratio of the widths of the two mass windows will be used to scale down the background level from the wide mass window to the tight window.

Two more selection criteria are used to further reduce the background level. First, the PID log likelihood difference between the pion and electron hypotheses, shown in Fig. 6.6, is required to be larger than zero: $\Delta \ln \mathcal{L}_{\pi e}(\pi^{\pm}) > 0$. The next powerful criterion to discriminate between signal and background events is the angle between the $B^{\pm}$-meson flight direction, computed from the primary vertex and the $B^{\pm}$ decay vertex, and the direction given by its momentum. A drawing defining this angle is shown in Fig. 6.7 (a). The distribution of the cosine of this angle, which is used in the selection process, is shown
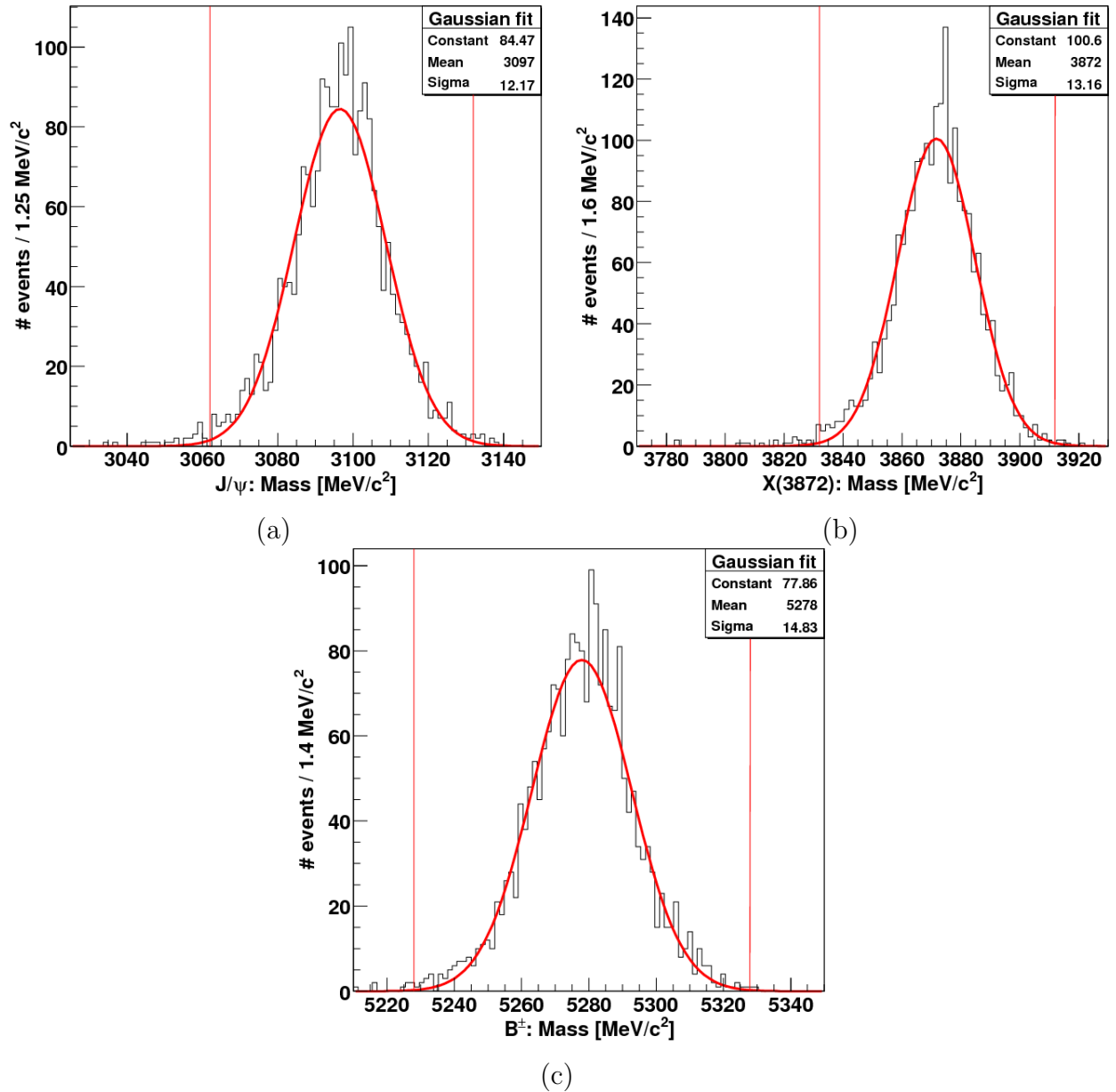
Figure 6.5: Mass distributions of (a) the $J/\psi$, (b) the $X(3872)$ and (c) the $B^{\pm}$ candidates in $B^{\pm} \to (X(3872) \to J/\psi\pi^+\pi^-)K^{\pm}$ events, after a loose pre-selection. Only candidates matched to a true decay in the Monte-Carlo truth are reported. The results of a Gaussian fit (red line on the histogram) are reported in the box in the upper-right corner. The red vertical lines indicate the tight mass window used in the final selection. These histograms are not normalised.
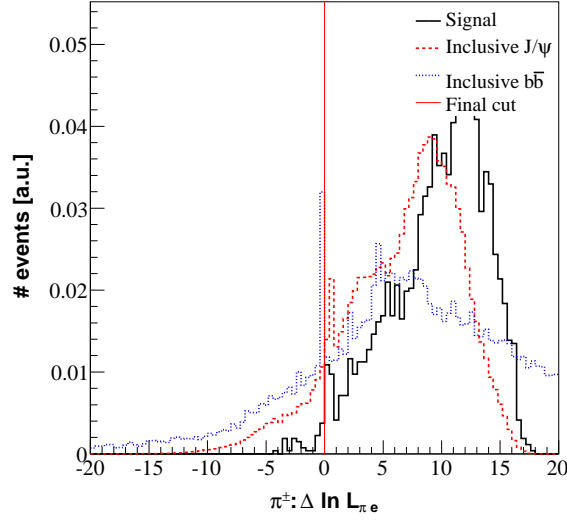
Figure 6.6: Distribution of the PID log likelihood difference between the pion and electron hypotheses for $\pi^{\pm}$ in $B^{\pm} \rightarrow (X(3872) \rightarrow J/\psi\pi^{+}\pi^{-})K^{\pm}$ events. The red vertical line indicates the value of the cut in the final selection.

in Fig. 6.7 (b). A cut is chosen at $\cos\theta_{B^{\pm}} > 0.99998$, which corresponds to an angle of 6.32 mrad.

Finally, the following criteria are thought to be the most discriminating ones:

$\chi^2/\text{dof}(B^{\pm}\ \text{vtx})$: The constraint on the vertex fit is very effective due to the combination of five tracks coming from the same vertex. Hence, the $B^{\pm}$ vertex $\chi^2/\text{dof}$, shown in Fig. 6.8 (a), is chosen as one of the optimisation variables.

$\text{FD}(B^{\pm})$: The fact that the $X(3872)$ is the product of a $B$-meson decay can be used by requiring the $X(3872)$ origin vertex to be displaced with respect to the primary vertex. The $B^{\pm}$ meson is required to have a positive flight distance (Fig. 6.8 (b)).

$\min(p_{\text{T}}(\pi^{+}), p_{\text{T}}(\pi^{-}))$: The two pions in the $X(3872)$ decay tend to have a large transverse momentum $p_{\text{T}}$, as visible in Fig. 6.9 (a).

$p_{\text{T}}(K^{\pm})$: The kaon in the $B$ decay tends to have a large transverse momentum $p_{\text{T}}$, as visible in Fig. 6.9 (b).

$\min(\Delta \ln \mathcal{L}_{K\mu}(K^{\pm}), \Delta \ln \mathcal{L}_{Ke}(K^{\pm}))$: The identification of the kaons is not perfect. They can be mis-identified as muons, electrons, pions or protons. In order to increase the purity of the selected kaon, the PID log likelihood differences between the kaon hypothesis and the muon or electron hypothesis are used to discriminate between signal and background events (Fig. 6.10).

Loose cuts are set on these variables in order to reject some background while allowing for a proper optimisation of the cuts. The cuts of the loose and tight pre-selections are summarised in the third and fourth columns of Table 6.2 respectively.

(a)          (b)
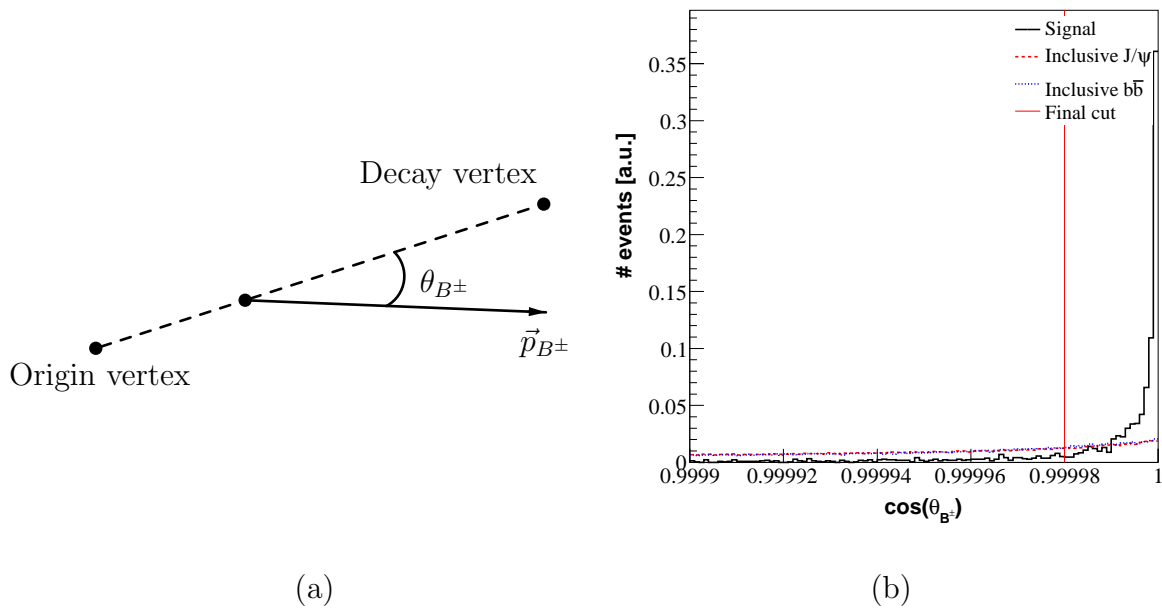
Figure 6.7: (a) Graphical definition of the direction angle of the $B^{\pm}$ meson, where $\vec{p}_{B\pm}$ is the reconstructed momentum. (b) Distribution of the cosine of this angle for $B^{\pm} \rightarrow X(3872)K^{\pm}$ candidates. The red vertical line indicates the value of the cut in the final selection.



(a)          (b)
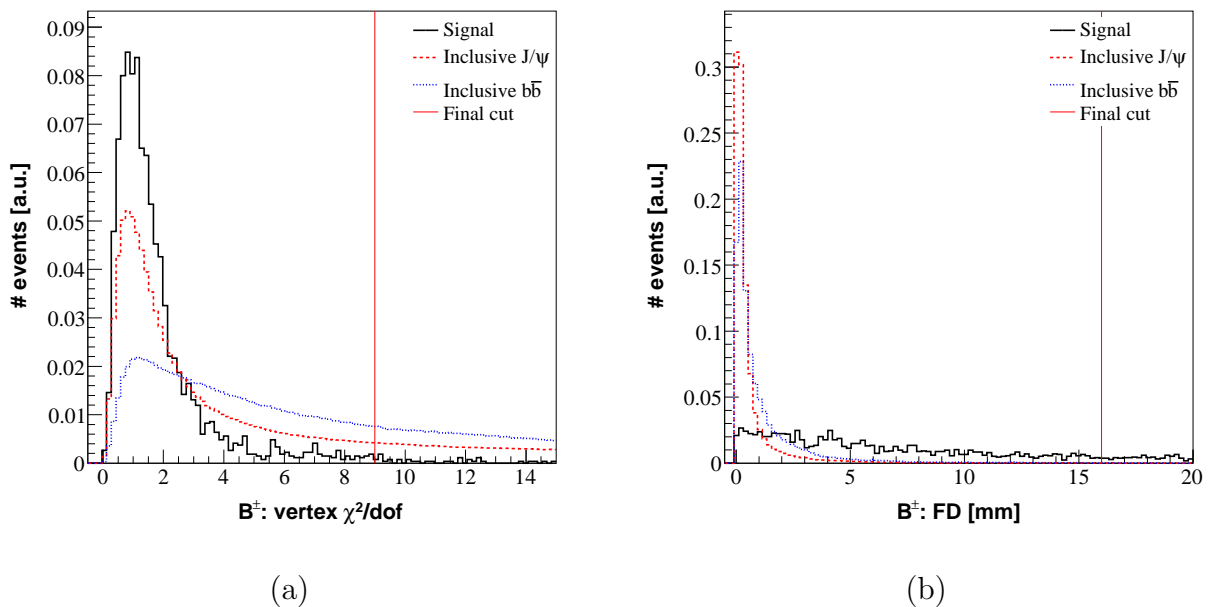
Figure 6.8: (a) Quality ($\chi^2$/dof) of the $B^{\pm}$ vertex fit and (b) $B^{\pm}$ flight distance in $B^{\pm} \rightarrow X(3872)K^{\pm}$ events after a loose pre-selection. The red vertical lines indicate the values of the cuts used in the final selection.

(a)                                                          (b)
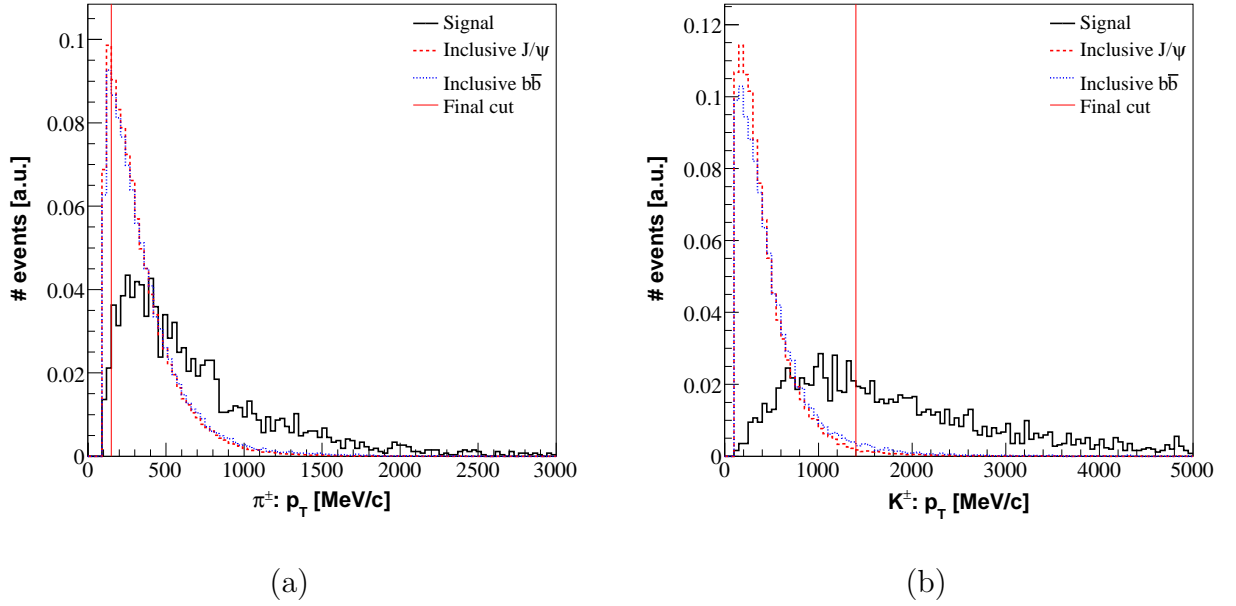
Figure 6.9: Transverse momentum distribution of (a) the two charged pions, and (b) the kaon in $B^{\pm} \rightarrow (X(3872) \rightarrow J/\psi \, \pi^{+}\pi^{-})K^{\pm}$ events, after a loose pre-selection. The vertical lines indicate the values of the cuts used in the final selection.



(a)                                                          (b)
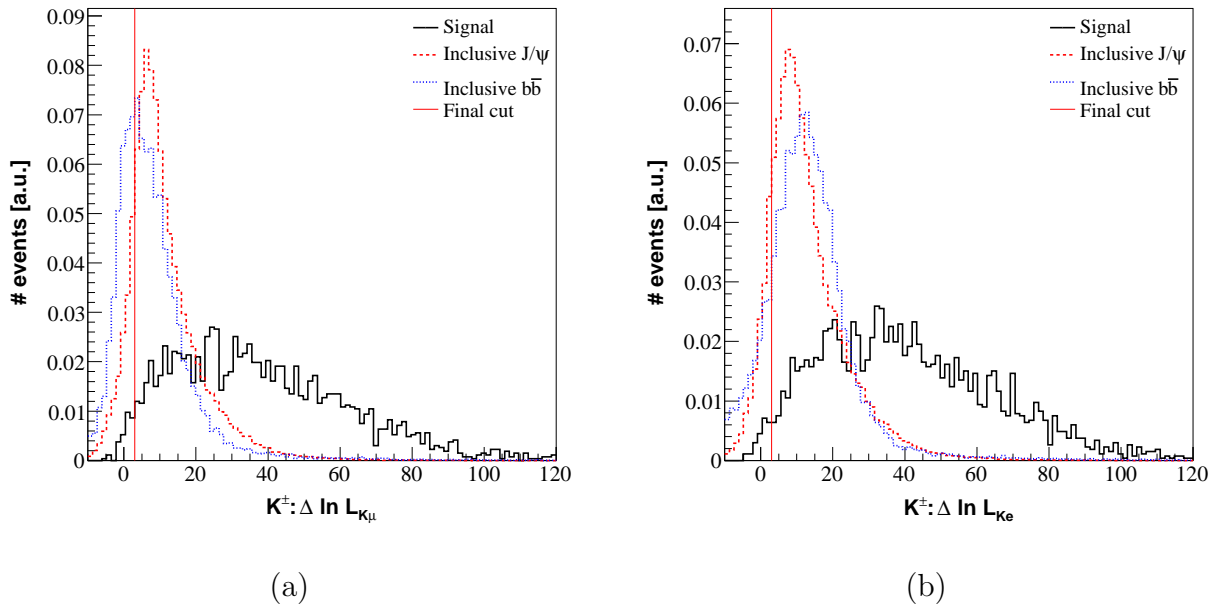
Figure 6.10: Distributions of the PID log likelihood differences between the kaon hypothesis and (a) the muon or (b) the electron hypothesis for the kaons in $B^{\pm} \rightarrow (X(3872) \rightarrow J/\psi\pi^{+}\pi^{-})K^{\pm}$ decays. The red vertical lines indicate the values of the cuts used in the final selection.

### 6.1.3   *X*(3872) Final Selection

The final selection is performed with the TMVA toolkit [142]. This package offers several methods to optimise a selection. Given a set of input variables, it returns a set of cut values maximising the signal with respect to a given background sample. The optimisation is performed against the inclusive $J/\psi$ sample.

The five variables given in Section 6.1.2 are used as input variables in TMVA. The method used is a simple cut method, where the variables are scanned recursively. The method maximises the signal significance defined as

$$\text{significance} = \frac{S}{\sqrt{B + S}}\,, \qquad (6.10)$$

where $S$ and $B$ are the expected numbers of selected signal and background events respectively (normalised to the same luminosity) in the $\pm 40 \,\text{MeV}/c^2$ $X$(3872) mass window.

In order to avoid excessive tuning, the cut values are required to be round numbers. The chosen values are reported in the fifth column of Table 6.2. Figure 6.11 shows the optimisation of the five cuts independently. Each plot shows the signal significance as a function of one of the cuts, with the four others set at their optimal values.

### 6.1.4   Results of the *X*(3872) Selection

Before a proper calculation of the selection efficiency is performed, useful numbers are defined here.

$N_{\mathbf{gen}}$: Number of true generated signal decays that are analysed in this study.

$N_{\mathbf{rec'ible}}$: Number of true reconstructible decays found in the $N_{\text{gen}}$ events. A candidate is defined as being reconstructible with long tracks if at least three $r$ and three $\phi$ VELO hits and at least one $x$ and one stereo hit in each of the three Tracking Stations are assigned to each of the tracks forming the decay of interest.

$N_{\mathbf{rec'ed}}$: Number of true reconstructed decays in the whole sample. The subset of reconstructed decays is not necessarily entirely included in the subset of reconstructible decays.

$N_{\mathbf{rec'ed/ible}}$: Number of true decays that are both reconstructible and reconstructed.

$N_{\mathbf{sel}}$: Number of true decays that pass all the selection criteria, except for the two levels of trigger.

$N_{\mathbf{L0}}$: Number of true selected decays that pass the Level-0 Trigger.

$N_{\mathbf{HLT}}$: Number of true offline- and L0-selected decays that pass the HLT1 and HLT2 requirements.

Applying the cuts defined in the two previous sections (pre-selection and final selection), a selection efficiency on the signal can be calculated. This total selection efficiency

(a)

(b)

(c)

(d)

(e)
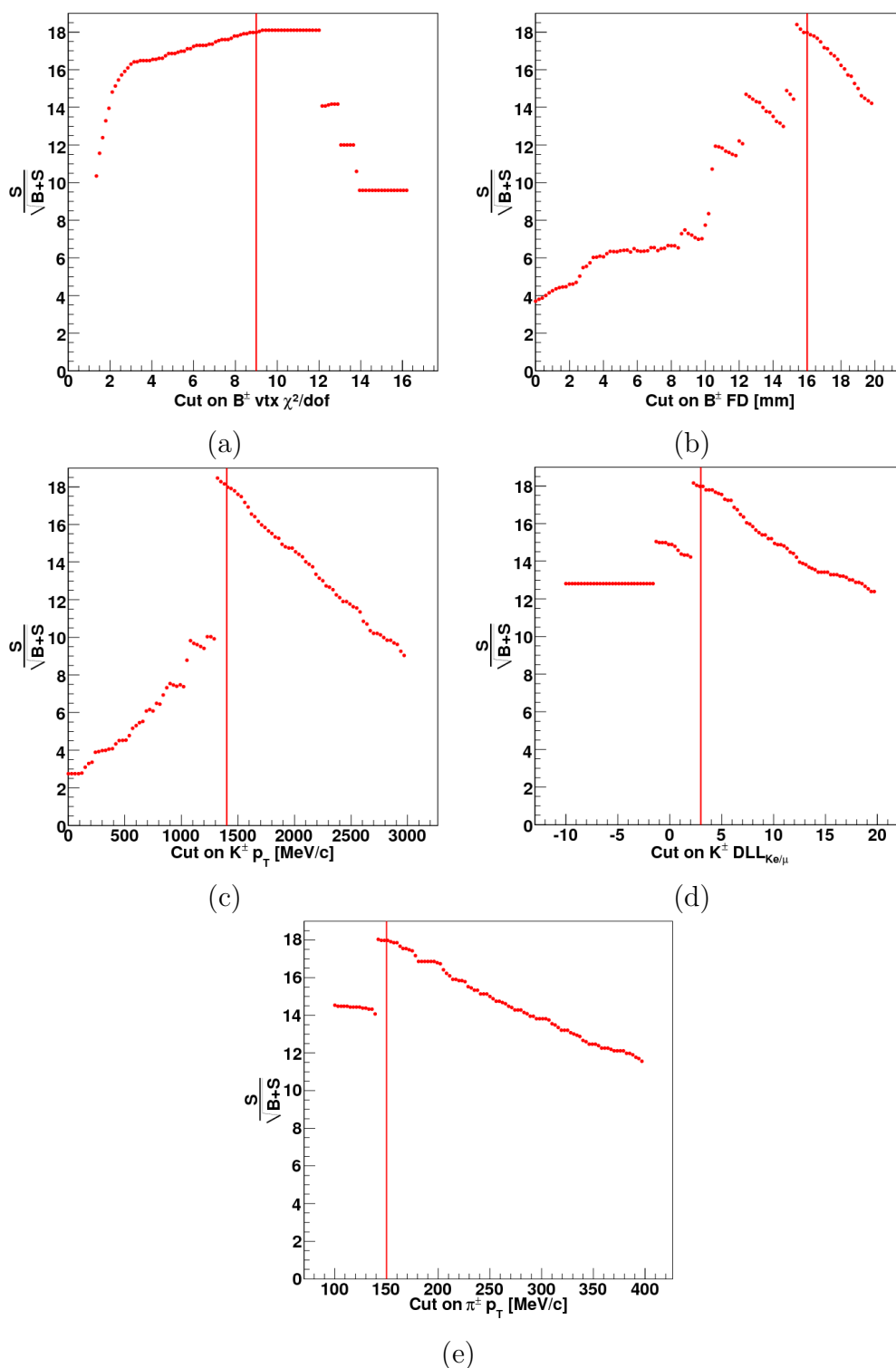
Figure 6.11: Optimisation of the five cuts chosen in Section 6.1.2. The optimisation is shown for each variable individually, with the other cuts set to their optimal values. (a) Cut on the $\chi^2/\text{dof}$ of the $B^{\pm}$-meson vertex. (b) Cut on the $B^{\pm}$-meson flight distance. (c) Cut on the $K^{\pm}$ transverse momentum. (d) Cut on the $K^{\pm}$ PID log likelihood difference. (e) Cut on the $\pi^{\pm}$ transverse momentum. The red vertical lines indicate the values of the cuts used in the final selection. Jumps are due to the low background statistics.

Table 6.2: Summary of the offline cuts used for the selection of the $X(3872) \to J/\psi \, \pi^+\pi^-$ signal in $B^\pm$ decays. The underlined cut values are the result of the optimisation described in Section 6.1.3.

| Variable | | Loose pre-selection | Tight pre-selection | Final selection |
|---|---|---|---|---|
| **$J/\psi$** | | | | |
| $\mu^\pm$: std. sel. defined in Section 3.1.5 | | | | |
| $\mu^\pm$: track $\chi^2/\mathrm{dof}$ | < | 12 | 2 | 2 |
| $\mu^\pm$: $p_\mathrm{T}$ | > | — | $1000\,\mathrm{MeV}/c$ | $1000\,\mathrm{MeV}/c$ |
| $\mu\mu$ vertex $\chi^2/\mathrm{dof}$ | < | 30 | 30 | 30 |
| $\left|m_{\mu\mu} - M_{J/\psi}\right|$ | < | $100\,\mathrm{MeV}/c^2$ | $35\,\mathrm{MeV}/c^2$ | $35\,\mathrm{MeV}/c^2$ |
| **$X(3872)$** | | | | |
| $\pi^\pm$: std. sel. defined in Section 3.1.5 | | | | |
| $\pi^\pm$: track $\chi^2/\mathrm{dof}$ | < | 12 | 2 | 2 |
| $\pi^\pm$: $p_\mathrm{T}$ | > | — | $100\,\mathrm{MeV}/c$ | $\underline{150\,\mathrm{MeV}/c}$ |
| $\pi^\pm$: $\Delta \ln \mathcal{L}_{\pi e}$ | > | — | 0 | 0 |
| $\mu\mu\pi\pi$ vertex $\chi^2/\mathrm{dof}$ | < | 25 | 25 | 25 |
| $\left|m_{\mu\mu\pi\pi} - M_{X(3872)}\right|^{\mathrm{sig}}$ | < | $500\,\mathrm{MeV}/c^2$ | $40\,\mathrm{MeV}/c^2$ | $40\,\mathrm{MeV}/c^2$ |
| $\left|m_{\mu\mu\pi\pi} - M_{X(3872)}\right|^{\mathrm{bkg}}$ | < | $500\,\mathrm{MeV}/c^2$ | $500\,\mathrm{MeV}/c^2$ | $500\,\mathrm{MeV}/c^2$ |
| **$B^\pm$** | | | | |
| $K^\pm$: std. sel. defined in Section 3.1.5 | | | | |
| $K^\pm$: track $\chi^2/\mathrm{dof}$ | < | 12 | 2 | 2 |
| $K^\pm$: $p_\mathrm{T}$ | > | — | $100\,\mathrm{MeV}/c$ | $\underline{1400\,\mathrm{MeV}/c}$ |
| $K^\pm$: $\Delta \ln \mathcal{L}_{K\mu}$ | > | — | — | $\underline{3}$ |
| $K^\pm$: $\Delta \ln \mathcal{L}_{Ke}$ | > | — | — | $\underline{3}$ |
| $\mu\mu\pi\pi K$ vertex $\chi^2/\mathrm{dof}$ | < | 15 | 15 | $\underline{9}$ |
| $\left|m_{\mu\mu\pi\pi K} - M_{B^\pm}\right|$ | < | $100\,\mathrm{MeV}/c^2$ | $50\,\mathrm{MeV}/c^2$ | $50\,\mathrm{MeV}/c^2$ |
| $B^\pm$: $\cos\theta_{B^\pm}$ | > | — | 0.99998 | 0.99998 |
| $B^\pm$: flight distance | > | — | — | $\underline{16\,\mathrm{mm}}$ |

can be broken down into the offline selection efficiency, the L0-Trigger efficiency and the HLT efficiency:

$$\epsilon_{\text{tot}} = \epsilon_{\text{off}} \times \epsilon_{\text{L0}} \times \epsilon_{\text{HLT}}. \tag{6.11}$$

The offline selection efficiency can further be separated into the detection efficiency (including the angular acceptance of the detector and the fraction of events that are reconstructible in the detector), the reconstruction efficiency (the fraction of reconstructible events that are reconstructed) and the selection efficiency (the fraction of reconstructed events that are selected by the final set of cuts):

$$\epsilon_{\text{off}} = \epsilon_{\text{det}} \times \epsilon_{\text{rec/det}} \times \epsilon_{\text{sel/rec}} = \frac{N_{\text{sel}}}{N_{\text{gen}}} \times \epsilon_{\theta}^{B^{\pm} \to X(3872)K^{\pm}}. \tag{6.12}$$

The number of generated events is reported in Table 6.1 for both the signal and the background samples. The factor $\epsilon_{\theta}^{B^{\pm} \to X(3872)K^{\pm}}$ is reported in Table 6.1. The reconstruction and selection efficiencies are obtained using the numbers defined above:

$$\epsilon_{\text{rec/det}} = \frac{N_{\text{rec'ed/ible}}}{N_{\text{rec'ible}}} \text{ and } \epsilon_{\text{sel/rec}} = \frac{N_{\text{sel}}}{N_{\text{rec'ed}}}. \tag{6.13}$$

From the above definitions, the detection efficiency can be calculated as

$$\epsilon_{\text{det}} = \frac{\epsilon_{\text{off}}}{\epsilon_{\text{rec/det}} \times \epsilon_{\text{sel/rec}}}. \tag{6.14}$$

Finally, the trigger efficiencies are calculated as

$$\epsilon_{\text{L0}} = \frac{N_{\text{L0}}}{N_{\text{sel}}} \quad \text{and} \quad \epsilon_{\text{HLT}} = \frac{N_{\text{HLT}}}{N_{\text{L0}}}. \tag{6.15}$$

The number of selected events is equal to 266 before trigger, which is reduced to 243 by the two levels of trigger. These numbers are reported in Table 6.3. A total efficiency of $(0.17 \pm 0.01)\%$ is found, with the breakdown reported in Table 6.4. The uncertainties quoted on these efficiencies, on the signal yield and on the $B/S$ ratio only reflect the Monte Carlo statistics. Other uncertainties, such as those on the assumed values of the cross sections, are not taken into account in the error propagation.

### 6.1.4.a Annual $X(3872)$ Signal Yield

The annual signal yield, $N_{\text{phys}}$, is defined as the number of reconstructed, selected and triggered signal events in one nominal year. A nominal year is defined as $10^7$ seconds of data taking at the design luminosity of $2 \times 10^{32}\,\text{cm}^{-2}\text{s}^{-1}$ corresponding to an integrated luminosity of $\mathcal{L}_{\text{int}} = 2\,\text{fb}^{-1}$. $N_{\text{phys}}$ is obtained by multiplying the total number of expected events produced in the $pp$ collisions at LHCb by the total reconstruction, selection and trigger efficiency:

$$N_{\text{phys}} = \mathcal{L}_{\text{int}} \times \sigma_{b\bar{b}} \times 2 \times f_{B^{\pm}} \times \mathcal{B}_{\text{vis}}^{\text{sig}} \times \epsilon_{\text{tot}}^{\text{sig}} = \frac{\mathcal{L}_{\text{int}}}{\mathcal{L}_{\text{int}}^{B^{\pm} \to X(3872)K^{\pm}}} \times N_{\text{sel}}, \tag{6.16}$$

where $\mathcal{L}_{\text{int}}^{B^{\pm} \to X(3872)K^{\pm}}$ is the integrated luminosity, reported in Table 6.1, corresponding to the statistics of the signal sample. The total selection efficiency is reported in Table 6.4.

Table 6.3: Number of signal events in the $B^{\pm} \to (X(3872) \to (J/\psi \to \mu^+\mu^-)\pi^+\pi^-)K^{\pm}$ signal sample that are generated, reconstructible, reconstructed, selected, triggered by L0 and triggered by HLT.

| | |
|---|---|
| $N_{\text{gen}}$ | 50734 |
| $N_{\text{rec'ible}}$ | 5499 |
| $N_{\text{rec'ed}}$ | 4532 |
| $N_{\text{rec'ed/ible}}$ | 4130 |
| $N_{\text{sel}}$ | 266 |
| $N_{\text{L0}}$ | 253 |
| $N_{\text{HLT}}$ | 243 |

Table 6.4: Summary of the signal efficiencies for the selection of $B^{\pm} \to (X(3872) \to (J/\psi \to \mu^+\mu^-)\pi^+\pi^-)K^{\pm}$ events.

| Factors (in %) forming $\epsilon_{\text{tot}}$ (in %) | | | | |
|---|---|---|---|---|
| $\epsilon_{\text{tot}} = \epsilon_{\text{det}} \times \epsilon_{\text{rec/det}} \times \epsilon_{\text{sel/sec}} \times \epsilon_{\text{trg/sel}}$ | | | | |
| $\epsilon_{\text{det}}$ | $\epsilon_{\text{rec/det}}$ | $\epsilon_{\text{sel/rec}}$ | $\epsilon_{\text{trg/sel}}$ | $\epsilon_{\text{tot}}$ |
| $4.1 \pm 0.4$ | $75 \pm 1$ | $5.9 \pm 0.4$ | $91 \pm 2$ | $0.17 \pm 0.01$ |

Using these numbers, an annual signal yield at the nominal running conditions can be calculated:

$$N_{\text{phys}}^{B^{\pm} \to X(3872)K^{\pm}} = 1850 \pm 120\,. \tag{6.17}$$

This result can be compared with the number of events collected by CDF at the Tevatron. Figure 1.10 shows the latest results for the measurement of the $X(3872)$ mass in the $J/\psi\,\pi^+\pi^-$ channel. The number of selected $X(3872)$ candidates is around 6000. This number of candidates was found in data collected between February 2002 and August 2007, i.e. more than 5 years of data taking, in a sample corresponding to an integrated luminosity of $2.4\,\text{fb}^{-1}$. This CDF sample takes into account both the $X(3872)$ in $b$-hadron decays and the "prompt" $X(3872)$ created directly in the $\bar{p}p$ collisions at a centre-of-mass energy of $\sqrt{s} = 1.96\,\text{TeV}$. According to a preliminary result from the CDF collaboration, based on a sample corresponding to $220\,\text{pb}^{-1}$ of integrated luminosity, the fraction of "long-lived" $X(3872)$ (found in $b$-hadron decays) is $(16.1 \pm 4.9 \pm 2.0)\,\%$ [143]. This means that they reconstructed around 1000 $X(3872)$ candidates from $b$-hadron decays. However, this number is made of various sources and no estimate is given of the $B^{\pm} \to X(3872)K^{\pm}$ contribution to this yield. Hence, LHCb should quickly (in less than a nominal year) reach and exceed the CDF statistics, even with a first phase at $\sqrt{s} = 7$ or $10\,\text{TeV}$, for which the expectation value from the Monte Carlo generator for the $b\bar{b}$ cross section is reduced by 50 or 30 % respectively. In addition, the event sample that pass the selection presented in this study will be a pure source of $B^{\pm} \to X(3872)K^{\pm}$ decays, which allow to disentangle between the two $X(3872)$ spin hypotheses, as visible in Fig. 6.1.

### 6.1.4.b $B/S$ Estimate for the $X(3872)$ Selection

In order to study the quantum numbers of the $X(3872)$ and to constrain the models explaining its nature, studies of the angular distribution of the decay products are needed. These studies are sensitive to the background level as it dilutes the distributions and complicates the measurement. An important number to assess the quality of the selection is the background-to-signal ratio, $B/S$, estimated as

$$\frac{B}{S} = \frac{N_{\text{phys}}^{\text{bkg}}}{N_{\text{phys}}^{\text{sig}}} \times \frac{\delta M^{\text{sig}}}{\delta M^{\text{bkg}}} . \tag{6.18}$$

The last factor comes from the fact that the number of events is counted in a tight mass window around the $X(3872)$ mass for the signal, but in a loose mass window for the background, in order to artificially increase the background statistics. This factor is equal to $\frac{40}{500} = 0.08$ with the cuts described in the previous sections. The calculation assumes the background to have a linear distribution in the $\pm 500 \, \text{MeV}/c^2$ mass window around the $X(3872)$ signal mass peak. The annual signal yield $N_{\text{phys}}^{\text{sig}}$ is discussed in Section 6.1.4.a. The number of selected background events per year is calculated in a similar way, using the corresponding integrated luminosities reported in Table 6.1:

$$N_{\text{phys}}^{\text{incl. } J/\psi} = \frac{\mathcal{L}_{\text{int}}}{\mathcal{L}^{\text{incl. } J/\psi}} \times N_{\text{HLT}}^{\text{incl. } J/\psi} , \tag{6.19}$$

$$N_{\text{phys}}^{\text{incl. } b\bar{b}} = \frac{\mathcal{L}_{\text{int}}}{\mathcal{L}^{\text{incl. } b\bar{b}}} \times N_{\text{HLT}}^{\text{incl. } b\bar{b}} . \tag{6.20}$$

The number of selected events is counted after the offline selection and the L0 and HLT Triggers.

Running the full selection on the sample of inclusive $J/\psi$ events, one candidate passes all the cuts, i.e. $N_{\text{HLT}}^{\text{incl. } J/\psi} = 1$. Using Equations 6.18 and 6.19 with the number of generated events from Table 6.1 and the annual signal yield from Equation 6.17, the contribution of the inclusive $J/\psi$ sample to the $B/S$ ratio is estimated to be 1.0. Looking at the Monte Carlo truth, the selected event appears to be an incompletely reconstructed exclusive decay $B^+ \to (J/\psi \to \mu^+\mu^-)(K_2^{+*}(1430) \to (K^{0*}(892) \to K^+\pi^-\gamma)\pi^+\gamma)$, where all the charged tracks are reconstructed, but not the two photons. However, since the two photons have a low energy, the $B$ meson is reconstructed within the $50 \, \text{MeV}/c^2$ mass window around the true $B^{\pm}$ mass. This is an indication of a possible background to analyse in further studies.

Next, the sample of inclusive $b\bar{b}$ events is studied. One event is selected out of the 26 millions that were generated. Using Equations 6.18 and 6.20 with the relevant numbers, the contribution of the inclusive $b\bar{b}$ sample to the $B/S$ ratio is estimated to be 1.5. Looking at the Monte Carlo truth, it appears that this decay is a fully reconstructed decay mimicking the signal: $B^- \to \pi^-(J/\psi \to \mu^-\mu^+)(K^{0*}(892) \to \pi^+K^-)$. This decay is similar to that found in the sample of inclusive $J/\psi$ events with a true $J/\psi$ and an excited $K$ state from a $B$-meson decay. In further studies, these decays should be analysed in order to have a better estimate of the background level to expect and the mass distributions in the $X(3872)$ mass window. Indeed, in case the background peaks outside the tight mass window (this information is not known with such low statistics), the background level could be over-estimated in the present studies.

From the studies of the two selected decays in the two inclusive background samples, the assumption can be made that the background is dominated by $b \to J/\psi$ decays, i.e. events where a $b$ hadron decays to a final state with a $J/\psi$ meson. Since the two inclusive samples are independent, they can be added in order to increase the background statistics. However, since the two samples have not been generated identically, the total background level is not the sum of Equations 6.19 and 6.20. First, it can be checked from the values of the corresponding integrated luminosities given in Table 6.1 that the selections of one candidate in each sample corresponding to the confidence interval [0.11, 4.36] at 90 % CL (taken from Ref. [144]) are statistically compatible. Next, the expected annual number of $b \to J/\psi$ background events is calculated as

$$N_{\mathrm{phys}}^{\mathrm{bkg}} = \mathcal{L}_{\mathrm{int}} \times \frac{N_{\mathrm{HLT}}^{\mathrm{incl.}\,J/\psi} + N_{\mathrm{HLT}}^{\mathrm{incl.}\,b\bar{b}}}{\mathcal{L}_{\mathrm{int}}^{\mathrm{incl.}\,J/\psi} + \mathcal{L}_{\mathrm{int}}^{\mathrm{incl.}\,b\bar{b}}} \ . \tag{6.21}$$

Since the number of selected events is low (two events from the two inclusive samples counted together), it is better to use confidence intervals for the background level in the calculation of the $B/S$ estimate. Using the Feldman-Cousins technique described in [144], for two events observed, the interval [0.53, 5.91] is given at 90 % confidence level. Using this interval in Equation 6.21 and combining with the numbers of generated events from Table 6.1 and the annual signal yield from Equation 6.17, the $B/S$ ratio is estimated to lie within the interval [0.3, 3.4] at 90 % CL. The assumption discussed above that the background has a linear distribution in the $\pm 500\,\mathrm{MeV}/c^2$ window around the $X(3872)$ mass is made here, although it will need to be verified on a larger background sample. Figure 6.12 shows the $X(3872)$ mass peak in the $\pm 500\,\mathrm{MeV}/c^2$ mass window with the two sources of background discussed here. The distributions of inclusive $J/\psi$ and $b\bar{b}$ are scaled such as to indicate the level of a linear distribution corresponding to a $B/S$-ratio of 1.0 and 1.5 respectively. In order to have a better estimate of the background level and further confirm the hypothesis that only $b \to J/\psi$ events contribute to the background, more statistics are needed, both for the sample of inclusive $J/\psi$ events and for the inclusive $b\bar{b}$ events. Also, the possible contribution from minimum bias events could be investigated with a larger sample (no event is selected in the available sample of 19.2 million events).

The annual signal yield can be increased by relaxing some selection criteria. For example, relaxing the cut on the kaon transverse momentum to $1\,\mathrm{GeV}/c$ increases the yield by 25 %, but at the cost of a $B/S$ contribution from the inclusive $J/\psi$ of 10.3, including a decay reconstructed from a prompt $J/\psi$. Also, the value of the cut on the $B^{\pm}$-meson flight distance given by the optimisation process seems tight, as visible in Fig. 6.8 (b). But the statistics after the cuts are very low. Performing the optimisation on larger data samples could allow to loosen this cut. Larger background samples are also needed to study additional selection criteria to further reduce the background level.

Finally, the number of signal events will be increased by the sample of prompt $X(3872)$ coming directly from the $pp$ collision. As discussed in the introduction of this chapter, prompt $X(3872)$ are a pollution in the angular distributions used to discriminate between the two $X(3872)$ spin hypotheses. However, the cuts described in Sections 6.1.2 and 6.1.3 are expected to be powerful enough to reject most of this background source. Especially, the cut on the $B^{\pm}$ flight distance will make sure that most of the prompt component is rejected. This should be verified on a sample of prompt $X(3872)$ from $pp$ collisions,
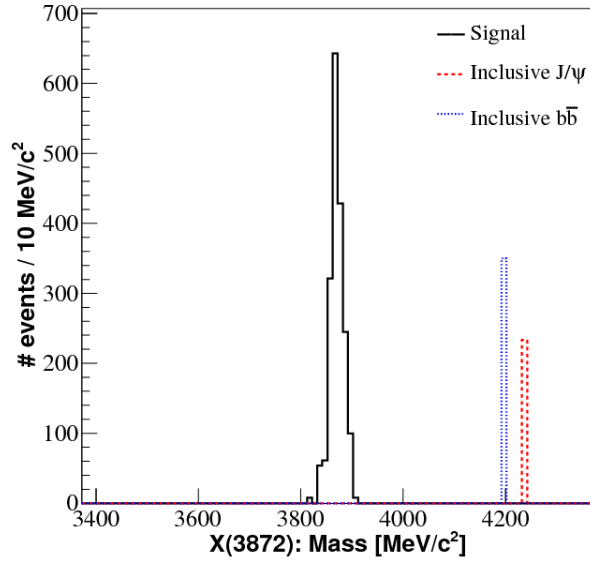
Figure 6.12: Mass distribution of the $X(3872)$ in the $\pm 500\,\mathrm{MeV}/c^2$ mass window after selection. The events selected in the inclusive $J/\psi$ and $b\bar{b}$ samples are scaled such as to reflect the corresponding individual contribution to the $B/S$ ratio (given in the text).

but no such sample is available at the time of this study. If, on the other hand, a selection of prompt $X(3872)$ is needed, a proper optimisation is required. As described in Sections 6.1.2 and 6.1.3, three cuts are related to the $B^{\pm}$ meson from which the $X(3872)$ originates: the $B^{\pm}$ mass, vertex $\chi^2/\mathrm{dof}$ and flight distance. Furthermore, the track fit quality of the kaon, its transverse momentum and the PID log likelihood differences are also used as selection criteria. These cuts are powerful for the selection of $B^{\pm} \rightarrow X(3872)K^{\pm}$ events. Removing them of the selection process to select prompt $X(3872)$ candidates will also allow many more background events to pass the selection. These problems need to be addressed in a subsequent study.

## 6.2 $Z(4430)^{\pm}$ Selection

The selection of the $Z(4430)^{\pm} \rightarrow \psi(2S)\pi^{\pm}$ decay in the $B^0 \rightarrow Z(4430)^{\pm}K^{\mp}$ channel follows the same steps as the selection of the $X(3872)$ described in Section 6.1.

### 6.2.1 Data Samples Used in the $Z(4430)^{\pm}$ Study

The selection is performed using a sample of 18'397 events with a $B^0 \rightarrow (Z(4430)^{\pm} \rightarrow (\psi(2S) \rightarrow \mu^+\mu^-)\pi^{\pm})K^{\mp}$ signal decay chain, generated using GAUSS v36r2, digitised with BOOLE v17r2 and reconstructed in BRUNEL v34r1p1. The requirement at the generation level is that the signal $B^0$ meson is found in the geometrical acceptance. The efficiency of this requirement doesn't depend on the $B$-meson species nor on its decay chain. The value of this efficiency is therefore the same as for the $B^{\pm} \rightarrow X(3872)K^{\pm}$: $\epsilon_{\theta}^{B^0 \rightarrow Z(4430)^{\pm}K^{\mp}} = (34.6 \pm 0.1)\,\%$. In addition to the signal sample, the following background samples are studied:

**Inclusive $J/\psi$:** This sample is described in Section 6.1.1. The $J/\psi$ is significantly lighter than the $\psi(2S)$ and should therefore not be a problematic background in this study.

**Inclusive $\psi(2S)$:** A sample of 28'353 inclusive $\psi(2S) \to \mu^+\mu^-$ events has been generated with GAUSS v36r2, digitised with BOOLE v17r2 and reconstructed in BRUNEL v34r1p1. The requirement for this sample is that at least one $\psi(2S)$ decaying to a di-muon pair must be found in the event with each muon in the LHCb geometrical acceptance. The efficiency of this generation level requirement is $\epsilon_\theta^{\text{incl. }\psi(2S)} = (19.09 \pm 0.15)\,\%$. The expected production cross-section in $4\,\pi$, given by the Pythia event generator, has a value of $\sigma_{\text{incl. }\psi(2S)} = (8.5 \pm 1)\,\mu\text{b}$.

**Inclusive $b\bar{b}$:** This sample is described in Section 6.1.1.

**Minimum bias:** This sample is described in Section 6.1.1.

The value of the acceptance factor for the data types studied here are reported in Table 6.5. These factors are taken into account in the calculation of the annual signal yield in Section 6.2.4.a and of the $B/S$ ratio in Section 6.2.4.b. The integrated luminosity corresponding to the statistics of the sample is again reported. The calculation of this value is give in Equation 6.1. The detailed calculation is shown here for the total cross sections of the two new data samples, the $B^0 \to Z(4430)^{\pm}K^{\mp}$ signal sample and the inclusive $\psi(2S)$ background sample:

$$\sigma_{\text{tot}}^{B^0 \to Z(4430)^{\pm}K^{\mp}} = \sigma_{b\bar{b}} \times 2 \times f_{B^0} \times \mathcal{B}_{\text{vis}}^{B^0 \to Z(4430)^{\pm}K^{\mp}} \times \epsilon_\theta^{B^0 \to Z(4430)^{\pm}K^{\mp}}, \quad (6.22)$$

$$\sigma_{\text{tot}}^{\text{incl. }\psi(2S)} = \sigma_{\psi(2S)} \times \mathcal{B}_{\text{vis}}^{\text{incl. }\psi(2S)} \times \epsilon_\theta^{\text{incl. }\psi(2S)}. \quad (6.23)$$

The fraction $f_{B^0}$, in Equation 6.22, of $b$ quarks that hadronise to a $B^0$ mesons is assumed to be equal to $f_{B^\pm} = (39.9 \pm 1.1)\,\%$. The combined branching ratio for the signal decay $B^0 \to Z(4430)^{\pm}K^{\mp}$ with $Z(4430)^{\pm} \to \psi(2S)\pi^{\pm}$ is given in Equation 1.38. The visible branching ratio is then equal to

$$\begin{aligned}
\mathcal{B}_{\text{vis}}^{B^0 \to Z(4430)^{\pm}K^{\mp}} &= \mathcal{B}(B^0 \to Z(4430)^{\pm}K^{\mp}) \times \mathcal{B}(Z(4430)^{\pm} \to \psi(2S)\pi^{\pm}) \times \\
&\quad \mathcal{B}(\psi(2S) \to \mu^+\mu^-) \\
&= (4.1 \times 10^{-5}) \times (0.73\,\%) = 2.99 \times 10^{-7}. \quad (6.24)
\end{aligned}$$

The branching fraction of the $\psi(2S) \to \mu^+\mu^-$ decay, to which the visible $\psi(2S)$ branching ratio reduces, is taken from Ref. [16]. The inclusive $\psi(2S)$ production cross-section in Equation 6.23, is discussed in the description of the data and the geometrical acceptance for both samples are reported in Table 6.5. Taking all these numbers into account, the integrated luminosity corresponding to the data samples studied here can be calculated and are reported in the second column of Table 6.5.

## 6.2.2 $Z(4430)^{\pm}$ Pre-Selection

The topology of the $B^0 \to (Z(4430)^{\pm} \to (\psi(2S) \to \mu^+\mu^-)\pi^{\pm})K^{\mp}$ decay is represented in Fig. 6.13.

Table 6.5: Summary of the data used to study the selection of the $B^0 \to Z(4430)^{\pm}K^{\mp}$ decay channel. The integrated luminosity $\mathcal{L}_{\mathrm{int}}^{\mathrm{sample}}$ corresponding to the sample and the efficiency $\epsilon_\theta$ of the acceptance cut at the generator level are reported.

| Data sample | $\mathcal{L}_{\mathrm{int}}^{\mathrm{sample}}$ | $\epsilon_\theta$ | # events |
|---|---|---|---|
| $B^0 \to Z(4430)^{\pm}K^{\mp}$ | $2.2 \times 10^5\,\mathrm{nb}^{-1}$ | $(34.6 \pm 0.1)\,\%$ | 18'397 |
| Inclusive $\psi(2S)$ | $2'400\,\mathrm{nb}^{-1}$ | $(19.09 \pm 0.15)\,\%$ | 28'353 |
| Inclusive $J/\psi$ | $90\,\mathrm{nb}^{-1}$ | $(20.92 \pm 0.17)\,\%$ | 291'299 |
| Inclusive $b\bar{b}$ | $60\,\mathrm{nb}^{-1}$ | $(43.21 \pm 0.29)\,\%$ | $\sim 26.4 \times 10^6$ |
| Minimum bias | $0.19\,\mathrm{nb}^{-1}$ | $1$ | $\sim 19.2 \times 10^6$ |
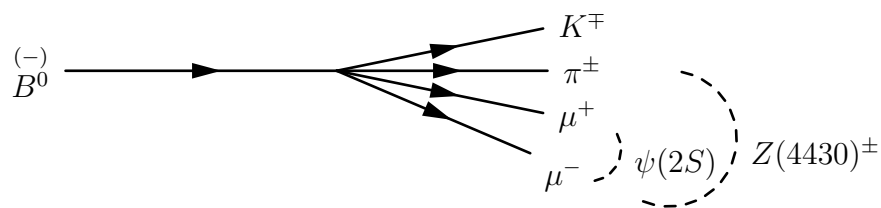


Figure 6.13: The topology of the $\overset{(-)}{B^0} \to Z(4430)^{\pm}K^{\mp}$ decay, with $Z(4430)^{\pm} \to \psi(2S)\,\pi^{\pm}$ and $\psi(2S) \to \mu^+\mu^-$.

Before looking at the kinematic variables, the two levels of trigger are applied. In order to be selected, an event must pass both the Level-0 and the High-Level Trigger cuts.

The other selection criteria chosen for this pre-selection are similar to those described in Section 6.1.2. The $\chi^2/\text{dof}$ of the fit of the four charged tracks is required to be smaller than 12. These cuts are subsequently tightened to $\chi^2/\text{dof} < 2$. The corresponding distributions are similar to those shown in Fig. 6.3 and hence not reported here. In the first step of the reconstruction, two oppositely-charged muons are combined to form a $\psi(2S)$ candidate. A loose cut is set on the $\chi^2$ of the vertex fit at $\chi^2/\text{dof} < 30$. A charged pion is then added to make the $Z(4430)^{\pm}$ and the vertex quality is required to be better than $\chi^2/\text{dof} < 25$. Finally, a charged kaon is combined with the $Z(4430)^{\pm}$ to reconstruct the $B^0$ meson. A cut on the vertex fit quality is set at $\chi^2/\text{dof} < 15$.

Finally, mass criteria are used to reduce the combinations. The cut on the $Z(4430)^{\pm}$ mass is loose ($\pm 500\,\text{MeV}/c^2$) in order to be able to study the $Z(4430)^{\pm}$ mass distribution and get information on the background from the side-bands. On the other hand, $\pm 100\,\text{MeV}/c^2$ windows are defined around the value of the $\psi(2S)$ and $B^0$ masses used in the Monte Carlo generation. The masses used are those reported in Ref. [16] with values of $M_{\psi(2S)} = 3686.09\,\text{MeV}/c^2$ and $M_{B^0} = 5279.53\,\text{MeV}/c^2$. These mass selection criteria can be tightened by studying the shape of the signal distributions. Figure 6.14 shows the $\psi(2S)$, $Z(4430)^{\pm}$ and $B^0$ mass distributions. Only candidates matched to the true Monte Carlo decay chain are shown in these distributions. The mass resolutions, taken from single-Gaussian fits, are respectively

$$\sigma_{M_{\psi(2S)}} = 12.9\,\text{MeV}/c^2\,, \tag{6.25}$$

$$\sigma_{M_{Z(4430)^{\pm}}} = 17.7\,\text{MeV}/c^2\,, \tag{6.26}$$

$$\sigma_{M_{B^0}} = 13.5\,\text{MeV}/c^2\,. \tag{6.27}$$

A cut is again chosen as a $\pm 3\sigma$ window around the central value. A rounded value of $\pm 45\,\text{MeV}/c^2$ is chosen for the $B^0$ mass window and $\pm 40\,\text{MeV}/c^2$ for the $\psi(2S)$ mass window. The cut on the $Z(4430)^{\pm}$ mass is tightened to $\pm 55\,\text{MeV}/c^2$ only for the signal events in a first step, while selecting all the background events in a $\pm 500\,\text{MeV}/c^2$ window around the $Z(4430)^{\pm}$ peak to artificially increase the statistics. Assuming a linear background distribution in the wide mass window, a factor of $\frac{55}{500}$ is then applied to the expected background level to tighten from the loose to the tight mass window.

The next set of cuts is used to increase the purity of the pion and kaon samples. Two cuts are used to discriminate good pions from kaons and protons. The corresponding distributions are shown in Fig. 6.15. For the kaon, requirements are set on the log likelihood difference between the kaon hypothesis and the pion, electron and muon hypotheses. The relevant histograms are reported in Fig. 6.16. The chosen value for the cuts are

$$\Delta \ln \mathcal{L}_{\pi K/p} > 0\,,$$
$$\Delta \ln \mathcal{L}_{K\pi} > 10\,,$$
$$\Delta \ln \mathcal{L}_{K\mu/e} > 15\,,$$

Another powerful criterion to discriminate between signal and background events is the angle between the $B^0$-meson flight direction and its momentum. This angle is schematised
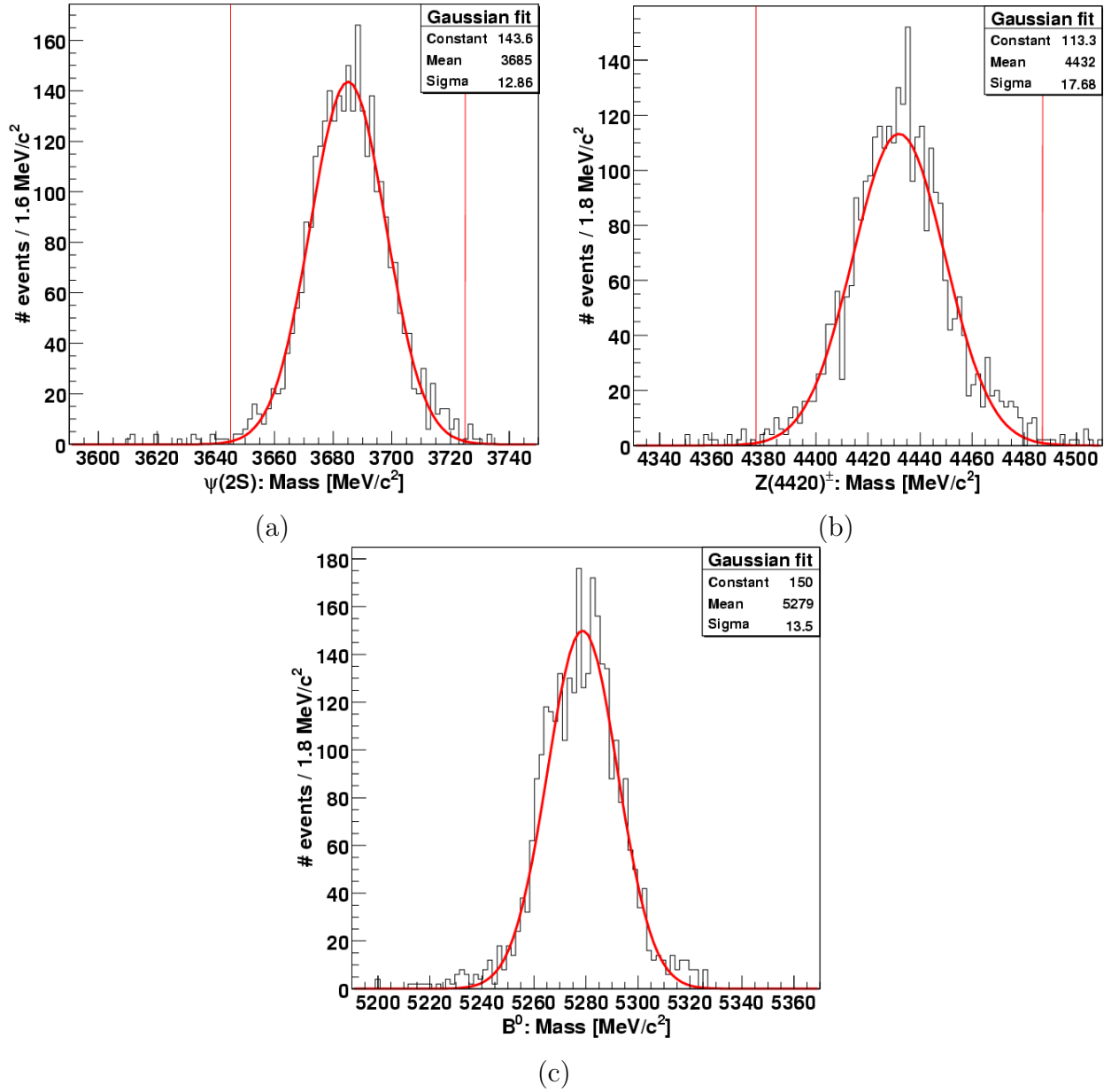
Figure 6.14: Mass distributions of (a) the $\psi(2S)$, (b) the $Z(4430)^{\pm}$ and (c) the $B^0$ candidates in $B^0 \to (Z(4430)^{\pm} \to \psi(2S)\pi^{\pm})K^{\mp}$ events, after a loose pre-selection. Only candidates matched to a true decay in the Monte-Carlo truth are reported. The results of a Gaussian fit (red line on the histogram) are reported in the box in the upper-right corner. The red vertical lines indicate the tight mass window used in the final selection. These histograms are not normalised.

(a)                                                    (b)
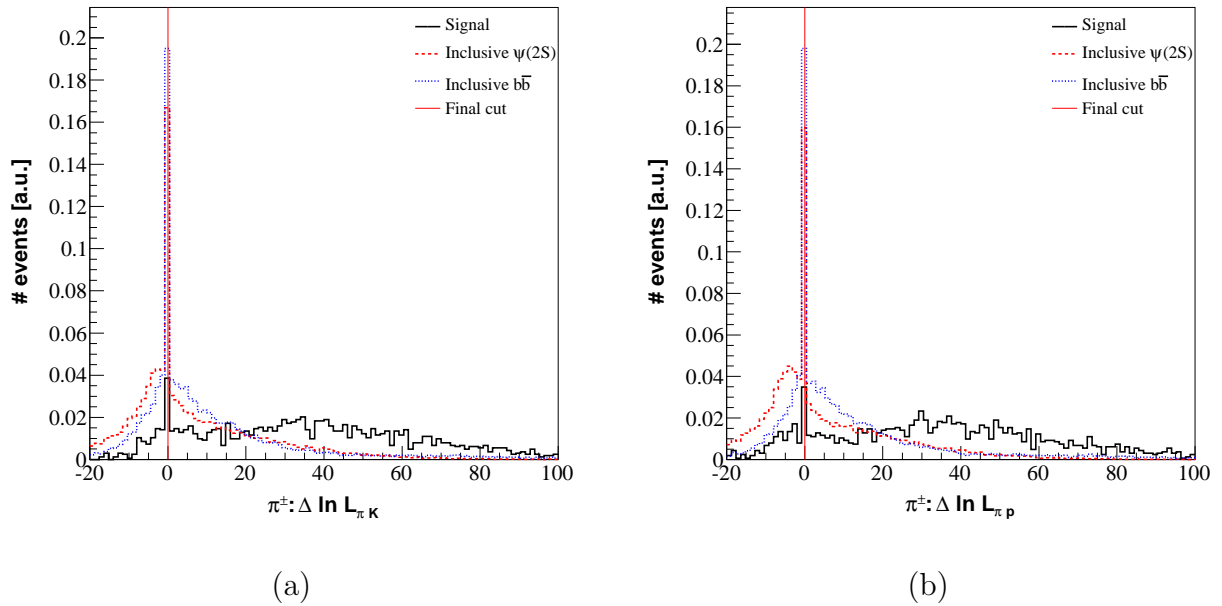
Figure 6.15: Distributions of the log likelihood difference between the pion hypothesis and (a) the kaon or (b) the proton hypothesis, for the pions created in $B^0 \to (Z(4430)^{\pm} \to \psi(2S)\pi^{\pm})K^{\mp}$ decays.

in the case of the $B^{\pm} \to X(3872)K^{\pm}$ decay in Fig. 6.7 (a). The distribution of the cosine of this angle for signal and background events is shown in Fig. 6.17. A value of $\cos \theta_{B^0} > 0.99995$ is chosen for the cut.

Finally, the following variables, which are thought to be the most discriminating, are chosen for the optimisation process:

$\chi^2/\mathbf{dof}(B^0 \ \mathbf{vtx})$**:** Since there are four tracks coming from the same vertex, the quality of the $B^0$ vertex fit is expected to be good (see Fig. 6.18 (a)).

$\mathbf{FD}(B^0)$**:** The fact that the $Z(4430)^{\pm}$ is the product of a $B$-meson decay is used as a selection criteria by requiring the $B^0$ meson to have a positive flight distance (see Fig. 6.18 (b)).

$p_{\mathrm{T}}(\pi^{\pm})$**:** The pion in the $Z(4430)^{\pm}$ decay tends to have a large transverse momentum $p_{\mathrm{T}}$, as visible in Fig. 6.19 (a).

$p_{\mathrm{T}}(K^{\pm})$**:** The kaon in the $B$ decay also tends to have a large transverse momentum $p_{\mathrm{T}}$, as visible in Fig. 6.19 (b).

Loose cuts are set on these variables in order to reject some background while allowing for a proper optimisation of the cuts. The cuts of the loose and tight pre-selections are summarised in the third and fourth columns of Table 6.6 respectively.

(a)



(b)



(c)
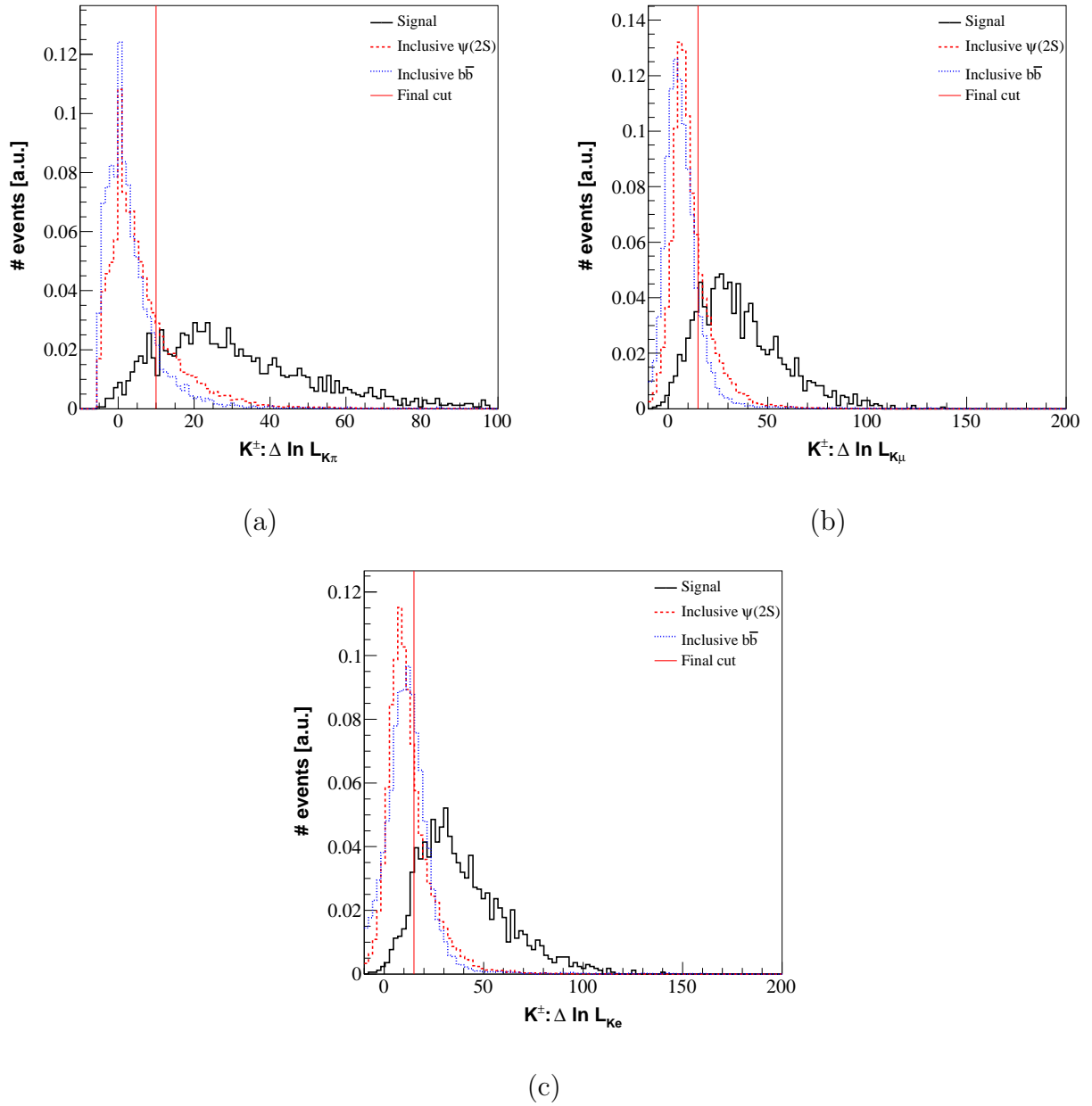
Figure 6.16: Distributions of the log likelihood difference between the kaon hypothesis and (a) the pion, (b) the muon or (c) the electron hypotheses, for the kaons in $B^0 \rightarrow (Z(4430)^\pm \rightarrow \psi(2S)\pi^\pm)K^\mp$ decays.
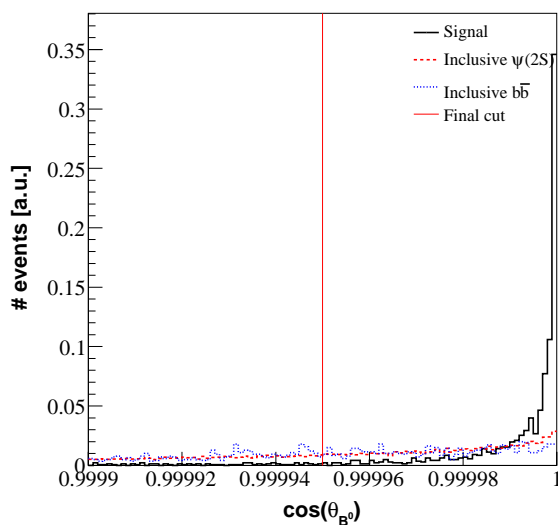
Figure 6.17: Distribution of $\cos \theta_{B^0}$ for $B^0 \rightarrow Z(4430)^{\pm}K^{\mp}$ signal events and selected background sources.



|     |     |
| :-: | :-: |
| (a) | (b) |
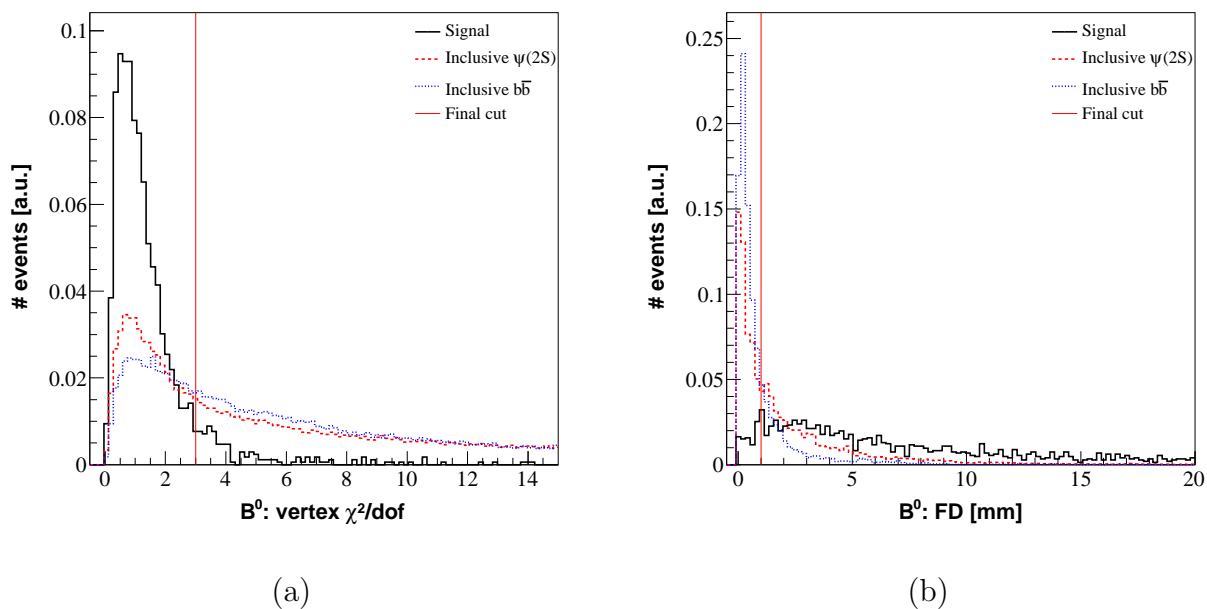
Figure 6.18: Distribution of (a) the $\chi^2$/dof of the $B^0$ vertex fit and (b) the $B^0$ flight distance of reconstructed $B^0 \rightarrow (Z(4430)^{\pm} \rightarrow \psi(2S)\pi^{\pm})K^{\mp}$ candidates.
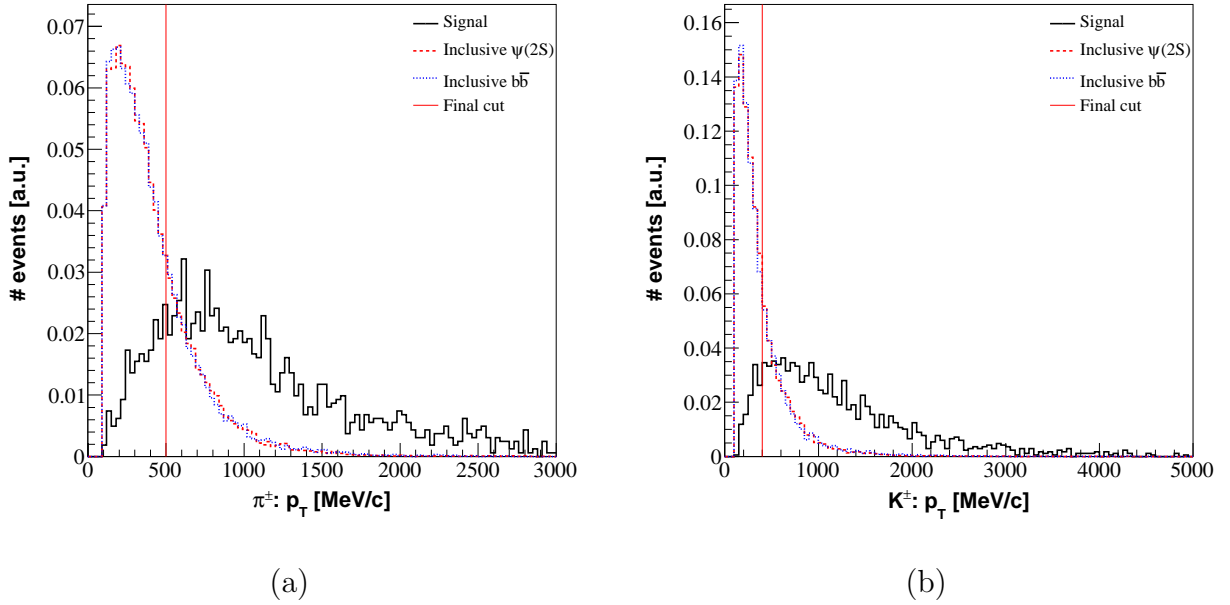
Figure 6.19: Transverse momentum distributions of (a) the $\pi^{\pm}$ and (b) the $K^{\mp}$ of reconstructed $B^0 \rightarrow (Z(4430)^{\pm} \rightarrow \psi(2S)\pi^{\pm})K^{\mp}$ candidates.

## 6.2.3   $Z(4430)^{\pm}$ Final Selection

The variables chosen for the optimisation are passed to the TMVA toolkit. The method used is again a simple cut method, as for the $X(3872)$ analysis, where the signal significance defined in Equation 6.10 is maximised considering only the inclusive $\psi(2S)$ background sample. The result of this process is given in the fifth column of Table 6.6. Figure 6.20 shows the signal significance as a function of each of the cuts, with the three others set at their optimal values.

## 6.2.4   Results of the $Z(4430)^{\pm}$ Selection

The total number of selected $B^0 \rightarrow (Z(4430)^{\pm} \rightarrow (\psi(2S) \rightarrow \mu^+\mu^-)\pi^{\pm})K^{\mp}$ events after the full selection is 664. This number is reported in Table 6.7, along with the other numbers defined in Section 6.1.4. The total efficiency for the $B^0 \rightarrow Z(4430)^{\pm}K^{\mp}$ decay is $(1.25 \pm 0.05)\,\%$ with the breakdown reported in Table 6.8. This total efficiency is significantly larger than that of the $B^{\pm} \rightarrow X(3872)K^{\pm}$ selection discussed in Section 6.1.4. Although it is surprising at first, because the decays are similar, this large difference can be explained by several facts. First, the detection and reconstruction efficiencies are significantly higher for the $B^0 \rightarrow Z(4430)^{\pm}K^{\mp}$ decay. Also, two cuts are set to much higher values in the selection of the $X(3872)$ state than for the $Z(4430)^{\pm}$, the cut on the $B$-meson flight distance (16 mm for the first selection, 1 mm for the second) and the transverse momentum of the kaon (1'500 MeV/c for the $X(3872)$ selection, 400 MeV/c for the $Z(4430)^{\pm}$ selection). Using the values from the $Z(4430)^{\pm}$ selection for these two cuts in the two selection, the total efficiency of the $X(3872)$ selection increases to 0.85 %,
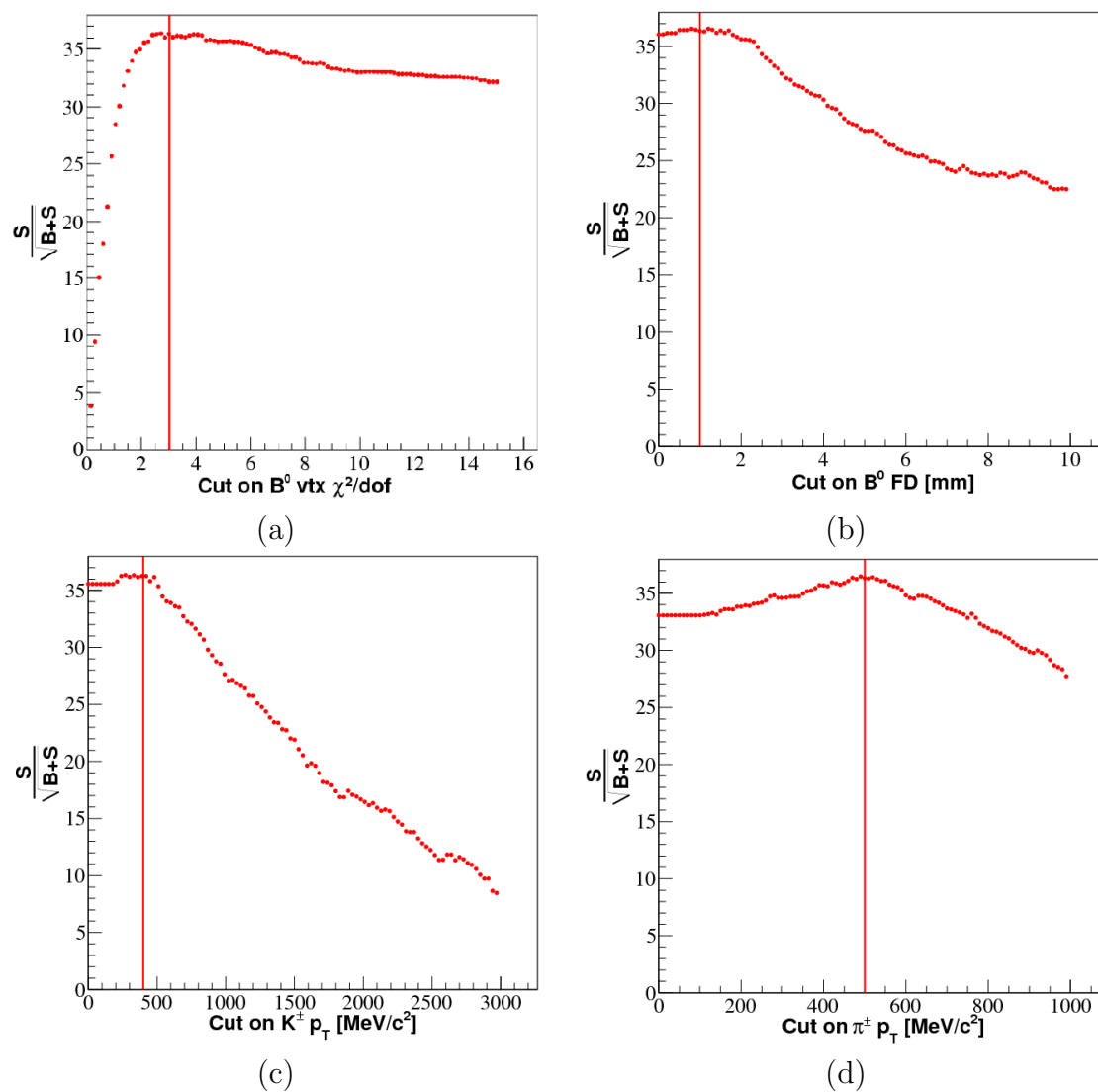
Figure 6.20: Optimisation of the four cuts chosen in Section 6.2.2. The optimisation is shown for each variable individually, with the other cuts set to their optimal value. (a) Cut on the $\chi^2/\mathrm{dof}$ of the $B^0$-meson vertex fit. (b) Cut on the $B^0$-meson flight distance. (c) Cut on the $K^{\mp}$ transverse momentum. (d) Cut on the $\pi^{\pm}$ transverse momentum. The red vertical lines indicate the values of the cuts used in the final selection.

Table 6.6: Summary of the offline cuts used for the selection of the $Z(4430)^\pm \to \psi(2S)\,\pi^\pm$ signal in $B^0$ decays. The underlined cut values are the result of the optimisation described in Section 6.2.3.

| Variable | | Loose pre-selection | Tight pre-selection | Final selection |
|---|---|---|---|---|
| | | $\psi(2S)$ | | |
| $\mu^\pm$: std. sel. defined in Section 3.1.5 | | | | |
| $\mu^\pm$: track $\chi^2/\mathrm{dof}$ | $<$ | 12 | 2 | 2 |
| $\mu\mu$ vertex $\chi^2/\mathrm{dof}$ | $<$ | 30 | 30 | 30 |
| $\left|m_{\mu\mu} - M_{\psi(2S)}\right|$ | $<$ | $100\,\mathrm{MeV}/c^2$ | $40\,\mathrm{MeV}/c^2$ | $40\,\mathrm{MeV}/c^2$ |
| | | $Z(4430)^\pm$ | | |
| $\pi^\pm$: std. sel. defined in Section 3.1.5 | | | | |
| $\pi^\pm$: track $\chi^2/\mathrm{dof}$ | $<$ | 12 | 2 | 2 |
| $\pi^\pm$: $p_\mathrm{T}$ | $>$ | — | $100\,\mathrm{MeV}/c$ | $\underline{500\,\mathrm{MeV}/c}$ |
| $\pi^\pm$: $\Delta\ln\mathcal{L}_{\pi K}$ | $>$ | — | 0 | 0 |
| $\pi^\pm$: $\Delta\ln\mathcal{L}_{\pi p}$ | $>$ | — | 0 | 0 |
| $\mu\mu\pi$ vertex $\chi^2/\mathrm{dof}$ | $<$ | 25 | 25 | 25 |
| $\left|m_{\mu\mu\pi} - M_{Z(4430)^\pm}\right|^{\mathrm{sig}}$ | $<$ | $500\,\mathrm{MeV}/c^2$ | $55\,\mathrm{MeV}/c^2$ | $55\,\mathrm{MeV}/c^2$ |
| $\left|m_{\mu\mu\pi} - M_{Z(4430)^\pm}\right|^{\mathrm{bkg}}$ | $<$ | $500\,\mathrm{MeV}/c^2$ | $500\,\mathrm{MeV}/c^2$ | $500\,\mathrm{MeV}/c^2$ |
| | | $B^0$ | | |
| $K^\mp$: std. sel. defined in Section 3.1.5 | | | | |
| $K^\mp$: track $\chi^2/\mathrm{dof}$ | $<$ | 12 | 2 | 2 |
| $K^\mp$: $p_\mathrm{T}$ | $>$ | — | $100\,\mathrm{MeV}/c$ | $\underline{400\,\mathrm{MeV}/c}$ |
| $K^\mp$: $\Delta\ln\mathcal{L}_{K\pi}$ | $>$ | — | 10 | 10 |
| $K^\mp$: $\Delta\ln\mathcal{L}_{K\mu}$ | $>$ | — | 15 | 15 |
| $K^\mp$: $\Delta\ln\mathcal{L}_{Ke}$ | $>$ | — | 15 | 15 |
| $\mu\mu\pi K$ vertex $\chi^2/\mathrm{dof}$ | $<$ | 15 | 15 | $\underline{3}$ |
| $\left|m_{\mu\mu\pi K} - M_{B^0}\right|$ | $<$ | $100\,\mathrm{MeV}/c^2$ | $45\,\mathrm{MeV}/c^2$ | $45\,\mathrm{MeV}/c^2$ |
| $B^0$: $cos\theta_{B^0}$ | $>$ | — | 0.99995 | 0.99995 |
| $B^0$: flight distance | $>$ | — | — | $\underline{1\,\mathrm{mm}}$ |

Table 6.7: Number of signal events in the $B^0 \to (Z(4430)^\pm \to (\psi(2S) \to \mu^+\mu^-)\pi^\pm)K^\mp$ signal sample that are generated, reconstructible, reconstructed, selected, triggered by L0 and triggered by HLT.

| | |
|---|---|
| $N_{\text{gen}}$ | 18397 |
| $N_{\text{rec'ible}}$ | 3387 |
| $N_{\text{rec'ed}}$ | 2994 |
| $N_{\text{rec'ed/ible}}$ | 2816 |
| $N_{\text{sel}}$ | 764 |
| $N_{\text{L0}}$ | 722 |
| $N_{\text{HLT}}$ | 664 |

Table 6.8: Summary of the signal efficiencies for the selection of $B^0 \to (Z(4430)^\pm \to (\psi(2S) \to \mu^+\mu^-)\pi^\pm)K^\mp$ events.

| Factors (in %) forming $\epsilon_{\text{tot}}$ (in %) | | | | $\epsilon_{\text{tot}}$ |
|---|---|---|---|---|
| $\epsilon_{\text{tot}} = \epsilon_{\text{det}} \times \epsilon_{\text{rec/det}} \times \epsilon_{\text{sel/sec}} \times \epsilon_{\text{trg/sel}}$ | | | | |
| $\epsilon_{\text{det}}$ | $\epsilon_{\text{rec/det}}$ | $\epsilon_{\text{sel/rec}}$ | $\epsilon_{\text{trg/sel}}$ | $\epsilon_{\text{tot}}$ |
| $6.8 \pm 0.3$ | $83 \pm 1$ | $26 \pm 1$ | $87 \pm 1$ | $1.25 \pm 0.05$ |

compared to $1.25\,\%$. Also, since there is one more charged track to reconstruct in the $X(3872)$ decay, this leads to a factor $95\,\%$ between the two cases.

### 6.2.4.a   Annual $Z(4430)^\pm$ Signal Yield

The annual signal yield can be calculated for the $B^0 \to Z(4430)^\pm K^\mp$ channel using Equation 6.16, where the integrated luminosity corresponding to the signal sample is taken from Table 6.5. Using these values, along with the efficiency calculated in Section 6.2.4, in Equation 6.16 leads to an annual signal yield of

$$N_{\text{phys}}^{B^0 \to Z(4430)^\pm K^\mp} = 6200 \pm 240 \,. \tag{6.28}$$

This number can be compared with the number of events observed by Belle at the time of the discovery of the $Z(4430)^\pm$ state. They found $121 \pm 30$ events in the signal peak, based on an analysis of $605\,\text{fb}^{-1}$ [10]. However, the $\psi(2S)$ charmonium state was reconstructed in more than just the di-muon channel. For example, they also included the $\psi(2S) \to J/\psi\,\pi^+\pi^-$ channel. Reconstructing the $\psi(2S)$ in more decay channels at LHCb would increase the statistics.

### 6.2.4.b   $B/S$ Estimate for the $Z(4430)^\pm$ Selection

The full selection is run on each of the background samples listed in Table 6.5 in order to estimate the background-to-signal ratio.

No event is selected neither in the inclusive $J/\psi$ sample, nor in the minimum bias sample. However, one candidate is selected in the inclusive $b\bar{b}$ sample. Studying the true decay corresponding to the reconstructed candidate shows that it is a fully reconstructed $\bar{B}^0 \to (\bar{K}^{0*}(892) \to \pi^+ K^-)\mu^+\mu^-$ decay, which mimics the signal. The Feldman and Cousins confidence interval for one selected event is [0.11, 4.36] at 90 % CL. Using Equation 6.18 and the signal yield calculated in Section 6.2.4.a, the contribution from the inclusive $b\bar{b}$ sample to the $B/S$ ratio is expected to lie within the interval [0.1, 2.7] at 90 % confidence level [2]. The assumption is made here that the background has a linear distribution over the $\pm 500\,\mathrm{MeV}/c^2$ mass window around the $Z(4430)^{\pm}$ mass. This will need to be verified with a larger background sample.

Finally, the contribution to the $B/S$ ratio from the inclusive $\psi(2S)$ sample is calculated using Equation 6.18, with the number of expected background events being

$$N_{\mathrm{phys}}^{\mathrm{incl.}\ \psi(2S)} = \frac{\mathcal{L}_{\mathrm{int}}}{\mathcal{L}_{\mathrm{int}}^{\mathrm{incl.}\ \psi(2S)}} \times N_{\mathrm{HLT}}^{\mathrm{incl.}\ \psi(2S)}, \tag{6.29}$$

where the integrated luminosity is taken from Table 6.5. The distribution of the background events in the wide $Z(4430)^{\pm}$ mass window is not linear, as visible in Fig. 6.21. However, it can be assumed to be linear in a $\pm 300\,\mathrm{MeV}/c^2$ mass window around the $Z(4430)^{\pm}$ mass. The calculation is the same as presented above, except for the scaling factor (ratio of the widths of the tight and loose mass windows), which is now $\frac{55}{300}$. With a number of 106 triggered and selected events in the $\pm 300\,\mathrm{MeV}/c^2$ mass window, the contribution to the $B/S$ ratio is expected to be

$$\frac{B^{\mathrm{incl.}\ \psi(2S)}}{S} = 2.6 \pm 0.3. \tag{6.30}$$

Adding the two contributions discussed above, the total $B/S$ ratio is estimated to be in the range [2.7, 5.3]. Figure 6.21 shows the $Z(4430)^{\pm}$ mass peak in the $\pm 500\,\mathrm{MeV}/c^2$ mass window with the two sources of background discussed here. The distribution corresponding to the inclusive $\psi(2S)$ sample is scaled to the same integrated luminosity as that of the signal sample. The distribution of inclusive $b\bar{b}$ is scaled such as to indicate the height of a linear distribution corresponding to a $B/S$ ratio of 0.6.

In the early phase of data analysis at LHCb, the aim will not be to do precise measurement of the $Z(4430)^{\pm}$ properties. However, LHCb will be able to confirm whether the signal observed by Belle is real. A peak with a statistical significance of $5\,\sigma$ is needed. Using the signal yield and the upper limit on the $B/S$ ratio, the integrated luminosity needed to achieve this significance can be calculated as

$$\left.\begin{array}{l} S > 5 \times \sqrt{B+S} \\ \frac{B}{S} \in [2.7, 5.3] \end{array}\right\} \Rightarrow S > 25 \times 6.3 \sim 160. \tag{6.31}$$

This means that 160 events are needed, i.e. with $\frac{160}{6200} \times 2\,\mathrm{fb}^{-1} = 52\,\mathrm{pb}^{-1}$ of integrated luminosity, a mass peak with a statistical significance of $5\,\sigma$ could be measured, confirming Belle discovery if the $Z(4430)^{\pm}$ exists. This corresponds to less than 3 % of one nominal

---

[2] Using one selected event in the $B/S$ calculation leads to a single value of 0.6, which is used in the normalisation of the background level in Fig. 6.21.
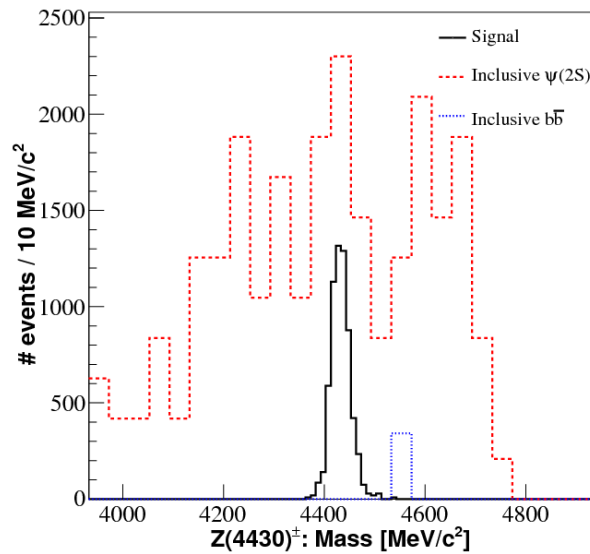
Figure 6.21: Mass distribution of the $Z(4430)^{\pm}$ in the $\pm 500\,\mathrm{MeV}/c^2$ mass window after selection. The selected events of inclusive $\psi(2S)$ and $b\bar{b}$ are shown, scaled such as to reflect the corresponding contribution to the $B/S$ ratio.

year of data taking. However, it is now expected that the LHC machine will start operating with a low energy phase at a centre-of-mass energy of 7 TeV instead of the nominal 14 TeV. At such energy, the $b\bar{b}$ production cross-section is expected to be a factor of two lower. Hence, the time needed for the measurement will be longer than what is calculated here. Furthermore, the selection efficiency has not been tested on data simulated with the expected early phase centre-of-mass energy. This needs additional studies.

Additional selection criteria can be used to further reduce the background level. As discussed in Section 2.1, the number of $pp$ interactions in an event may be greater than one. If more than one interaction occur, the track multiplicity is increased and hence the number of wrong combinations. Two cuts can be used to further reduce the combinatorial background. Selecting only events with one primary vertex, and requiring in addition that no more than 60 tracks are reconstructed as coming from this vertex, no event from the inclusive $b\bar{b}$ sample is selected and the $B/S$ contribution from the inclusive $\psi(2S)$ sample is reduced to 2.4. As a counterpart, the annual signal yield is reduced to around 3100 events.

## 6.3 Discussion of the $X(3872)$ and $Z(4430)^{\pm}$ Selections

A first study of the selection of the new charmonium-like states $X(3872)$ and $Z(4430)^{\pm}$ in $B$-meson decays at LHCb has been performed. The aim of this study was to show the feasibility of these selections in $pp$ collisions at $\sqrt{s} = 14$ TeV. The annual signal yield (in $2\,\mathrm{fb}^{-1}$) and the expected $B/S$ ratio for these two signal decays are reported in Table 6.9.

The selection of $X(3872) \to J/\psi\,\pi^+\pi^-$ decays in the $B^{\pm} \to X(3872)K^{\pm}$ channel

Table 6.9: Summary of the annual signal yield and the expected $B/S$ ratio from the most obvious background sources for the $B^{\pm} \to X(3872)K^{\pm}$ and $B^0 \to Z(4430)^{\pm}K^{\mp}$ decays.

|  | Annual yield | $B/S$ |
|---|---|---|
| $B^{\pm} \to X(3872)K^{\pm}$ | $1850 \pm 120$ | [0.3, 3.4] at 90 % CL |
| $B^0 \to Z(4430)^{\pm}K^{\mp}$ | $6200 \pm 240$ | [2.7, 5.3] at 90 % CL |

presented in this study shows that LHCb is expected to play an important role in the measurement of the $X(3872)$ quantum numbers. With an annual yield of 1850 signal events at the nominal energy and luminosity conditions, LHCb will be able to disentangle between the two spin hypotheses, as discussed in Ref. [140]. However, further studies are needed for this measurement. For example, it is not yet known how well the angular analysis can be performed when taking into account the expected background level. Also, due to the first LHC running phase at low energy and the consequent lower $b\bar{b}$ production cross-section, with an expected integrated luminosity of $0.3\,\text{fb}^{-1}$ in the first year of running, this study might not lead to an early-phase measurement. Also, additional background studies are needed in order to have a better feeling of the expected background level. The studies presented in Section 6.1 show that the expected dominant source of background originates from $b \to J/\psi$ decays. For a further understanding of the background sources and a better estimate of the $B/S$ ratio, a large sample of this inclusive background should be studied. Also, the two specific decays selected in the sample of inclusive $J/\psi$ and $b\bar{b}$ should be analysed in detail. These decays are

- $B^+ \to (J/\psi \to \mu^+\mu^-)(K_2^{+*}(1430) \to (K^{0*}(892) \to K^+\pi^-\gamma)\pi^+\gamma)$ and

- $B^- \to \pi^-(J/\psi \to \mu^-\mu^+)(K^{0*}(892) \to \pi^+K^-)$.

The selection of the $Z(4430)^{\pm} \to \psi(2S)\pi^{\pm}$ channel in $B$-meson decays is promising at LHCb. With more than 6000 signal events expected in one nominal year, the Belle discovery will be confirmed or ruled out quickly. Actually, with such high statistics, this measurement could possibly be performed in the LHC startup phase in 2010, even with an integrated luminosity ten times lower than a nominal year of data taking and a centre-of-mass energy of $\sqrt{s} = 7\,\text{TeV}$. In any case, LHCb should still be able to reconstruct a few hundreds of candidates with a $B/S$ ratio around 2. Once the existence of the $Z(4430)^{\pm}$ state is confirmed, the visible branching ratio of the $B^0 \to (Z(4430)^{\pm} \to \psi(2S)\pi^{\pm})K^{\mp}$ decay will be measured. This measurement will need to be normalised to another known $B$ decay. For example, the $B^0 \to \psi(2S)K^*$ decay is close to the $B^0 \to Z(4430)^{\pm}K^{\mp}$. However, the visible branching ratio of the $B^0 \to J/\psi\,K^*$ is more precisely known. This branching-ratio measurement should be addressed in an additional study. Also, more sources of background should be analysed. For example, the exclusive $\bar{B}^0 \to (\bar{K}^{0*}(892) \to \pi^+K^-)\mu^+\mu^-$ decay reconstructed and selected in the sample of inclusive $b\bar{b}$ could be generated and analysed, along with a larger sample of inclusive $\psi(2S)$ events.

# Conclusion

𝕿HE studies presented in this thesis cover two different aspects of the LHCb experiment. The first one is separated into two parts: the alignment of the Tracking Stations using Monte Carlo simulated data and the alignment of the Inner Tracker stations using the first recorded data at LHCb. The second subject, the selection of the $X(3872)$ and $Z(4430)^{\pm}$ states in $pp$ collisions at $\sqrt{s} = 14\,\mathrm{TeV}$, is only starting to trigger interest at LHCb. The analysis discussed in this work is a feasibility study of these selections. The important results of these two subjects are briefly reviewed below.

In Chapter 3, a new method to align the LHCb detector is presented which uses Kalman-fitted tracks coming from the standard track fit. The new feature in the procedure lies in the derivation of the global track covariance matrix after a Kalman-filter track-fit.

In Chapter 4, two different realistic scenarios are presented on which this alignment procedure is tested. The first one uses simulated beam–gas events with $450\,\mathrm{GeV}$ protons colliding into residual gas molecules in the beam pipe. The magnetic field is turned off in this study. A general strategy for the alignment of the Tracking Stations is defined. This strategy includes the use of an evolving cut on the track $\chi^2/\mathrm{dof}$. It is also shown that drift time information for the Outer Tracker can be used after a few iterations to improve the alignment precision. Starting from a realistic day-1 misalignment scenario, the detector is aligned with a precision of two and ten microns for the IT and OT layers respectively. Refitting tracks from $J/\psi$ di-muon decays, it is shown that the alignment procedure is able to fully recover the shape of the track $\chi^2/\mathrm{dof}$ distribution as well as the $J/\psi$ mass bias and resolution. The largest difference in mass resolution between the ideal case and the geometry after alignment is of the order of 3 % for high momentum particles (above $80\,\mathrm{GeV}/c$).

A second scenario is presented where the OT layers and IT boxes, layers and ladders are aligned simultaneously starting from realistic day-1 misalignments. For this second exercise, minimum bias events produced at a proton–proton centre-of-mass energy of $14\,\mathrm{TeV}$ are used, with the LHCb magnet on. The procedure is adapted here to the high misalignment complexity and big number of degrees of freedom by aligning step by step, starting from a coarse granularity (IT boxes and OT layers separately) and moving to the finest granularity (IT ladders and OT layers together). It is shown in particular that the detector can be aligned with a precision good enough to not affect the $J/\psi$ mass resolution by more than 2 % (for momenta above $80\,\mathrm{GeV}/c$).

In Chapter 5, the Inner Tracker is aligned using the first tracks seen in the detector. These tracks are reconstructed using data taken during the LHC synchronisation tests (TED runs) of August–September 2008. Although the occupancy in the detector is high, a sample of good tracks is selected and used to internally align the Inner Tracker. At the

ladder level, the alignment along the $x$ direction is precise to $20\,\mu$m, compared to a single hit resolution of $57\,\mu$m. This information is obtained by studying the unbiased residuals in all the ladders before and after alignment. The number of reconstructed tracks is increased over the alignment process by more than $10\,\%$. These results have been verified with the June 2009 TED run. Cosmics events collected over the same period have also been studied but the statistics are too low to allow a precision alignment.

The combined results of Chapters 4 and 5 are very promising for the LHCb collaboration, a few months prior to the new LHC startup. A good alignment of the Tracking Stations is crucial to achieve the expected outstanding performance of LHCb. Potential residual misalignments of the tracking sub-system worsen the momentum resolution, which in turn has a negative impact on the mass resolution. The latter is crucial in the event selection, because a good resolution allows to use smaller mass windows in the selection process and hence reject more background. The momentum estimate is also important for the study of $B$-meson proper time distributions, from which the $B$-mixing parameters are extracted.

In the last chapter of this thesis, a first study is made of the new $XYZ$ charmonium-like states in $pp$ collisions at $\sqrt{s} = 14\,$TeV. Two such states are studied in this thesis: the $X(3872)$ and the $Z(4430)^{\pm}$. The selection proposed here is the first attempt to find $X(3872)$ and $Z(4430)^{\pm}$ signals at LHCb. The $X(3872)$ state has been discovered in 2003 by Belle and has been confirmed and observed by other experiments. However, two questions remain about it. The first one is about its nature, which is still unknown. Simple theoretical interpretations, such as charmonium state, di-meson molecule or tetraquark, cannot account for all its properties. More complex models, involving quantum superpositions of two such states, are arising and seem to explain the nature of the $X(3872)$. The signal yield for the $X(3872) \to J/\psi\,\pi^+\pi^-$ channel in $B^{\pm} \to X(3872)K^{\pm}$ decays is expected to be 1850 events per nominal year of data taking. The corresponding $B/S$ ratio from the two most obvious sources of background, inclusive $J/\psi$ and $b\bar{b}$, is expected to be in the interval [0.3, 3.4] at $90\,\%$ CL. With such figures, LHCb is expected to play an important role in the uncovering of the $X(3872)$ nature, since it should become possible to disentangle between the two possible $J^{PC}$ quantum numbers: $1^{++}$ or $2^{-+}$. This measurement will however probably not be possible in the early running phase at low energy.

The $Z(4430)^{\pm} \to \psi(2S)\pi^{\pm}$ decay has been discovered at Belle in 2008 in the $B^0 \to Z(4430)^{\pm}K^{\mp}$ channel, with a statistical significance of $6.5\,\sigma$. However, BaBar could not confirm the discovery. Assuming the Belle value of the visible branching ratio of $\mathcal{B}(B^0 \to Z(4430)^{\pm}K^{\mp}) \times \mathcal{B}(Z(4430)^{\pm} \to \psi(2S)\pi^{\pm}) = 4.1 \times 10^{-5}$, it is expected that LHCb will reconstruct 6200 such decays per nominal year of data taking, with an expected background-to-signal ratio in the interval [2.7, 5.3], based on the study of the two most obvious background sources: the inclusive $\psi(2S)$ and $b\bar{b}$. With such statistics, LHCb is expected to be able to confirm the Belle discovery even in the first phase of data taking, at lower energy.

# Appendix A

# Additional Monte Carlo Alignment Studies

## A.1 Cut on the (Fit Match) $\chi^2$ for IT-OT Tracks

$\mathfrak{I}$ᴺ Section 4.1.1, the $\chi^2/\mathrm{dof}$ and fit match $\chi^2$ of good, bad and ghost tracks were presented for tracks going only through the Inner Tracker (i.e. without OT hits). In this appendix, the same distributions are presented for long tracks going through both the OT and the IT. The data sample used is a sample of minimum-bias events. By comparing the plots and tables presented here with the corresponding plots and numbers in Section 4.1.1, it is visible that the cut on the track quality (especially the $\chi^2_{\mathrm{m}}$) is much more powerful with tracks going through IT only. This implies that when these cuts are applied, the sample of tracks selected to align the Inner Tracker will be much less polluted than the sample selected to align the Outer Tracker. This implies a more precise alignment of the Inner Tracker, which can then be used as a constraint for the Outer Tracker.

Table A.1: Long track selection efficiencies and ghost rate before and after track quality requirements on $\chi^2/\mathrm{dof}$ and $\chi^2_{\mathrm{m}}$ in the misaligned case. The data used is a sample of simulated minimum bias events.

| Cut | Efficiency | | Ghost rate |
|---|---|---|---|
| | Good tracks | Bad tracks | |
| No cut | 100 % | 100 % | 17.50 % |
| $\chi^2/\mathrm{dof} < 100$ | 100 % | 99.99 % | 17.44 % |
| $\chi^2_{\mathrm{m}} < 100$ | 99.07 % | 93.68 % | 14.73 % |

(a) good tracks

(b) bad tracks

(c) ghost tracks

Figure A.1: Distributions of the track fit $\chi^2/\mathrm{dof}$ for (a) good, (b) bad and (c) ghost tracks with the misalignment scenario presented in Section 4.3.1.

(a) good tracks

(b) bad tracks

(c) ghost tracks

Figure A.2: Distributions of the track fit $\chi^2$/dof for (a) good, (b) bad and (c) ghost tracks with the ideal geometry.
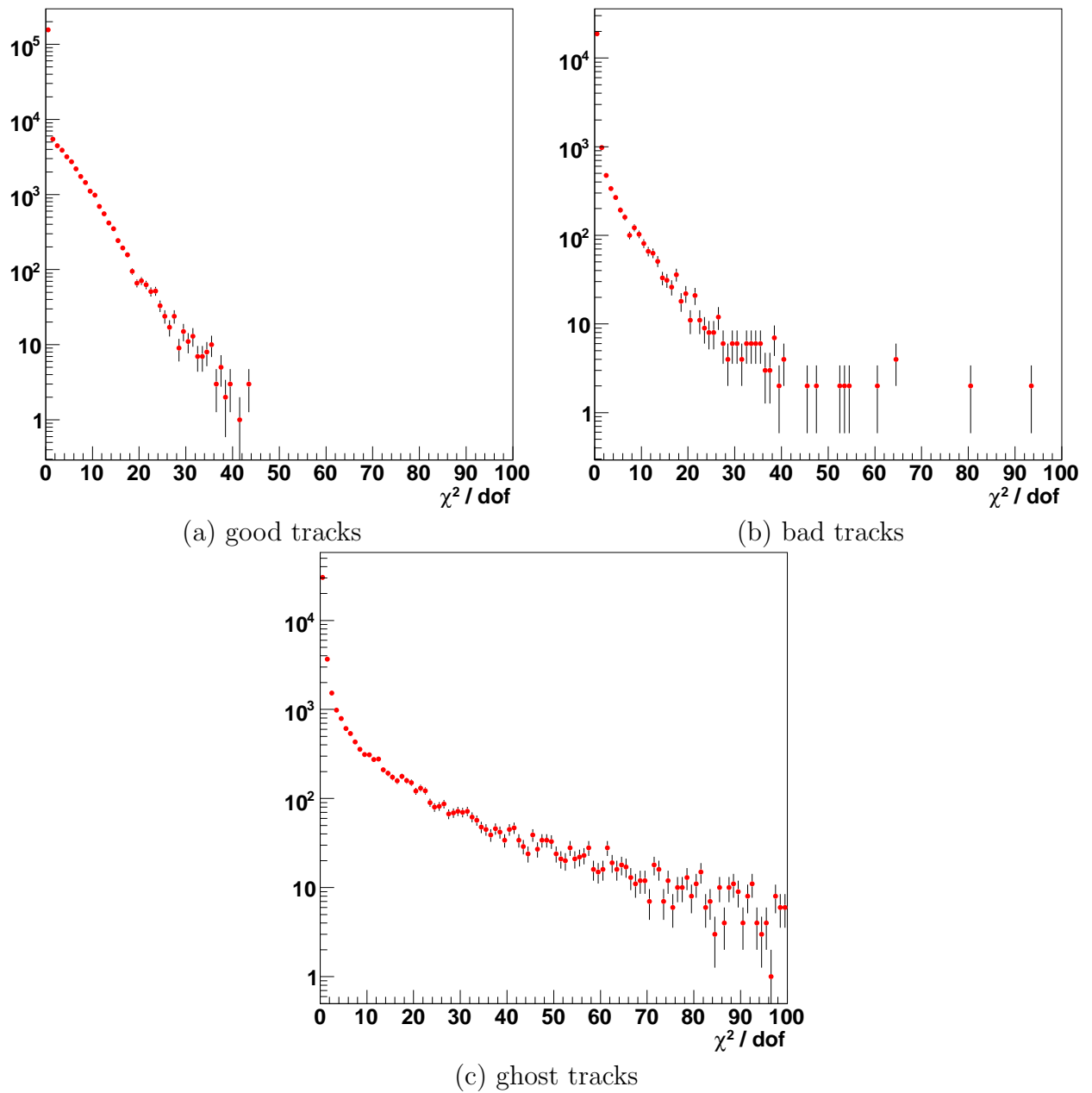
(a) good tracks

(b) bad tracks

(c) ghost tracks

Figure A.3: Distributions of the track $\chi^2_\mathrm{m}$ for (a) good, (b) bad and (c) ghost tracks with the misalignment scenario presented in Section 4.3.1.
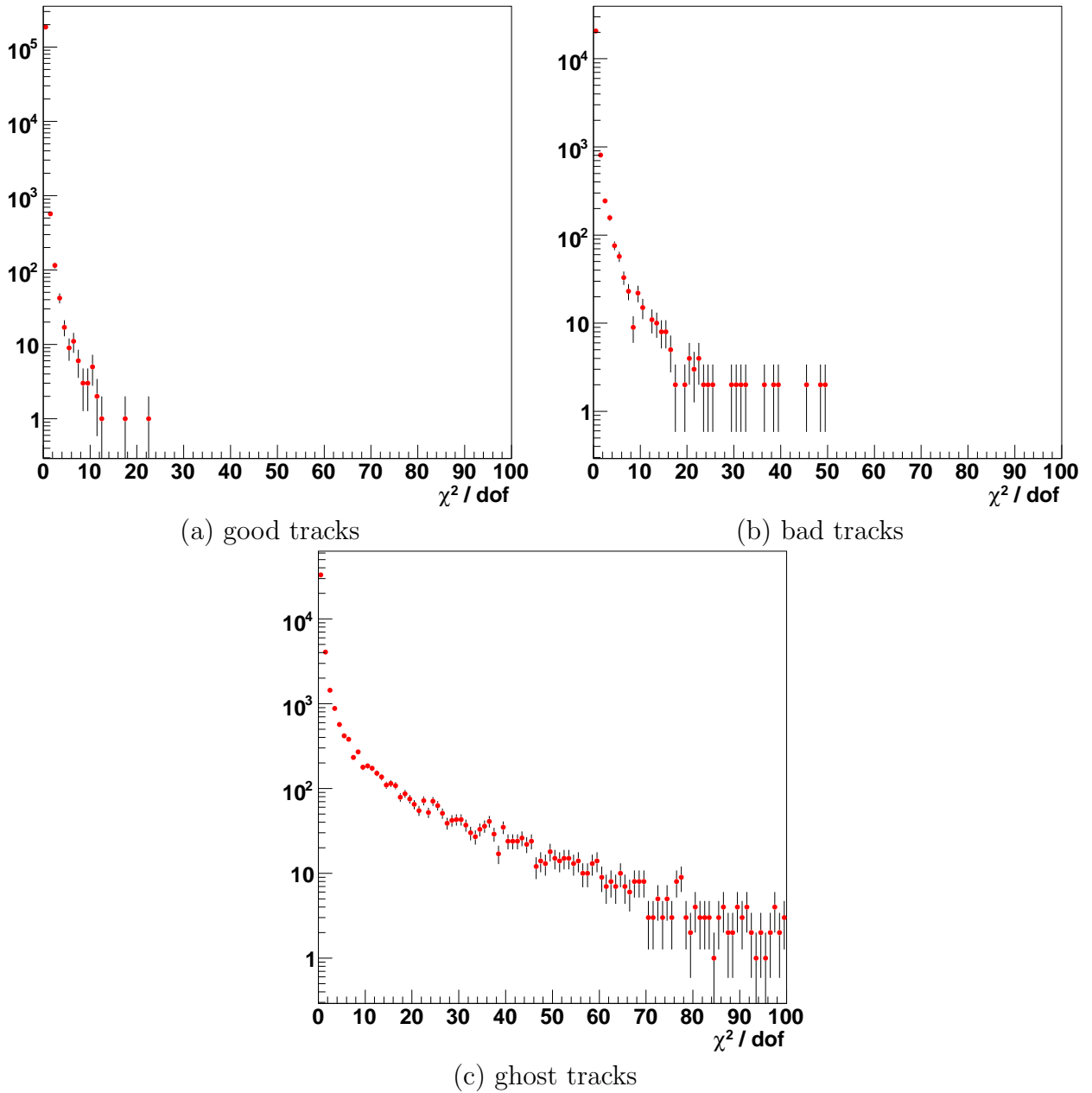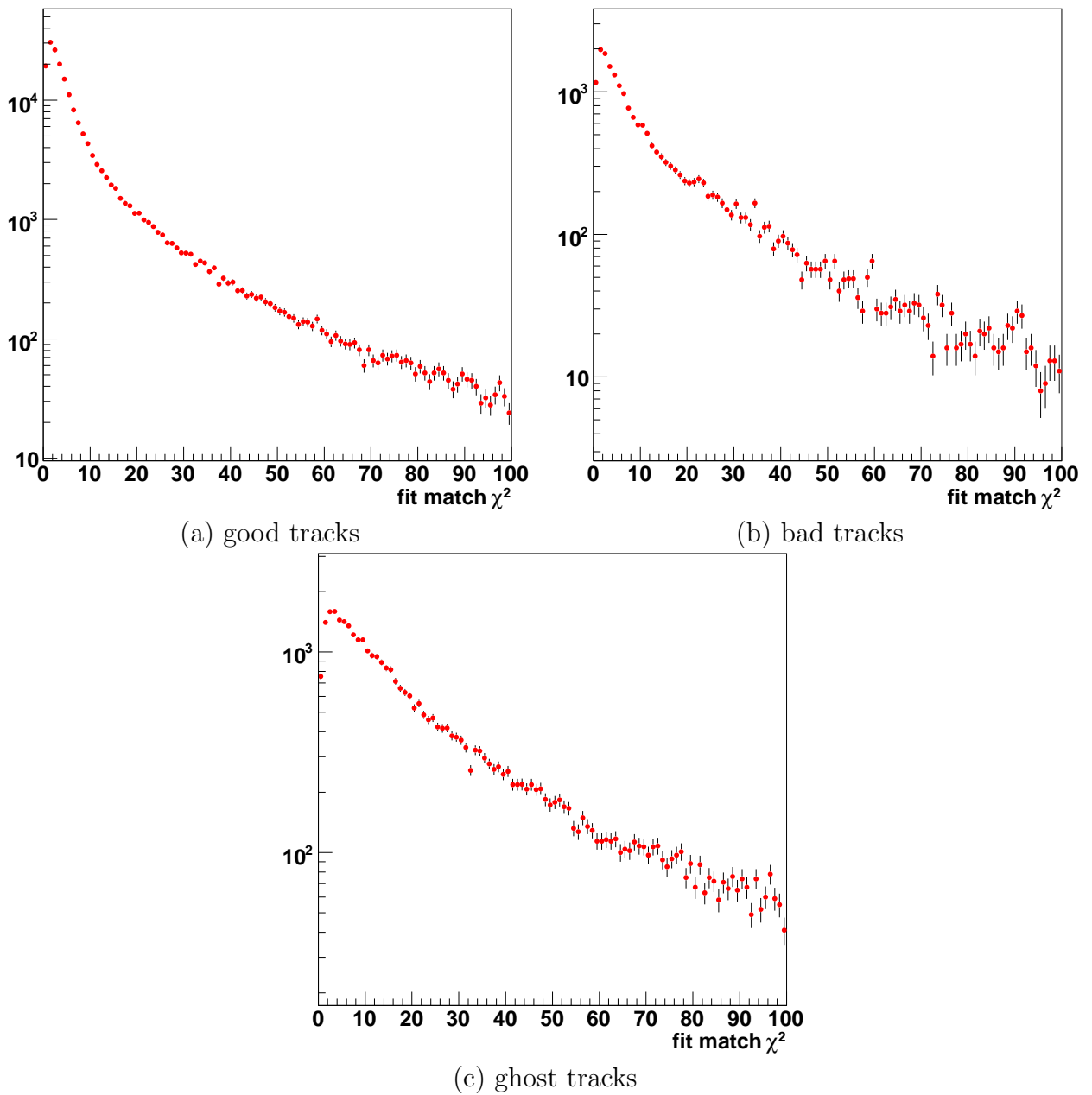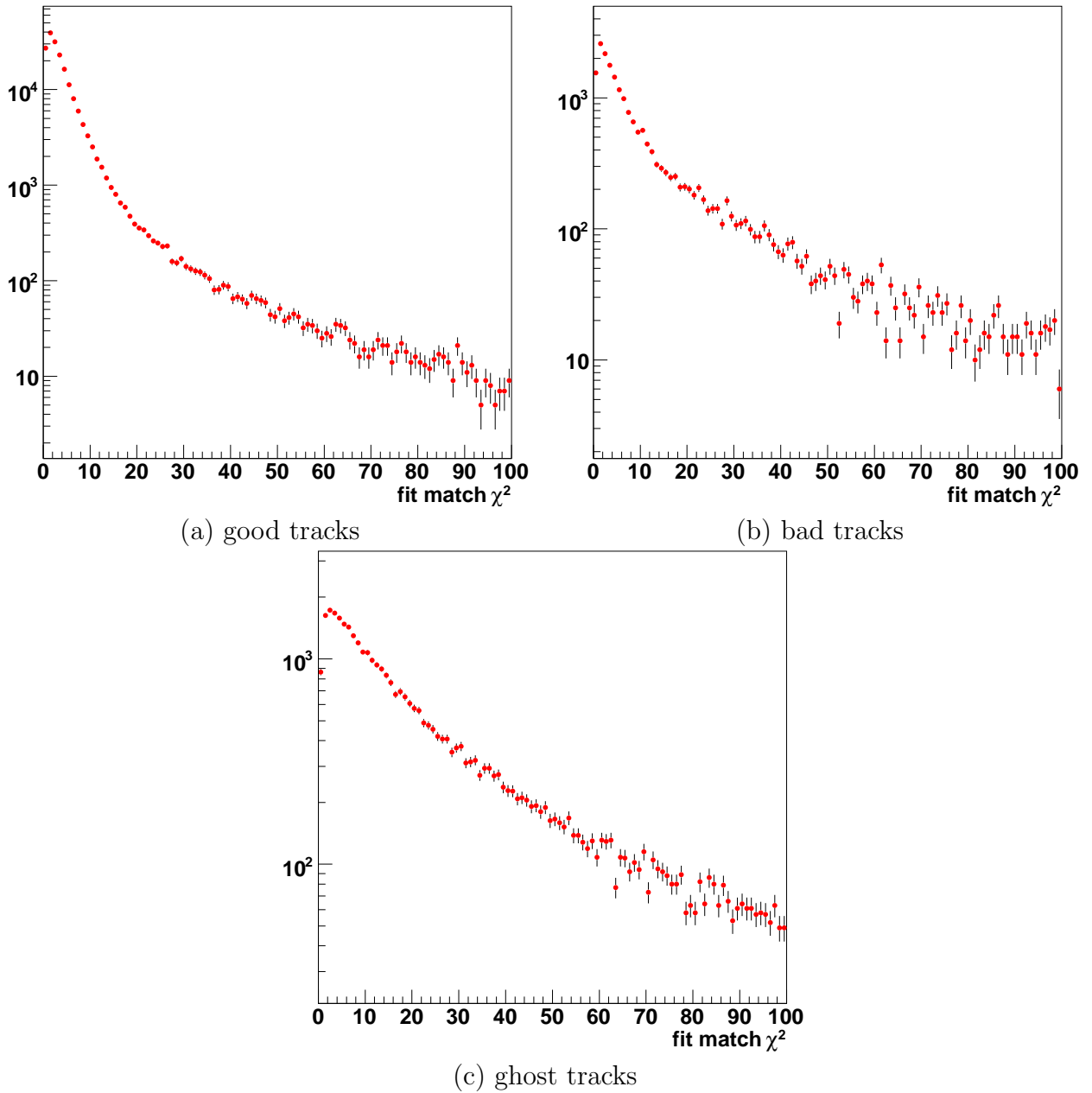
(a) good tracks

(b) bad tracks

(c) ghost tracks

Figure A.4: Distributions of the track $\chi^2_{\mathrm{m}}$ for (a) good, (b) bad and (c) ghost tracks with the ideal geometry.

Table A.2: Long track selection efficiencies and ghost rate before and after track quality requirements on $\chi^2/\mathrm{dof}$ and $\chi^2_\mathrm{m}$ in the case of the ideal geometry. The data used is a sample of simulated minimum bias events.

| Cut | Efficiency | | Ghost rate |
|---|---|---|---|
| | Good tracks | Bad tracks | |
| No cut | 100 % | 100 % | 17.47 % |
| $\chi^2/\mathrm{dof} < 10$ | 99.99 % | 99.55 % | 16.59 % |
| $\chi^2_\mathrm{m} < 30$ | 98.23 % | 82.83 % | 11.63 % |

# Appendix B

# Additional TED Alignment Studies

## B.1   Additional Studies of Unbiased Residual Distributions

The distributions of unbiased residuals in the IT layers obtained with Inner Tracker tracks from the TED data have been fitted individually with a Gaussian. Figure B.1 shows the distribution of the bias of these Gaussian fits. The $X$ and stereo layers are shown separately. The fit has been performed on the distribution both before and after alignment. A clear improvement is visible after the alignment procedure, as was already visible with the distributions separated by ladders, shown in Section 5.1.7.a.

## B.2   TT Confirmation of the IT Alignment Results

Another method investigated to validate the results of the Inner Tracker alignment is to propagate the tracks found in the Inner Tracker to the Tracker Turicensis (TT) [93]. The distribution of the residuals of TT hits with respect to the extrapolated IT tracks should indeed improve during the alignment process. The resolution of the distribution is then reported at each step of the alignment (before alignment, after box, layer and ladder alignment). This has been performed using an independent data sample which included hits in the TT.

Figure B.2 shows the evolution of (a) the residuals in the Layer TTaX with respect to tracks going through the IT Top Box, and (b) the residuals in the Layer TTbV with respect to tracks going through the IT A-side Box. Although the first plot shows a nice evolution, with the resolution decreasing at each alignment step, it has to be noted that most of the other evolution plots look more like the second plot. Also, the improvement is not significant compared to the large errors.

The fact that most of the evolution plots do not behave as expected (the resolution should improve at each alignment step) shows that the confirmation using TT information is not as powerful as the unbiased residuals. This is due to several reasons. During the whole alignment process, several IT layers are fixed. This means that the alignment is only internal to the Inner Tracker but doesn't account for any global movement (whether it be a translation, a rotation, a shearing or a more complex movement) of the Inner
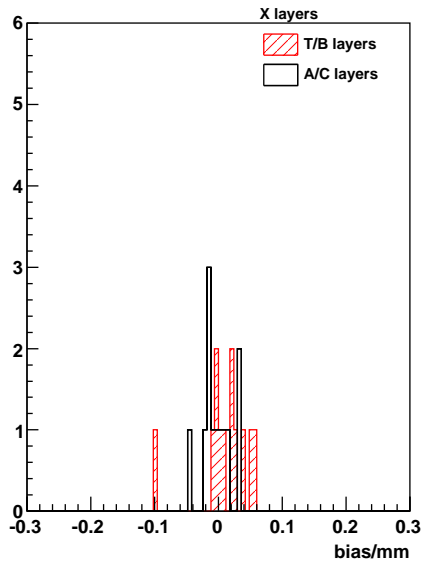
(a) $X$ layers before alignment
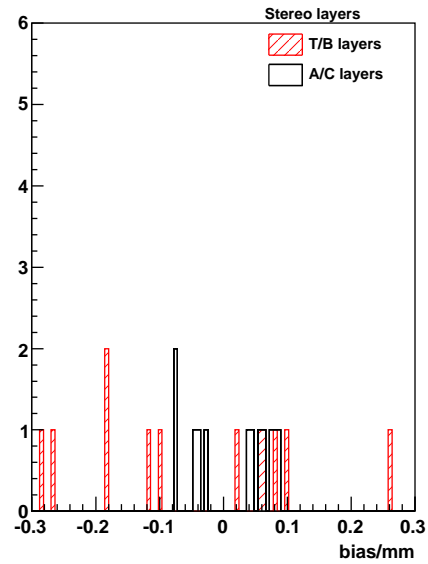
(b) stereo layers before alignment
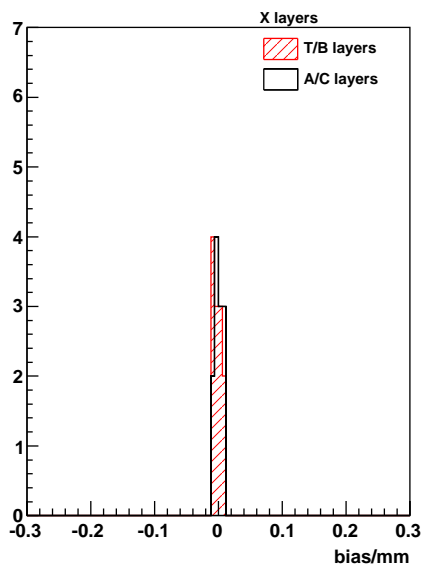
(c) $X$ layers after alignment
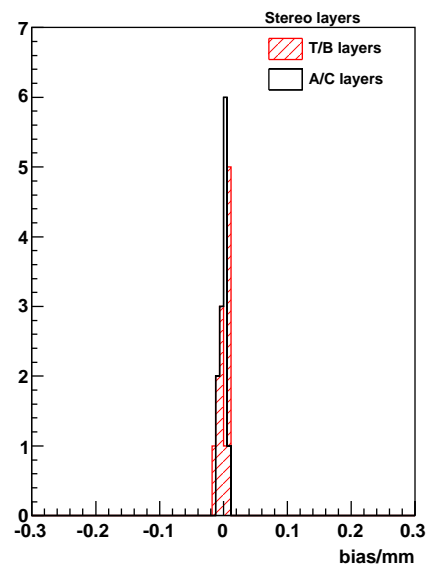
(d) stereo layers after alignment

Figure B.1: Bias of the distribution of unbiased residuals for individual IT layers. (a) shows the $X$ layers before alignment, (b) the stereo layers before alignment, (c) the $X$ layers after alignment and (d) the stereo layers after alignment.

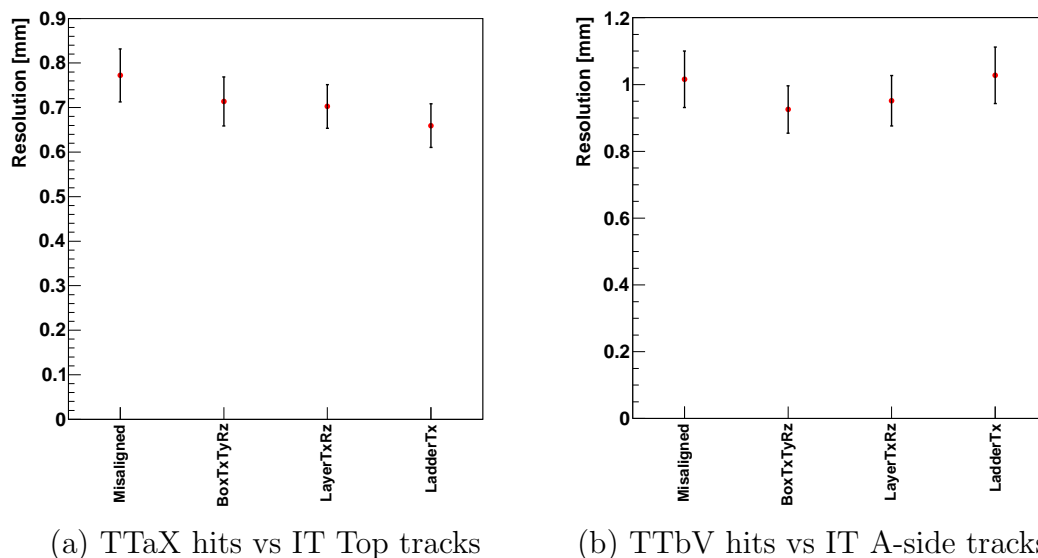(a) TTaX hits vs IT Top tracks          (b) TTbV hits vs IT A-side tracks

Figure B.2: Evolution of the resolution of the distributions of residuals of TT hits with respect to tracks going through the IT. The plot on the left shows the residuals in the TTaX Layer with respect to tracks from the IT Top Box. The plot on the right shows the residuals in the TTbV Layer with respect to tracks coming from the IT A-side Box.

Tracker boxes, layers or modules. This means, in particular, that the Inner Tracker is not aligned with respect to the rest of the LHCb detector (for example the TT used here).

Another reason for the worse performance of the TT confirmation is that this sub-detector has not been internally aligned prior to this study. This effect should be smaller than the first one as alignment corrections to the survey measurements are expected to be small for the TT.

Finally, due to the large propagation distance between the Inner Tracker and the Tracker Turicensis, a rotation of the former during alignment induces a worse resolution in the latter. This problem will be solved when relative TT–IT alignment will be performed.

# Bibliography

[1] J. H. Christenson *et al.*, *Evidence for the 2 π Decay of the $K_2^0$ Meson*, Phys. Rev. Lett. **13**, 138 (1964).

[2] European Organization for Nuclear Research, *Convention for the Establishment of a European Organization for Nuclear Research (1953)*.
http://dsu.web.cern.ch/dsu/ls/conventionE.htm

[3] J. D. Lykken, *Introduction to Supersymmetry*, arXiv:hep-th/9612114 (1996).

[4] N. Arkani-Hamed, A. G. Cohen and H. Georgi, *Electroweak Symmetry Breaking from Dimensional Deconstruction*, Phys. Lett. B **513**, 232 (2001).

[5] C. Currat, *Direct Search for Higgs Boson in LHCb*, Ph.D. thesis, EPFL, Lausanne, Switzerland, CERN-THESIS-2001-024 (2001).

[6] L. Locatelli, *Direct Search for Higgs Boson in LHCb and Contribution to the Development of the Vertex Detector*, Ph.D. thesis, EPFL, Lausanne, Switzerland, CERN-THESIS-2007-073 (2007).

[7] V. Coco, *Reconstruction et Identification de Jets Beaux dans l'Expérience LHCb en Vue d'Étudier sa Sensibilié à un Boson de Higgs Standard se Désintégrant en Paires $b\bar{b}$*, Ph.D. thesis, Université de Savoie, Annecy, France, CERN-THESIS-2008-101 (2008).

[8] S.-K. Choi *et al.* (Belle Collaboration), *Observation of a Narrow Charmoniumlike State in Exclusive $B^{\pm} \rightarrow K^{\pm}\pi^+\pi^- J/\psi$ Decays*, Phys. Rev. Lett. **91**, 262001 (2003).

[9] B. Aubert *et al.* (BaBar Collaboration), *Observation of a Broad Structure in the $\pi^+\pi^- J/\psi$ Mass Spectrum Around $4.26\,\mathrm{GeV}/c^2$*, Phys. Rev. Lett. **95**, 142001 (2005).

[10] S.-K. Choi, S. L. Olsen *et al.* (Belle Collaboration), *Observation of a Resonancelike Structure in the $\pi^{\pm}\psi'$ Mass Distribution in Exclusive $B \rightarrow K\pi^{\pm}\psi'$ Decays*, Phys. Rev. Lett. **100**, 142001 (2008).

[11] C. Hanhart *et al.*, *Reconciling the $X(3872)$ with the Near-Threshold Enhancement in the $D^0\bar{D}^{*0}$ Final State*, Phys. Rev. D **76**, 034007 (2007).

[12] B. A. Li, *Is $X(3872)$ a Possible Candidate as a Hybrid Meson?*, Phys. Lett. B **605**, 306 (2005).

[13] N. A. Törnqvist, *Isospin Breaking of the Narrow Charmonium State of Belle at 3872 MeV as a Deuson*, Phys. Lett. B **590**, 209 (2004).

[14] L. Maiani *et al.*, *Diquark-Antidiquark States with Hidden or Open Charm and the Nature of X(3872)*, Phys. Rev. D **71**, 014028 (2005).

[15] L. Maiani *et al.*, *Indications of a Four-Quark Structure for the X(3872) and X(3876) Particles from Recent Belle and BaBar Data*, Phys. Rev. Lett. **99**, 182003 (2007).

[16] C. Amsler *et al.* (Particle Data Group), *Review of Particle Physics*, Phys. Lett. B **667**, 1 (2008).

[17] C. S. Wu *et al.*, *Experimental Test of Parity Conservation in Beta Decay*, Phys. Rev. **105**, 1413–1415 (1957).

[18] A. Angelopoulos *et al.* (CPLear Collaboration), *First Direct Observation of Time-Reversal Non-Invariance in the Neutral-Kaon System*, CERN-EP/98-154, published in Phys. Lett. B **444**, 43 (1998).

[19] M. Adinolfi *et al.* (LHCb Collaboration), *The Tree-Level Determination of $\gamma$ at LHCb*, LHCb-ROADMAP5-002 in preparation (2009).

[20] N. Cabibbo, *Unitary Symmetry and Leptonic Decays*, Phys. Rev. Lett. **10**, 531–533 (1963).

[21] M. Kobayashi and T. Maskawa, *CP-Violation in the Renormalizable Theory of Weak Interaction*, Prog. Theor. Phys. **49**, 652–657 (1973).

[22] M. Gell-Mann, *A Schematic Model of Baryons and Mesons*, Phys. Lett. **8**, 214–215 (1964).

[23] G. Zweig, *An $SU_3$ Model for Strong Interaction Symmetry and its Breaking*, CERN-Reports TH-401 and TH-412 (1964).

[24] L. Wolfenstein, *Parametrisation of the Kobayashi-Maskawa Matrix*, Phys. Rev. Lett. **51**, 1945–1947 (1983).

[25] M. Veltman, *Diagrammatica: The Path to Feynman Diagrams*, Cambridge Lecture Notes in Physics (1994).

[26] J. Charles *et al.* (CKMfitter Group), *CP Violation and the CKM Matrix: Assessing the Impact of the Asymmetric B Factories*, arXiv:hep-ph/0406184
Updated results and plots available at: `http://ckmfitter.in2p3.fr` (2005).

[27] A. Bates *et al.* (LHCb Collaboration), *Road Map for Charmless Charged Two-Body B Decays at LHCb*, LHCb-ROADMAP6-001 in preparation (2009).

[28] CDF/DØ $\Delta\Gamma_s$, $\beta_s$ Combination Working Group, *Combination of DØ and CDF Results on $\Delta\Gamma_s$ and the CP-Violating Phase $\beta_s^{J/\psi\phi}$*, CDF/PHYS/BOTTOM/CDFR/9787, DØ Note 5928-CONF (2009).

[29] J. Albrecht *et al.* (LHCb Collaboration), *Search for New Physics in Mixing-Induced CP Violation in* $B_s^0 \rightarrow J/\psi\,\phi$, LHCb-ROADMAP3-001 in preparation (2009).

[30] A. Abulencia *et al.* (CDF Collaboration), *Observation of* $B_s^0 - \bar{B}_s^0$ *Oscillations*, arXiv:hep-ex/0609040 (2006).

[31] L. Fernandez, *Exclusive Trigger Selections and Sensitivity to the* $B_s - \bar{B}_s$ *Mixing Phase at LHCb*, Ph.D. thesis, EPFL, Lausanne, Switzerland, CERN-THESIS-2006-042 (2006).

[32] M.-O. Bettler (LHCb Collaboration), *The LHCb Analysis for* $B_s^0 \rightarrow \mu^+\mu^-$, arXiv:hep-ex/0908-4066 (2009).

[33] M.-O. Bettler (LHCb Collaboration), *LHCb Prospects for Rare Decays* .

[34] M. Blanke *et al.*, *Minimal Flavour Violation Waiting for Precise Measurements of* $\Delta M_s$, $S_{\psi\phi}$, $A_{\mathrm{SL}}^s$, $|V_{ub}|$, $\gamma$ *and* $B_{s,d}^0 \rightarrow \mu^+\mu^-$, arXiv:hep-ph/0604057 (2006).

[35] T. Aaltonen *et al.* (CDF Collaboration), *Search for* $B_s^0 \rightarrow \mu^+\mu^-$ *and* $B^0 \rightarrow \mu^+\mu^-$ *Decays in 3.7 fb$^{-1}$ of* $p\bar{p}$ *Collisions with CDF II*, CDF Public Note 9892 (2009).

[36] V. M. Abazov *et al.* (DØ Collaboration), *A New Upper Limit for the Rare Decay* $B_s^0 \rightarrow \mu^+\mu^-$ *Using 2 fb$^{-1}$ of Run II Data*, DØ Note 5344-CONF (2007).

[37] D. Martinez Santos *et al.* (LHCb Collaboration), *Analysis of the Decay* $B_s^0 \rightarrow \mu^+\mu^-$ *at LHCb*, LHCb-ROADMAP1-002 in preparation (2009).

[38] B. Aubert *et al.* (BaBar Collaboration), *Measurements of Branching Fractions, Rate Asymmetries, and Angular Distributions in the Rare Decays* $B \rightarrow Kl^+l^-$ *and* $B \rightarrow K^*l^+l^-$, arXiv:hep-ex/0604007 (2006).

[39] I. Adachi *et al.* (Belle Collaboration), *Measurement of the Differential Branching Fraction and Forward-Backward Asymmetry for* $B \rightarrow K^{(*)}l^+l^-$, arXiv:hep-ex/0810.0335 (2008).

[40] T. Aaltonen *et al.* (CDF Collaboration), *Search for the Rare Decays* $B^+ \rightarrow \mu^+\mu^-K^+$, $B^0 \rightarrow \mu^+\mu^-K^*(892)^0$ *and* $B_s^0 \rightarrow \mu^+\mu^-\phi$ *at CDF*, arXiv:hep-ex/0804.3908 (2009).

[41] S. L. Glashow, J. Illiopoulos and L. Maiani, *Weak Interactions with Lepton-Hadron Symmetry*, Phys. Rev. D **2**, 1285–1292 (1970).

[42] J. J. Aubert *et al.* (E598 Collaboration), *Experimental Observation of a Heavy Particle J*, Phys. Rev. Lett. **33**, 1404–1406 (1974).

[43] J. E. Augustin *et al.* (SLAC-SP-017 Collaboration), *Discovery of a Narrow Resonance in* $e^+e^-$ *Annihilation*, Phys. Rev. Lett. **33**, 1406–1408 (1974).

[44] E. S. Swanson, *The New Heavy Mesons: a Status Report*, arXiv:hep-ph/0601110 (2006).

[45] S. Godfrey and S. L. Olsen, *The Exotic XYZ Charmonium-Like Mesons*, Annu. Rev. Nucl. Part. Sci. **58**, 51–73 (2008).

[46] S. Okubo, *Phi Meson and Unitary Symmetry Model*, Phys. Lett. **5**, 165–168 (1963).

[47] J. Iizuka, *A Systematics and Phenomenology of Meson Family*, Prog. Th. Phys. Suppl. **37-38**, 21–34 (1966).

[48] D. Acosta *et al.* (CDF Collaboration), *Observation of the Narrow State $X(3872) \to J/\psi\,\pi^+\pi^-$ in $\bar{p}p$ Collisions at $\sqrt{s} = 1.96$ TeV*, Phys. Rev. Lett. **93**, 072001 (2004).

[49] V.M. Abazov *et al.* (DØ Collaboration), *Observation and Properties of the $X(3872)$ Decaying to $J/\psi\,\pi^+\pi^-$ in $p\bar{p}$ Collisions at $\sqrt{s} = 1.96$ TeV*, Phys. Rev. Lett. **93**, 162002 (2004).

[50] B. Aubert *et al.* (BaBar Collaboration), *Study of the $B^- \to J/\psi\,K^-\pi^+\pi^-$ Decay and Measurement of the $B^- \to X(3872)K^-$ Branching Fraction*, Phys. Rev. D **71**, 071103 (2005).

[51] S. L. Olsen, *What's New with the XYZ Mesons?*, arXiv:hep-ex/0801.1153 (2008).

[52] G. V. Pakhlova, *Exotic $c\bar{c}$ Spectroscopy*, arXiv:hep-ex/0810.4114 (2008).

[53] J. L. Rosner *et al.* (CLEO Collaboration), *Observation of the $h_c(^1P_1)$ State of Charmonium*, Phys. Rev. Lett. **95**, 102003 (2005).

[54] S.-K. Choi *et al.* (Belle Collaboration), *Observation of the $\eta_c(2S)$ in Exclusive $B \to KK_S^0K^-\pi^+$ Decays*, Phys. Rev. Lett. **89**, 102001 (2002).

[55] S. Uehara *et al.* (Belle Collaboration), *Observation of a $\chi'_{c2}$ Candidate in $\gamma\gamma \to D\bar{D}$ Production at Belle*, Phys. Rev. Lett. **96**, 082003 (2005).

[56] T. Barnes, S. Godfrey, *Charmonium Options for the X(3872)*, Phys. Rev. D **69**, 054008 (2004).

[57] S. Godfrey and J. Napolitano, *Light-Meson Spectroscopy*, Rev. Mod. Phys. **71**, 1411–1462 (1999).

[58] N. A. Törnqvist, *From the Deuteron to Deusons, an Analysis of Deuteron-Like Meson-Meson Bound States*, Z. Phys. C **61**, 525 (1994).

[59] S. Weinberg, *Effective Chiral Lagrangians for Nucleon-Pion Interactions and Nuclear Forces*, Nucl. Phys. B **363**, 3 (1991).

[60] D. V. Bugg, *Reinterpreting Several Narrow 'Resonances' as Threshold Cusps*, Phys. Rev. Lett. B **598**, 8–14 (2004).

[61] S. Uehara *et al.* (CDF Collaboration), *Update on $Z(4430)^\pm$ and $X(3872)$ at Belle*, arXiv:hep-ex/0905.4313 (2009).

[62] T. Aaltonen *et al.* (CDF Collaboration), *Precision Measurement of the $X(3872)$ Mass in $J/\psi\pi^+\pi^-$ Decays*, arXiv:hep-ex/0906.5218 (2009).

[63] K. Abe *et al.* (Belle Collaboration), *Experimental Constraints on the Possible $J^{PC}$ Quantum Numbers of the $X(3872)$*, arXiv:hep-ex/0505038 (2005).

[64] B. Aubert *et al.* (BaBar Collaboration), *Study of the $X(3872)$ and $Y(4260)$ in $B^0 \to J/\psi\pi^+\pi^- K^0$ and $B^\pm \to J/\psi\pi^+\pi^- K^\pm$ Decays*, arXiv:hep-ex/0507090 (2006).

[65] B. Aubert *et al.* (BaBar Collaboration), *Search for $B^+ \to X(3872)K^+$, $X(3872) \to J/\psi\gamma$*, Phys. Rev. D **74**, 071101 (2006).

[66] K. Abe *et al.* (Belle Collaboration), *Evidence for $X(3872) \to \gamma J/\psi$ and the Sub-Threshold Decay $X(3872) \to \omega J/\psi$*, arXiv:hep-ex/0505037 (2005).

[67] D. Abulencia *et al.* (CDF Collaboration), *Analysis of the Quantum Numbers $J^{PC}$ of the $X(3872)$ Particle*, Phys. Rev. Lett. **98**, 132002 (2007).

[68] K. Trabelsi *et al.* (Belle Collaboration), *Study of $X(3872)$ in B Meson Decays*, arXiv:hep-ex/0809.1224 (2008).

[69] B. Aubert *et al.* (BaBar Collaboration), *Study of $B \to X(3872)K$, with $X(3872) \to J/\psi\,\pi^+\pi^-$*, Phys. Rev. D **77**, 111101 (2008).

[70] G. Gokhroo *et al.* (Belle Collaboration), *Observation of a Near-Threshold $D^0\bar{D}^0\pi^0$ Enhancement in $B \to D^0\bar{D}^0\pi^0 K$ Decays*, Phys. Rev. Lett. **97**, 162002 (2006).

[71] N. Zwahlen, T. Aushev *et al.* (Belle Collaboration), *Study of the $B \to X(3872)(D^{*0}\bar{D}^0)K$ Decay*, arXiv:hep-ex/0810.0358 (2008).

[72] B. Aubert *et al.* (BaBar Collaboration), *Study of Resonances in Exclusive B Decays to $\bar{D}^{(*)}D^{(*)}K$*, Phys. Rev. D **77**, 011102 (2008).

[73] B. Aubert *et al.* (BaBar Collaboration), *Evidence for $X(3872) \to \psi(2S)\gamma$ in $B^\pm \to X(3872)K^\pm$ Decays, and a Study of $B \to c\bar{c}\gamma K$*, arXiv:hep-ex/0809.0042 (2008).

[74] D. Abulencia *et al.* (CDF Collaboration), *Measurement of the Dipion Mass Spectrum in $X(3872) \to J/\psi\pi^+\pi^-$ Decays*, Phys. Rev. Lett. **96**, 102002 (2006).

[75] B. Aubert *et al.* (BaBar Collaboration), *Search for a Charged Partner of the $X(3872)$ in the B Meson Decay $B \to X^- K$, $X^- \to J/\psi\pi^-\pi^0$*, Phys. Rev. D **71**, 031501 (2005).

[76] A. G. Mokhtar, *Searches for Exotic $X$, $Y$, and $Z-$ States with BaBar*, arXiv:hep-ex/0810.1073 (2008).

[77] R. Mizuk *et al.* (Belle Collaboration), *Dalitz Analysis of $B \to K\pi^+\psi'$ Decays and the $Z(4430)^+$*, arXiv:hep-ex/0905.2869 (2009).

[78] M. A. Shifman, A. I. Vainshtein and V. I. Zakharov, *QCD and Resonance Physics. Theoretical Foundations*, Nucl. Phys. B **147**, 385–447 (1979).

[79] L. J. Reinders, H. Rubinstein, S. Yazaki, *Hadron Properties from QCD Sum Rules*, Phys. Rep. B **127**, 1–97 (1985).

[80] S. H. Lee *et al.*, *QCD Sum Rules Study of the Meson $Z^+(4430)$*, Phys. Lett. B **661**, 28–32 (2008).

[81] L. Maiani, A. D. Polosa and V. Riquer, *The Charged Z(4433): Towards a New Spectroscopy*, arXiv:hep-ph/0708.3997 (2007).

[82] P. Pakhlov *et al.* (Belle Collaboration), *Observation of a Charmoniumlike State Produced in Association with a $J/\psi$ in $e^+e^-$ Annihilation at $\sqrt{s} \approx 10.6\,GeV$*, Phys. Rev. Lett. **98**, 082001 (2007).

[83] S. K. Choi, S. L. Olsen *et al.* (Belle Collaboration), *Observation of a Near-Threshold $\omega J/\psi$ Mass Enhancement in Exclusive $B \to K\omega J/\psi$ Decays*, Phys. Rev. Lett. **94**, 182002 (2005).

[84] B. Aubert *et al.* (BaBar Collaboration), *Observation of a Broad Structure in the $\pi^+\pi^- J/\psi$ Mass Spectrum Around $4.26\,GeV/\mathrm{c}^2$*, Phys. Rev. Lett. **95**, 142001 (2005).

[85] T. E. Coan *et al.* (CLEO Collaboration), *Charmonium Decays of $Y(4260)$, $\psi(4160)$, and $\psi(4040)$*, Phys. Rev. Lett. **96**, 162003 (2006).

[86] C. Z. Yuan *et al.* (Belle Collaboration), *Measurement of the $e^+e^- \to \pi^+\pi^- J/\psi$ Cross Section via Initial-State Radiation at Belle*, Phys. Rev. Lett. **99**, 182004 (2007).

[87] B. Aubert *et al.* (BaBar Collaboration), *Evidence of a Broad Structure at an Invariant Mass of $4.32\,GeV/\mathrm{c}^2$ in the Reaction $e^+e^- \to \pi^+\pi^-\psi(2S)$ Measured at BaBar*, Phys. Rev. Lett. **98**, 212001 (2007).

[88] X. L. Wang *et al.* (Belle Collaboration), *Observation of Two Resonant Structures in $e^+e^- \to \pi^+\pi^-\psi(2S)$ via Initial-State Radiation at Belle*, Phys. Rev. Lett. **99**, 142002 (2007).

[89] T. Aaltonen *et al.* (CDF Collaboration), *Evidence for a Narrow Near-Threshold Structure in the $J/\psi\phi$ Mass Spectrum in $B^+ \to J/\psi\phi K^+$ Decays*, arXiv:hep-ex/0903.2229 (2009).

[90] R. Mizuk, R. Chistov *et al.* (Belle Collaboration), *Observation of Two Resonance-Like Structures in the $\pi^+\chi_{c1}$ Mass Distribution in Exclusive $\bar{B}^0 \to K^-\pi^+\chi_{c1}$ Decays*, arXiv:hep-ex/0806.4098 (2008).

[91] B. Aubert *et al.* (BaBar Collaboration), *Observation of $Y(3940) \to J/\psi\omega$ in $B \to J/\psi\omega K$ at BaBar*, Phys. Rev. Lett. **101**, 082001 (2008).

[92] P. Pakhlov *et al.* (Belle Collaboration), *Production of New Charmoniumlike States in $e^+e^- \to J/\psi D^{(*)}\bar{D}^{(*)}$ at $\sqrt{s} \approx 10.6\,GeV$*, Phys. Rev. Lett. **100**, 202001 (2008).

[93] A. Augusto Alves Jr *et al.* (LHCb Collaboration), *The LHCb Detector at LHC*, J. of Inst. **3**, S08005 (2008).

[94] M. Needham, *Performance of the LHCb Track Reconstruction*, CERN-LHCb-2007-144 (2007).

[95] M. Needham, *Classification of Ghost Tracks*, CERN-LHCb-2007-128 (2007).

[96] R. Antunes Nobrega *et al.* (LHCb Collaboration), *LHCb Reoptimized Detector Design and Performance*, CERN/LHCC 2003-030 (2003).

[97] M. Needham, *Silicon Tracker Occupancies and Clustering*, CERN-LHCb-2007-024 (2007).

[98] M. Calvi, O. Leroy and M. Musy, *Flavour Tagging Algorithms and Performances in LHCb*, CERN-LHCb-2007-058 (2007).

[99] J. Borel, L. Nicolas *et al.*, *The $B_s^0 \to D_s\pi$ and $B_s^0 \to D_s K$ Selections*, CERN-LHCb-2007-017 (2007).

[100] G. Barrand *et al.*, *GAUDI - A Software Architecture and Framework for Building LHCb Data Processing Applications*, Proceedings CHEP 2000, Padova, Italy, Feb. 2000.

[101] LHCb Collaboration, *The GAUDI Project.*
http://proj-gaudi.web.cern.ch/proj-gaudi/

[102] LHCb Collaboration, *The GAUSS Project.*
http://lhcb-release-area.web.cern.ch/LHCb-release-area/DOC/gauss/

[103] T. Sjörstrand, S. Mrenna and P. Skands, *The PYTHIA Generator Program.*
http://projects.hepforge.org/pythia6/

[104] D. J. Lange, *The EvtGen Particle Decay Simulation Package*, Nucl. Instr. and Meth. A **462**, 152–155 (2001).

[105] D. Lange and A. Ryd, *The EVTGEN Event Generator.*
http://www.slac.stanford.edu/~lange/EvtGen/

[106] Geant4 Collaboration, *The GEANT4 Toolkit.*
http://geant4.web.cern.ch/geant4/

[107] LHCb Collaboration, *The BOOLE Project.*
http://lhcb-release-area.web.cern.ch/LHCb-release-area/DOC/boole/

[108] LHCb Collaboration, *The BRUNEL Project.*
http://lhcb-release-area.web.cern.ch/LHCb-release-area/DOC/brunel/

[109] LHCb Collaboration, *The DAVINCI Project.*
http://lhcb-release-area.web.cern.ch/LHCb-release-area/DOC/davinci/

[110] LHCb Collaboration, *The PANORAMIX Project.*
http://lhcb-release-area.web.cern.ch/LHCb-release-area/DOC/panoramix/

[111] LHCb Collaboration, *The ALIGNMENT Project.*
http://lhcb-release-area.web.cern.ch/LHCb-release-area/DOC/alignment/

[112] T. Laštovička, *Generic VELO Pattern Recognition*, CERN-LHCb-2007-002 (2008).

[113] D. Hutchcroft, *VELO Pattern Recognition*, CERN-LHCb-2007-013 (2007).

[114] R. Forty and M. Needham, *Standalone Track Reconstruction in the T-Stations*, CERN-LHCb-2007-022 (2007).

[115] R. Forty and M. Needham, *Updated Performance of the T-Seeding*, CERN-LHCb-2007-023 (2007).

[116] O. Callot and M. Schiller, *PatSeeding – A Standalone Track Reconstruction Algorithm*, CERN-LHCb-2008-042 (2008).

[117] O. Callot and S. Hansmann-Menzemer, *The Forward Tracking: Algorithm and Performance Studies*, CERN-LHCb-2007-015 (2007).

[118] M. Needham and J. van Tilburg, *Performance of the Track Matching*, CERN-LHCb-2007-020 (2007).

[119] M. Needham, *Performance of the Track Matching*, CERN-LHCb-2007-129 (2007).

[120] O. Callot, *Downstream Tracking and PatSeeding*, LHCb Tracking and Alignment Workshop, Heidelberg, Germany (2007).
http://indico.cern.ch/materialDisplay.py?
contribId=13&sessionId=1&materialId=slides&confId=12233

[121] E. Rodrigues, *Dealing with Clones in the Tracking*, CERN-LHCb-2006-057 (2006).

[122] J. van Tilburg, *Track Simulation and Reconstruction in LHCb*, Ph.D. thesis, Vrije University, Amsterdam, The Netherlands, CERN-THESIS-2005-040 (2005).

[123] M. Needham, *Private Communication* .

[124] M. Gersabeck, J. Nardulli and E. Rodrigues, *Impact of Misalignments on the Analysis of B Decays*, CERN-LHCb-2008-012 (2008).

[125] W. Baldini *et al.*, *LHCb Alignment Strategy*, CERN-LHCb-2006-035 (2006).

[126] S. Viret *et al.*, *LHCb VELO Software Alignment - Part I : the Alignment of the VELO Modules in their Half Boxes*, CERN-LHCb-2005-101 (2005).

[127] S. Viret *et al.*, *LHCb VELO Software Alignment - Part II : the Alignment of the VELO Detector-Halves*, CERN-LHCb-2007-067 (2007).

[128] M. Gersabeck *et al.*, *LHCb VELO Software Alignment - Part III : the Alignment of the Relative Sensor Positions*, CERN-LHCb-2007-138 (2008).

[129] V. Blöbel, *Software Alignment for Tracking Detectors*, Nucl. Instr. and Meth. A **5**, 566 (2006).

[130] M. Deissenroth (LHCb Collaboration), *Experience with LHCb Alignment Software on First Data*, Proceedings CHEP 09 Conference, Prag, Czech Republic, Mar. 2009, CERN-LHCb-CONF-2009-009.

[131] G. Conti and F. Blanc, *IT Survey Measurements Analysis and Implementation in the LHCb Software*, CERN-LHCb-2008-069 (2008).

[132] M. Needham, *First Alignment of the Inner Tracker Using Data from the TI-8 Sector Test*, CERN-LHCb-2009-030 (2009).

[133] W. Hulsbergen, *The Global Covariance Matrix of Tracks Fitted with a Kalman Filter and an Application in Detector Alignment*, arXiv:physics.ins-det/0810.2241 (2008).

[134] L. Nicolas *et al.*, *First Studies of T-Station Alignment with Simulated Data*, CERN-LHCb-2008-065 (2008).

[135] E. Simioni, *Weak Modes in T Alignment*, LHCb Tracking and Alignment Workshop, CERN, Geneva, Switzerland (2008).
`http://indico.cern.ch//materialDisplay.py?`
`contribId=26&sessionId=20&resId=1&materialId=slides&confId=33862`

[136] L. Nicolas and M. Needham, *Alignment of the Inner Tracker Stations Using First Data*, CERN-LHCb-PUB-2009-012 (2009).

[137] M. Needham, *Track Reconstruction in the LHCb Inner Tracker*, CERN-LHCb-PUB-2009-005 (2009).

[138] M. Merk *et al.*, *Performance of the LHCb OO Track Fitting*, LHCb-note-2000-086 (2000).

[139] M.-O. Bettler *et al.*, *Assembly of the Inner Tracker Detector Boxes*, CERN-LHCb-2008-074 (2009).

[140] N. Mangiafave, J. Dickens and V. Gibson, *A Study of the Angular Properties of the $X(3872) \to J/\psi\, \pi^+\pi^-$ Decay*, CERN-LHCb-PUB-2009-xxx note in preparation (2009).

[141] R. Brun and F. Rademakers, *ROOT - An Object Oriented Data Analysis Framework*, Proceedings AIHENP'96 Workshop, Lausanne, Switzerland, Sep. 1996, Nucl. Inst. and Meth. in Phys. Res. A **389**, 81-86 (1997).
`http://root.cern.ch/`

[142] A. Hoecker *et al.*, *TMVA - Toolkit for Multivariate Data Analysis*, arXiv:physics.data-an/0703039 (2009).

[143] The CDF Collaboration, *The "Lifetime" Distribution of $X(3872)$ Mesons Produced in $\bar{p}p$ Collisions at CDF*, CDF Note 7159 (2004).

[144] G. J. Feldman and R. D. Cousins, *Unified Approach to the Classical Statistical Analysis of Small Signals*, Phys. Rev. D **57**, 3873–3889 (1998).

# Meanwhile...

During my four years as a Ph.D. student, I have

- become married to my wonderful wife Audrey;

- become the father of my beautiful son Aaron;

- listened to thousands of hours of music (including mainly: United, Keziah Jones, Muse, The Raconteurs, The Roots, K.O.L.O, Massive Attack, Moby, TV on the Radio, Wax Tailor, Ben Harper, Radiohead, Saul Williams, Portishead, Roots Manuva);

- moved from Begnins to Crassier, from Crassier to Gland and from Gland to Genolier, all in the canton Vaud, Switzerland;

- travelled $\sim 60'000$ km to go to work every day. That's one and a half times around the Earth;

- moved from Fedora Core 3, all the way to Fedora 12;

- been to the military service for five and a half months... for nothing;

- drunk $\sim 400$ litres of espressos, up to 8 or 10 per day in the hard times;

- moved from HEP (High Energy Physics) to HEP (Haute École Pédagogique).

In this period from 2005 to 2009, the following events happened:

- the JVAL Festival in Begnins (VD), Switzerland, was born;

- Barrack Obama became the first African-American president of the United States of America;

- the world faced a severe financial crisis;

- Roger Federer has won 11 Grand Slam Titles, for a total of 15, becoming the record holder and the best tennis player of all times;

- the price of the diesel fuel went up from CHF 1.69 per litre to CHF 2.31, then down to CHF 1.50 and up again to CHF 1.71;

- the price of a coffee in a cafe went up from to CHF 2.50 to 3.50;

- ICF Geneva has finally found a place for the church services every Sunday, after having visited 8 other places, including the open-air *Parc des Bastions*;

- Sadam Hussein was hanged and Slobodan Milosevic died from a heart attack;

- the first Chinese taikonaut was sent into space;

- Michal Jackson has died;

- Switzerland co-hosted the European Football Championship... and didn't win.

# Louis Nicolas

Route de Trélex 23
1272 Genolier (VD)
Switzerland

E-mail: `louis.nicolas@a3.epfl.ch`

| | |
|---|---|
| Date of birth | April 15, 1982 |
| Nationality | Swiss |
| Marital status | Married |

## Education and degrees

| | |
|---|---|
| November 2009 | Ph.D. Thesis in High-Energy Physics on *Alignment of the LHCb Tracking Stations and Selection of $X(3872)$ and $Z(4430)^{\pm}$ in pp Collisions at 14 TeV*, LPHE, EPFL, Switzerland |
| January 2008 | CHIPP Ph.D. Winter School, Näfels, Switzerland |
| 2005 – 2009 | Ph.D. Studies in High-Energy Physics at LPHE (EPFL), Switzerland |
| 2004 – 2009 | Member of the LHCb collaboration |
| 2004 – 2005 | Master Thesis in High-Energy Physics on *Selection and Study of the $B_s^0 \to D_s^- \pi^+$ Decay at LHCb*, Laboratory of High Energy Physics (LPHE), Swiss Federal School of Technology (EPFL), Switzerland |
| 2000 – 2004 | Physics Studies at EPFL |

## Publications

- L. Nicolas and M. Needham, *Alignment of the Inner Tracker Stations Using First Data*, CERN-LHCb-PUB-2009-012 (2009).

- L. Nicolas *et al.*, *First Studies of T-Station Alignment with Simulated Data*, CERN-LHCb-2008-065 (2008).

- L. Nicolas *et al.*, *Tracking Stations Alignment with Kalman Tracks at LHCb*, IEEE Nuclear Science Symposium Conference Record, N20-3, 1714–1719 (2008).

- J. Borel, L. Nicolas, O. Schneider and J. van Hunen, *The $B_s \to D_s^- \pi^+$ and $B_s \to D_s^{\mp} K^{\pm}$ Selections*, CERN-LHCb-2007-017 (2007).

- L. Nicolas, *Selection and Study of the $B_s^0 \to D_s^- \pi^+$ Decay at LHCb*, EPFL, Lausanne, Switzerland, CERN-THESIS-2005-035 (2005).